

DETERMINATION OF ELECTRONIC ENERGY LEVELS OF MOLECULES  
BY 90° LOW ENERGY ELECTRON SCATTERING\*

Thesis by  
Pax Samuel Pin Wei

In Partial Fulfillment of the Requirements  
For the Degree of  
Doctor of Philosophy

California Institute of Technology  
Pasadena, California  
October 10, 1967

\*Work supported in part by the  
United States Atomic Energy Commission

Dedicated To

My

Parents

## ACKNOWLEDGEMENT

The author wishes to express his gratitude to Professor Aron Kuppermann for suggesting the project described in this thesis and for his guidance and help given throughout the course of the investigation.

He wishes to acknowledge also the immense help given by Dr. L. M. Raff, who taught him many experimental techniques during the time from June, 1962 to January, 1963.

He wishes to thank Professor G. S. Hammond for suggesting the studies on two molecules, norbornadiene and quadricyclene, and for many helpful discussions. The preparation of these two samples by Carl C. Wamser is appreciated.

Thanks are due to A. Lonnie Lane for furnishing information concerning the purities of several hydrocarbon samples, to Dr. S. Trajmar and J. K. Rice for communications of their experimental results before publication, and to Dr. L. Robbin Martin for reading the manuscript.

The encouragement and understanding of Amy, his wife, during this research is gratefully acknowledged.

DETERMINATION OF ELECTRONIC ENERGY LEVELS OF MOLECULES  
BY 90° LOW ENERGY ELECTRON SCATTERING

Abstract

A review of the theory of electron scattering indicates that low incident beam energies and large scattering angles are the favorable conditions for the observation of optically forbidden transitions in atoms and molecules.

An apparatus capable of yielding electron impact spectra at 90° with incident electron beam energies between 30 and 50 electron volts is described. The resolution of the instrument is about 1 electron volt.

Impact spectra of thirteen molecules have been obtained. Known forbidden transitions to the helium  $2^3S$ , the hydrogen  $b^3\Sigma_u^+$ , the nitrogen  $A^3\Sigma_u^+$ ,  $B^3\Pi_g$ ,  $a^1\Pi_g$  and  $C^3\Pi_u$ , the carbon monoxide  $a^3\Pi$ , the ethylene  $\tilde{a}^3B_{1u}$ , and the benzene  $\tilde{a}^3B_{1u}$  states from the corresponding ground states have been observed.

In addition, singlet-triplet vertical transitions in acetylene, propyne, propadiene, norbornadiene and quadricyclene, peaking at 5.9, 5.9, 4.5, 3.8, and 4.0 eV ( $\pm 0.2$  eV), respectively, have been observed and assigned for the first time.

Table 1. Observed Electronic Transitions In This Work

molecule	peak of observed band	assignment
helium	19.8 $\pm$ 0.2 ev 21.0* 22.8*	$2^3S$ $2^3P$ & $2^1P$ $3^3S, 3^1S, \text{etc}$
hydrogen	10.2 12.7*	$b^3\Sigma_u^+$ $B^1\Sigma_u^+, a^3\Sigma_g^+, c^3\Pi_u$ & $C^1\Pi_u$
nitrogen	8.5* 11.1 13.2* 16.0	$A^3\Sigma_u^+, B^3\Pi_g$ & $a^1\Pi_g$ $C^3\Pi_u$ $b^1\Pi_u, \text{etc}$
carbon monoxide	6.2 8.5 10.6* 13.5*	$a^3\Pi$ $A^1\Pi$ $b^3\Sigma^+$
ethylene	4.4 7.8* 10.0	$\tilde{a}^3B_{1u}$ (or T) $\tilde{A}^1B_{1u}$ & $\tilde{B}$ (or V & R)
acetylene	5.9* 9.4	T & $\tilde{A}^1A_u$
propyne	5.9*	T & $\tilde{A}$
propadiene	4.5 7.6* 8.7* 9.5*	T
propane	---	onset of continuum at 8.0 ev
1,3-butadiene	5.9 9.7	$\tilde{A}$ (or $V_1$ ) $V_4$
benzene	3.8 7.0* 10.0	$\tilde{a}^3B_{1u}$ $\tilde{B}^1B_{1u}$ & $\tilde{C}^1E_{1u}$
norbornadiene	3.8 7.4	T
quadricyclene	4.0	T

\* = not resolved

## TABLE OF CONTENTS

	Page
I. INTRODUCTION	1
II. THEORY OF ELECTRON SCATTERING	3
II.1. The Classical Picture	3
II.2. Motion of Electron Wave Packets	4
II.3. Definition of Scattering Cross Sections	4
II.4. Quantum Theory of Scattering of Electrons by Hydrogen Atoms	6
II.4.1. Direct Collisions	6
II.4.2. Born Approximation for Direct Collisions	9
II.4.3. Differential Cross Sections From Probability Currents	12
II.4.4. Selection Rules From the Born Approximation	14
II.4.5. Energy Dependence of Cross Sections	17
II.4.6. Exchange Collisions Born-Oppenheimer Approximation	19
II.4.7. Exchange Collisions and Indistinguishable Electrons	21
II.5. Scattering of Electrons by Helium Atoms Born-Oppenheimer Approximation	25
II.6. Limitations of the Born-Oppenheimer Approximation	26
II.7. Method of Partial Waves	27
II.7.1. Asymptotic Form of the Radial Partial Wave Function $\mathcal{G}_l(r)$	30
II.7.2. Solution of $\mathcal{G}_l(r)$ for A Free Particle	31

	Page
II.7.3. Differential Cross Sections From Phase Shifts	33
II.7.4. Total Cross Sections and Partial Cross Sections	37
II.7.5. Comparison of Classical and Quantum mechanical Partial Cross Sections	39
II.7.6. Angular Distributions of Scattered Electrons	41
II.7.7. Conservation of Particles in Elastic Scattering	42
II.7.8. Maximum Inelastic Cross Section For a Given Angular Momentum	44
II.8. Method of Distorted Waves	47
II.9. Close-Coupling Approximation	49
II.10. Ochkur-Born-Oppenheimer Approximation for Exchange Scattering	51
II.10.1. Prior and Post Interactions	52
II.10.2. Exchange Scattering Amplitude	53
II.10.3. Cross Sections for Triplet Excitations in Helium	55
II.10.4. Rudge's Correction of Ochkur's Formula	57
II.11. Theory of Electron Scattering by Molecules	58
II.11.1. Electronic Excitations in Diatomic Molecules The Franck-Condon Principle	59
II.11.2. Electronic Excitation Cross Sections	61
II.11.3. Statistical Average of the Differential Cross Sections	64
II.12. General Properties of Inelastic Cross Sections	67

	Page
III. HISTORICAL BACKGROUND	69
III.1. Forward Scattering Measurements Lassettre Et Al	70
III.2. Forward Scattering Measurements Simpson Et Al	72
III.3. Electronic Excitation at Threshold Trapped-Electron Method	72
III.4. Large-Angle Measurements	74
IV. EXPERIMENTAL	75
IV.1. Apparatus	75
IV.1.1. Vacuum System	76
IV.1.2. Electron Gun	80
IV.1.3. Collision Chamber	84
IV.1.4. Inlet System	88
IV.1.5. Helmholtz Coils	88
IV.1.6. Measuring Equipments and Power Supplies	89
IV.2. Experimental Procedure	90
IV.2.1. Pump-Down and Bake-Out	90
IV.2.2. Degassing and Activation of the Cathode	91
IV.2.3. Functions of the Electrodes and Grids	92
IV.2.4. Introduction of Gas Samples	94
IV.2.5. Procedure for Taking a Spectrum	95
IV.3. Characteristics of the Apparatus	95
IV.3.1. El and Cathode As a Diode	95
IV.3.2. Electron Beam Currents Measured At $E^4$	96
IV.3.3. Estimate of the Cathode Temperature	99
IV.3.4. Effect of the Earth's Magnetic Field	101

	Page
IV.3.5. Background Current as A Function of Magnetic Field	102
IV.3.6. The Lozier Grid	104
IV.3.7. Behaviour of the G2 Grid	105
IV.3.8. Holding Potential on the Beam Collector	107
IV.3.9. Full Width at Half Maximum of Elastic Peaks	110
IV.3.10. Helium Spectra As A Function of the Holding Potential Between SC and G3	112
IV.3.11. The Rising Background	115
IV.3.12. Limitations of the Present Apparatus	117
IV.3.13. Comparison of Performance of Present Apparatus with Previous Version	120
V. RESULTS AND DISCUSSIONS	123
V.1. Helium	126
V.1.1. Summary of Previous Electron Impact Work	126
V.1.2. Electron Impact Spectra of Helium	132
V.2. Hydrogen	134
V.2.1. Summary of Previous Electron Impact Work	136
V.2.2. Electron Impact Spectra of Hydrogen	137
V.3. Nitrogen	142
V.3.1. Summary of Previous Electron Impact Work	144
V.3.2. Electron Impact Spectra of Nitrogen	146

	Page
V.4. Carbon Monoxide	151
V.4.1. Summary of Previous Electron Impact Work	153
V.4.2. Electron Impact Spectra of Carbon Monoxide	155
V.5. Ethylene	160
V.5.1. Summary of Previous Electron Impact Work	162
V.5.2. Electron Impact Spectra of Ethylene	164
V.6. Acetylene	169
V.6.1. Summary of Previous Electron Impact Work	171
V.6.2. Electron Impact Spectra of Acetylene	173
V.7. Propyne	177
V.7.1. Summary of Previous Electron Impact Work	178
V.7.2. Electron Impact Spectra of Propyne	179
V.8. Propadiene	184
V.8.1. Summary of Theoretical Calculations	185
V.8.2. Electron Impact Spectra of Propadiene	186
V.9. Propane	191
V.9.1. Summary of Previous Electron Impact Work	192
V.9.2. Electron Impact Spectra of Propane	193
V.10. 1,3-Butadiene	197
V.10.1. Summary of Previous Electron Impact Work	200

	Page
V.10.2 Electron Impact Spectra of 1,3-Butadiene	201
V.11. Benzene	206
V.11.1. Summary of Previous Electron Impact Work	208
V.11.2. Electron Impact Spectra of Benzene	209
V.12. Norbornadiene and Quadricyclene	215
V.12.1. Electronic Structure and Spectrum of Norbornadiene	218
V.12.2. Electron Impact Spectra of Norbornadiene	219
V.12.3. Ultraviolet Absorption Spectrum of Quadricyclene	223
V.12.4. Electron Impact Spectra of Quadricyclene	224
REFERENCES	229
PROPOSITIONS	
I. A Nitrogen Atom Beam From Active Nitrogen	240
II. Reactive Collisions In Crossed Molecular Beams. The Reaction Of Nitrogen Atoms With Oxygen Molecules	246
III. Electronic Absorption Spectra of OH and OD Radicals Trapped in Rare Gas Matrices	258
IV. A study of the Angular Distribution of Photoelectrons	271
V. The Neon Resonance Line Lamp	276
VITA	282

## I. Introduction

The usual experimental techniques in studying the electronic energy levels of atoms and molecules can be described as follows. One excites the molecules with some appropriate energy source and observes the excitation process by measuring the energy involved. Excited electronic states below the first ionization potential of a molecule usually lie between a few electron volts to about 20 electron volts above the ground state. These energy levels are of great interest in the field of chemistry and physics because they provide information on molecular structures and properties.

Energy sources generally used for the excitation purpose are electrons and photons. The latter have been adopted most widely because of experimental high resolution and accuracy. However, there are two restrictions accompanying the use of photons. First, energy range beyond about 7 electron volts corresponds to the vacuum ultraviolet region which presents experimental difficulties. Second, there are certain selection rules based on theory and experiment that a transition caused by a photon must obey. In particular it is well known that optical transitions between levels of different multiplicity are highly forbidden if spin-orbit interaction is negligible. This is often the case for atoms and molecules of small atomic number.

Fortunately, by using low energy electrons as an energy source these defects can be overcome.

The term "low energy" means that the energy of the electrons is of the same order of magnitude as that of the

energy of the molecular electrons. In practice, electron beams having energies from a few electron volts to a few tens of electron volts can be employed.

It was first pointed out by Oppenheimer<sup>(1)</sup> that in the collision of an electron with an atom the electron exchange effect of the incident electron with one of those in the atom may be important. Physically speaking a transition involving a change in spin multiplicity may thus be induced.

The purpose of this research is to obtain information about low-lying electronic states of molecules which is not available from optical spectroscopy.

## II. Theory of Electron Scattering

### II.1. The classical picture

From the classical mechanical point of view an electron with kinetic energy  $V$  electron volts travels in space with the speed

$$v = 0.593 \times 10^8 \sqrt{V} \text{ cm/sec.} \quad (1)$$

From this formula the following table results.

Kinetic energy of electron (e v)	1	10	30	50	100
Speed of electron ( $10^8$ cm/sec)	0.593	1.87	3.24	4.19	5.93

On the other hand, the root-mean-square velocity  $v_{rms}$  of a gas molecule of mass  $m$  at temperature  $T$  is given by

$$v_{rms} = (3KT/m)^{\frac{1}{2}} \quad (2)$$

where  $K = 1.380 \times 10^{-16}$  erg/deg./molecule is Boltzmann's constant. At room temperature,  $T = 298^\circ\text{K}$ . Therefore,  $v_{rms}$  equals

$$\begin{aligned} &0.515 \times 10^5 \text{ cm/sec for } N_2 \text{ and} \\ &1.93 \times 10^5 \text{ cm/sec for } H_2 . \end{aligned}$$

Thus, when a beam of low-energy electrons is fired into a box containing gas molecules, the latter can be assumed stationary. To a good approximation, the laboratory coordinate system can be taken as the center-of-mass coordinate system.

## II.2. Motion of electron wave packets

According to de Broglie's theory of matter waves<sup>(2)</sup> when a particle is traveling with linear momentum  $p$ , there is always a wave of wavelength

$$\lambda = \frac{h}{p} = \frac{h}{mv} \quad (3)$$

associated with it, where  $h$  is Planck's constant.

In the case of low-energy electrons this wavelength is given in the table below for several electron energies.

Kinetic energy of electron (e v )	1	10	30	50	100
Wavelength of associated wave (Å)	12.27	3.88	2.24	1.735	1.227

The physical size of a gas molecule usually is of the order of  $1\sim 3$  Å in diameter. Thus the region of interaction of an incident electron with a molecule is of the same order of magnitude as the wavelength of the electron wave. Hence the problem must be treated with quantum mechanics.

## II.3. Definition of Scattering Cross Sections

Consider a beam of electrons with known kinetic energy, passing through a hypothetical gas consisting of "hard sphere" atoms of cross-sectional area  $Q$ . If the number density of the gas is  $N$ , and the original electron current density is  $I$ , then the decrease in current density

due to scattering after traveling a small distance  $dx$  is given by

$$dI = -NQ I dx \quad (4)$$

On integration of equation (4), we have

$$I = I_0 \exp(-NQx) \quad (5)$$

where  $I_0$  is the current density at  $x=0$ .

In reality gas molecules are not hard spheres. Electrons are scattered by molecules through some interaction potential. However, equation (5) can still be used to define  $Q$ . It is called the total collision cross section and is a function of the relative kinetic energy  $E$  in general.

The collision of an electron with a gas molecule can be classified elastic or inelastic depending on whether or not there is energy transfer from the electron into the internal degrees of freedom of the molecule.

Thus  $Q$  can be expressed as

$$Q = Q_0 + \sum_{j=1}^n Q_j \quad (6)$$

where  $Q_0$  = total elastic cross section,

$Q_j = j$ -th total inelastic cross section,

$n$  = number of all possible inelastic processes.

In practice, it is convenient to define the differential cross section  $\sigma_j$  as the cross section per unit solid angle. Thus  $\sigma_j d\Omega$  represents the cross section for scattering into the solid angle  $d\Omega$  through the  $j$ -th

process. The following relation holds:

$$Q = \sum_{j=0}^n Q_j = \sum_{j=0}^n \int_{\Omega} \sigma_j d\Omega . \quad (7)$$

If a spherical polar coordinate system centered on the molecule is used, then

$$Q_j = \int_{\phi=0}^{\phi=2\pi} \int_{\theta=0}^{\theta=\pi} \sigma_j \sin\theta d\theta d\phi . \quad (8)$$

In general,  $\sigma_j$  is a function of  $E$ ,  $\theta$ , and  $\phi$ . If we know all the  $\sigma_j$  then we know all about the scattering process.

#### II.4. Quantum theory of Scattering of electrons by hydrogen atoms

In order to treat the scattering process by quantum mechanics, the scattering system must be described by wave functions that are solutions of Schroedinger's equation and which satisfy appropriate boundary conditions. The simplest case is the collision between an electron and a hydrogen atom. The arguments and derivations presented below serve only as a brief review of the field. More detailed discussion can be found in the book by Mott and Massey<sup>(3)</sup>.

##### II.4.1. Direct Collisions

If we assume there is no exchange effect and that electrons are distinguishable, then the incident electron and the atomic electron can be labeled by subscripts 1 and 2, respectively. The Schroedinger equation for the system

can be written as

$$H \Psi(\vec{r}_1, \vec{r}_2) = E \Psi(\vec{r}_1, \vec{r}_2) \quad (9)$$

where

$H$  = Hamiltonian of the system (neglecting spin)

$$= \left( -\frac{\hbar^2}{2m} \nabla_2^2 - \frac{e^2}{r_2} \right) + \left( -\frac{\hbar^2}{2m} \nabla_1^2 - \frac{e^2}{r_1} + \frac{e^2}{r_{12}} \right) \quad (10)$$

$\Psi$  = wave function of the system (space part only),

$E$  = total energy of the system,

$\vec{r}_j$  = radius vector from the proton to the  $j$ -th electron,  $j = 1$  or  $2$ ,

$r_{12}$  = distance between electrons 1 and 2,

$m$  = mass of an electron and

$\nabla_j^2 = \frac{\partial^2}{\partial x_j^2} + \frac{\partial^2}{\partial y_j^2} + \frac{\partial^2}{\partial z_j^2}$  = the Laplacian operator for the  $j$ -th electron.

We note that  $E = E_0 + T_0$ , where  $E_0$  is the ground state energy of the atom and  $T_0$  is the kinetic energy of the incident electron. In the absence of the atom, the wave function of electron 1 can be written as  $e^{i\vec{k}_0 \cdot \vec{r}_1}$  and satisfies the wave equation of a particle in free space

$$-\frac{\hbar^2}{2m} \nabla_1^2 e^{i\vec{k}_0 \cdot \vec{r}_1} = T_0 e^{i\vec{k}_0 \cdot \vec{r}_1} \quad (11)$$

Therefore,

$$\vec{k}_0^2 = 2m T_0 / \hbar^2 = \frac{2m}{\hbar^2} (E - E_0) \quad (12)$$

where  $\vec{k}_0 = k_0 \vec{n}_0$  = incident wave number vector,

and  $\vec{n}_0$  = unit vector along the incident direction.

If  $\psi_j(\vec{r}_2)$  are solutions for the Schrodinger equation of the hydrogen atom

$$\left[ -\frac{\hbar^2}{2m} \nabla_2^2 - \frac{e^2}{r_2} \right] \psi_j(\vec{r}_2) = E_j \psi_j(\vec{r}_2), \quad (13)$$

where  $j = 0, 1, 2, \dots$ ,

then the  $\psi_j(\vec{r}_2)$  form a complete orthonormal set in the  $\vec{r}_2$  space.

Thus we can expand  $\bar{\Psi}(\vec{r}_1, \vec{r}_2)$  in the  $\vec{r}_2$  space as

$$\bar{\Psi}(\vec{r}_1, \vec{r}_2) = e^{i\vec{k}_0 \cdot \vec{r}_1} \psi_0(\vec{r}_2) + \sum_{j=0,1,2,\dots} F_j(\vec{r}_1) \psi_j(\vec{r}_2). \quad (14)$$

On the right hand side of equation (14), the first term represents the incident wave and the ground state of the atom; the term in the summation corresponding to  $j=0$  represents elastic scattering from the atom; the others, with  $j \geq 1$  are associated with the inelastic scattering processes, the sum extending all possible discrete and continuum states of the atom. For states with energy higher than the incident energy, the asymptotic forms of  $F_j$  will be a dying exponential. Including these states in the summation is necessary since, for the expansion to be correct, the set of basis functions must be complete.

In order to solve for  $F_j(\vec{r}_1)$ , we substitute equation (14) into equation (9), multiply both sides by  $\psi_n^*(\vec{r}_2)$ , and integrate over  $\vec{r}_2$ . Making use of equation (11) and (13) and the orthonormality of the  $\psi_j(\vec{r}_2)$ ,

we obtain

$$\left[ \frac{\hbar^2}{2m} \nabla_1^2 + (E - E_n) \right] F_n(\vec{r}_1) \quad (15)$$

$$= V_{on} e^{i\vec{k}_0 \cdot \vec{r}_1} + \sum_{j=0,1,2,\dots} F_j(\vec{r}_1) V_{jn} ,$$

where

$$V_{jn}(r_1) = \int \psi_n^*(\vec{r}_2) \left[ -\frac{\epsilon^2}{r_1} + \frac{\epsilon^2}{r_{12}} \right] \psi_j(\vec{r}_2) d\vec{r}_2 . \quad (16)$$

Equation (15) is a set of coupled partial differential equations. In principle if we know  $\psi_n(\vec{r}_2)$  then we can calculate  $V_{jn}$ . Since  $E$  is also known we can solve for  $F_n(\vec{r}_1)$ . Hence the total wave function  $\Psi(\vec{r}_1, \vec{r}_2)$  can be obtained.

#### II.4.2. Born Approximation for direct collisions

The Born approximation is applicable whenever the incident electron energy is much higher than the interaction energy such that the scattered wave is small compared to the incident wave. This means that the first term on the right hand side of equation (14) is the dominating term of the total wave function. Consequently,  $V_{jn}$  and  $F_j(\vec{r}_1)$  in equation (15) are all small compared to  $V_{on}$  and  $e^{i\vec{k}_0 \cdot \vec{r}_1}$ , respectively, and may be neglected. This is actually the first order perturbation method applied to scattering theory.

When the Born approximation is valid, we can rewrite equation (15) as

$$(\nabla_i^2 + k_n^2) F_n(\vec{r}_i) = \frac{2m}{\hbar^2} V_{0n} e^{i \vec{k}_0 \cdot \vec{n}_0 \cdot \vec{r}_i}, \quad (17)$$

where

$$k_n^2 = \frac{2m}{\hbar^2} (E - E_n). \quad (18)$$

Now equation (17) is a set of uncoupled inhomogeneous partial differential equations for  $n = 0, 1, 2, \dots$  etc.

For a realistic scattering potential,  $F_n(\vec{r}_i)$  is everywhere finite, and at large distances from the atom ( $r_i \rightarrow \infty$ ), the scattered wave must be close to the form of a spherical wave. With these ideas in mind we see that equation (17) is a special kind of partial differential equations solvable by the method of Green's function<sup>(4)</sup>.

Thus the asymptotic form of the solution  $F_n(\vec{r}_i)$  from equation (17) can be written as<sup>(4)</sup>:

$$F_n(\vec{r}_i) \underset{(r_i \rightarrow \infty)}{\sim} \int_{\vec{r}'} \left[ -\frac{1}{4\pi} \frac{e^{i k_n |\vec{r}_i - \vec{r}'|}}{|\vec{r}_i - \vec{r}'|} \right] \left[ \frac{2m}{\hbar^2} V_{0n} e^{i \vec{k}_0 \cdot \vec{n}_0 \cdot \vec{r}'} \right] d\vec{r}'. \quad (19)$$

If we define  $\vec{n}$  to be in the direction of  $\vec{r}_i$ , namely, the direction of scattering, then

$$|\vec{r}_i - \vec{r}'| \underset{(r_i \rightarrow \infty)}{\sim} r_i - \vec{n} \cdot \vec{r}' + \left( \text{terms of order } \frac{1}{r_i} \right) + \dots \quad (20)$$

Substituting equation (20) into equation (19), we have

$$F_n(\vec{r}_i) \underset{(r_i \rightarrow \infty)}{\sim} \left( \frac{e^{i k_n r_i}}{r_i} \right) \int_{\vec{r}'} \left[ -\frac{1}{4\pi} e^{-i k_n \vec{n} \cdot \vec{r}'} \right] \left[ \frac{2m}{\hbar^2} V_{on} e^{i k_o \vec{n}_o \cdot \vec{r}'} \right] d\vec{r}'. \quad (21)$$

Since the only dependence on  $\vec{r}_i$  in the integral on the right hand side of equation (21) is through  $\vec{n}$ , the direction of scattering, it is customary to define

$$f_n(\theta_i, \phi_i) = \int_{\vec{r}'} \left[ -\frac{1}{4\pi} e^{-i k_n \vec{n} \cdot \vec{r}'} \right] \left[ \frac{2m}{\hbar^2} V_{on} e^{i k_o \vec{n}_o \cdot \vec{r}'} \right] d\vec{r}'. \quad (22)$$

Hence, at large  $r_i$ , the solution of equation (17) becomes:

$$F_n(\vec{r}_i) \underset{(r_i \rightarrow \infty)}{\sim} \frac{e^{i k_n r_i}}{r_i} f_n(\theta_i, \phi_i). \quad (23)$$

$F_n(\vec{r}_i)$  is associated with the amplitude of the scattered wave through the  $n$ -th process. It can be obtained in the Born approximation from equation (21).

#### II.4.3. Differential cross sections from probability currents

Associated to a particle described by a certain wave function  $\psi(\vec{r})$ , there is a probability current density  $\vec{S}$  defined by (5)

$$\vec{S} = \frac{\hbar}{2mi} (\psi^* \vec{\nabla} \psi - \psi \vec{\nabla} \psi^*), \quad (24)$$

where  $\vec{\nabla}$  is the gradient operator.  $\vec{S}$  satisfies the equation

$$\frac{\partial P}{\partial t} + \text{div } \vec{S} = 0, \quad (25)$$

where  $P = |\psi|^2$ , which is analogous to the continuity equation in hydrodynamics,

$$\frac{\partial \rho}{\partial t} + \text{div } \vec{j} = 0, \quad (26)$$

where  $\rho$  is fluid density and  $\vec{j}$  its current density.

In our scattering problem, the incident wave may be described as a plane wave in the  $z$ -direction

$$\psi(\vec{r}_i) = C e^{i\vec{k}_0 \cdot \vec{r}_i} = C e^{i k_0 z_i}, \quad (27)$$

where  $C$  is a normalization constant.

Hence the probability current density associated with the incident plane wave in the  $z$ -direction is

$$S_{\text{incident}} = \frac{\hbar k_0}{m} |C|^2. \quad (28)$$

Now the scattered wave at large  $r_1$  is, from equation(23)

$$F_n(\vec{r}_1) \cong C \frac{e^{i k_n r_1}}{r_1} f_n(\theta_1, \phi_1), \quad (29)$$

where  $C$  is the same normalization constant.

The gradient operator in spherical polar coordinates is given by

$$\vec{\nabla} = \vec{u}_r \frac{\partial}{\partial r} + \vec{u}_\theta \frac{1}{r} \frac{\partial}{\partial \theta} + \vec{u}_\phi \frac{1}{r \sin \theta} \frac{\partial}{\partial \phi}, \quad (30)$$

where  $\vec{u}_r$ ,  $\vec{u}_\theta$ ,  $\vec{u}_\phi$  are unit vectors associated with the  $r$ ,  $\theta$ ,  $\phi$ , coordinates, respectively.

In order to obtain the probability current  $dS_{out}$  coming out an element of solid angle  $d\Omega_1$  at large  $r_1$ , we simply multiply the radial component of the probability current density vector by the element of surface area at a distance  $r_1$  subtended by  $d\Omega_1$ .

$$dS_{out} = \left( \frac{\hbar k_n}{m} \right) |C|^2 \left| f_n(\theta_1, \phi_1) \right|^2 d\Omega_1, \quad (31)$$

The ratio of  $dS_{out}$  to  $S_{inc.}$  is the probability current scattered into solid angle  $d\Omega_1$  per unit incoming probability current through the  $n$ -th scattering process. By definition, it is equal to the differential cross section  $\sigma_n(E, \theta_1, \phi_1)$  times  $d\Omega_1$ . Thus, from equations (28) and (31) we have

$$\sigma_n(E, \theta_1, \phi_1) = \frac{k_n}{k_0} \left| f_n(\theta_1, \phi_1) \right|^2. \quad (32)$$

Substituting the definition of  $f_n(\theta, \phi_1)$  from equation (22) into equation (32) yields

$$\sigma_n(E, \theta, \phi_1) = \frac{4\pi^2 m^2}{\hbar^4} \left( \frac{k_n}{k_0} \right) \left| \int V_{on} e^{i(k_0 \vec{n} - k_n \vec{n}) \cdot \vec{r}'} d\vec{r}' \right|^2, \quad (33)$$

where  $V_{on}$  is defined in equation (16). We see that equation (33) is the expression for the differential cross section derived from the Born approximation of direct scattering.

#### II.4.4. Selection rules from the Born Approximation

For the case of inelastic electron scattering by a hydrogen atom ( $n > 0$ ), we may further simplify the expression for  $\sigma_n(E, \theta, \phi_1)$  by substituting  $V_{on}$  into equation (33) and making use of the following equation for small  $\Delta \vec{k}$  <sup>(6)</sup>

$$\int \frac{e^{i \Delta \vec{k} \cdot \vec{r}'}}{|\vec{r}' - \vec{r}_2|} d\vec{r}' \cong \frac{4\pi}{(\Delta k)^2} e^{i \Delta \vec{k} \cdot \vec{r}_2}, \quad (34)$$

where

$$\Delta \vec{k} = k_0 \vec{n}_0 - k_n \vec{n}_n, \quad (35)$$

is the wave number transfer vector, and

$$(\Delta k)^2 = k_0^2 + k_n^2 - 2 k_0 k_n \cos \theta_1. \quad (36)$$

Thus from equations (16), (33), (34), (35), and (36),

we have:

$$\sigma_n(E, \theta_1, \phi_1) = \frac{4\pi^2 m^2}{\hbar^4} \left( \frac{k_n}{k_0} \right) \left| \frac{4\pi\epsilon^2}{(\Delta k)^2} \int \psi_n^*(\vec{r}_2) e^{i(\Delta k) \cdot \vec{r}_2} \psi_0(\vec{r}_2) d\vec{r}_2 \right|^2 \quad (37)$$

In order to simplify equation (37), let us choose  $\vec{\Delta k}$  to be along the  $z_2$ -direction, thus

$$e^{i \vec{\Delta k} \cdot \vec{r}_2} = e^{i(\Delta k) z_2} \quad (38)$$

In general, if  $[i(\Delta k) z_2] \ll \infty$ , we have the following expansion (7)

$$\begin{aligned} e^{i(\Delta k) z_2} &= 1 + \frac{i(\Delta k) z_2}{1!} + \frac{[i(\Delta k) z_2]^2}{2!} + \dots \\ &= \sum_{l=0}^{\infty} \frac{[i(\Delta k) z_2]^l}{l!} \end{aligned} \quad (39)$$

Substituting equation (39) into equation (37), we obtain

$$\sigma_n(E, \theta_1, \phi_1) = \frac{64\pi^4 m^2 \epsilon^4}{\hbar^4 (\Delta k)^4} \left( \frac{k_n}{k_0} \right) \left| \sum_{l=0}^{\infty} \left[ \frac{(i \Delta k)^l}{l!} \right] \langle z_2^l \rangle_{on} \right|^2 \quad (40)$$

where

$$\langle z_2^l \rangle_{on} = \int \psi_n^* z_2^l \psi_0 d\vec{r}_2 .$$

The first term in the summation with  $\ell = 0$  is zero for  $n = 0$  because of the orthonormality of the wave functions  $\psi_n(\vec{r}_2)$ .

From equation (36) we see that the requirements for  $\Delta k$  to be small are that:

- a).  $\vec{k}_0$  and  $\vec{k}_n$  are approximately of the same magnitude,
- b). the scattering angle  $\theta$  is small. These are also the conditions for the Born approximation to be valid.

When the assumption

$$(\Delta k)^2 \gg (\Delta k)^4 \quad (41)$$

is introduced into equation (40), the resulting

$\sigma_n(E, \theta, \phi_i)$  depends on the electric dipole transition moment  $\langle \vec{z}_i \rangle_{0n}$  only. This dependence is the same as that of the transition probability of an electric dipole interacting with an electromagnetic field (8). In other words, the small - angle inelastic scattering of sufficiently high energy electrons by H - atoms obeys the same electric-dipole selection rules as do the optical transitions. This conclusion may be generalized for many-electron atoms and molecules and is actually observed experimentally by many authors. (See part III. below.)

Whenever in equation (40) the term for  $\ell = 1$  is zero but that for  $\ell = 2$  is non-zero, we have a quadrupole-allowed transition analogous to the electric quadrupole allowed but dipole forbidden optical transitions.

#### II.4.5. Energy dependence of cross sections

We have seen above that the Born approximation should be valid for large incident energies and small scattering angles only. However, the agreement of experiment with theory has been surprisingly good down to fairly low beam energies ( $\sim 200$  e v ) and up to fairly large scattering angles ( $\sim 15^\circ$ ). Furthermore, the differential cross section decreases rapidly with angle. ( See Section III.1.)

Therefore, it seems worthwhile to estimate the energy dependence of inelastic cross sections  $Q_n$  from the Born approximation although it breaks down at large angles.

From equation (8), we have for the cross-section  $Q_n(E)$  for excitation of the  $n$ -th state

$$Q_n(E) = \int_{\phi=0}^{2\pi} \int_{\theta=0}^{\pi} \sigma_n(E, \theta, \phi) \sin \theta \, d\theta \, d\phi . \quad (42)$$

In our case, a central potential problem, there is no  $\phi$ -dependence, and therefore

$$Q_n(E) = 2\pi \int_{\theta=0}^{\pi} \sigma_n(E, \theta) \sin \theta \, d\theta . \quad (43)$$

It is convenient to change the variable of integration (11) from  $\theta$  to  $\Delta k$  because  $\sigma_n(E, \theta)$  is readily obtained in terms of  $\Delta k$ . Thus, from equation (36) we have (dropping the subscripts 1 )

$$\sin \theta d\theta = \frac{(\Delta k) d(\Delta k)}{k_0 k_n} \quad (44)$$

The limits for integration, from equation (36), are now

$$k_0 - k_n \quad \text{and} \quad k_0 + k_n .$$

Thus equation (43) becomes:

$$Q_n(E) = 2\pi \int_{k_0 - k_n}^{k_0 + k_n} \sigma_n(E, \Delta k) \frac{(\Delta k) d(\Delta k)}{k_0 k_n} \quad (45)$$

For the optically allowed electric dipole transition ( $\langle \mathcal{D}_2 \rangle_{on} \neq 0$ ) at large incident energy  $E$ , we have<sup>(9)</sup>

$$Q_n(E) \cong \frac{8\pi^3 m E^4}{\hbar^2} \left| \langle \mathcal{D}_2 \rangle_{on} \right|^2 \frac{1}{E} \log \frac{E}{\frac{1}{4}(E_n - E_0)} \quad (46)$$

Similarly, for the electric quadrupole transition (optically forbidden) at large incident energy  $E$ , we have:

$$Q_n(E) \cong \frac{16\pi^5 m^2 E^4}{\hbar^4} \left| \langle \mathcal{D}_2^2 \rangle_{on} \right|^2 \frac{E_0}{E} \quad (47)$$

Thus we see that the optically forbidden transitions depend on  $E$  more strongly than does the optically allowed ones.

#### II.4.6. Exchange Collisions      Born-Oppenheimer Approximation

The theory of scattering of electrons by hydrogen atoms which we have developed so far has been limited to direct collisions. We have assumed that electrons are distinguishable and that there is no exchange. The corresponding results are in agreement with experiment under the conditions of high incident energy and low scattering angle mentioned above. However, at low incident energies and large scattering angles the contribution from electron exchange becomes non-negligible.

In equation (40), we obtained a differential cross section for the incident electron being scattered into a given direction after exciting the H-atom to the n-th state. It is also possible that the incident electron may be captured by the atom into the n-th state, and the atomic electron ejected. This phenomenon is known as electron exchange. It was first taken into account by Oppenheimer <sup>(1)</sup> in treating the problems of elastic scattering of electrons by hydrogen and helium atoms.

In order to calculate the probability of exchange scattering, the total wave function  $\Psi(\vec{r}_1, \vec{r}_2)$  may be expanded in a linear combination of  $\psi_n(\vec{r}_1)$  with coefficients  $G_n(\vec{r}_2)$  to be determined in a way similar to the direct collision case

$$\Psi(\vec{r}_1, \vec{r}_2) = \sum_n G_n(\vec{r}_2) \psi_n(\vec{r}_1) , \quad (48)$$

where  $\psi_n(\vec{r}_1)$  satisfy the H-atom Schroedinger equation and form a complete orthonormal set in  $\vec{r}_1$  space, (because the incident electron 1 is captured by the atom after scattering).

(10) It can be shown that  $G_n(\vec{r}_2)$  has the asymptotic form

$$G_n(\vec{r}_2) \underset{(r_2 \rightarrow \infty)}{\sim} \frac{e^{ik_n r_2}}{r_2} g_n(\theta_2, \phi_2). \quad (49)$$

Physically this may be visualized as  $G_n(\vec{r}_2)$  taking the form of an outgoing spherical wave when  $r_2$  becomes large.

Thus the differential cross section for capture of electron 1 into the  $n$ -th state and ejection of electron 2 into the direction  $\Omega_2(\theta_2, \phi_2)$ , is then

$$\sigma_n^{\text{exchange}}(E, \theta_2, \phi_2) = \frac{k_n}{k_0} \left| g_n(\theta_2, \phi_2) \right|^2. \quad (50)$$

In order to calculate  $g_n(\theta_2, \phi_2)$ , we may proceed as we did for the direct collision case by substituting equation (48) into Schroedinger's equation (9), multiplying by  $\psi_n^*(\vec{r}_1)$ , and integrating over  $\vec{r}_1$ . Thus we obtain

$$(\nabla_2^2 + k_n^2) G_n(\vec{r}_2) = \frac{2m}{\hbar^2} \int \psi_n^*(\vec{r}_1) \left[ -\frac{E^2}{r_2} + \frac{e^2}{r_{12}} \right] \Psi(\vec{r}_1, \vec{r}_2) d\vec{r}_1. \quad (51)$$

If the conditions for the Born approximation are valid such that the dominating contribution to the total wave function comes from the incident wave, we may write

$$\Psi(\vec{r}_1, \vec{r}_2) \cong e^{ik_0 \vec{n}_0 \cdot \vec{r}_1} \psi_0(\vec{r}_2). \quad (52)$$

Substituting equation (52) into equation (51) and using the method of Green's function<sup>(4)</sup>, we obtain

$$G_n(\vec{r}_2) \underset{(r_2 \rightarrow \infty)}{\sim} \frac{e^{i\vec{k}_n r_2}}{r_2} g_n(\theta_2, \phi_2) \quad (53)$$

where

$$g_n(\theta_2, \phi_2) = -\frac{2\pi m}{\hbar^2} \iint e^{-i\vec{k}_n \vec{n} \cdot \vec{r}'} \psi_n^*(\vec{r}') \left[ -\frac{e^2}{r'} + \frac{e^2}{|\vec{r}' - \vec{r}|} \right] \cdot e^{i\vec{k}_0 \vec{n}_0 \cdot \vec{r}'} \psi_0(\vec{r}') d\vec{r}' d\vec{r}'', \quad (54)$$

and  $\vec{n}$  is a unit vector in the direction  $(\theta_2, \phi_2)$  of scattering. ( $\vec{r}'$  serves as the integration variable of the ejected electron 2). Equation (54) is then an expression for the amplitude due to exchange collisions calculated from the Born approximation.

#### II.4.7. Exchange Collision and Indistinguishable Electrons

According to the Pauli principle, electrons are indistinguishable. Hence the wave function of the system (space part) can not <sup>be</sup> correctly represented by either equation (14) or equation (48) alone. On taking into account the indistinguishability of electrons, the wave function before collision, normalized to represent a stream of unit incident current density, can be written as a linear combination of two wave functions<sup>(1)</sup>

$$\Psi_0^\pm(\vec{r}_1, \vec{r}_2) = \frac{1}{\sqrt{2}} \left[ e^{i\vec{k}_0 \cdot \vec{r}_1} \psi_0(\vec{r}_2) \pm e^{i\vec{k}_0 \cdot \vec{r}_2} \psi_0(\vec{r}_1) \right], \quad (55)$$

where the plus sign and the minus sign designate the symmetric and antisymmetric wave functions, respectively.

If the atom is excited to an n-th state after the collision then the normalized wave functions can be written as

$$\bar{\Psi}_n^\pm(\vec{r}_1, \vec{r}_2) = \frac{1}{\sqrt{2}} \left[ e^{i\vec{k}_n \cdot \vec{r}_1} \psi_n(\vec{r}_2) \pm e^{i\vec{k}_n \cdot \vec{r}_2} \psi_n(\vec{r}_1) \right]. \quad (56)$$

The operator which connects the initial state to the final state to give rise to scattering amplitudes is of the form

$$V(\vec{r}', \vec{r}) = -\frac{e^2}{r'} + \frac{e^2}{|\vec{r}' - \vec{r}|}, \quad (57)$$

where  $\vec{r}'$  is the coordinate of the scattered or ejected electron and  $\vec{r}$  is the coordinate of the electron remaining in the atom. We see that  $V(\vec{r}', \vec{r})$  is a symmetric operator.

The Pauli exclusion principle<sup>(11)</sup> states that the wave function representing an actual state of a system containing two or more electrons must be antisymmetric in both space and spin coordinates of the electrons; in other words, the wave function must change sign on interchanging the coordinates of any two electrons.

If we assume that the spin-orbit interaction is negligible in the scattering problem, then the spin part and the space part of the total wave function can be factored. The space part must be symmetric if the spin part is antisymmetric, and vice versa. Hence, only initial and final states of the same symmetry in the space part may give rise to non-vanishing matrix elements for the symmetric

operator  $V(\vec{r}', \vec{r})$ . These matrix elements are

$$\begin{aligned} V_{0n}^{\pm} &= \iint \bar{\Psi}_n^{\pm *} V \bar{\Psi}_0^{\pm} d\vec{r}_1 d\vec{r}_2 \\ &= Z_{\text{direct}}^{\pm} Z_{\text{exchange}} \end{aligned} \quad (58)$$

where

$$\begin{aligned} Z_{\text{direct}} &= \iint e^{-i\vec{k}_n \cdot \vec{r}_1} \psi_n^*(\vec{r}_2) \left[ -\frac{\epsilon^2}{r_1} + \frac{\epsilon^2}{r_{12}} \right] \\ &\quad \cdot e^{i\vec{k}_0 \cdot \vec{r}_1} \psi_0(\vec{r}_1) d\vec{r}_1 d\vec{r}_2 \end{aligned} \quad (59)$$

and

$$\begin{aligned} Z_{\text{exchange}} &= \iint e^{-i\vec{k}_n \cdot \vec{r}'} \psi_n^*(\vec{r}) \left[ -\frac{\epsilon^2}{r'} + \frac{\epsilon^2}{|\vec{r}' - \vec{r}|} \right] \\ &\quad \cdot e^{i\vec{k}_0 \cdot \vec{r}} \psi_0(\vec{r}') d\vec{r}' d\vec{r} \end{aligned} \quad (60)$$

( $\vec{r}'$  is used in equation (60) as the integration variable for the ejected electron).

Comparisons of equations (22), (37) and (59), and (54), (50) and (60) suggest that the formula for differential cross sections should be modified into the following form

$$\begin{aligned} \sigma_n(\epsilon, \theta, \phi) &= \frac{k_n}{k_0} \left( -\frac{2\pi m}{\hbar^2} \right)^2 \left[ a \left| Z_{\text{dir.}} + Z_{\text{ex.}} \right|^2 + b \left| Z_{\text{dir.}} - Z_{\text{ex.}} \right|^2 \right] \\ &= \frac{k_n}{k_0} \left[ a \left| f_n + g_n \right|^2 + b \left| f_n - g_n \right|^2 \right] \end{aligned} \quad (61)$$

where a and b are constants determined by the number of electrons and the multiplicities of the states involved. For the case of electron scattering by an H-atom, the spin wave function associated with  $V_{on}^+$  must be antisymmetric, and it can be written as

$$S^- = \frac{1}{\sqrt{2}} \left[ \alpha(1) \beta(2) - \beta(1) \alpha(2) \right], \quad (62)$$

where  $\alpha(1)$  stands for the spin function of electron 1 with spin up and  $\beta(2)$  stands for that of electron 2 with spin down, etc.

Similarly, the spin wave function associated with  $V_{on}^-$  must be symmetric, and it can be written as

$$\begin{aligned} S^+ &= \alpha(1) \alpha(2), \\ &\text{or } \frac{1}{\sqrt{2}} \left[ \alpha(1) \beta(2) + \beta(1) \alpha(2) \right], \\ &\text{or } \beta(1) \beta(2). \end{aligned} \quad (63)$$

If we assume that the scattering process can take place with equal probability through any one of the four possible spin state channels given in equation (62) and (63) then when this process does occur it has a probability of  $\frac{1}{4}$  of occurring through  $S^-$  and a probability of  $\frac{3}{4}$  of occurring through  $S^+$ . Thus we have

$$\sigma_n(E, \theta, \phi) = \frac{k_n}{k_0} \left[ \frac{1}{4} |f_n + g_n|^2 + \frac{3}{4} |f_n - g_n|^2 \right], \quad (64)$$

where the subscripts 1 and 2 have been omitted because they all refer to the scattered electron. Equation (64) is the expression for the differential cross section of scattering by the n-th process derived from the Born-Oppenheimer approximation.

## II.5. Scattering of Electrons by Helium Atoms Born-Oppenheimer Approximation

The theory of scattering of electrons by H-atoms may be generalized to many-electron atoms. Let us consider the simple example of the helium atom which has two atomic electrons and a nucleus with charge  $+2\epsilon$ . If we label the incident electron 1, and the atomic electrons 2 and 3, with the origin of the coordinate system at the nucleus, then the direct scattering amplitude from the Born approximation can be written as

$$f_n(\theta, \phi) = \frac{-2\pi m\epsilon^2}{\hbar^2} \iiint e^{-i\vec{k}_n \cdot \vec{r}_1} \psi_n^*(\vec{r}_2, \vec{r}_3) \left[ -\frac{2}{r_1} + \frac{1}{r_{12}} + \frac{1}{r_{13}} \right] \cdot e^{i\vec{k}_0 \cdot \vec{r}_1} \psi_0(\vec{r}_2, \vec{r}_3) d\vec{r}_1 d\vec{r}_2 d\vec{r}_3 . \quad (65)$$

Similarly, the exchange scattering amplitude from the Born-Oppenheimer approximation is

$$g_n(\theta, \phi) = \frac{-2\pi m\epsilon^2}{\hbar^2} \iiint e^{-i\vec{k}_n \cdot \vec{r}_2} \psi_n^*(\vec{r}_1, \vec{r}_3) \left[ -\frac{1}{r_2} + \frac{1}{r_{12}} + \frac{1}{r_{23}} \right] \cdot e^{i\vec{k}_0 \cdot \vec{r}_1} \psi_0(\vec{r}_2, \vec{r}_3) d\vec{r}_1 d\vec{r}_2 d\vec{r}_3 . \quad (66)$$

The ground state of the helium atom is a singlet state, and excitation can occur either to a singlet or a triplet state. In the former case, in which no multiplicity change occurs, the differential cross section is found to be<sup>(12)</sup>

$$\sigma_n^{\text{singlet}} = \frac{k_n}{k_0} \left| f_n - g_n \right|^2 . \quad (67)$$

The excitation to triplet states can only arise from electron exchange. Thus the differential cross section is (12)

$$\sigma_n^{\text{triplet}} = 3 \frac{k_n}{k_0} |g_n|^2. \quad (68)$$

## II.6. Limitations of the Born-Oppenheimer Approximation

It is well known<sup>(13)</sup> that the probability of exchange scattering of an electron by an atom falls off rapidly as the incident energy increases. The observed and calculated excitation cross-sections for the helium  $2^3S$ ,  $4^3S$ , and  $5^3S$  states serve as a typical example.

On the other hand the Born approximation holds only when the incident energy is large compared to the interaction energy and when the scattering angle is small. This means that calculations based on the Born-Oppenheimer approximation can not yield satisfactory results in the region where exchange scattering is appreciable.

The difficulty associated with the Born-Oppenheimer approximation may be understood as follows. We recall that the expansions of  $\Psi(\vec{r}_1, \vec{r}_2)$  in equations (14) and (48) are exact and that the following orthogonality relations must hold

$$\int [\Psi - F_n(\vec{r}_1) \psi_n(\vec{r}_2)] \psi_n^*(\vec{r}_2) d\vec{r}_2 = 0, \quad (69)$$

$$\int [\Psi - G_n(\vec{r}_2) \psi_n(\vec{r}_1)] \psi_n^*(\vec{r}_1) d\vec{r}_1 = 0. \quad (70)$$

However, in obtaining solutions to the Schroedinger equation we have used the following approximate wave function

$$\Psi(\vec{r}_1, \vec{r}_2) \cong e^{i\vec{k}_0 \cdot \vec{r}_0 \cdot \vec{r}_1} \psi_0(\vec{r}_2). \quad (71)$$

Equation (71) actually does not satisfy equations (69) and (70). But for high impact energy  $F_n(\vec{r}_1)$  and  $G_n(\vec{r}_2)$  are small so that the error is small.

## II.7. Method of Partial Waves

Since the Born approximation fails to work for low energy collisions, we must find some other method to analyze the problem of exchange scattering. One such method, proved to be very powerful and useful, is the method of partial waves<sup>(14)</sup>. This method is mainly used for spherically symmetrical potentials. The idea is to expand the total wave function as a series of Legendre polynomials multiplied by radial wave functions and then substitute the wave function into the Schroedinger's equation and solve the radial part of the differential equation subject to appropriate boundary conditions.

To demonstrate how this method works, let us consider the simplest situation of an electron scattered by a center of force. The problem of elastic scattering of an electron by an H-atom can be considered to belong to this category,

because we may approximately treat the interaction between the electron and the atom through some effective potential  $V(r)$ <sup>(15)</sup>. The Schrodinger equation of the one-particle system can be written as

$$\left[ \nabla^2 + \frac{2m}{\hbar^2} (E - V) \right] = 0 . \quad (72)$$

If we assume that the particle with energy  $E$  is incident from the  $Z$ -direction, and that  $V$  represents a central field, then  $\psi$  possesses cylindrical symmetry about the  $Z$ -axis and is not a function of  $\phi$ . The Laplacian operator in terms of spherical polar coordinates  $(r, \theta, \phi)$  can be written as

$$\nabla^2 = \frac{1}{r^2} \frac{\partial}{\partial r} \left( r^2 \frac{\partial}{\partial r} \right) - \frac{L^2}{r^2 \hbar^2} , \quad (73)$$

Where  $L^2$  is the total angular momentum operator:

$$L^2 = -\hbar^2 \left[ \frac{1}{\sin \theta} \frac{\partial}{\partial \theta} \sin \theta \frac{\partial}{\partial \theta} + \frac{1}{\sin^2 \theta} \frac{\partial^2}{\partial \phi^2} \right] . \quad (74)$$

Since  $\psi$  is not a function of  $\phi$ , we can expand  $\psi$  into the following linear combination

$$\psi(r, \theta) = \frac{1}{r} \sum_{l=0}^{\infty} \varphi_l(r) P_l(\cos \theta) , \quad (75)$$

where the  $P_l(\cos \theta)$  are the Legendre polynomials<sup>(16)</sup> which satisfy the differential equation

$$L^2 P_l = \hbar^2 l(l+1) P_l , \quad (76)$$

and obey the orthonormality relation

$$\frac{2l+1}{2} \int_{-1}^1 P_l(x) P_m(x) dx = \delta_{lm}, \quad (77)$$

where

$$\begin{aligned} \delta_{lm} &= 1 && \text{when } l=m, \\ &= 0 && \text{otherwise.} \end{aligned} \quad (78)$$

Each term in the expansion of equation (75) is called a "partial wave" corresponding to a particular value of  $l$ . The names s-, p-, d-, f-, waves are associated with  $l=0,1,2,3,\dots$ , respectively. This terminology is derived from optical spectroscopy.

Substituting equation (75) into the Schroedinger equation (72) and making use of (76), we have

$$\sum_l \frac{1}{r} \left[ \frac{d^2 \varphi_l}{dr^2} - \frac{l(l+1)}{r^2} \varphi_l + (k_0^2 - U(r)) \varphi_l \right] P_l(\cos\theta) = 0, \quad (79)$$

where

$$k_0^2 = \frac{2mE}{\hbar^2}, \quad (80)$$

and

$$U(r) = \frac{2m}{\hbar^2} V(r). \quad (81)$$

Since the  $P_l(\cos\theta)$  are orthogonal functions and non-vanishing for an arbitrary  $\theta$ , and  $\frac{1}{r}$  is non-zero for finite  $r$ ,

we must have

$$\frac{d^2 \varphi_l}{dr^2} - \frac{l(l+1)}{r^2} \varphi_l + (k_0^2 - U) \varphi_l = 0, \quad l=0,1,2,\dots \quad (82)$$

Equation (82) is the differential equation that we want to solve once  $U(r)$  is given. If we can find  $\varphi_l(r)$  then we know the wave function and the problem is solved.

### II.7.1. Asymptotic Form of the Radial Partial Wave Function

$$\varphi_l(r)$$

For a physically real scattering potential,  $\psi$  is everywhere finite, continuous, single valued and, for our scattering problem, must have the asymptotic form

$$\psi(r, \theta) \underset{(r \rightarrow \infty)}{\sim} e^{ik_0 z} + \frac{e^{ik_0 r}}{r} f(\theta). \quad (83)$$

Hence the boundary conditions for  $\varphi_l(r)$  must be such that  $\varphi_l(r)$  is continuous and finite everywhere, equal to zero at the origin and satisfy equation (83). Also,  $U(r)$  goes to zero at large distances  $r$ . If in equation (82) we neglect both terms  $U(r)$  and  $\frac{l(l+1)}{r^2}$  at large distances, the asymptotic solution of equation (82) can be written as

$$\varphi_l(r) \underset{(r \rightarrow \infty)}{\sim} A_l \sin(k_0 r + B_l), \quad (84)$$

where  $A_l$  and  $B_l$  are constants to be determined by solving

equation (82).

### II.7.2. Solution of $\psi_l(r)$ for a Free Particle

In order to get some feeling about the relationship between the constants  $A_l$ ,  $B_l$  and the potential energy  $U(r)$ , let us consider the case of a particle in free space, such that

$$U(r) = 0, \quad (85)$$

The differential equation then becomes

$$\frac{d^2 \psi_l}{dr^2} - \frac{l(l+1)}{r^2} \psi_l + k_0^2 \psi_l = 0. \quad (86)$$

We see that equation (86) is of the same form as the differential equation that generates the spherical Bessel functions<sup>(17)</sup>. The general solution to equation (86) can be written as

$$\psi_l(r) = k_0 r \left[ A'_l j_l(k_0 r) + B'_l n_l(k_0 r) \right], \quad (87)$$

where  $A'_l$  and  $B'_l$  are constants, and  $j_l(k_0 r)$  and  $n_l(k_0 r)$  are two independent spherical Bessel functions defined by the following

$$j_l(k_0 r) = \sqrt{\frac{\pi}{2k_0 r}} J_{l+\frac{1}{2}}(k_0 r), \quad (88)$$

$$n_{\ell}(k_0 r) = (-1)^{\ell+1} \sqrt{\frac{\pi}{2k_0 r}} J_{-(\ell+\frac{1}{2})}(k_0 r), \quad (89)$$

where  $J_{\ell+\frac{1}{2}}(k_0 r)$  and  $J_{-(\ell+\frac{1}{2})}(k_0 r)$  are Bessel functions (16).

We note however, that  $J_{-(\ell+\frac{1}{2})}(k_0 r)$  starts out as  $(k_0 r)^{-(\ell+\frac{1}{2})}$  at small  $r$  (18), and does not satisfy the condition that  $\varphi_{\ell}(0)$  must be zero. Hence we must choose

$$B'_1 = 0. \quad (90)$$

The asymptotic form of the Bessel function  $J_n(x)$  when  $|x| \rightarrow \infty$  and  $|x| \gg |n|$  is given by (19)

$$J_n(x) \underset{|x| \rightarrow \infty}{\sim} \sqrt{\frac{2}{\pi x}} \cos \left[ x - \left( n + \frac{1}{2} \right) \frac{\pi}{2} \right]. \quad (91)$$

Therefore the asymptotic form of equation (87), with  $B'_1 = 0$ , is

$$\varphi_{\ell}(r) \underset{k_0 r \rightarrow \infty}{\sim} A'_{\ell} \sin \left[ k_0 r - \frac{\ell \pi}{2} \right]. \quad (92)$$

Comparing equations (92) and (84), we see that the phase  $B_{\ell}$  is equal to  $-\frac{\ell \pi}{2}$  for the case of particle in free space, while the constants  $A_{\ell}$  and  $A'_{\ell}$  are determined by the normalization conditions.

### II.7.3. Differential Cross Sections From Phase Shifts

In view of equation (84) and (92), the asymptotic solution for equation (82) may be written in the following form

$$\varphi_l(r) \underset{r \rightarrow \infty}{\sim} A_l \sin\left(k_0 r - \frac{l\pi}{2} + \eta_l\right), \quad (93)$$

where  $\eta_l$  is the phase shift arising from the scattering potential  $U(r)$ . In general,  $\eta_l$  must be determined by solving the differential equation subject to the boundary conditions that  $\varphi_l = 0$  at the origin and have the form given by equation (93) at large  $r$ .

A physical interpretation of  $\eta_l$  may be given by saying that introduction of  $U$  makes the phase of the scattered wave to increase by  $\eta_l$  when compared with free spherical wave (i.e.,  $U = 0$ ).

Substituting equation (93) into equation (75), the asymptotic form of the wave function  $\psi(r, \theta)$  becomes

$$\psi(r, \theta) \underset{r \rightarrow \infty}{\sim} \frac{1}{r} \sum_{l=0}^{\infty} A_l \sin\left[k_0 r - \frac{l\pi}{2} + \eta_l\right] P_l(\cos \theta). \quad (94)$$

Now equations (94) and (83) are two asymptotic forms of the same function  $\psi(r, \theta)$ , and hence should be equivalent. For convenience of comparison, we will also expand equation (83) in a linear combination of the complete orthonormal set of  $P_l(\cos \theta)$ . Algebraic manipulation<sup>(20)</sup> shows that the first term on the right hand side of equation (83) becomes

$$\begin{aligned}
 e^{ik_0 z} &= e^{ik_0 r \cos \theta} \\
 &= \sum_{l=0}^{\infty} (2l+1) i^l j_l(k_0 r) P_l(\cos \theta), \quad (95)
 \end{aligned}$$

where  $j_l(k_0 r)$  is the spherical Bessel function defined in equation (88). Making use of equations (88) and (91), the asymptotic form of equation (95) can be written as

$$e^{ik_0 z} \underset{r \rightarrow \infty}{\sim} \sum_{l=0}^{\infty} (2l+1) i^l \left[ \frac{1}{k_0 r} \sin(k_0 r - \frac{l\pi}{2}) \right] P_l(\cos \theta). \quad (96)$$

Similarly, the second term on the right hand side of equation (83) can be expanded as

$$\frac{e^{ik_0 r}}{r} f(\theta) = \frac{e^{ik_0 r}}{r} \sum_{l=0}^{\infty} C_l P_l(\cos \theta), \quad (97)$$

where  $C_l$  is a coefficient to be determined. Thus equation (83) becomes

$$\begin{aligned}
 \psi(r, \theta) \underset{r \rightarrow \infty}{\sim} \sum_{l=0}^{\infty} \left\{ (2l+1) i^l \left[ \frac{1}{k_0 r} \sin(k_0 r - \frac{l\pi}{2}) \right] + \right. \\
 \left. + \frac{e^{ik_0 r}}{r} C_l \right\} P_l(\cos \theta). \quad (98)
 \end{aligned}$$

Making use of the mathematical identities

$$i^l = e^{il\frac{\pi}{2}}, \quad (99)$$

and

$$\sin \theta = \frac{1}{2i} (e^{i\theta} - e^{-i\theta}), \quad (100)$$

equation (98) can be written as

$$\begin{aligned} \psi(r, \theta) \underset{\text{eq. (93)}}{\sim} \underset{r \rightarrow \infty}{\sim} \sum_{l=0}^{\infty} \left\{ \left[ \frac{a_{l+1}}{2ik_0} + C_l \right] e^{ik_0 r} - \right. \\ \left. - \left[ \frac{(2l+1)e^{i\frac{l\pi}{2}}}{2k_0 i} \right] e^{-ik_0 r} \right\} \frac{1}{r} P_l(\cos \theta). \end{aligned} \quad (101)$$

Similarly, equation (94) can be written as

$$\begin{aligned} \psi(r, \theta) \underset{\text{eq. (94)}}{\sim} \underset{r \rightarrow \infty}{\sim} \sum_{l=0}^{\infty} \left\{ \left[ \frac{A_l}{2i} e^{-i\frac{l\pi}{2}} e^{i\eta_l} \right] e^{ik_0 r} - \right. \\ \left. - \left[ \frac{A_l}{2i} e^{i\frac{l\pi}{2}} e^{-i\eta_l} \right] e^{-ik_0 r} \right\} \frac{1}{r} P_l(\cos \theta). \end{aligned} \quad (102)$$

A mathematical theorem states that if

$$Ae^{ix} + Be^{-ix} \equiv 0 \quad (103)$$

then

$$\overline{A} = \overline{B} = 0 \quad (104)$$

Since equations (101) and (102) are equivalent, we must have

$$\left[ \frac{2l+1}{2ik_0} + C_l \right] - \left[ \frac{A_l}{2i} e^{-i\frac{l\pi}{2}} e^{i\eta_l} \right] = 0, \quad (105)$$

$$\frac{(2l+1)e^{i\pi}}{2k_0 i} - \left[ \frac{A_l}{2i} e^{i\frac{l\pi}{2}} e^{-i\eta_l} \right] = 0. \quad (106)$$

}  $l = 0, 1, 2, \dots$

Solving equations (105) and (106), we have

$$A_l = \frac{i^l (2l+1)}{k_0} e^{i\eta_l}, \quad (107)$$

$$C_l = \frac{(2l+1)}{2ik_0} (e^{i2\eta_l} - 1). \quad (108)$$

Thus

$$\begin{aligned}
 f(\theta) &= \sum_{l=0}^{\infty} C_l P_l(\cos\theta) \\
 &= \sum_{l=0}^{\infty} \frac{(2l+1)}{2ik_0} (e^{i2\eta_l} - 1) P_l(\cos\theta).
 \end{aligned}
 \tag{109}$$

In view of equation (32), the differential cross section for elastic scattering in terms of the phase shifts is

$$\begin{aligned}
 \sigma_e(E, \theta) &= |f(\theta)|^2 \\
 &= \frac{1}{k_0^2} \left| \sum_{l=0}^{\infty} \frac{2l+1}{2} (e^{i2\eta_l} - 1) P_l(\cos\theta) \right|^2.
 \end{aligned}
 \tag{110}$$

The  $\eta_l$  are obtained by solving the Schroedinger equation (82) subject to the boundary condition  $\psi_l(0) = 0$  and the asymptotic condition of equation (93). From the  $\eta_l$  one can calculate  $\sigma_e(E, \theta)$  according to equation (110).

#### II.7.4. Total Cross Sections and Partial Cross Sections

The total cross section  $Q(E)$  can be obtained by integrating the differential cross section over all solid angles.

$$\begin{aligned}
Q_0(E) &= \int_{\phi=0}^{2\pi} \int_{\theta=0}^{\pi} \sigma_0(E, \theta) \sin \theta \, d\theta \, d\phi \\
&= \frac{2\pi}{k_0^2} \int_{\theta=0}^{\pi} \left| \sum_{l=0}^{\infty} \frac{2l+1}{2} (e^{i2\eta_l} - 1) P_l \right|^2 \sin \theta \, d\theta \quad (111) \\
&= \frac{4\pi}{k_0^2} \sum_{l=0}^{\infty} (2l+1) \sin^2 \eta_l \quad ,
\end{aligned}$$

where we have made use of the orthonormality properties of the Legendre polynomials given by equation (77).

We see from equation (111) that the total cross section  $Q_0(E)$  can be expressed as a sum of the partial cross sections  $Q_0^l(E)$ , defined by

$$Q_0^l(E) = \frac{4\pi}{k_0^2} (2l+1) \sin^2 \eta_l \quad , \quad l=0, 1, 2, \dots \quad (112)$$

It is of interest to estimate the maximum partial cross section for a given angular momentum quantum number  $l$ . The function  $\sin^2 \eta_l$  is an oscillating function between 0 and 1. Therefore, by letting  $\eta_l = n\pi + \frac{\pi}{2}$ , where  $n$  is an integer, we have

$$[Q_{\max}^l] = \frac{4\pi}{k_0^2} (2l+1) \quad (113)$$

II.7.5. Comparison of Classical and Quantum Mechanical  
Partial Cross Sections

Let us consider a particle with mass  $m$  and velocity  $v$  moving towards a scattering center in a central field potential. Then the classical angular momentum  $\mathcal{L}$  associated with an impact parameter  $b$  can be written as

$$\mathcal{L} = mvb. \quad (114)$$

Thus

$$b = \frac{\mathcal{L}}{mv} \quad (115)$$

$$db = \frac{d\mathcal{L}}{mv} \quad (116)$$

The increment of cross section  $dQ$  associated with an increment in impact parameter from  $b$  to  $b + db$  is then

$$\begin{aligned} dQ &= 2\pi b db \\ &= \frac{2\pi}{(mv)^2} \mathcal{L} d\mathcal{L} \end{aligned} \quad (117)$$

If we define

$$\mathcal{L} = \hbar l \quad (118)$$

and

$$d\mathcal{L} = \hbar dl \quad (119)$$

with  $l$  being classically a continuous variable,

then

$$\begin{aligned}
 Q_{\text{class}}^{\text{total}} &= \int dQ = \int \frac{2\pi}{\left(\frac{mv}{\hbar}\right)^2} l dl \\
 &= \int \left[ \frac{\pi}{k_0^2} 2l \right] dl \quad .
 \end{aligned}
 \tag{120}$$

Hence the classical partial cross section at  $l$  per unit  $l$ -range is just

$$Q_{\text{class}}^{(l)} = \frac{\pi}{k_0^2} 2l \tag{121}$$

Comparing this classical  $Q_{\text{class}}^{(l)}$  with the partial cross section in equation (112), we see that the factor  $4(2l + 1)\sin^2\eta_l$  instead of  $2l$  is a quantum mechanical result.

We also observe that if all the phase shift  $\eta_l$  due to some scattering potential is equal to an integral multiple of  $\pi$  for nonzero  $k_0$ , then the total cross section  $Q_0(E)$  vanishes. Experimentally, it has been found that for slow electrons elastically scattered from noble gas atoms the cross section undulates with electron beam energy. It turns out that the scattering cross section for a few tenths of an  $\text{\AA}^{\text{ev}}$  electron may be unusually small. This is known as the Ramsauer-Townsend effect<sup>(21)</sup>

### II.7.6. Angular Distributions of Scattered Electrons

The general expression for the differential cross section for elastic scattering obtained in equation (110) is a function of incident wave number  $k_0$ , the phase shift  $\eta_l$ , and the Legendre polynomials  $P_l(\cos\theta)$ . Thus it is important to understand the qualitative behavior arising from these polynomials. The first few Legendre polynomials are listed below<sup>(22)</sup>.

$$\begin{aligned}
 P_0(x) &= 1 \\
 P_1(x) &= x \\
 P_2(x) &= \frac{1}{2}(3x^2 - 1) \\
 P_3(x) &= \frac{1}{2}(5x^3 - 3x) \\
 P_4(x) &= \frac{1}{8}(35x^4 - 30x^2 + 3) .
 \end{aligned} \tag{122}$$

In our case  $x = \cos\theta$ , where  $\theta$  is the scattering angle. For convenience of discussion, the differential cross section can be written as:

$$\sigma_0(E, \theta) = \left| \sum_{l=0}^{\infty} C_l P_l(\cos\theta) \right|^2, \tag{123}$$

where  $C_l$  is a function of  $l$ ,  $k_0$  and  $\eta_l$ , as defined in equation (108).

If we assume that  $l_{\max}$  is the maximum  $l$  beyond which contributions to a certain scattering process are negligible, then the differential cross section  $\sigma_0(E, \theta)$  for  $l_{\max} = 0, 1, 2, \dots$  can be written as:

$$\sigma_0(l_{\max} = 0) = C_0^* C_0, \tag{124}$$

$$\sigma_0(l_{\max}=1) = [C_0^* + C_1^* \cos \theta] [C_0 + C_1 \cos \theta], \quad (125)$$

$$\sigma_0(l_{\max}=2) = \left| C_0 + C_1 \cos \theta + \frac{C_2}{2} (3 \cos^2 \theta - 1) \right|^2. \quad (126)$$

We see from equation (124) that for scattering processes for which the only important term is that for  $l=0$  the differential cross section is not a function of angle. Whereas for  $l_{\max}=1,2,\dots$ etc, the differential cross sections are polynomials of  $\cos \theta$  of the order  $2l_{\max}$ . Since  $\cos^n \theta$  is a sharply peaking function around  $\theta=0^\circ$  for large  $n$ , the differential cross section is sharply forward peaked for large  $l_{\max}$ .

The above is also true for inelastic scattering. For spin forbidden transitions, which require electron exchange and can only occur with small impact parameters, the contributing  $l$  values must be small. Hence the differential cross sections have a much more uniform angular dependence. The optically allowed transitions, on the other hand, have sharply forward peaked distribution.

#### II.7.7. Conservation of Particles<sup>in</sup> Elastic Scattering

In section II.7.3. we obtained the expression for  $C_l$  in equation (108) by comparing the two asymptotic forms of the same wave function  $\psi(r,\theta)$  in equations (83) and (94). However, we will see that the expression for  $C_l$  may also be derived from the principle of conservation of particles alone.

From equation (98) the radial wave function associated with angular momentum  $\frac{\hbar}{2}[\ell(\ell+1)]^{1/2}$  at large  $r$  is given by

$$\varphi_{\ell}(r) = (2\ell+1) i^{\ell} \left[ \frac{1}{k_0 r} \sin(k_0 r - \frac{\ell\pi}{2}) \right] + \frac{e^{ik_0 r}}{r} C_{\ell} \quad (127)$$

Using equation (24), the inward probability current in the radial direction associated with  $\varphi_{\ell}(r)$  is then

$$S'_{\ell, \text{rad.}} = -\frac{\hbar}{mr^2} \left[ -\frac{i}{2}(2\ell+1)(C_{\ell}^* - C_{\ell}) + k_0 |C_{\ell}|^2 \right]. \quad (128)$$

For the case of elastic scattering, the net inward radial probability current must be zero because of conservation of particles, thus

$$-\frac{i}{2}(2\ell+1)(C_{\ell}^* - C_{\ell}) + k_0 |C_{\ell}|^2 = 0. \quad (129)$$

It can be easily shown that equation (129) is true when

$$C_{\ell} = \frac{2\ell+1}{2ik_0} (e^{2i\eta_{\ell}} - 1), \quad (130)$$

where  $\eta_{\ell}$  is a real constant. We see that equation (130) is of the same form as equation (108).

II.7.8. Maximum Inelastic Cross-Section for A Given Angular Momentum

So far in the partial wave method we have only considered the problem of elastic scattering of electrons by a center of force, with both the interacting potential  $U(r)$  and the phase shift  $\eta_l$  being real quantities. If we now assume that  $U(r)$  is complex in the one-particle problem then this produces destruction of particles which otherwise would be scattered elastically. From a complex potential  $U(r)$ , the resulting phase shift  $\eta_l$  also becomes complex. Thus we may write

$$\eta_l = \lambda_l + i \mu_l \quad (131)$$

where both  $\lambda_l$  and  $\mu_l$  are real. The imaginary part of the phase shift will then completely determine the inelastic cross sections<sup>(23)</sup>. This is the one-particle description for inelastic scattering.

The partial elastic cross section  $Q_e^l$  using equation (97), can be written as

$$\begin{aligned} Q_e^l &= 2\pi \int |C_l P_l(\cos\theta)|^2 \sin\theta \, d\theta \\ &= \frac{4\pi}{2l+1} |C_l|^2 \end{aligned} \quad (132)$$

Equation (132) can be reduced to equation (112), by using equation (130).

Since inelastic collisions can now occur, the net inward radial probability current will be equal to the flux of particles which have suffered inelastic collisions. At a large distance  $r$  from the center the net inward flux will therefore be given by<sup>(23)</sup>

$$S_{\ell, \text{rad}} = \left(\frac{v}{r^2}\right) \frac{2\ell+1}{4\pi} [Q_{\text{inelastic}}^{\ell}], \quad (133)$$

where  $Q_{\text{inelastic}}^{\ell}$  is the partial inelastic cross-section summed over all possible processes.

Equation (133) and (128) must be equivalent, and thus we have

$$[Q_{\text{total}}^{\ell}] = [Q_{\text{inel.}}^{\ell}] + Q_0^{\ell} = \frac{2\pi i}{k_0} (c_{\ell}^* - c_{\ell}), \quad (134)$$

where  $[Q_{\text{total}}^{\ell}]$  is the partial cross section for all collisions, both elastic and inelastic.

Since

$$|c_{\ell}|^2 \geq \left| \frac{c_{\ell}^* - c_{\ell}}{2} \right|^2, \quad (135)$$

we have

$$Q_0^{\ell} = \frac{4\pi}{2\ell+1} |c_{\ell}|^2 \geq \frac{[Q_{\text{total}}^{\ell}]^2}{[Q_{\text{max}}^{\ell}]}, \quad (136)$$

where  $[Q_{\text{max}}^{\ell}] = \frac{4\pi}{k_0^2} (2\ell+1)$  is the same as in equation (113).

In reality  $Q_0^l \leq [Q^l \text{ total}]$  (137)

Hence from equations (136) and (137)

$$[Q^l \text{ total}] \leq [Q_{\text{max}}^l]. \quad (138)$$

Furthermore

$$\begin{aligned} [Q^l \text{ inelastic}] &= [Q^l \text{ total} - Q_0^l] \\ &\leq [Q^l \text{ total}] - [Q^l \text{ total}]^2 / [Q_{\text{max}}^l] \end{aligned} \quad (139)$$

The maximum value of the right-hand side occurs when

$$[Q^l \text{ total}] = \frac{1}{2} [Q_{\text{max}}^l] \quad (140)$$

so

$$[Q^l \text{ inelastic}] \leq \frac{\pi}{k_0^2} (2l+1) \quad (141)$$

In equation (141), the equality only arises when

$$Q_0^l = \frac{\pi}{k_0^2} (2l + 1). \quad (142)$$

Equation (141) is an expression for the maximum inelastic partial cross section summed over all inelastic processes. This turns out to be a very useful formula for checking theoretical calculations.

## II.8. Method of Distorted Waves

In the direct collision case, we obtained a set of coupled partial differential equations in the following form

$$[\nabla_i^2 + k_n^2] F_n(\vec{r}_i) = \frac{2m}{\hbar^2} V_{on} e^{i k_0 \vec{n}_0 \cdot \vec{r}_i} + \sum_{j=0,1,2,\dots} F_j(\vec{r}_i) V_{jn}, \quad (143)$$

from equations (15) and (18).

In order to solve them, we made the assumption that the incident energy of the electrons is large compared to the interaction energy such that the only significant term on the right hand side is

$$\frac{2m}{\hbar^2} V_{on} e^{i k_0 \vec{n}_0 \cdot \vec{r}_i}$$

This is known as the Born approximation.

Unfortunately, many of the interesting cases happen at lower incident energies. Therefore, let us make the less drastic assumption that the non-diagonal matrix elements  $V_{jm}$  are so small that we may neglect all products on the right hand side except  $V_{nn}F_n$  and  $V_{on}e^{i\vec{k}_0 \cdot \vec{r}_1}$ . Hence we obtain the series of equations:

$$[\nabla_1^2 + k_0^2] F_0(\vec{r}_1) = \frac{2m}{\hbar^2} V_{on} e^{i\vec{k}_0 \cdot \vec{r}_1}, \quad (144)$$

$$[\nabla_1^2 + k_n^2] F_n(\vec{r}_1) = \frac{2m}{\hbar^2} [V_{on} e^{i\vec{k}_0 \cdot \vec{r}_1} + V_{nn} F_n(\vec{r}_1)], \quad (145)$$

( for  $n \neq 0$  )

which must satisfy the boundary conditions

$$F_n(\vec{r}_1) \underset{r_1 \rightarrow \infty}{\sim} \frac{e^{ik_n r_1}}{r_1} f_n(\theta_1, \phi_1), \quad n = 0, 1, 2, \dots \quad (146)$$

The above approximation is often called the distorted wave method. Massey and Moiseiwitsch<sup>(24,25)</sup> were able to use this method to calculate the excitation of the  $2^1S$  and  $2^3S$  states<sup>(24)</sup> and the  $2^3P$  state<sup>(25)</sup> of helium by electron impact. The excitation cross sections calculated by these authors showed considerable improvements over the previous calculations using the Born-Oppenheimer approximation<sup>(13)</sup>. However, as pointed out by these authors, substantial discrepancies from the observed data still remained.

## II.9. Close-Coupling Approximation

In the collisions of electrons and atoms, it is possible that atomic states other than the initial and final states may have contributions to a particular scattering process. For example, in the scattering of electrons by H-atoms, the incident electron may excite the atom to an excited state, then the atom in its excited state may again interact with this scattered electron and lose its excitation energy. The scattered electron thus coming out would appear to have been scattered elastically.

In order to have a complete treatment of the problem, the total wave function for the electron plus H atom case can be expanded in the antisymmetrized form

$$\psi(\vec{r}_1, \sigma_1, \vec{r}_2, \sigma_2) = \frac{1}{\sqrt{2}} \sum_{\Gamma} \left\{ \psi_{\Gamma}(\vec{r}_1, \sigma_1, \hat{r}_2, \sigma_2) \frac{F_{\Gamma}(r_2)}{r_2} - \psi_{\Gamma}(\vec{r}_2, \sigma_2, \hat{r}_1, \sigma_1) \frac{F_{\Gamma}(r_1)}{r_1} \right\}, \quad (147)$$

where  $\sigma_i$  and  $\hat{r}_i$  are the spin coordinate and unit vector along the direction of  $\vec{r}_i$  of the  $i$ -th electron, respectively,  $i = 1$  or  $2$ .

Here, in the notation of Percival and Seaton <sup>(26)</sup>,

$\Gamma$  represents the set of quantities

$$\Gamma = (n \ k_n \ l_1 \ l_2 \ L \ M_L \ S \ M_S), \quad (148)$$

where  $n$  and  $l_1$  are the principal and angular momentum quantum numbers, respectively, of the atomic electron;  $l_2$  and  $k_n$  are the orbital angular momentum and the wave number, respectively, of the scattered electron;  $L$  is the total angular momentum quantum number and  $S$  is the total spin; and  $M_L$  and  $M_S$  are the components of  $L$  and  $S$ , respectively, along the  $z$  - direction.

The sum over  $\Gamma$  in equation (147) must in principle include all the discrete and continuum states of the H-atom. However, due to practical difficulties we can only include a finite number of states. The following designations are listed by Burke and Smith<sup>(27a)</sup>

- a). Static approximation when only the 1S state of the H-atom is used in equation (147).
- b). Strong-coupling approximation when 1S and 2S states of the H-atom are used.
- c). Close-coupling approximation when 1S, 2S and 2P states of the H-atom are used.

Burke and Schey<sup>(27b)</sup> were able to use the close-coupling approximation to calculate the differential cross sections of elastic scattering of electrons by H-atoms for incident energies below the first excited state of the H-atom (10.2 e v ).

Later, Burke, Schey and Smith<sup>(28)</sup> reported further work using this approximation to calculate the elastic and inelastic differential cross sections of electrons scattered by H-atoms with incident energies in the range from 11.0

to 54.4 e v. The results presented by these authors showed that the differential cross sections of elastic and optically allowed inelastic collisions were in general strongly forward peaked. However, the magnitude of the cross sections were too large compared to available experimental values.

#### II.10. Ochkur-Born-Oppenheimer Approximation for Exchange Scattering

Recently, Ochkur<sup>(29)</sup> reported a simple formula which permitted one to calculate the exchange scattering of electrons by atoms with approximately the same degree of accuracy as that yielded by the Born formula in the direct collision case. The excitation functions were calculated for the  $2^3S$  and  $2^3P$  levels in helium. The results showed considerably better agreement with experiments than previous calculations by other authors (13,24,25,).

The principal idea in Ochkur's work is to expand the exchange amplitude  $g_n(E, \theta, \phi)$  in a series in inverse powers of  $k_0$ , then to truncate the series, keeping only the lowest order terms in  $\frac{1}{k_0}$ , with the assumption that  $k_0$  and  $k_n$  are both large compared to  $\Delta k$ . The reason for discarding higher order terms in  $\frac{1}{k_0}$  is that these terms are not consistent with first order perturbation theory. If such terms are retained, then as the energy is decreased they start dominating at energies at which otherwise first order perturbation theory might be expected to apply and give unreasonnable results.

### II.10.1. Prior and Post Interactions

The exchange scattering amplitude for the case of helium from the Born-Oppenheimer approximation can be written as

$$g_{0n}(E, \theta, \phi) = \frac{-2\pi m e^2}{\hbar^2} \iiint e^{-i \vec{k}_n \cdot \vec{r}_2} \psi_n^*(\vec{r}_1, \vec{r}_3) V_{ex} \cdot e^{i \vec{k}_0 \cdot \vec{r}_1} \psi_0(\vec{r}_2, \vec{r}_3) d\vec{r}_1 d\vec{r}_2 d\vec{r}_3, \quad (149)$$

where  $V_{ex}$  is the operator for the exchange interaction, and can have the following two forms:

$$V_{ex}^{prior} = \left( -\frac{1}{r_1} + \frac{1}{r_2} + \frac{1}{r_{13}} \right), \quad (150)$$

$$V_{ex}^{post} = \left( -\frac{1}{r_2} + \frac{1}{r_1} + \frac{1}{r_{13}} \right). \quad (151)$$

The "prior" interaction represents the interaction of the incident electron with the atom and the "post" interaction represents the interaction of the ejected electron with the atom. If  $\psi_n$  and  $\psi_0$  are exact wave functions of the

atom, then the prior and the post interactions are equivalent. However, in practice, we do not have exact solutions for atoms with two or more electrons. Thus, some approximate wave functions must be used. It can be shown that <sup>(30)</sup> if the Hartree self-consistent field approximate wave functions are used, then the post-prior problem does not arise. But this is not true for other types of approximation <sup>(13b)</sup>.

We note that equation (66) in section II.5. was written with the post interaction. The choice was arbitrary.

#### II.10.2. Exchange Scattering Amplitude

From equations (149) and (150), the exchange scattering amplitude for the case of helium can be written as

$$g_n(E, \theta, \phi) = \frac{-2\pi m E^2}{\hbar^2} \iiint \left[ -\frac{1}{r_1} + \frac{1}{r_{12}} + \frac{1}{r_{13}} \right] e^{i(\vec{k}_0 \cdot \vec{r}_1 - \vec{k}_n \cdot \vec{r}_2)} \cdot \psi_n^*(\vec{r}_1, \vec{r}_3) \psi_0(\vec{r}_2, \vec{r}_3) d\vec{r}_1 d\vec{r}_2 d\vec{r}_3 \quad (152)$$

This amplitude can be written as a sum of three terms as follows

$$g_n(E, \theta, \phi) = g_n^{(1)}\left(-\frac{1}{r_1}\right) + g_n^{(2)}\left(\frac{1}{r_{12}}\right) + g_n^{(3)}\left(\frac{1}{r_{13}}\right). \quad (153)$$

Ochkur<sup>(29)</sup> showed that these three terms were given by:

$$g_n^{(1)} = -\frac{2\pi m \epsilon^2}{\hbar^2} \left( \frac{4\pi}{k_0^2} \right) \int \psi_n^*(\vec{r}_3, \vec{r}_2) \psi_0(\vec{r}_2, \vec{r}_3) e^{i\Delta\vec{k} \cdot \vec{r}_2} d\vec{r}_2 d\vec{r}_3$$

+ (higher order terms), (154)

$$g_n^{(2)} = O\left(\frac{1}{k_0^6}\right), \quad (155)$$

$$g_n^{(3)} = O\left(\frac{1}{k_0^6}\right). \quad (156)$$

Hence, to within order  $\frac{1}{k_0^2}$ ,  $g_n^{(2)}$  and  $g_n^{(3)}$  can be neglected in the framework of first order perturbation theory. (When  $\psi_0$  and  $\psi_n$  have different space symmetry,  $g_n^{(2)} = O\left(\frac{1}{k_0^2}\right)$ ).

Thus the exchange amplitude can be written as

$$g_n(E, \theta, \phi) = \left( -\frac{8\pi^2 m \epsilon^2}{\hbar^2} \right) \frac{1}{k_0^2} \int \psi_n^*(\vec{r}_3, \vec{r}_2) \psi_0(\vec{r}_2, \vec{r}_3) \cdot e^{i\Delta\vec{k} \cdot \vec{r}_2} d\vec{r}_2 d\vec{r}_3. \quad (157)$$

where  $g_n$  has an explicit dependence of  $\frac{1}{k_0}$ . We recall from equations (32) and (37) that the direct scattering amplitude for the case of the H-atom can be written as

$$f_n(E, \theta, \phi) = \left( -\frac{8\pi^2 m e^2}{\hbar^2} \right) \frac{1}{(\Delta k)^2} \int \psi_n^*(\vec{r}_2) e^{i\Delta\vec{k} \cdot \vec{r}_2} \psi_0(\vec{r}_2) d\vec{r}_2. \quad (158)$$

Thus we see that  $f_n$  and  $g_n$  have similar forms except that the expression for  $g_n$  has a dependence on  $\frac{1}{k_0^2}$  while the expression for  $f_n$  has a dependence on  $\frac{1}{(\Delta k)^2}$ . This difference leads to different energy dependence of the cross sections.

It should be pointed out that in Ochkur's treatment the problem of "prior or post interaction" is eliminated by neglecting the higher order terms in  $(\frac{1}{k_0})$ .

### II.10.3. Cross Sections for Triplet Excitations in Helium

The differential cross section for the excitation from the ground state to a triplet state by electron exchange in helium is given in equation (68) as

$$\sigma_n^{\text{triplet}} = 3 \frac{k_n}{k_0} |g_n|^2$$

where the expression for  $g_n$  is now given in equation (157).

The total cross section is then

$$Q_n^{\text{triplet}} = 3 \frac{k_n}{k_0} \int_{\phi=0}^{2\pi} \int_{\theta=0}^{\pi} |g_n|^2 \sin\theta \, d\theta \, d\phi, \quad (159)$$

For a central potential problem such as this, there is no  $\phi$  dependence. Furthermore, we can change the integration variable from  $d\theta$  to  $d(\Delta k)$ . Using equation (44), the total cross section is given by

$$Q_n^{\text{triplet}} = \frac{384 \pi^5 m^2 E^4}{\hbar^4} \left( \frac{1}{k_0^6} \right) \cdot \int_{k_0 - k_n}^{k_0 + k_n} |\langle n | e^{i \Delta \vec{k} \cdot \vec{r}_2} | 0 \rangle|^2 (\Delta k) \, d(\Delta k), \quad (160)$$

where

$$\begin{aligned} \langle n | e^{i \Delta \vec{k} \cdot \vec{r}_2} | 0 \rangle &= \\ &= \int \psi_n^*(\vec{r}_2, \vec{r}_2) \psi_0(\vec{r}_2, \vec{r}_2) e^{i \Delta \vec{k} \cdot \vec{r}_2} \, d\vec{r}_2 \, d\vec{r}_3. \end{aligned} \quad (161)$$

We see from equation (160) that since

$$\frac{l}{k_0} \gg \Delta k = | \vec{k}_0 - \vec{k}_n | , \quad (162)$$

the integral over  $\Delta k$  is relatively independent of  $k_0$ .<sup>(29)</sup> Therefore the cross section has the following energy dependence

$$Q_n^{\text{triplet}} \sim \frac{1}{E^3} , \quad (163)$$

at large  $E$ .

Ochkur<sup>(29)</sup> states that there exists a preference for transitions without a change of the angular momentum quantum number  $l$  of the excited electron, and that transitions with  $\Delta l = 2$  were much less probable. He also shows that the dependence of cross sections on the principal quantum number  $n$  for fixed  $l$  is approximately

$$Q_n \sim n^{-3} . \quad (164)$$

#### II.10.4. Rudge's Correction of Ochkur's Formula

In a recent letter, Rudge<sup>(31)</sup> pointed out that the exchange scattering amplitude obtained from Ochkur's method in equation (157) was in a sense incorrect, and that it

should be replaced by the following form

$$f_n(E, \theta, \phi) \cong \left( -\frac{8\pi^2 m e^2}{\hbar^2} \right) \left[ \frac{-1}{(k_n - i)^2} \right] \langle n | e^{i\Delta\vec{k} \cdot \vec{r}} | 0 \rangle, \quad (165)$$

in order to be consistent with results derived from the variational principle.

Rudge<sup>(32)</sup> also reported some calculations on the elastic scattering of electrons by the H-atom in its ground state and the excitation of the  $2S$  state from the ground state. In both cases the exchange collisions were taken into account based on formulae derived from the variational principle. The results showed encouraging improvements over the previous calculations.

The total and differential cross sections for excitations in helium from the ground state to the  $2^3S$  and  $2^3P$  states have recently been calculated by Cartwright<sup>(33)</sup> with the Ochkur and Ochkur-Rudge approximations.

## II.11. Theory of Electron Scattering by Molecules

In this section, we will consider a few important points related to the collisions of electrons with molecules. The term "molecule" used here applies to diatomic or polyatomic molecules. Since a molecule is composed of two or more atoms, most of the early discussions about single atoms should be applicable to a molecule if we can make it stand still and fire electrons at it. However,

in addition to the electronic motion and translational motion associated with an atom, there are also vibrational and rotational degrees of freedom associated with the nuclei of a molecule. In order to handle the problem properly, we must describe the system by a total wave function of the incoming electron, the molecular electrons and the nuclei.

In elastic scattering, interference occurs between the electron waves scattered from different atoms in the same molecule. This is apparent in the angular distribution of the scattered electrons, and serves as a tool in studying molecular structures.

The inelastic collisions include the possibilities of electronic excitation, vibrational and rotational excitation, molecular dissociation, negative and positive ion formation. In the present work, we will focus our interests only on the electronic excitation and ionization of molecules.

#### II.11.1. Electronic Transitions in Diatomic Molecules The Franck-Condon principle

It is well known in optical spectroscopy that the electron jump in a molecule takes place so rapidly in comparison to the vibrational and rotational motion that immediately afterwards the nuclei still have very nearly the same relative position and velocity as before the jump. This is called the Franck-Condon principle.

Discussions on the emission and absorption of radiation by molecules and a wave-mechanical proof of

the Franck-Condon principle can be found in standard references<sup>(8)</sup>.

Our present concern is whether or not this principle holds for electronic excitation by electron impact.

For molecules like  $H_2$  and  $N_2$ , the vibrational constants,  $\omega_e$  of the ground electronic states are given by (8)

$$\omega_e(H_2) = 4395.24 \text{ cm}^{-1} \quad (166)$$

$$\omega_e(N_2) = 2359.61 \text{ cm}^{-1} .$$

The period  $T$  of a classical simple harmonic oscillator at frequency  $\nu$  is given by

$$T = \frac{1}{\nu} = \frac{1}{c\nu} \quad , \quad (167)$$

where  $c$  is the speed of light in vacuum and is approximately equal to  $3 \times 10^{10}$  cm/sec.

At room temperature, for  $H_2$ , most of the molecules are in the ground vibrational state with zero-point energy  $\frac{1}{2}\omega_e$ . Therefore, the vibrational period is of the order of  $1.5 \times 10^{-14}$  sec. For heavier molecules the vibrational periods are even longer than that of  $H_2$ .

On the other hand, from section II.1. the average time an electron of 30 electron volts will spend around the neighborhood of a molecule of linear dimensions of about 1 Å is of the order of  $3 \times 10^{-17}$  sec.

From these simple calculations, we see that the motion of a low energy electron is fast compared to the nuclear motion. Hence if electronic excitation of the molecule takes place during a collision it is very likely that the Franck-Condon principle will still hold.

### II.11.2. Electronic Excitation Cross Sections

In order to demonstrate how to calculate the cross sections for molecular electronic excitations by electron impact, let us consider the simplest problem of direct excitation by an electron of a  $H_2$  molecule. A detailed treatment has been given by Cartwright and Kuppermann<sup>(34)</sup>.

The scattering amplitude from the Born approximation is given by

$$f_n(\vec{k}_0, \theta, \phi) = \frac{-2\pi m e^2}{\hbar^2} \int e^{-i\vec{k}_n \cdot \vec{r}_i} \Phi_n^* V e^{i\vec{k}_0 \cdot \vec{r}_i} \Phi_0 d\tau d\vec{r}_i, \quad (168)$$

where  $\Phi_0$  and  $\Phi_n$  are the molecular wave functions of the ground and the n-th excited state of the  $H_2$  molecule respectively,  $V$  is the interaction potential for direct collisions, and  $d\tau$  is the volume element for all the necessary coordinates.

If we label the incident electron 1, and the molecular electrons 2 and 3, with the origin of coordinate

system sitting at the center of mass of the  $H_2$  molecule, and designate the nuclei by subscripts A and B then the interaction potential can be written as

$$V = -\frac{1}{r_{1A}} - \frac{1}{r_{1B}} + \frac{1}{r_{12}} + \frac{1}{r_{13}} \quad (169)$$

Further, since the electronic motion is much faster than the nuclear motion, let us assume that the molecular wave functions can be written as products of the electronic, vibrational, and rotational wave functions. Thus we have

$$\bar{\Phi}_0 = \psi_0(\vec{r}_2, \vec{r}_3, R) \xi_{0v} (R) Y_J^m(\chi, \varphi), \quad (170)$$

$$\bar{\Phi}_n = \psi_n(\vec{r}_2, \vec{r}_3, R) \xi_{nv'} (R) Y_{J'}^{m'}(\chi, \varphi), \quad (171)$$

where  $R$  is the internuclear distance and  $\chi, \varphi$  are the orientation coordinates of the molecule;  $\xi_{0v}(R)$  and  $\xi_{nv'}(R)$  are the vibrational wave functions of the ground and excited electronic states respectively; and  $Y_J^m(\chi, \varphi)$  and  $Y_{J'}^{m'}(\chi, \varphi)$  are the rotational wave functions of the ground and excited states, respectively.

Substituting equations (169), (170) and (171) into equation (168), we have

$$f_n(k_0, \theta, \phi) = \frac{-2\pi m \epsilon^2}{\hbar^2} \int \left[ \xi_{n\nu'} Y_{J'}^{m'} \right]^* \left[ T_{on}^{direct} \right] \left[ \xi_{0\nu} Y_J^m \right] d\vec{R} \quad (172)$$

where

$$T_{on}^{direct} = T_{on}^{direct} (k_0, \vec{\Delta k}, \vec{R}) \quad (173)$$

$$= \iiint \left[ \int e^{i(\vec{\Delta k}) \cdot \vec{r}_1} \left( -\frac{1}{r_{1A}} - \frac{1}{r_{1B}} + \frac{1}{r_{12}} + \frac{1}{r_{13}} \right) d\vec{r}_1 \right] \cdot \psi_n^* \psi_0 d\vec{r}_2 d\vec{r}_3$$

We see that the integration over  $\vec{r}_1$  may be simplified using equation (34), provided  $\Delta k$  is small.

Thus from equation (32) the differential cross section can be written as

$$\begin{aligned} \sigma_n(k_0, \theta, \phi) &= \frac{k_n}{k_0} |f_n|^2 \\ &= \frac{4\pi^2 m^2 \epsilon^4}{\hbar^4} \left( \frac{k_n}{k_0} \right) \left| \int_{\chi, \varphi} \left[ Y_{J'}^{m'} \right]^* \left[ \xi_{n\nu'}^* T_{on}^{dir.} \xi_{0\nu} R^2 dR \right] \cdot Y_J^m \sin \chi d\chi d\varphi \right|^2 \end{aligned} \quad (174)$$

### II.11.3. Statistical Average of the Differential Cross Sections

The expression for the differential cross sections from the Born approximation for direct scattering of electrons by the  $H_2$  molecule that we obtained in equation (174) represents excitations from a particular groundstate  $(0, \nu, J, M,)$  to a particular excited state  $(n, \nu', J', M')$ . Thus, let us redefine the differential cross sections as follows

$$\sigma_{\nu \nu' J M}^{n \nu' J' M'} \equiv \sigma_n(\hat{k}_0, \theta, \phi) . \quad (175)$$

For practical purposes we do not consider the cross sections for excitations to the individual rotational states, but the sum over all final rotational states.

Since the following relationship holds for an arbitrary function  $G(x, \varphi)$ ,<sup>(35)</sup>

$$\begin{aligned} \sum_{J', m'} \left| \int \int [Y_{J'}^{m'}(x, \varphi)]^* G(x, \varphi) Y_J^m(x, \varphi) \sin x \, dx \, d\varphi \right|^2 \\ = \int \int |Y_J^m(x, \varphi) G(x, \varphi)|^2 \sin x \, dx \, d\varphi \end{aligned} \quad (176)$$

therefore from equation (174), we have

$$\begin{aligned} \sigma_{\nu \nu' J M}^{n \nu' J' M'} \equiv \sum_{J', m'} \sigma_{\nu \nu' J M}^{n \nu' J' M'} = \frac{4\pi^2 \epsilon^4 m^2}{\hbar^4} \left( \frac{k_n}{k_0} \right) \int \int_{x, \varphi} |Y_J^m \cdot \\ \cdot \left[ \int \left\{ \sum_{\nu \nu'}^* T_{on}^{dir.} \left\{ \sum_{\nu \nu'} R^2 dR \right\} \right\} \right]^2 \sin x \, dx \, d\varphi , \end{aligned} \quad (177)$$

where we have made the assumption that the separations between rotational levels are small compared to the excitation energies, such that  $k_n$  is almost independent of  $J'$  and  $M'$ . Actually the energy states are degenerate with respect to the quantum numbers  $M'$  in the absence of an external magnetic field. Furthermore, because of the mass differences between electrons and molecules, electrons are very inefficient in producing angular momentum excitations. Thus excitations from a certain ground state  $(0, \nu, J, M)$  to a certain excited state  $(n, \nu', J', M')$ , will only have appreciable intensity within a narrow range of  $J'$ .

Under usual experimental conditions, the target gasses are at a certain temperature  $T$ , say room temperature. The various rotational states of the ground vibrational state are populated according to their statistical weights. Thus we have

$$\sigma_{0\nu}^{n\nu'} = \frac{\sum_{J=0}^{\infty} \sum_{M=-J}^J e^{-\frac{J(J+1)\hbar^2}{2I kT}} \sigma_{0\nu JM}^{n\nu'}}{\sum_J \sum_M e^{-\frac{J(J+1)\hbar^2}{2I kT}}} \quad (178)$$

Since

$$\sum_{m=-J}^J |Y_J^m|^2 = \frac{1}{4\pi} \quad , \quad (179)$$

equation (178) can be rewritten as

$$\sigma_{\nu\nu'}^{n\nu'} = \left( \frac{4\pi^2 m^2 \epsilon^4}{\hbar^4} \right) \frac{\langle \bar{k}_n \rangle}{k_0} \int_{x,\varphi} \left| \int \int \int_{\nu\nu'}^* T_{\text{on}}^{\text{dir.}} \int_{\nu\nu'} R^2 dR \right|^2 \frac{\sin x dx d\varphi}{4\pi}, \quad (180)$$

where

$$\langle \bar{k}_n \rangle = \frac{\sum_J (2J+1) e^{-\frac{J(J+1)\hbar^2}{2IkT}} k_n}{\sum_J (2J+1) e^{-J(J+1)\hbar^2/2IkT}}, \quad (181)$$

and

$$k_n \cong \left[ k_0^2 - \frac{2m}{\hbar^2} (E_{n\nu'} - E_{\nu\nu J}) \right]. \quad (182)$$

If we further assume that the scattering amplitude  $[T_{\text{on}}^{\text{direct}}]$  is independent of  $R$ , (this is usually assumed in optical spectroscopy and is known as the Franck-Condon principle), then equation (180) becomes

$$\sigma_{\nu\nu'}^{n\nu'} \cong \frac{4\pi^2 m^2 \epsilon^4}{\hbar^4} \frac{\langle \bar{k}_n \rangle}{k_0} g_{\nu\nu'}^{n\nu'} \langle |T_{\text{on}}^{\text{dir.}}|^2 \rangle_{x,\varphi} \quad (183)$$

where

$$\langle |T_{0n}^{dir.}|^2 \rangle_{x,y} = \int_{x,y} |T_{0n}^{dir.}|^2 \frac{\sin x \, dx \, dy}{4\pi} \quad (184)$$

= orientational average of  $|T_{0n}^{dir.}|^2$ ,

and

$$g_{0v}^{nv'} = \left| \int \xi_{nv'}^*(R) \xi_{0v}(R) R^2 dR \right|^2 \quad (185)$$

= Franck-Condon factor in  
electron impact spectroscopy.

Equation (183) is the expression for the differential cross sections for direct scattering of electrons by  $H_2$  molecules summed over all rotational levels of the excited states and averaged over all rotational states of the ground state. Similar expression can be derived for exchange scatterings.

## II.12 General Properties of Inelastic Cross Sections

In conclusion of the theory of electron scattering and as a guide to the experiments, it seems worthwhile to emphasize once more some of the important aspects which are well established on both theoretical and experimental grounds<sup>(9)</sup> in connection with inelastic scattering of electrons by atoms and molecules. These aspects may be

summarized as follows.

A. Energy Dependence of Cross Sections at Large E

- (1) Optically allowed (electric dipole allowed) transitions fall off at the rate of  $\sim \frac{\log E}{E}$ .
- (2) Optically forbidden (electric quadrupole allowed) transitions not involving a change in spin fall off at the rate of  $\sim \frac{1}{E}$ .
- (3) Spin forbidden (from exchange scattering only) transitions fall off at the rate of  $\sim \frac{1}{E^3}$ .

B. Angular Distribution of Scattered Electrons

- (1) Optically allowed transitions and elastic scattering have sharply forward peaked distributions.
- (2) Optically forbidden transitions and spin forbidden transitions have more uniform angular distributions.

C. Magnitude of Cross Sections

- (1) Elastic scattering is approximately two orders of magnitude larger than inelastic scattering.
- (2) At high electron energies the optically allowed transitions are considerably larger than other inelastic processes.
- (3) Spin forbidden transitions are only appreciable if at all, at electron energies in a narrow range close to the threshold.

D. Franck-Condon Principle

Is observed in the electronic excitations of molecules by low energy electron impact.

### III. Historical Background

About half a century ago, Franck and Hertz<sup>(36)</sup> were the first workers to study the inelastic collisions of electrons with atoms and molecules. They found that<sup>(36c)</sup> for metal vapors such as Hg, Zn, and Cd the optical spectral lines could be excited by low energy electrons, and for the alkali and alkali earth atoms the ionization potentials obtained from the electron impact method agreed with the optical values. At that time this was a confirmation of Bohr's old quantum theory, and was also the introduction of a new experimental technique (Franck-Hertz experiment) for the study of electronic spectra.

Because of experimental difficulties in studying single collision processes, so far only very little information is available about the differential cross sections  $\sigma_n(E, \theta, \phi,)$  for all energies  $E$  and scattering angles  $\theta$  of a given process "n" for any given atom or molecule. The main electron impact experiments which have been done to present may be summarized as follows.

- A. The total ionization cross sections as a function of electron energy.
- B. Analysis of the ionization cross sections into contributions from single, double, etc., ionization processes.
- C. Cross sections for inner-shell ionization as a function of energy of some metallic atoms.
- D. Electronic excitation cross sections from optical measurements.
- E. Angular distribution functions for elastic collisions with atoms at fixed electron energies.

- F. Electron diffraction studies on gas molecules.
- G. Vibrational and rotational excitation measurements with gas molecules.
- H. Negative ion formation and dissociative transition measurements.
- I. Scattering studies on crystals.
- J. Electronic excitation cross section measurements by energy analysis of the scattered electrons (see below).

For the interests of the present research we will briefly review the recent progress in the field of atomic and molecular electronic excitation measurements by energy analysis of the scattered electrons.

### III.1. Forward Scattering Measurements Lassetre et al

In a series of papers Lassetre<sup>(37)</sup> and his coworkers reported their work on electron impact of He, H<sub>2</sub>, N<sub>2</sub>, CO, O<sub>2</sub>, CH<sub>4</sub>, C<sub>2</sub>H<sub>6</sub>, C<sub>2</sub>H<sub>4</sub>, and H<sub>2</sub>O molecules. The energy range of the incident electrons was between 250 and 600 ev; and the observation angles were smaller than 15°. The impact spectra thus obtained resembled generally the corresponding optical absorption spectra. The conclusion was that the optical selection rules were obeyed under the said experimental conditions.

These authors were able to show that by increasing the scattering angle from 3.8° to 15.3° at a beam energy of about 500 ev, the intensity of the helium 1'S → 2'P transition fell off rapidly while the angular momentum forbidden transition 1'S → 2'S gradually gained intensity relative to that of the 1'S → 2'P transition. Also, by

lowering the beam energies from 350 to 250 ev at a fixed scattering angle of  $0^\circ$ , this forbidden transition started to show up. However, no spin forbidden transitions were observed in this high energy range.

Further work reported by Lassettre<sup>(38)</sup> and his coworkers on successive studies of  $N_2$  showed the observation of three "electric dipole forbidden but quadrupole allowed" transitions located at 8.7 to 9.6 ev, 11.86 ev and 12.25 ev, respectively, for beam energies between 60 and 500 ev and at small scattering angles. The first one mentioned above was due to the transition  $a^1\pi_g \leftarrow X^1\Sigma_g^+$ , the so called Lyman-Birge-Hopfield band.

Most recently, Skerbele, Dillon, and Lassettre<sup>(39)</sup> reported further observations in  $N_2$  and CO at still lower beam energies using counting techniques. Singlet-triplet transitions were observed.

The nitrogen  $A^3\Sigma_u^+$ ,  $B^3\pi_g$  and  $C^3\pi_u$  transitions showed up clearly between  $0^\circ$  and  $16^\circ$  scattering angles and 35 to 50 ev beam energies. The intensities of these triplet states and that of the  $a^1\pi_g$  electric quadrupole allowed transition were about 1% and 10% respectively, of that of the optically allowed transitions. The carbon monoxide  $a^3\pi$  and  $b^3\Sigma^+$  transitions at  $2^\circ$  angle and 50 ev beam energy also showed intensities about 0.5%~1% of that of the allowed transitions. The energy resolution in these experiments was in general better than 0.1 ev and was achieved using  $180^\circ$  spherical electrostatic analyzers. The ratios of vibrational line intensities showed good agreement with those calculated from Franck-Condon factors.

However, these authors pointed out that a survey of the spectra of 16 polyatomic molecules at beam energies of 35 ev and higher had failed to reveal any singlet-triplet transition. They predicted that beam energies closer to threshold might be needed to excite such states in polyatomic

molecules at small angles.

### III.2. Forward Scattering Measurements Simpson et al

A few years ago Simpson<sup>(40)</sup> constructed a forward scattering high resolution (0.030 ev) electron impact spectrometer. The results obtained with it were similar to those of Lassette. At 0° scattering angle and 50 ev beam energy Simpson and Mielczarek<sup>(41)</sup> were unable to detect spin-forbidden transitions in He or C<sub>2</sub>H<sub>4</sub>. Furthermore, Kuyatt, Simpson and Mielczarek<sup>(42)</sup> were again unable to find spin-forbidden transitions in H<sub>2</sub>, HD or D<sub>2</sub> with electron beam energies ranging between 30 and 90 ev, nor with H<sub>2</sub>O with beam energies as low as 9 ev.

After the operation of this instrument was improved, Chamberlain, Heideman, Simpson and Kuyatt<sup>(43)</sup> found several singlet-triplet transitions in He at beam energies up to 50 ev. Recently, Heideman, Kuyatt and Chamberlain<sup>(44,45)</sup> also reported seeing triplet states in N<sub>2</sub><sup>(44)</sup> with beam energies between 15.7 and 35 ev and in H<sub>2</sub><sup>(45)</sup> with beam energies between 13.7 and 50.7 ev.

### III.3. Electronic Excitation at Threshold Trapped-Electron Method

Another low energy electron impact method for studying the electronic transitions at threshold in atoms and molecules was developed by Schulz<sup>(46)</sup>. This technique involves trapping inelastically scattered electrons which have lost practically all of their energy in an electrostatic potential well of about 0.1 to 0.3 ev depth and letting them move randomly in this well until they strike a collector.

In taking a spectrum, the incident beam energy is scanned. The collimation of the electron beams is achieved by means of a magnetic field of about 100 gauss along the beam direction. This method is called the "trapped-electron method". Using this method, Schulz obtained threshold excitation spectra on He, H<sub>2</sub>, and H<sub>2</sub><sup>(46)</sup>, on N<sub>2</sub>, CO and He<sup>(47)</sup>, on H<sub>2</sub>O<sup>(48)</sup>, on N<sub>2</sub>O<sup>g(49)</sup>, and on O<sub>2</sub><sup>(50)</sup>.

The spectra obtained with this method agreed very well with the optical spectra. Furthermore, in addition to the optically allowed states Schulz also observed singlet-triplet transitions due to electron exchange. The intensities of the optically allowed and spin-forbidden transitions were of the same order of magnitude. In cases like He, N<sub>2</sub> and CO the singlet-triplet transitions appeared with higher intensities than the optically allowed transitions.

Recently, Bowman and Miller<sup>(51)</sup> reported low energy electron impact studies of molecules by means of the trapped-electron technique. Excitation spectra were obtained over the subionization energy range for methane, ethane, ethylene, propylene, acetylene, propyne, and 1-butyne. The helium 2<sup>3</sup>S transition was so pronounced that these authors used this peak at 19.81 ev to establish the incident electron energy scale.

Further work by Bowman<sup>(52)</sup> using the same technique also yielded excitation spectra of hydrogen cyanide, nitrogen, methyl cyanide, ethyl cyanide, and butadiene.

Very recently, a high resolution (about 0.1 ev) trapped-electron spectrometer has been put into operation by Brongersma and Oosterhoff<sup>(53)</sup>. Threshold excitation spectra of CO and N<sub>2</sub> have been obtained. Vibrational structure of the CO a<sup>3</sup>π←X transition is partially resolved, whereas the first strong transition in N<sub>2</sub> is shown to be the B<sup>3</sup>π<sub>g</sub>←X'<sup>1</sup>Σ<sub>g</sub><sup>+</sup>, instead of the A<sup>3</sup>Σ<sub>u</sub><sup>+</sup>←X'<sup>1</sup>Σ<sub>g</sub><sup>+</sup> transition suggested

by Schulz<sup>(47)</sup>.

A difficulty of the trapped-electron method is that low energy negative ions produced in the system are also trapped and detected. Therefore, to get the trapped-electron current, it is necessary to obtain the negative ion current with zero well depth in a separate run and subtract it from the total current.

#### III.4. Large-Angle Measurements

Recently, Kuppermann and Raff<sup>(54,55,56)</sup> reported some low energy electron impact spectra on helium, argon, hydrogen and ethylene. The beam energies were between 25 and 75 ev. Scattered electrons within an angular range from  $22^\circ$  to  $112^\circ$  were energy analyzed simultaneously by a retardation potential method. Spin forbidden transitions were reported in addition to the optically allowed ones.

Most recently, Doering<sup>(57)</sup> used a single cylindrical electrostatic analyzer to study low energy electron impact spectra of helium at  $90^\circ$ . The beam energies were between 40 and 100 ev, and the resolution was about 1 ev. However, he was unable to detect the  $2^3S$  state in helium

Doering<sup>(58)</sup> also studied ethylene at incident beam energies of 25, 50 and 70 ev and at a fixed scattering angle of  $90^\circ$ . The most intense inelastic peak was found to be a 8 ev, corresponding to number of unresolved allowed transitions. A peak was observed at 4.6 ev which was assigned to the forbidden singlet-triplet transition detected by Kuppermann and Raff<sup>(54,55)</sup>. The intensity of the 4.6 ev peak was about 10% of that of the 8 ev peak at 35 ev beam energy.

#### IV. Experimental

From the foregoing discussions of theory and experimental background, we see that by using low energy electrons as an energy source we may obtain valuable information about spin-forbidden energy levels of many simple molecules because of electron exchange.

Both theory and experiments have indicated that exchange collisions are appreciable only for incident energies within a narrow range beyond the threshold of excitation. Furthermore, the ratio of differential cross sections for the spin forbidden and optically allowed transitions seems to increase with increasing scattering angle  $\theta$ . Thus we see that low-energy and large-angle are the two favorable conditions for the observation of optically forbidden transitions.

In this section, we present a description of the experimental details of the  $90^\circ$  low-energy electron impact spectrometer we used in the present work.

##### IV.1. The Apparatus

The design and construction of our electron impact spectrometer is based upon the apparatus used by Arnot and Baines<sup>(59)</sup> in their work on collision cross sections of the mercury atom. The original work on setting-up of our spectrometer was done by Raff<sup>(60)</sup>. He introduced differential pumping between the cathode and the sample regions to avoid cathode poisoning and sample contamination. The use of bakeable metal high vacuum systems and of electronic circuits for current and voltage measurements are the improvements over Arnot and Baines' apparatus.

In the present work, one of the grids used by Raff was substituted by a stack of parallel disks, along the lines of the Lozier gun<sup>(61)</sup>, as described below. This selects electrons scattered at  $90^\circ$ , which sharpens the energy resolution when using retardation potential method.

#### IV.1.1. The Vacuum System

The vacuum system consists of two cylindrical chambers. One houses the electron gun and is referred to as the gun chamber; the other contains the grids necessary for the energy analysis of the scattered electrons and is referred to as the collision chamber or the scattering chamber. These two chambers are separately pumped. They are interconnected by a 1.5 mm diameter pinhole through which the electron beam produced in the gun chamber enters the collision chamber. A schematic diagram of the spectrometer is shown in Figure 1.

##### A. The vacuum chambers

The vacuum enclosures for the electron gun and the collision chamber consist of two brass tubes,  $3\frac{3}{8}$ " in inner diameter, with a wall thickness of  $\frac{1}{16}$ ", and  $10\frac{7}{16}$ " and  $5\frac{1}{16}$ " in length, respectively. These tubes are closed at the ends by 304-stainless steel flanges through which the electrical leads pass via glass to metal seals. The two chambers are mechanically joined by means of a double flange; however, the only internal vacuum connection between them is through the 1.5 mm pinhole at the center of this double flange.

The gun chamber is provided with four one-inch side-flanges for the connection of auxiliary components to the system. The collision chamber is provided with five such entry flanges.

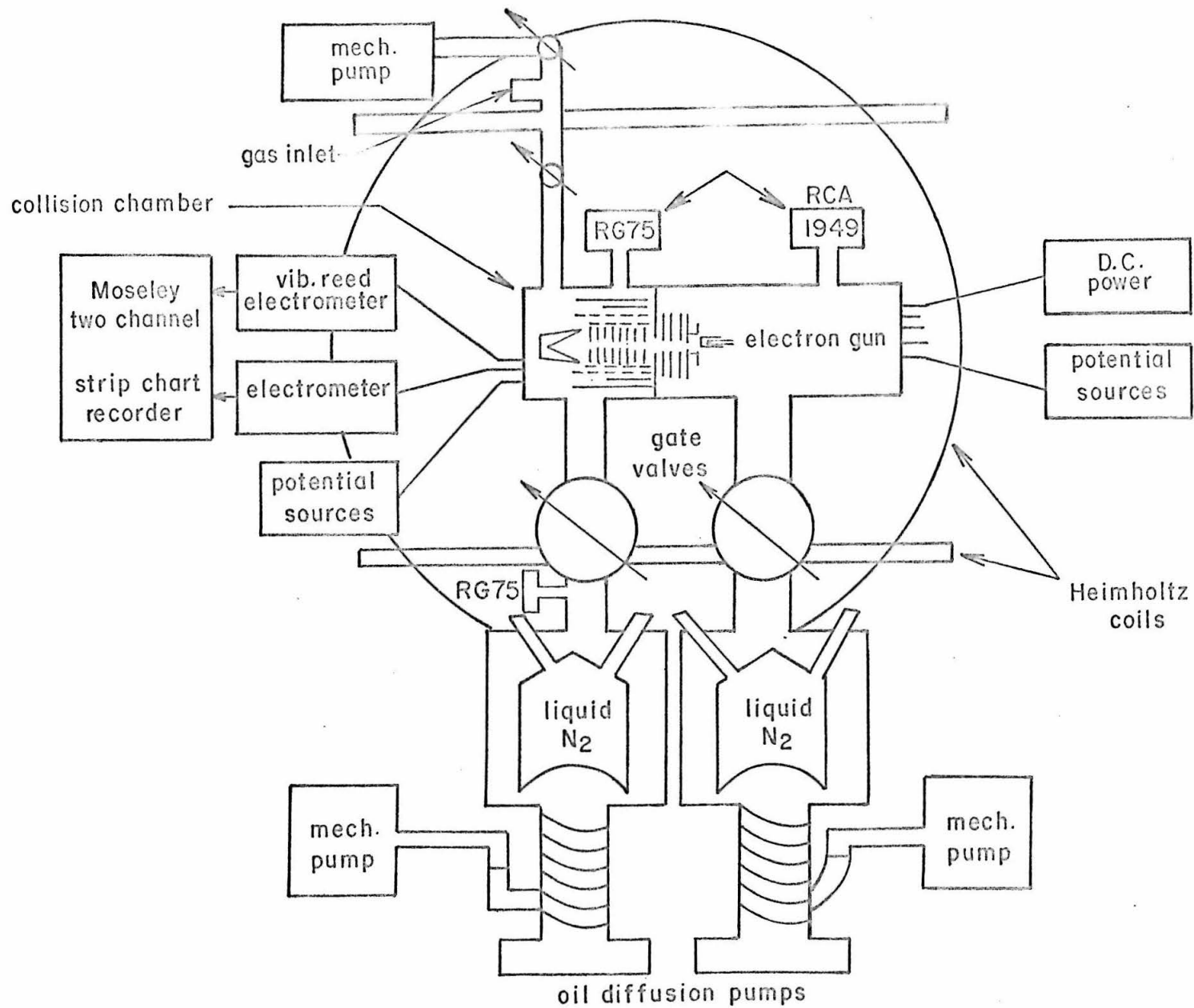


Figure 1. Schematic diagram of the 90° electron impact spectrometer.

### B. The gold wire gaskets

All vacuum seals in the gun and collision chamber regions are made by means of gold wire gaskets. These are prepared by cutting off proper lengths of 0.030" gold wire, annealing it in an oxygen-gas torch, and then sealing the ends to each other by fusing them with a small, intense flame. After forming, the gaskets are again annealed before use.

### C. The gate valves

The gun chamber is connected to a 2" gate valve through 2" brass tubing while the collision chamber is joined to a second two inch gate valve via 1½" brass tubing. At the gate valves and below, all seals are made by means of rubber O-rings coated with a thin layer of Apiezon-N vacuum grease.

### D. The liquid nitrogen traps

Below each of the gate valves is a large liquid nitrogen trap which serves as a baffle for the oil diffusion pumps. These traps consist of an inner and an outer can. The inner can, constructed of copper, is cylindrical with a concave bottom and a convex top. The capacity of this inner can is about 3 liters and it will hold its charge of liquid nitrogen for a period of about seven hours. Automatic filling of the traps is accomplished with the use of two solenoid valves, one for each trap, connected to a compressed air line, and two pairs of Eagle Cyclo-Flex automatic timers. One clock of each pair controls the time between fillings and the other the duration of each filling.

The outer vacuum jacket of the traps is a brass tube 10" in diameter and 12" in length. This tube is covered by a circular plate to which the inner can is attached by means of two thin-wall inconel tubings. The seal between

the cover and the tube is made by means of an O-ring. The traps are shown Schematically in Figure 1.

E. The vacuum pumps

The pumping system for the gun chamber consists of a W.M. Welch single-stage duo-seal mechanical pump with a free-air capacity of 33.4 l/mm. This is connected to a Consolidated Electrodynamics MCF-300 three state 4" oil diffusion pump, which has an optimum unbaffled pumping speed of 300 l/sec.

The pumping system for the collision chamber is identical to that of the gun chamber except that a W.M. Welch two-stage duo-seal pump is used to back up the MCF-300 oil diffusion pump. This mechanical pump has a free air capacity of 140 l/mm.

F. The ionization gauges

The pressure in each of the chambers is monitored by means of ion gauges connected to the side flanges. In the gun chamber an RCA 1949 gauge tube is used while in the collision chamber a Veeco RG-75 type gauge is used. There is also another RG-75 gauge tube mounted below the gate valve on the collision chamber side.

G. The bake-out oven

The purpose of the bake out is to increase the degassing rate of the components inside the vacuum chamber in order to obtain the ultimate vacuum within a short time. The gold wire seals allow the system to be baked at temperatures up to 280°C. This bake-out is accomplished by the use of an external oven, made of  $\frac{1}{4}$ " thick transite, measuring  $27\frac{1}{2}$ " x  $15\frac{1}{2}$ " x  $11\frac{1}{2}$ ". The oven contains 3840 Watts of heating elements mounted on four sides and the top. The temperature inside the oven is monitored with an iron-constantan thermocouple.

After bakeout at 280°C for a period of about 24 hours, an ultimate vacuum below  $5 \times 10^{-7}$  torr can usually be obtained in each of the two chambers.

#### H. The differential pumping

Since the two chambers are connected by only a small 1.5 mm pinhole, good differential pumping can be maintained between them. In general, the pressure within the gun chamber can be maintained at a value of  $\frac{1}{50}$  that of the collision chamber for a collision chamber pressure of the order of  $10^{-4}$  torr.

### IV.1.2. The Electron Gun

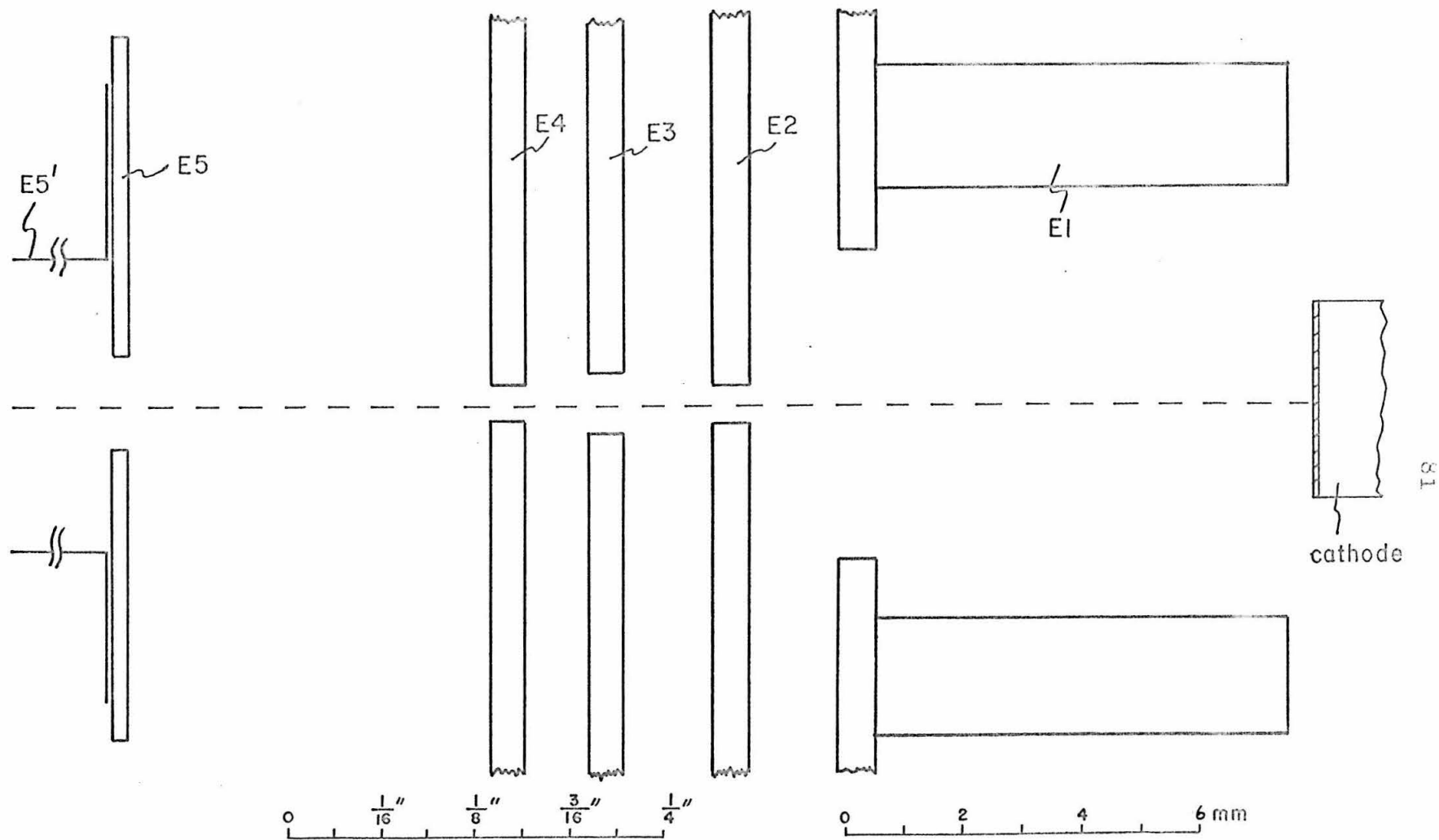
The electron gun consists of a cathode with a heating element and five planar electrodes. The purpose of the gun is to produce a beam of electrons, of energy between 30 and 70 ev, well-collimated, and with an intensity of around  $10^{-7}$  amp measured in the collision chamber. Figure 2 shows a cross section through the axis of the cylindrically symmetrical electron gun.

#### A. The cathode

The cathode used in the electron gun is a KB623B-N10985 RCA oxide cathode. The cathode is mounted in an I16061-C230F ceramic spacer which serves to insulate it from other elements of the electron gun assembly. Electrical connections to the cathode are made with the help of two metal tabs spot-welded to its body.

#### B. The heating element

The oxide cathode assembly is indirectly heated by an RCA MCH 8004D ceramic coated heater, wound up as a double



18

Figure 2. Cross section through the axis of the cylindrically symmetrical electron gun.

helix. This tungsten filament has an apparent length of about 15 mm (the total length of the uncoiled wire being much longer) and fits into the metal compartment directly behind the oxide coated surface of the cathode. It is rated for 6.3 v and 0.6 amp but can be operated at currents up to 0.9 amp. With currents in this range temperatures between 1000° and 1300°K can easily be obtained. At these temperatures the total emission from the cathode is sufficient for the purposes of this experiment.

#### C. The E1 electrode

Mounted about  $\frac{1}{24}$ " in front of the cathode is the electrode E1 which is used to withdraw a large number of electrons from the surface of the oxide emitter. (see Figure 2).

E1 is made by spot-welding an inconel cylinder (with 7 mm inner diameter and  $\frac{35}{728}$ " in length) onto a  $1\frac{7}{8}$ " diameter inconel plate (with a 4.9 mm diameter center hole and  $\frac{3}{733}$ " in thickness).

#### D. The E2, E3, E4 and electrodes

The electrodes E2, E3 and E4 have the purpose of collimation and focusing the beam. These three electrodes are all made of  $1\frac{7}{8}$ " diameter inconel plates ( $\frac{3}{728}$ " in thickness). The center hole diameters in these electrodes are 0.572, 1.015 and 0.572 mm for E2, E3 and E3, respectively. The spacings between them are (see Figure 2) E2 to E1 = 1.50 mm, E3 to E2 = 1.50 mm, and E4 to E3 = 1.06 mm.

#### E. The E5 electrode

The final electrode E5 in the electron gun assembly is a small gold disk mounted in the center of the stainless steel flange connecting the gun chamber with the collision chamber. The spacing between E5 and E4 is 6.2 mm.

This gold disk is 0.010" thick and has a 1.5 mm diameter hole in the center. It is attached by epoxy resin to a 1" diameter quartz disk ( $\frac{1}{16}$ " in thickness and with a  $\frac{1}{2}$ " hole in its center). The hole in the gold disk allows the electron beam to pass into the collision chamber. The quartz disk is itself attached to the stainless steel flange by epoxy resin. This arrangement serves to insulate E5 from the center flange.

The potential on E5 relative to the cathode determines the energy of the electrons that enter the collision chamber.

In order to eliminate the possibility of the electron beam being distorted by the ground potential of the steel flange or the dielectric materials of the quartz disk and epoxy resin, a small tantalum cylinder E5' with diameter about  $\frac{3}{16}$ " and length about  $\frac{3}{16}$ " is spot-welded onto the collision chamber side of E5 (see Figure 2). This shields the electron beam against stray fields.

#### F. The electron gun assembly

The cathode with its heating element along with the five electrodes constitute the electron gun. These elements are mounted under adequate alignment conditions and keep rigidly fixed in position<sup>(62)</sup>.

The accurate spacings and electrical insulation between these elements are achieved by means of precision sapphire balls placed into holes (with smaller diameters than the sapphire balls) drilled in the inconel plates. Three balls are placed between every two plates. The diameters of the hole and the ball determine the separation.

It should be pointed out that the present version of the electron gun follows very closely to that described by Raff<sup>(62)</sup>. The only differences are that in the present electron gun the center hole diameters of E2 and E4 are both 0.572 mm while previously they were both 0.5 mm.

### G. The improvement in alignment of the electron gun

An examination of Raff's electron gun assembly under a microscope with calibrated vertical and horizontal scales showed that the center of E<sup>4</sup> was displaced by 0.13 mm relative to the line between the centers of E<sup>2</sup> and E<sup>5</sup> (62).

We note that the average distance between E<sup>2</sup> and E<sup>4</sup> is 3.75 mm. Hence 0.13 mm off-centerness of E<sup>4</sup> would cause an angular deviation of 2° from the axis of symmetry.

This off-centerness has actually been observed and corrected on an optical comparator (with a 50 times magnifying lens) to less than 0.0005" or 0°±0.2° angular deviation.

### IV.1.3. The Collision Chamber

The collision chamber contains a beam collector (BC), a shielding grid (G1A), three sets of concentric cylindrical grids (G1, G2 and G3) and two sets of concentric cylinders (scattering collector SC, and the shield). Figure 3 shows a cross section through the axis of the cylindrically symmetrical collision chamber grid system.

#### A. The beam collector

The beam collector is a cone made of brass with  $\frac{7}{16}$ " in diameter at the open end. It rests in a cone-shaped space provided at the end of the boron nitride supporting rod and is  $1\frac{5}{8}$ " from E<sup>5</sup>. The electron beam is directed at this collector and the resulting current is measured during an experiment.

#### B. The G1 grid

The G1 grid is a major modification of Raff's apparatus based on the idea of Lozier (61). This grid gives

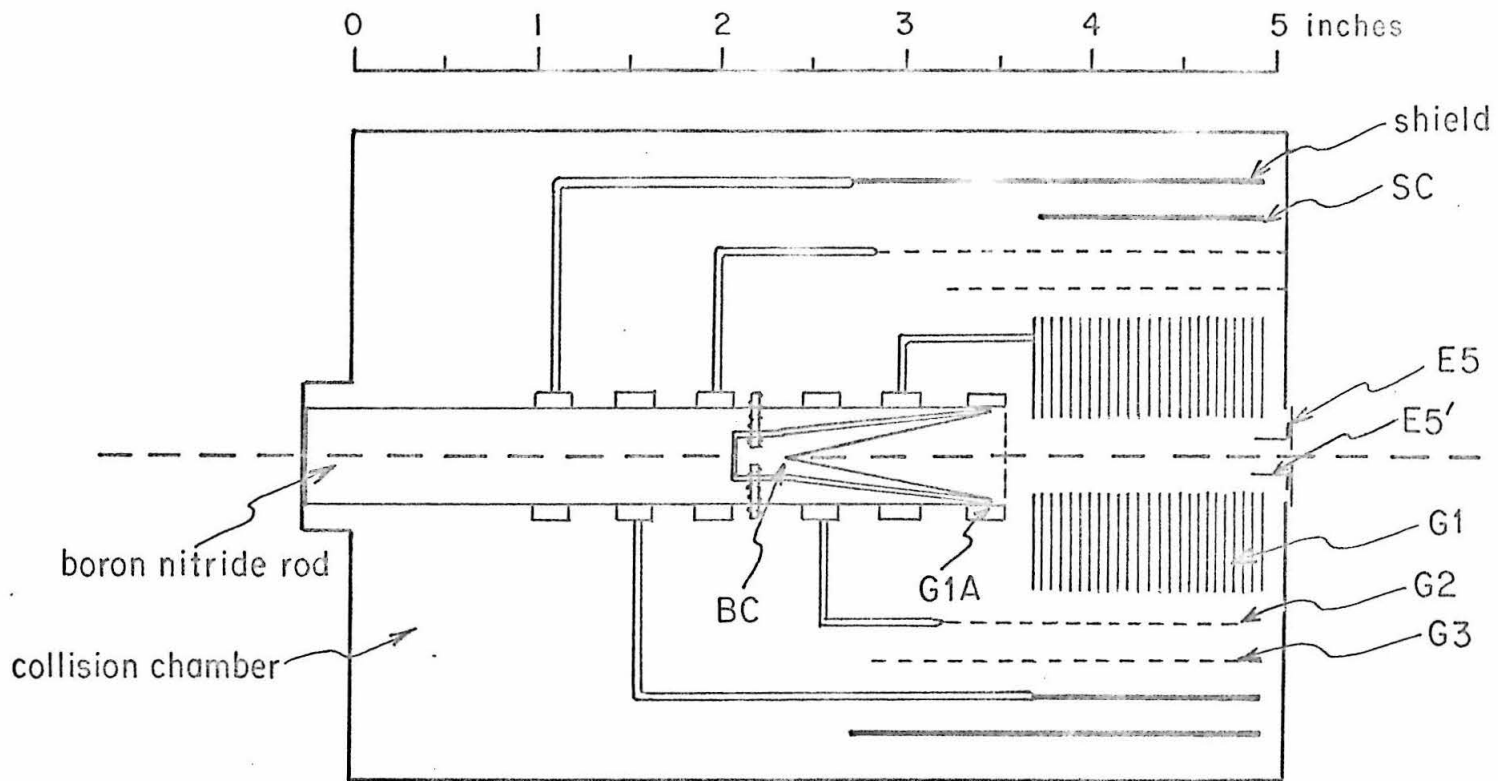


Figure 3. Cross section through the axis of the cylindrically symmetrical collision chamber grid system.

rise to a directional selectivity for electrons scattered around  $90^\circ$ .

This grid has a length of  $1\frac{1}{4}$ " and is made of a stack of 22 copper disks 0.010" in thickness  $1\frac{3}{8}$ " in diameter and with a center hole  $\frac{3}{8}$ " in diameter. These disks are in electrical contact with, and rigidly supported by, a brass tripod and are mechanically separated by small brass washers 0.050" in thickness. This gives 21 annular paths of 0.050" in width and 0.500" in length each for scattered electrons coming out in the radial direction (perpendicular to the electron beam axis. The tripod is made by silver-soldering 3 L-shaped brass rods ( $\frac{1}{16}$ " diameter) at  $120^\circ$  to each other onto a brass split ring (o.d. =  $\frac{5}{8}$ ", i.d. =  $\frac{1}{2}$ ", height =  $\frac{3}{32}$ "). The ring of the tripod is tightly fitted on the boron nitride rod and the three ends of the tripod are supported by a stainless steel end-plate through boron nitride washers as insulators.

#### C. The G1A grid

The G1A grid is a disk made from a piece of circular tungsten gauze which has a 100 x 100 mesh size (100 wires of 0.001" diameter per linear inch of gauze) with a transparency of 81%. A hole of about  $\frac{1}{4}$ " diameter is cut out at the center of G1A to permit the electron beam to reach BC without reflecting off G1A.

G1 and G1A are maintained at the same potential as E5 and E5' during an experiment so that electrons traveling in this region are not subject to electrostatic fields. The purpose of G1A is to prevent field penetration from BC into the scattering region enclosed by G1.

#### D. The G2 and G3 grids

The G2 and G3 grids are constructed of tantalum gauze which has a 50 x 50 mesh size (50 wires of 0.003"

diameter per linear inch of gauze) with a transparency of 72%. These cylindrical grids are  $1\frac{3}{4}$ " and  $2\frac{1}{8}$ " in length and  $1\frac{3}{4}$ " and  $2\frac{1}{8}$ " in diameter, respectively. They are supported by a brass tripod similar to that of G1.

#### E. The scattering collector

The scattering collector SC is a cylinder concentric with and surrounding G3. Its diameter is  $2\frac{1}{2}$ " and its length is  $1\frac{1}{4}$ ", the same in length as G1. The collector is made of tantalum foil, 0.001" thick, and is supported by a brass tripod similar to that of G1. All three legs of the tripod and leads to the collector are shielded by tantalum foil and ceramic insulators to minimize the back-ground current.

#### F. The shield

The shield is a cylinder (made of 0.001" thick tantalum foil) surrounding the scattering collector. Its diameter is  $2\frac{7}{8}$ " and its length is  $2\frac{1}{4}$ ". The rear end (the one furthest from the gun chamber) of the shield is partially closed by six leaves of tantalum foil extending toward the boron nitride supporting rod in order to collect stray electrons in this region. The shield is also supported by a brass tripod similar to that which supports G1.

#### G. Deposition of platinum black

In order to reduce reflection of electrons, all surfaces of the grids and collectors in the collision chamber are coated with a thin layer of platinum black. It is electrolytically deposited on the grids from a platinum anode in a solution of chloroplatinic acid containing a trace of lead acetate. For a current of 50 ma (at 3.5 v D.C.) a deposition time of 15 min is usually satisfactory.

#### IV.1.4. The Inlet System

The sample gas inlet to the collision chamber is through one of the side flanges attached to the chamber. A 3' length of  $\frac{1}{4}$ " copper tubing is silver-soldered onto this flange. This tubing is connected to a Hoke A413 High vacuum diaphragm-seal valve which serves to separate the chamber from the inlet manifold. The latter is equipped with an NRC-0521 thermocouple gauge and a bakeable Granville-Phillips variable leak valve whose conductance is continuously adjustable from 100 atm cm<sup>3</sup>/sec to 10<sup>-10</sup> atm cm<sup>3</sup>/sec. This variable leak regulates the flow of sample gas into the collision chamber.

The pumping system for the inlet manifold is a liquid nitrogen trap and a W.M. Welch single-stage, duo-seal mechanical pump which has a free air capacity of 33.4 l/min. A Veeco one-inch brass bellows valve is mounted between the inlet manifold and the cold trap. The pumping system is shut off from the manifold during an experiment.

#### IV.1.5. The Helmholtz Coils

Two pairs of Helmholtz coils are used to neutralize the earth's magnetic field in the collision chamber region. One pair is mounted horizontally for the neutralization of the vertical component, and the other vertically for the neutralization of one of the horizontal components. The whole apparatus is oriented in such a way that the horizontal component of the earth's magnetic field along the electron beam axis is zero. All metals used in the collision and gun chamber regions are non-magnetic.

The wire used for the Helmholtz coils is #32 B & S annealed copper of linear resistance of 0.5383 ohms/m,

at 20°C. The dimensions of the coils are given below.

	<u>Vertical pair</u>	<u>Horizontal Pair</u>
average diameter of coils	$38\frac{3}{8}$ "	$40\frac{5}{8}$ "
average separation of coils	$19\frac{3}{16}$ "	$20\frac{5}{16}$ "
number of turns per coil	1376	1622

#### IV.1.6. Measuring Equipments and Power Supplies

Pressure measurements are made with an NRC-763 thermocouple and ultrahigh vacuum ionization gauge control. An auxiliary filament power supply keeps the ion gauge filaments heated when they are not connected to the NRC-763 circuit.

Magnetic field measurements are made with a Bell Model 120 gaussmeter (0.1 to 30000 gauss in 12 ranges, full scale) equipped with an M1201 magna probe (100 time more sensitive in each specified range).

Voltage measurements are made with a John Fluke model 803 DC-AC differential voltmeter (accuracy: .001 v on 50 v range).

Electron beam currents are measured with a Keithley model 410 micro-micro ammeter.

Scattered currents are measured with a Cary model 31 vibrating reed electrometer.

Data recordings are made with a Moseley model 7100-AMR two channel strip chart recorder.

The Electron gun filament is operated by a Kepco model CK18-3m voltage/current regulated power supply (range: 0 to 18 v, 0 to 3 amp; stability: better than 0.01%).

The Potential to E1 electrode is supplied by a Kepco KR11-M voltage regulated power supply (range: 0 to 150 v; stability: 0.25%; resolution: about 0.05 v ).

The Potential between cathode and ground is supplied by a John Fluke model 407 regulated power supply (range: 0 to 555 v; stability: better than 0.01%; resolution: 2 mv).

The Helmholtz coils are operated by two separate Kepco model HB-2M voltage regulated power supplies (DC output: 0 to 325 v; stability: better than 0.1%; normal operating current: about 10 ma).

The Potential to E2 is supplied by a 6-volt car battery (rated for 55 amp-hour, normal operating current: about 1 ma).

Potentials to other electrodes and grids are from 90 volt B-batteries.

## IV.2. The Experimental Procedure

### IV.2.1. Pump-Down and Bakeout

After the system is assembled it is leak checked with a Consolidated Electrodynamics Corp. Model 24-120A helium leak detector, which has a sensitivity of about  $5 \times 10^{-10}$  atm cm<sup>3</sup>/sec/division. The diffusion pumps are then turned

on. After pumping for about one day the pressure in the gun chamber is in the region of  $10^{-6}$  torr while that of the collision chamber is of the order of  $10^{-5}$  torr. The system is then baked to about  $280^{\circ}\text{C}$  for 24 hours or longer while the pressure below the gate valve is monitored. After cooling down, the pressure in the gun chamber is usually  $2 \times 10^{-7}$  torr and that of the collision chamber is  $5 \times 10^{-7}$  torr.

#### IV.2.2. Degassing and Activation of the Cathode

The cathode of the electron gun is degassed by gradually increasing the D.C. heater current to about 0.80 or 0.90 amp. The gradual increase in the temperature of the cathode causes the electron emitting oxide to degas and consequently raises the pressure within the gun chamber. This pressure rise is followed by the ion gauge, and the filament current is increased slowly so that the pressure within the gun chamber never rises above  $2 \times 10^{-6}$  torr during the process. In general, this degassing procedure takes from one to two hours.

After degassing the cathode the activation process is begun. This consists in placing a positive potential on the electrode E1, and allowing a large current to be drawn from the cathode, which results in its activation. The emission current is generally a function of the cathode temperature (which is controlled by the heater current) and the electric field intensity. For a heater current of 0.88 amp and the E1 voltage at 50 v, the emission current measured at E1 is about 0.2 to 3 ma depending on the age of the cathode.

### IV.2.3. Functions of the Electrodes and Grids

After the cathode is activated, suitable potentials are applied to the electrodes and grids to produce an electron beam. Figure 4 shows the circuit diagram as well as a set of typical operating voltages. The functions of the electrodes and grids are as follows.

Cathode: source of electrons

E1: controls the emission current from the cathode at fixed heater current.

E2,E3,E4: electron-optical focusing lenses to minimize the background of scattered current and maximize the beam current. (The characteristics of these electrodes are described in the next section)

E5: controls the energy of the electron beam that enters the collision chamber.

G1,G1A: Provides a field-free space by being set at same potential as E5.

G2: prevents positive ions from being collected by the scattering collector by being set at 10 volts positive with respect to E5.

G3: energy-analyzes the scattered electrons. When G3 is at the cathode potential, no electrons should reach the scattering collector. However, when G3 is at some potential  $V$  with respect to the cathode, then electrons which have lost energies (in eV) equal to or less than  $V$  (in volts) can pass through G3.

SC: collects the scattered electrons. It is grounded through the input resistor of the electrometer.

Shield: shields SC from stray electrons.

BC: collects the incident electron beam.

The holding potential between SC and G3 and that between BC and G1A are determined by the experimental

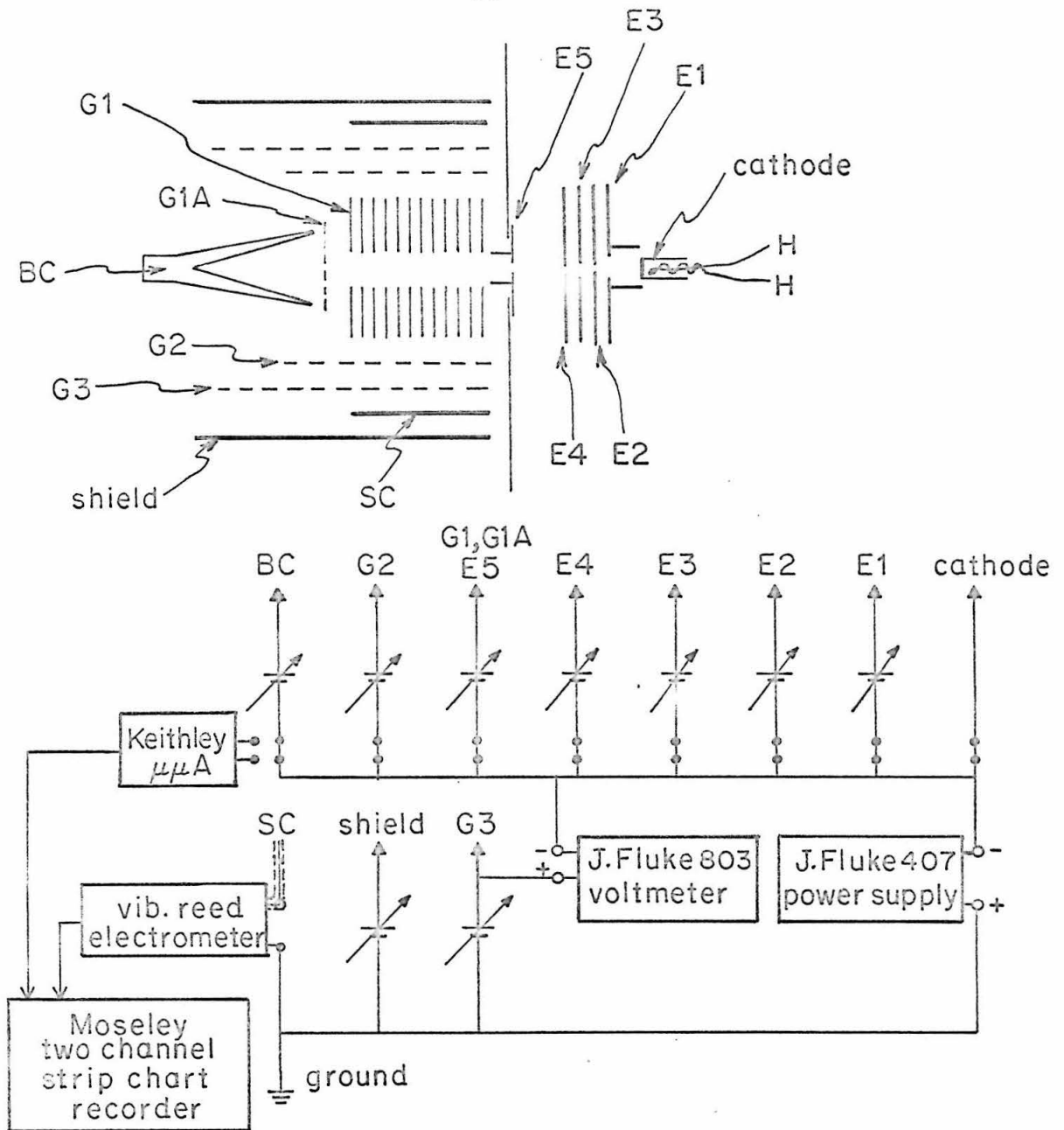


Figure 4. The circuit diagram. The set of potentials with respect to the cathode used for all experiments in Section V is:  $E_1=10\text{v}$ ,  $E_2=4.50\text{v}$ ,  $E_3=29.00\text{v}$ ,  $E_4=6.50\text{v}$ ,  $E_5, G_1, G_{1A}=30$  to  $50\text{v}$ ,  $G_2=E_5+10\text{v}$ ,  $BC=E_5+70\text{v}$ , and  $G_3=0$  to  $30\text{v}$ . The voltage difference between SC and G3 is equal to that between Shield and SC and kept constant at  $65\text{v}-E_5$  as the  $G_3$  voltage is swept.

condition of yielding a minimum background. Details of the behavior of the electrodes and grids are discussed in section IV.3.

#### IV.2.4. Introduction of Gas Samples

To do an experiment, the gas sample to be studied is introduced into the scattering chamber and is pumped away under dynamic conditions.

We note that if the mean free path for collisions of electrons with gas molecules is large compared to collision chamber dimensions then multiple electron collision processes will be much less probable than single collisions. Therefore the scattering chamber pressure ( $P_{sc}$ ) during a run is maintained of the order of  $10^{-4}$  torr such that the mean free path of 35 ev electrons in  $N_2$ , for example, is of the order of 175 cm at room temperature<sup>(63)</sup>.

In order to stabilize the pressure  $P_{sc}$ , a steady state of the flow of gas through the collision chamber must be obtained. To achieve this, the gate-valve between the collision chamber and the liquid nitrogen trap is held at an almost closed position to cut down the pumping speed to less than 1 l./sec. The volume of the collision chamber is approximately  $1\frac{1}{2}$  liters and therefore the time constant of the system is longer than 1 sec.

After the gate valve is set at the almost closed position, a suitable pressure  $P_{sc}$  is obtained by adjusting the opening of the Granville-Phillips variable leak valve.

#### IV.2.5. Procedure for Taking a Spectrum

With a beam current of about  $1 \times 10^{-7}$  amp measured at BC and a collision chamber pressure of about  $1 \times 10^{-4}$  torr (uncalibrated readings from the ion gauge), the total scattered current is of the order of  $10^{-11}$  amp.

The scattered current  $i_{sc}$  as a function of the retardation potential  $V_{G3}$  is recorded on the strip chart recorder. The ratio of increments  $\frac{\Delta i_{sc}}{\Delta V_{G3}}$  is then plotted against  $V_{G3}$  to give the energy loss spectrum.

It should be noted that  $V_{G3}$  is related to the energy loss of the scattered electron by an additive constant, commonly known as the "contact potential". In the present work, the elastically scattered current peak is taken as the zero of the energy scale. The value of  $V_{G3}$  at this point corresponds to the contact potential. Generally, the contact potential is a function of the potentials on the electrodes and grids and changes from day to day. Contact potentials ranging from 0.5 volts to 2 volts have been observed.

### IV.3. Characteristics of the Apparatus

#### IV.3.1. E1 and Cathode as a Diode

From the geometric construction of the electron gun shown in Figure 2, we see that the cathode and the electrode E1 in front of it can be regarded as a diode vacuum tube. A diode has the characteristics that the plate current increases with increasing plate voltage to a certain value and then levels off. The plate voltage

region before the leveling off is called the "space-charge limited region", and the region thereafter is called the "temperature limited region". The current in the latter is often called the saturation current.

Figure 5 shows a plot of  $\tilde{i}_{E1}$  versus  $V_{E1}$  for heater currents  $i_H$  ranging from 0.84 to 0.92 amp for an "aged" cathode. The full lines and dashed lines correspond to  $V_{E2}$  at 0.00 and 10.76 v, respectively. The undulations in these curves seem to be due to electron optical effects.

Figure 6 shows the emission current  $\tilde{i}_{E1}$  as a function of the plate voltage  $V_{E1}$  for a "fresh" cathode with heater current at 0.88 amp. The full line and dashed line correspond to  $V_{E2}$  at 1.13 and 4.75 volts, respectively. We see that under this fresh cathode condition this range of operation is a typical example of the "space-charge limited region".

It is found that the average life-time of the "fresh" cathode with heater currents above 0.8 amp is of the order of two hundred hours.

#### IV.3.2. Electron Beam Currents Measured at E4

We have set E5 to zero potential with respect to the cathode in order not to fire electrons into the scattering chamber and measure the electron currents to E4 as a function of  $V_{E2}$  at different  $V_{E1}$  voltages. Figure 7 shows an example of such measurements with the ratio of increments  $\frac{\Delta i_{E4}}{\Delta V_{E2}}$  plotted against  $V_{E2}$  while  $V_{E1}$ ,  $V_{E3}$  and  $V_{E4}$  are made equal to 5.01, 24.50 and 50.00 v, respectively. (All potentials are measured with respect to the cathode unless otherwise specified). The current reaching E3 is also measured, and it is only a few percent of that measured at

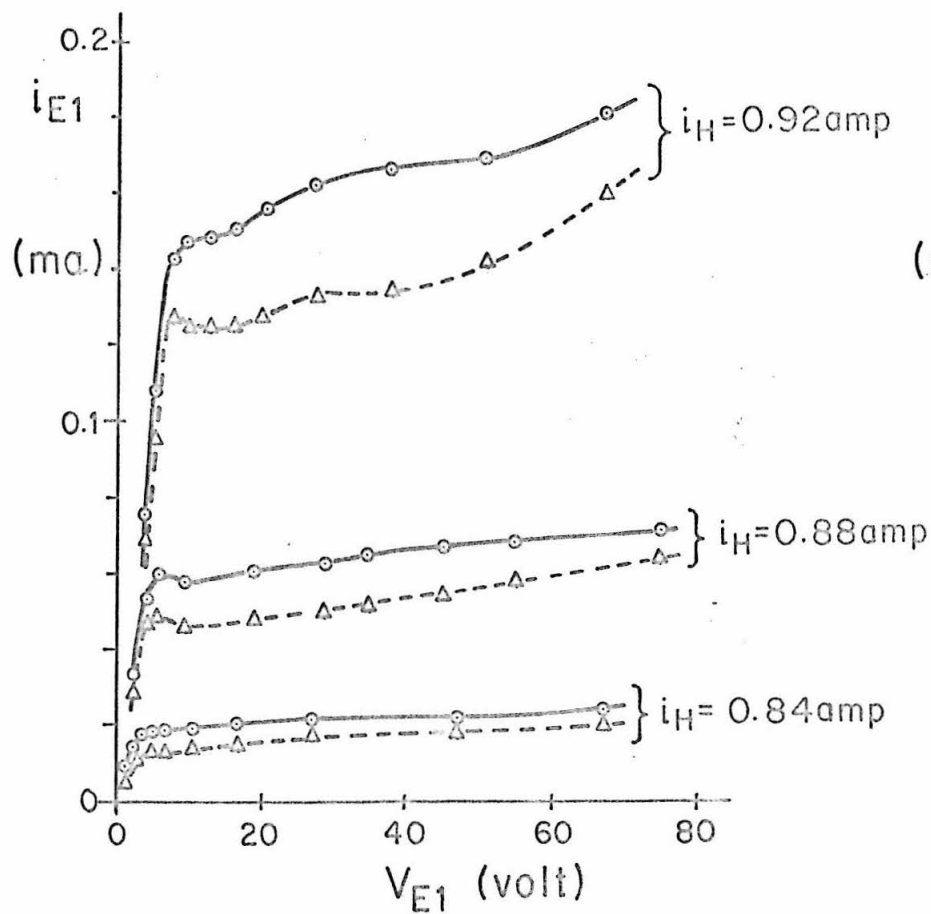


Figure 5. Emission current versus plate (E2) voltage for an "aged" cathode. Full line:  $V_{E2} = 0$  v, dashed line:  $V_{E2} = 10.76$  v.

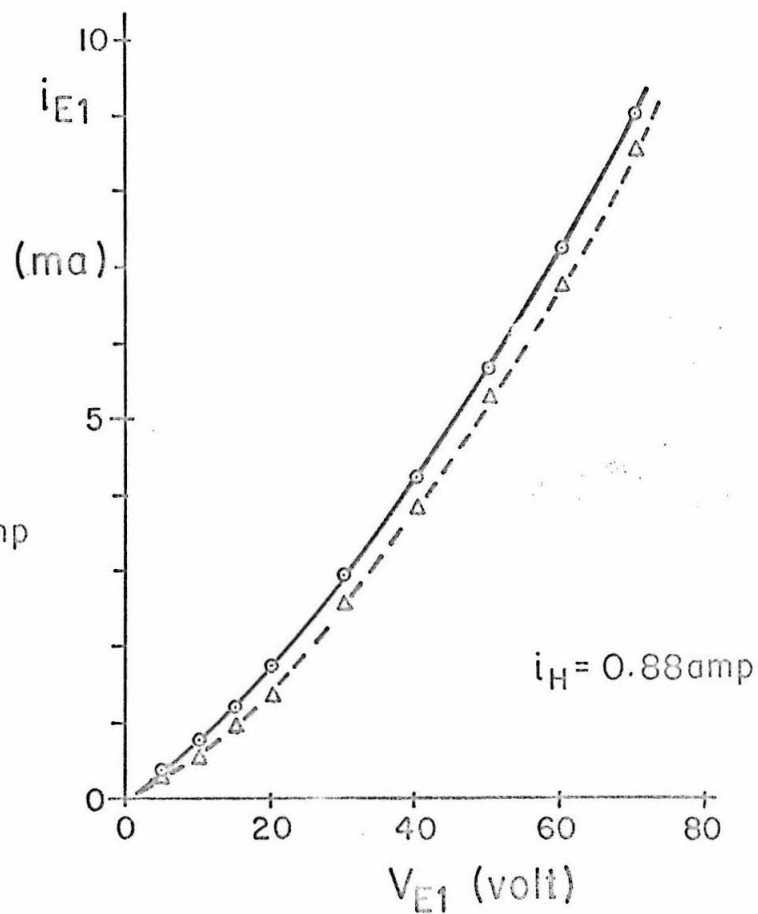


Figure 6. Emission current versus plate (E2) voltage for a "fresh" cathode. Full line:  $V_{E2} = 1.13$  v, dashed line:  $V_{E2} = 4.75$  v.

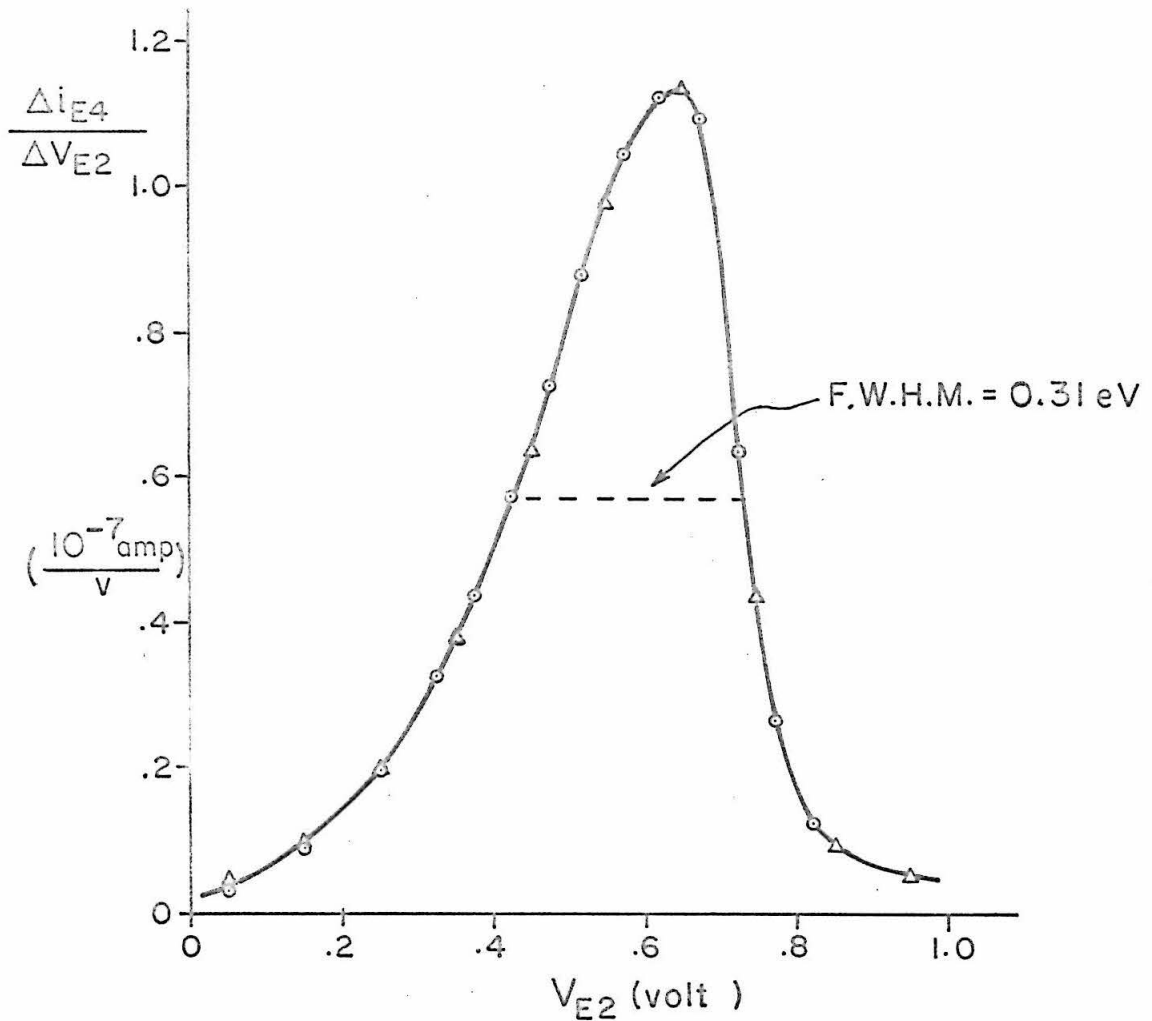


Figure 7. Derivative of electron beam currents measured at  $E_4$  with respect to  $V_{E2}$  as a function of  $V_{E2}$ , with  $i_H = 0.88$  amp,  $V_{E1} = 5.01v$ ,  $V_{E3} = 24.50v$ ,  $V_{E4} = 50.00v$ ,  $V_{E5} = 0v$ .

$E_4$  under these conditions.

We see that Figure 7 resembles the Boltzmann distribution curve with the high energy tail pointing towards negative values of  $V_{E2}$ . This is just what one would expect in a retardation potential measurement. In the particular example, the full width at half maximum (F.W.H.M.) is 0.31 ev, and the peak of the curve is located at  $V_{E2} = 0.65$  volts.

Experiments of this kind with  $V_{E1}$  varying from 10 to 50 v indicate that the full width at half maximum increases monotonically to about 1.1 ev (see Figure 8), and that the peak position shifts to larger  $V_{E2}$  values.

#### IV.3.3. Estimate of the Cathode Temperature

It is well known that for an ideal thermionic emitter the energy F.W.H.M. is given by<sup>(40)</sup>

$$\Delta E = 2.54 kT = \frac{2.54}{11600} T \quad (186)$$

where T is the temperature of the cathode in °K and  $\Delta E$  is in ev.

If we assume that the observed full width at half maximum of the " $\frac{\Delta i_{E4}}{\Delta V_{E2}}$  versus  $V_{E2}$ " curve at each value of  $V_{E1}$  represents the superimposed effects of the thermal energy distribution and the electron optical broadening<sup>(64)</sup> then from the extrapolated F.W.H.M. at  $V_{E1} = 0$  v we should be able to calculate the cathode temperature. According to Figure 8 this value is about 0.25 ev for a heater current of 0.88 amp. This corresponds to a cathode temperature of

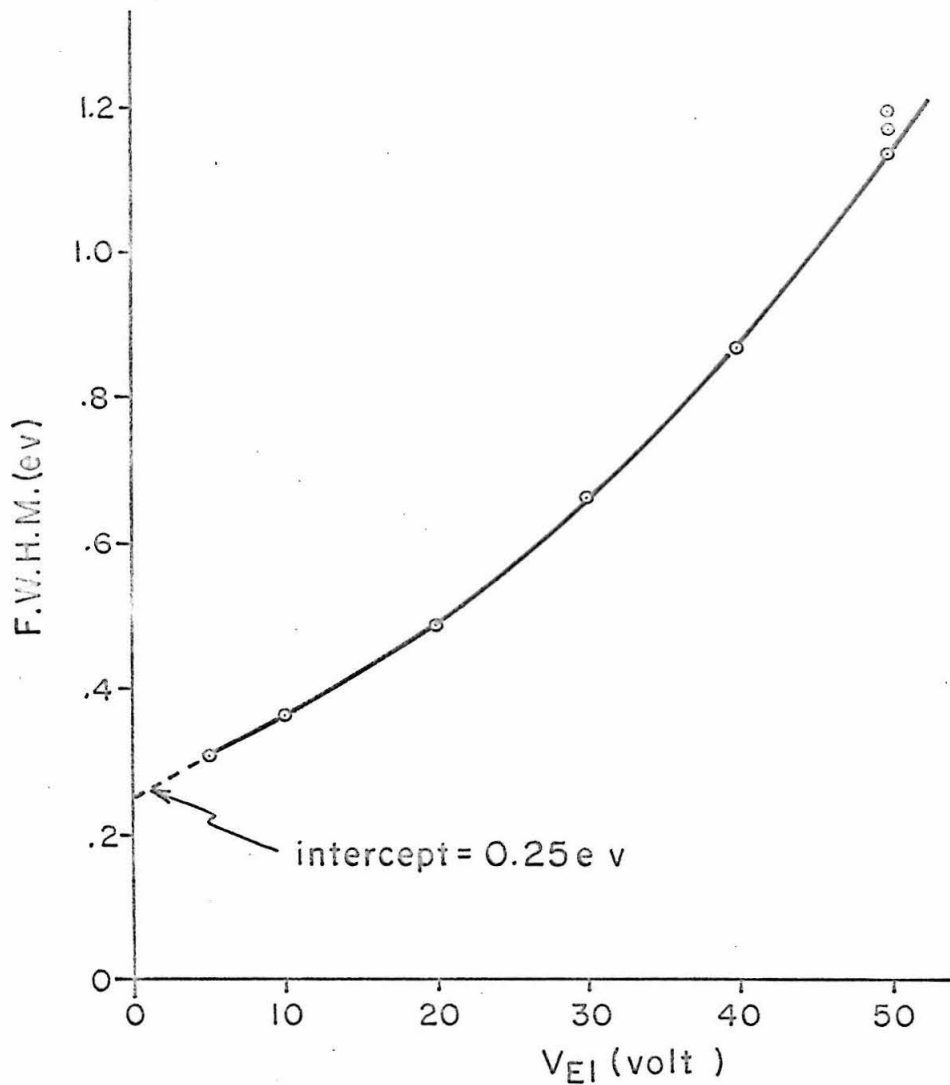


Figure 8. Full width at half maximum of the electron beam current derivative  $di_{E4}/dV_{E2}$  as a function of  $V_{E1}$ . The intercept of 0.25 eV corresponds to a cathode temperature of 1140°K.

1140°K for the case of an ideal thermionic emitter. This is a typical operation temperature for an oxide coated cathode.

#### IV.3.4. Effect of the Earth's Magnetic Field

A particle of charge  $q$  and velocity  $\vec{v}$  moving in a magnetic field  $\vec{B}$  is subject to a force

$$\vec{F} = q\vec{v} \times \vec{B}. \quad (187)$$

If  $\vec{v}$  is perpendicular to  $\vec{B}$ , and  $\vec{B}$  is homogeneous, then the particle will move in a circular path of radius

$$R = \frac{mv}{qB} \quad (188)$$

For the case of an electron with a kinetic energy of  $|V|$  ev and a homogeneous field of  $|B|$  gauss,  $R$  is given by

$$R = 3.37 \frac{|V|^{\frac{1}{2}}}{|B|} \text{ cm} \quad (189)$$

Thus for a 1 ev electron moving perpendicularly to the earth's magnetic field of 0.31 gauss in our laboratory, this radius is 10.9 cm. This is comparable to the dimensions of the apparatus. Therefore the earth's magnetic field must be neutralized.

Two pairs of Helmholtz coils described in section IV.1.5. are constructed based on these consideration. By properly adjusting the currents flowing through these coils

the earth's magnetic field can be neutralized to less than 0.5%, or about 1.5 milligauss. The average fluctuation of the magnetic field in our laboratory is found to be about 1% from day to day. However, the operation of a large magnet in an adjacent laboratory can sometimes cause an abrupt change of 10% in magnitude and  $15^\circ$  in direction of the ambient magnetic field vector.

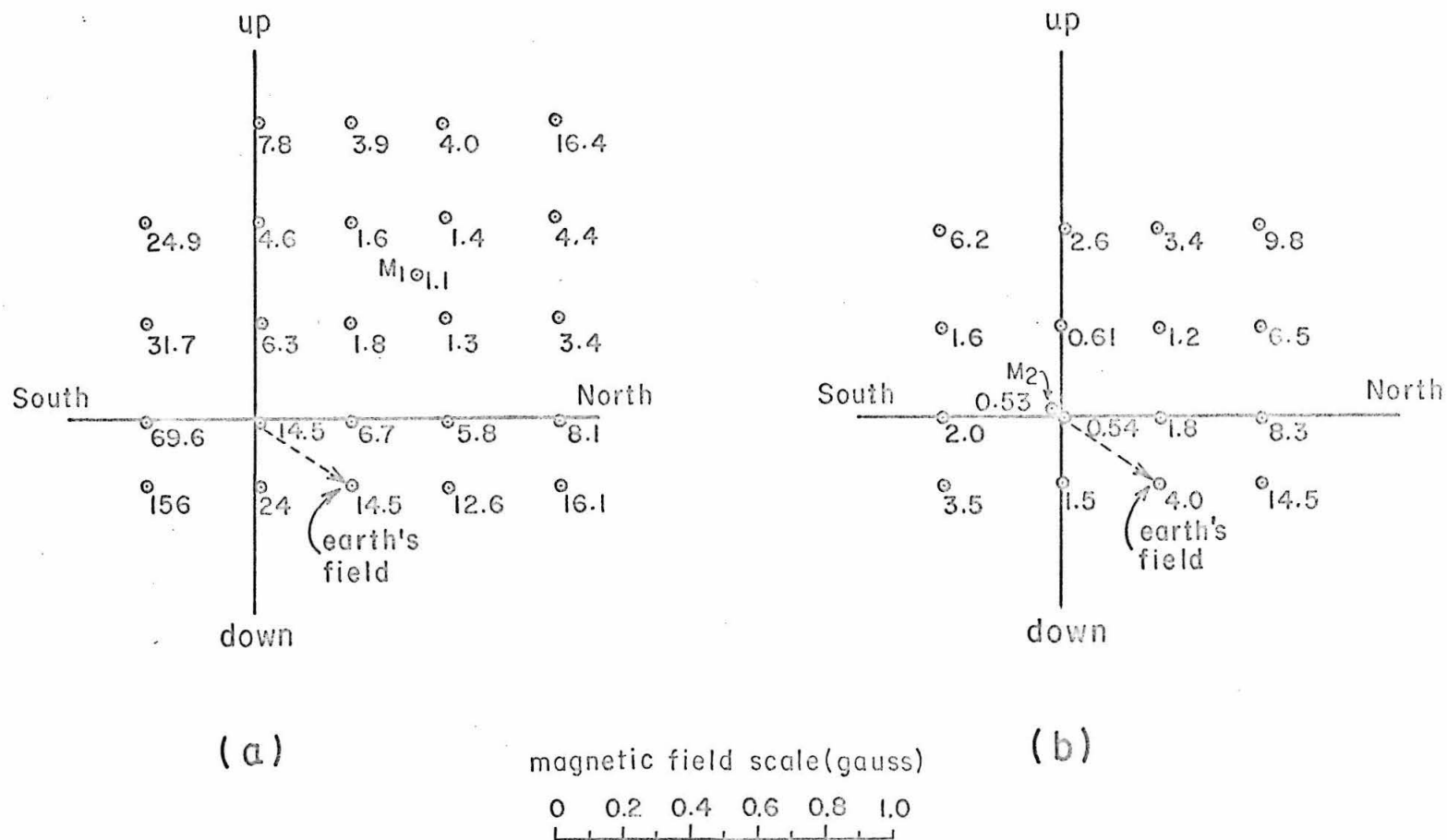
#### IV.3.5. Background Current As a Function of Magnetic Field

In addition to being able to cancel the ambient magnetic field, the two pairs of Helmholtz coils can also be used to generate magnetic fields between zero and two gauss pointing towards any given direction in the plane of their axes. (The upper limit is due to the particular coil design and the power supplies chosen). Thus the resultant magnetic field in the region of the apparatus can be varied.

As the electron beam is shot into the collision chamber, we can still detect a current on the scattering collector even if there is no gas sample present. This is referred to as the background current of the instrument.

If the axis of the electron gun and that of the collision chamber grid assemblies are not well aligned, we would expect to observe a larger background to beam current ratio than if they are properly aligned, provided there is no external magnetic field present.

Figure 9 (a) and (b) show the results when 50 ev electron beams are directed into the "empty" collision chamber at various magnetic fields. The direction of the electron beams is perpendicular to the paper and pointing upwards. The system is oriented such that the earth's magnetic field vector lies in the plane of the paper. The



magnetic field at each point is the radius vector from the origin of the coordinate system to that point. The number adjacent to each point is the ratio of scattered current to beam current in units of  $10^{-5}$ . G3 is arbitrarily set at 27 volts. The pressure in the collision chamber is about  $5 \times 10^{-7}$  torr. With the common conditions described above, Figure 9(a) describes the magnetic field when the end of the axis of the grid system is missed from the electron gun axis by  $\frac{1}{16}$ " in the plane containing E5; Figure 9(b) describes the field when the two axes are aligned to better than  $\frac{1}{123}$ " in the E5 plane.

We see from Figure 9(a) that the minimum value of  $\frac{i_{sc}}{i_{bc}}$  occurs at point  $M_1$  for which the magnetic field is 0.63 gauss. On the other hand, in Figure 9(b), when the system is well aligned, the minimum value of  $\frac{i_{sc}}{i_{bc}}$  occurs at point  $M_2$  which represents a magnetic field of only 0.03 gauss.

The information obtained from Figure 9 may be summarized as follows. In order to minimize the background to beam current ratio, the system must be well aligned and the earth's magnetic field must be reduced to a minimum.

#### IV.3.6. The Lozier Grid

In the present work, a retardation potential method is used to perform the energy analysis of the scattered electrons. Since only the normal velocity component of an electron is being affected by the retarding potential, an electron with energy  $E$  coming to a grid at an angle  $\Theta$  with respect to its axis of cylindrical symmetry would appear to the grid as if it only had an energy  $E \sin^2 \Theta$ . It is because of this that we have made G1 into a directional selection grid. This should sharpen the

instrument resolution. (see also section Iv.1.3.)

Figure 10(a) shows a sectional view of the annular paths defined by G1. If we assume that all electrons hitting the walls will be collected by the grid and not reach SC, then a transparency function  $T(\theta)$  can be calculated for a given set of parameters  $t$ ,  $d$ ,  $a$  and  $r$ .

In the present design the parameters  $t$ ,  $d$ ,  $a$  and  $r$  are chosen to be 0.010", 0.050", 0.500" and 0.1875", respectively. We have made simple calculation of  $T(\theta)$  for this case by dividing the length element PQ into 25 small segments and evaluating the angular range subtended by the center of each segment in slots A, B, and C. The number of segments accessible to a given angle is then counted for every half a degree interval. Effects at the two ends of the stack of disks are ignored.

Figure 10(b) shows the resulting transparency function of this set of grid system. The transparency at  $90^\circ$  is taken to be unity. We see that  $T(\theta)$  is approximately a triangle whose base extends from  $84^\circ$  to  $96^\circ$  with an apex at  $90^\circ$ . The F.W.H.M. of this distribution is  $6^\circ$ . If  $90^\circ \pm 6^\circ$  and  $90^\circ \pm 3^\circ$  are the maximum and average contributing angles, respectively, then the corresponding maximum and average relative energy spreads will be 1.01% and 0.27%, respectively. For electron energies of 50 eV or lower, the energy spread caused by G1 should then be comparable to the thermal energy spread from the oxide coated cathode, provided the reflection coefficient of the metal plate is zero.

#### IV.3.7. Behaviour of the G2 Grid

As described in section IV.2.3, the purpose of setting G2 at 10 volts positive with respect to E5 is to

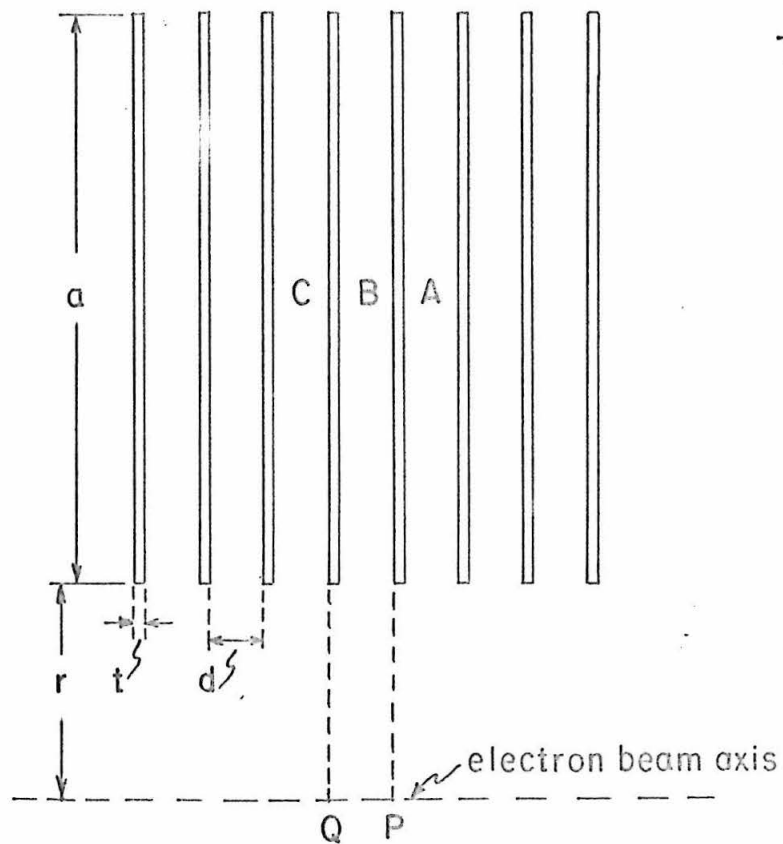


Figure 10(a). Sectional view of the annular paths defined by G1, with  $t=0.010''$ ,  $d=0.050''$ ,  $a=0.500''$  and  $r=0.1875''$ .

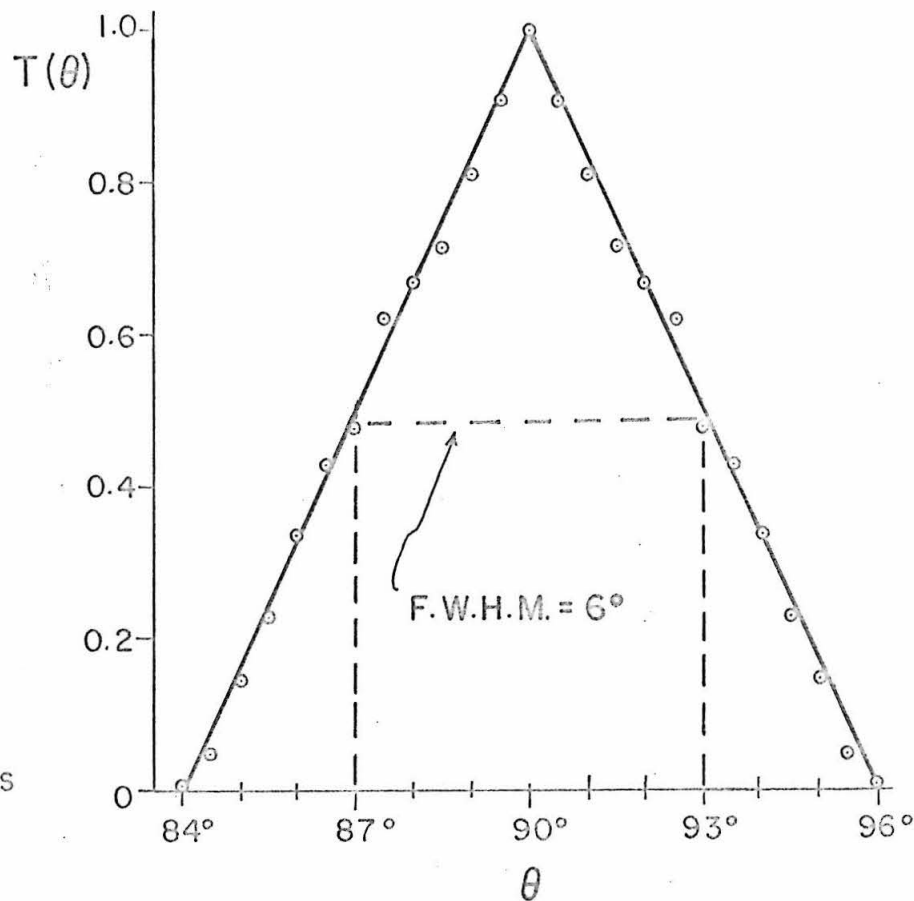


Figure 10(b). Transparency of G1, the Lozier grid, as a function of scattering angle.

prevent positive ions from being collected by the scattered electron collector.

Figure 11 shows the scattered current as a function of  $V_{G2}$  for G3 at 0, 1, and 2 v. The sample gas is nitrogen at  $5.6 \times 10^{-4}$  torr the electron beam energy and current are 50 ev and  $4.7 \times 10^{-7}$  amp, respectively. This experiment was done with a grid system similar to the previous apparatus described by Raff<sup>(60)</sup> in which G1 is a cylindrical mesh rather than a disk stack.

We see that the scattered currents reach steady values when G2 becomes 5 volts or more positive with respect to E5. The current increment for G3 between 0 and 1 volt (or between 1 and 2 volts) becomes a constant when  $(V_{G2} - V_{E5})$  is higher than 5 volts. Therefore the potential on G2 is chosen to be 10 volts positive with respect to E5 and G1.

#### IV.3.8. Holding Potential on the Beam Collector

In order to insure that electrons which reach the beam collector are indeed collected and not reflected back into the collision region, a holding potential of 70 volts is applied between the beam collector and G1A. (G1A, G1, and E5 are at the same potential).

Figure 12 shows the scattered current from helium as a function of  $V_{BC}$  for 30, 35, 40 and 50 ev beams. The pressure in the collision chamber is  $3.4 \times 10^{-4}$  torr (ion gauge reading). The scattered currents are normalized to the same beam current of  $1 \times 10^{-7}$  amp. G3 is set at 30 v with respect to the cathode, corresponding to a retarding potential difference of 20 v for the 50 ev beam and of 0v for the 30 ev beam.

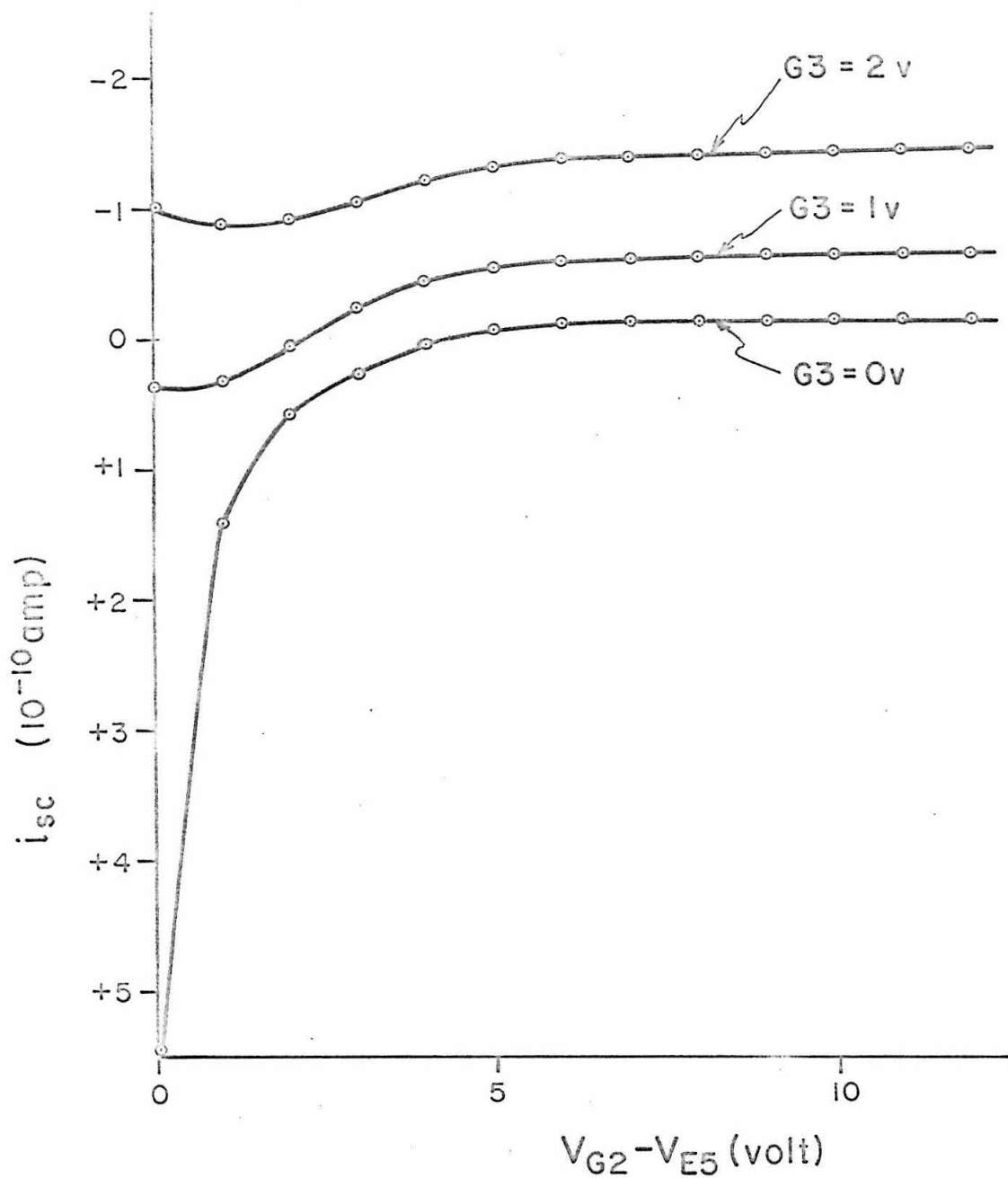


Figure 11. The scattered currents as a function of  $V_{G2}$ , for  $V_{G3}$  at 0, 1, and 2 v, with beam energy=50 ev.  $i_{BC} = 4.7 \times 10^{-7}$  amp,  $P_{SC}(N_2) = 5.6 \times 10^{-4}$  torr.

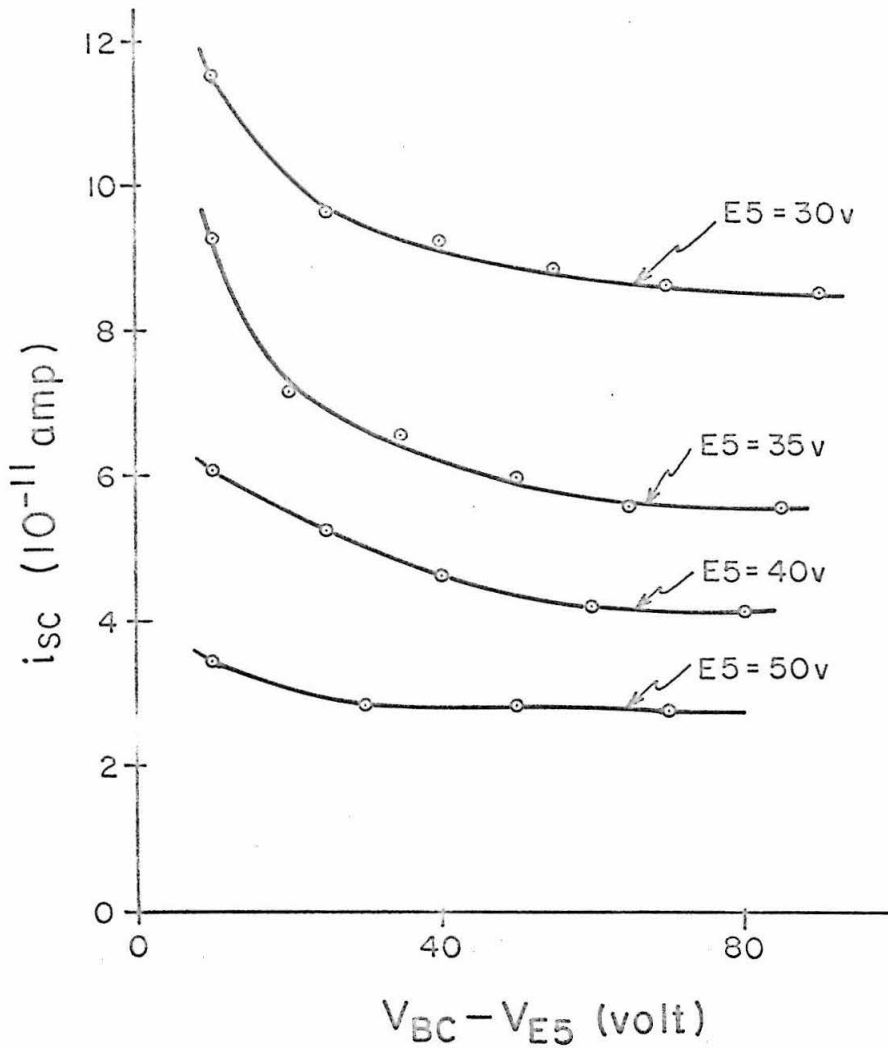


Figure 12. Total scattered current from helium as a function of  $V_{BC}$ , for 30, 35, 40, and 50 ev beams, with  $V_{G3} = 30v$ .  
 $i_{BC}^{BC} = 1.0 \times 10^{-7}$  amp,  $P_{SC}(\text{He}) = 3.4 \times 10^{-4}$  torr.

We see that for  $V_{BC} \geq V_{E5} + 50$  volts, the scattered current reaches a constant; the background current due to reflection of electrons from the beam collector is reduced to a minimum. The dependence of the width at half height of elastic peaks on  $V_{BC}$  is discussed in the following section.

#### IV.3.9. Full Width at Half Maximum of Elastic Peaks

The elastically scattered currents from various gases such as helium, hydrogen, nitrogen, ethylene, acetylene, etc. are measured. It is found that the scattered current depends linearly on the electron beam current and the gas pressure, for pressures lower than about  $10^{-3}$  torr. For  $V_{G3}$  between 0 and 3 volts, the peak shape shows no distinguishable difference for different molecules. However, it is observed that the peak shape is a function of the beam energy. The higher the energy the larger is the high energy loss tail of the elastic peak. It is thus characteristic of our Lozier grid that the resolution is energy-dependent.

The F.W.H.M. of the elastic peak can be measured for various conditions. In general, it increases almost linearly with the beam energy and with the holding potential between the scattering collector and G3 ( $V_{sc \text{ to } G3}$ ), and it decreases slowly with increasing  $V_{BC}$ , but it does not depend appreciably on the potential settings on electrodes E1, E2, E3 and E4.

Figures 13(a), (b) and (c) show the dependence of the F.W.H.M. on beam energy, holding potential  $V_{sc \text{ to } G3}$  and holding potential  $V_{BC}$ , respectively. The potential  $V_{S_{field} \text{ to } sc}$  is set at the same magnitude as that of  $V_{sc \text{ to } G3}$  in all experiments to reduce the edge effect

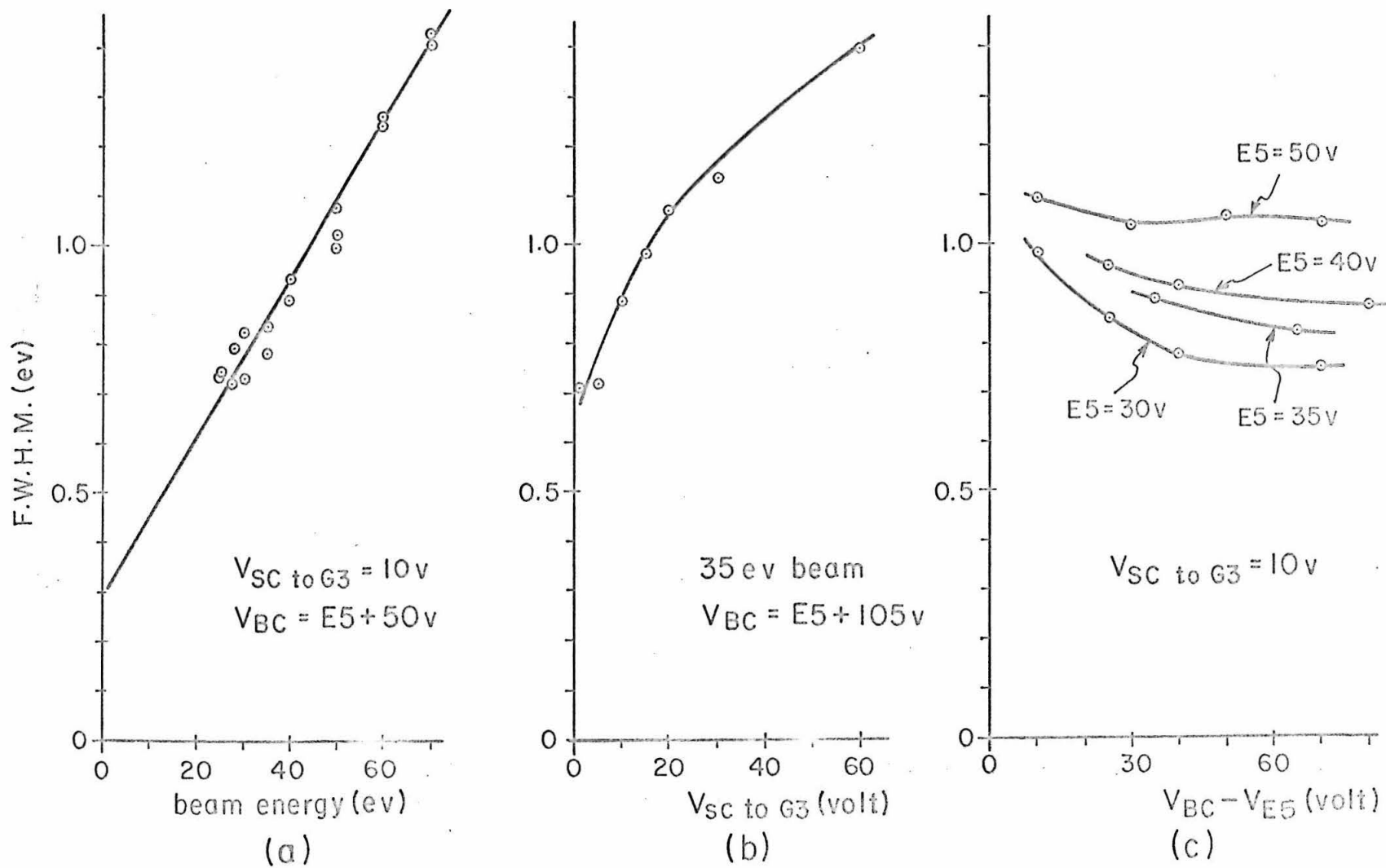


Figure 13. Full width at half maximum of elastic peaks of helium as a function of a) beam energies, b)  $V_{SC \text{ to } G3}$ , and c)  $V_{BC}$ .

of the electric fields.

Figure 14 shows the elastic peaks of helium for 30, 35, 40 and 50 ev incident beam energies. The lowest beam energy produced by the present geometry is about 28 ev. The electron beam diverges excessively if E5 is lower than 28 ev no matter what potentials are applied to E1, E2, E3 and E4. Therefore no experiment is made with beams of energy lower than 30 ev.

The F.W.H.M. of the elastic peaks represents the actual resolution of the instrument. This is about 1 ev for the present apparatus and is only good for distinguishing electronic energy levels with energy separation of about 1 ev. No fine structure of vibrational or rotational states can be resolved.

#### IV.3.10. Helium Spectra As a Function of the Holding Potential Between SC and G3

The holding potential  $V_{SC \text{ to } G3}$  not only has an effect on the full width at half maximum of the elastic peaks as shown in Figure 13(b) but also influences the electrostatic field in the scattering region.

Figure 15 shows three 50 ev helium spectra with  $V_{SC \text{ to } G3}$  set at 5, 10, and 15 volts. The elastic peak is plotted on 10 times less sensitive scale in Figure 15(c). The lowest electronically excited state of helium is the  $2^3S$  state at 19.81 ev above the ground state. The first optically allowed transition is the  $1^1S \rightarrow 2^1P$  transition at 21.21 ev.

We see from these 50 ev spectra that when  $V_{SC \text{ to } G3}$  is set at 5 or 10 volts there is an undulating background superimposed on the elastic and inelastic peaks.

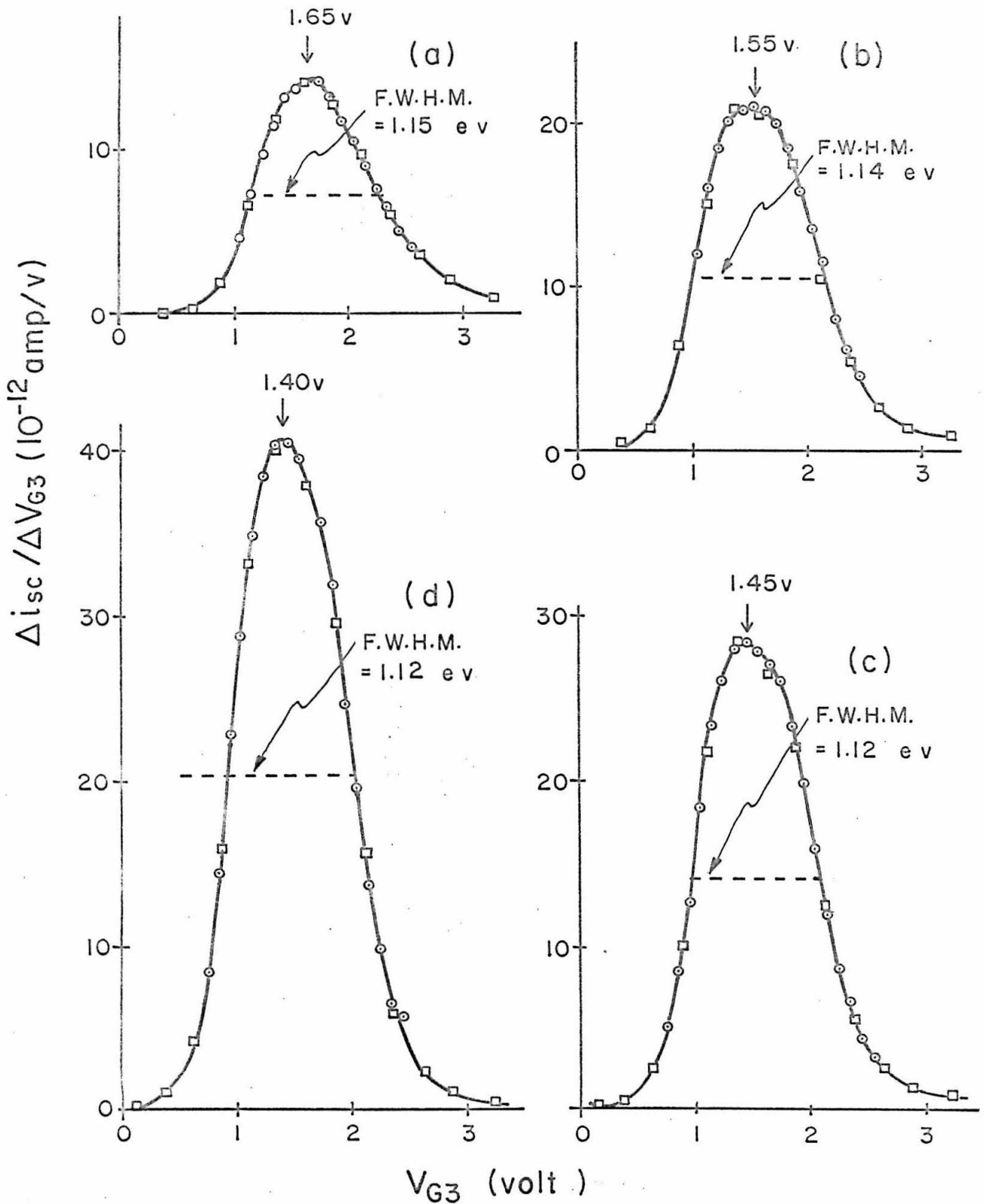


Figure 14. Elastic peaks of helium at beam energies of a) 50 ev, b) 40 ev, c) 35 ev, and d) 30 ev.  $i_{BC} = 0.98 \times 10^{-7}$  amp,  $P_{SC} = 3.2 \times 10^{-4}$  torr.

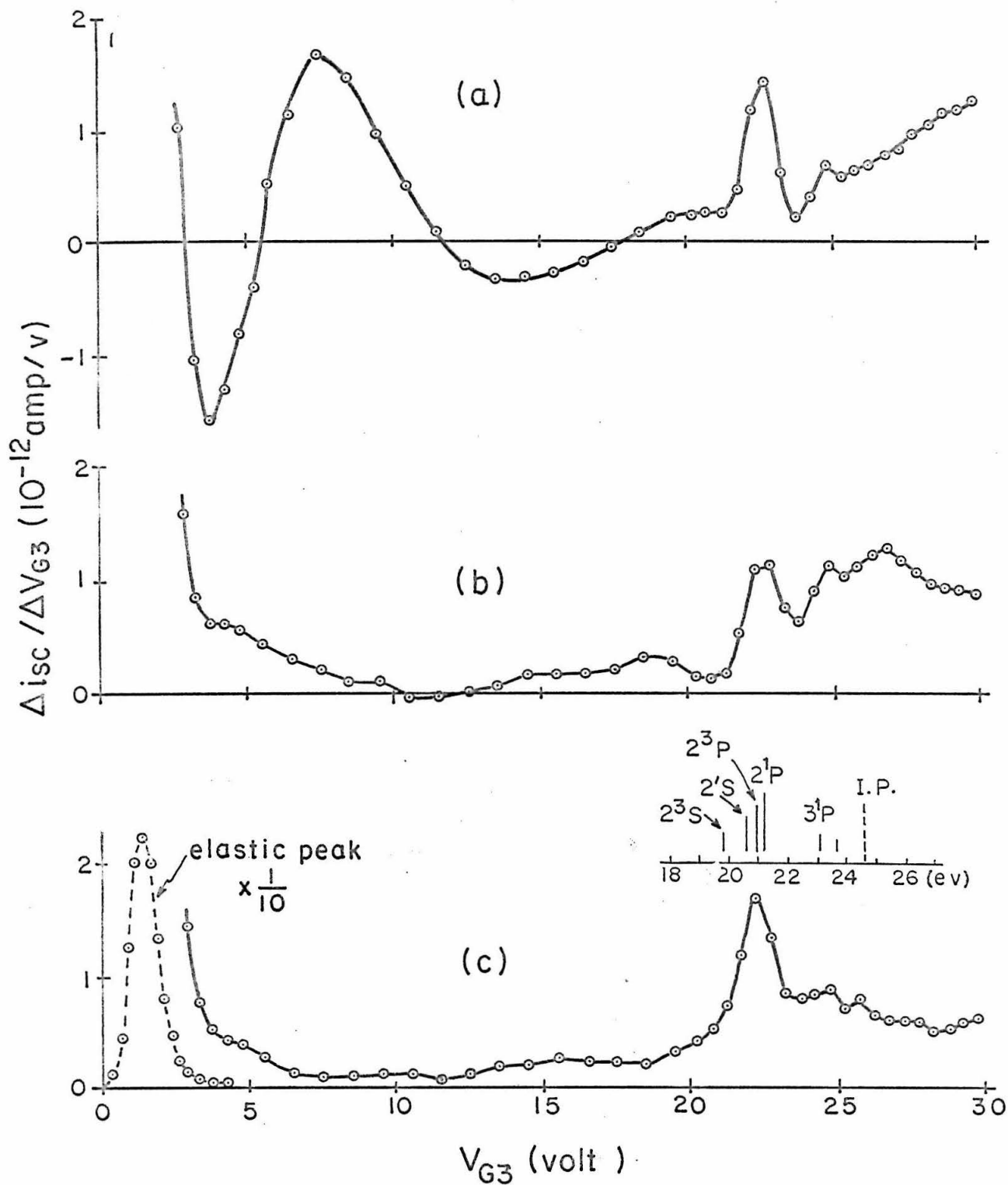


Figure 15. Helium spectra at  $90^\circ$  scattering angle and 50 eV beam energy, with  $V_{SC}$  to  $G_3$  at: a) 5v, b) 10v, and c) 15v.  $i_{BC} = 4.7 \times 10^{-7}$  amp,  $P_{SC} = 1.5 \times 10^{-4}$  torr.

The undulating background becomes small when  $V_{SC \text{ to } G3}$  is set at 15 volts.

Similar experiments for 40, 35, and 30 ev beams are made. It is found that the undulating background becomes small when  $V_{SC \text{ to } G3}$  is set at 25, 30 and 35 v for 40, 35 and 30 ev beams, respectively. In general, the background ceases to undulate when  $V_{SC \text{ to } G3} + V_{E5} \geq 65$  v. Since the resolution worsens as  $V_{SC \text{ to } G3}$  increases, we choose the minimum value of this quantity for which the background undulations become unimportant.

The reason for this undulating background is not clearly understood. It may be caused by some electrostatic effect. However, it is worthwhile to mention that the 50 ev helium spectrum with  $V_{SC \text{ to } G3}$  at 15 volts, Figure 15(c), agrees very well with the helium spectrum reported by Doering<sup>(57)</sup>. The details about the helium spectra will be discussed later.

#### IV.3.11. The Rising Background

A difficulty associated with the present method is the rising background in the region of large energy loss. The reason for this rise is that in measuring increments of the scattered current at large energy loss, we have to set  $V_{G3}$  at more and more positive potentials with respect to the cathode. The closer  $V_{G3}$  gets to the value of  $V_{G1}$  the greater is the field penetration into the electron beam region, with consequent withdrawal of beam electrons which then reach SC without having been scattered.

This problem becomes serious when we want to scan the large energy loss region with low energy beams. The 30 ev spectrum of helium in Figure 16 serves as a good

Figure 16. The 30 ev helium spectrum and a blank run. The inelastic peaks are superimposed on the rising background.

Helium run:

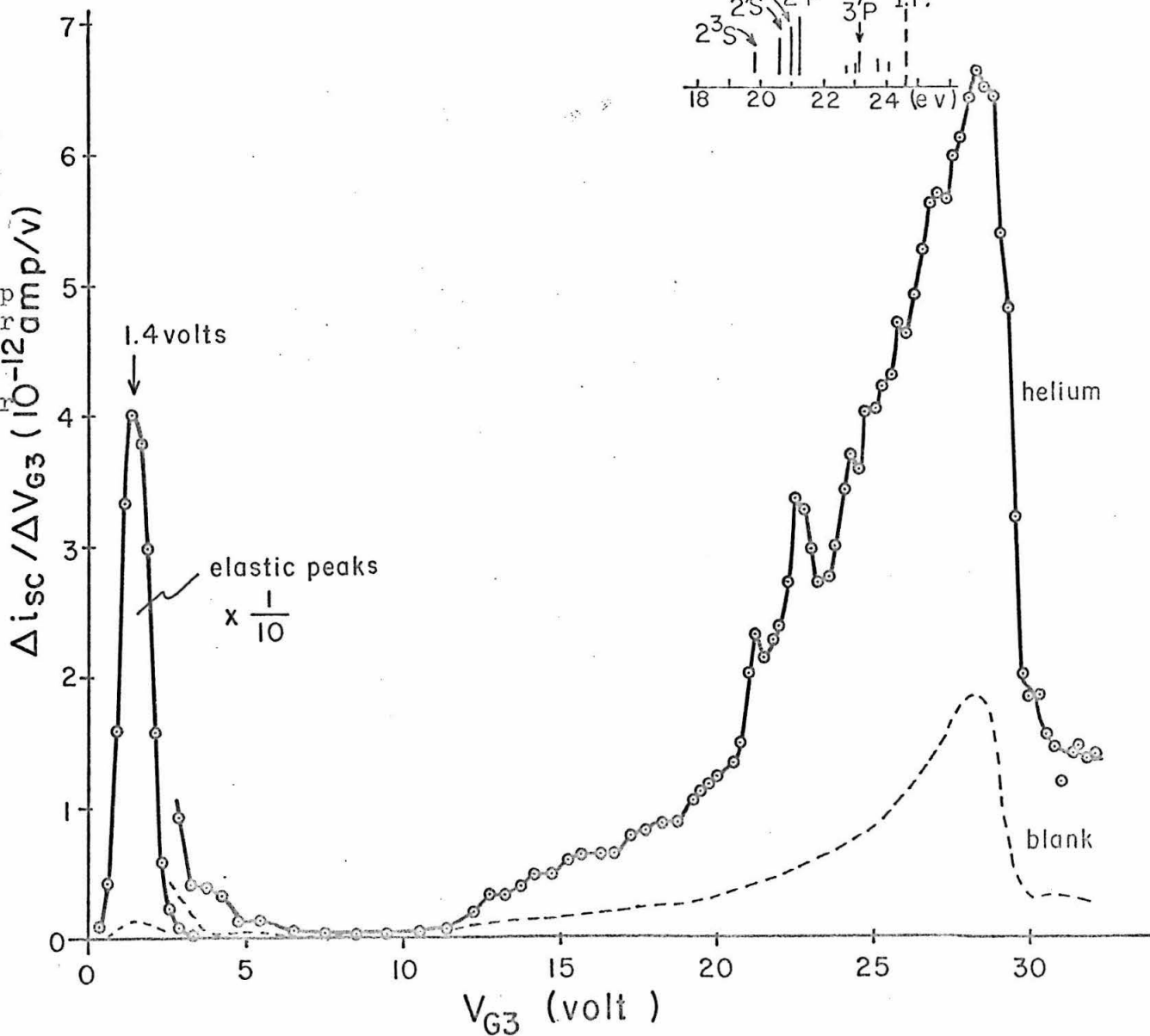
$$i_{sc} = 0.98 \times 10^{-7} \text{ amp}$$

$$P_{sc} = 3.2 \times 10^{-4} \text{ torr}$$

Blank run:

$$i_{sc} = 1.04 \times 10^{-7} \text{ amp}$$

$$P_{sc} = 0.14 \times 10^{-4} \text{ torr}$$



example for this situation. We see that at this beam energy the inelastic transitions in helium are partially masked by the fast rising background.

It would be convenient if we could subtract the instrumental background from a spectrum to obtain the net inelastic signal. However, it seems that this can not be done in a simple way. The dashed curve in Figure 16 represents a blank scan after the shut off of helium. It is obvious that the background is not simply related to either the pressure or the elastic peak.

Fortunately, the ionization potentials for many molecules are around 15 ev or lower and the important electronic energy levels are even lower. Thus, we can still use the present technique to obtain electron impact spectra for those molecules at incident beam energies of 30 ev or higher.

#### IV.3.12. Limitations of the Present Apparatus

From the preceding discussions we see that the present apparatus is capable of yielding electron impact spectra of molecules at  $90^\circ$  scattering angle for incident beam energies higher than 30 ev with a resolution of about 1 ev. However, there are a few conditions associated with the present apparatus which limit its use.

##### A. The tails of the elastic peaks

Since the elastic peaks are generally 10 times or more higher than the inelastic ones the tails of the former extend into the energy loss region of about 3 ev. Therefore, it is difficult to study low-lying excited states with excitation energies equal to or less than about 3 ev with the present set-up.

### B. The rising background

The background problem discussed in section IV.3.11. causes the observed spectra to be superimposed on a base line which rises as the energy loss increases. Thus, we can only obtain a qualitative estimate on the ratios of peak heights for the inelastic transitions observed. Quantitative measurements of the peak heights may be achieved only after this background problem is solved.

### C. The effective scattering volume

In a scattering experiment, if we know the number density of the scatterer, the intensity of the electron beam, the path length, and the scattered current intensity for a given solid angle, then we can calculate the differential scattering cross section. However, for charged particles such as electrons the collimation of the beam changes with beam energy. Therefore, the path length which is related to the effective scattering volume is a function of that energy. Thus the comparison of peak heights of the same transition at different beam energies is not meaningful unless the effective scattering volumes are taken into account.

Nevertheless, the ratio of peak heights of different types of inelastic transitions at the same beam energy can still be compared. The energy dependence of the ratio may shed light on the nature of the transitions involved.

### D. The problem of cathode poisoning

It is found that the type of oxide coated cathode used in the present work is good only for experiments involving inert or reducing gases. Molecules such as water, carbon dioxide, nitric oxide or oxygen introduced into the collision chamber in the usual way will decrease the emission current in a very short time. Fortunately

the emission current can be restored if a reducing gas is introduced into the system afterwards. This is probably due to some reversible oxidation-reduction change of the surface work function of the cathode.

The situation may be improved by increasing the effective pumping speed in the cathode region, and by redesigning an electron gun with its cathode not facing directly the flux of gas molecules from the collision chamber.

#### E. The conductance-limited pumping speeds

In the present vacuum system, although the 4" oil diffusion pumps are rated for pumping speeds of 300 l/sec actually the effective pumping speeds in the vacuum chambers are quite limited because of small conductance tubes and liquid nitrogen traps. A simple calculation using the formula for the molecular flow case given by Pirani and Yarwood<sup>(65)</sup> shows that the conductances of the tubes between the vacuum chambers and the diffusion pumps are 11 and 25 l/sec<sup>(66)</sup> for the collision and gun chamber sides, respectively. The conductance in the vicinity of the cathode would be still smaller because of the compact geometry of the electrodes. An improved vacuum system with higher pumping speed in the gun chamber may therefore enable us to study the oxidizing molecules.

IV.3.13. Comparison of Performance of Present Apparatus  
With Previous Version

The vacuum system, electron gun assembly, voltage supplies, measuring devices, and operation procedures used with the present apparatus are essentially the same as in the previous version used by Kuppermann and Raff<sup>(54, 55, 60)</sup>. The only important modification was the introduction of the Lozier grid into the scattering chamber. The general differences in the experimental conditions of these two versions can be summarized as follows.

	Previous apparatus	Present apparatus
1. Angular range of scattering observed	22° to 112°	84° to 96°
2. Electron beam energies used	between 25 and 75 ev	between 30 and 50 ev
3. Axis of the electron gun	2.0° deviated	corrected to 0°±0.2°
4. Magnetic material in the scattering chamber	small amounts of Kovar and nickel	none
5. A small magnet for collimating the electron beam	needed	not needed
6. Magnetic field in scattering region	inhomogeneous due to presence of small magnet	ambient field neutralized homogeneously to less than 0.5% of the earth's field

The modifications introduced produced very large differences in the resulting spectra, as listed below.

	Previous apparatus	Present apparatus
1. Size of total scattered signal	$2 \times 10^{-10}$ amp	$10^{-11}$ amp
2. Ionization process of molecules	appeared as a peak	appeared as an onset
3. Contact potential correction	based on the ionization peak	based on the elastic peak
4. Position of the elastic peak in spectrum	appeared as if it had lost energy of 2 ev	defined as zero energy loss
5. Ratio of elastic to inelastic peak heights	ranging from 1 to 5	always greater than 10
6. Ratio of allowed to forbidden inelastic peak heights	about 1	allowed ones generally much stronger than forbidden ones

Furthermore, in the previous work<sup>(54, 55, 60)</sup>, there are a few points which are not easily understood. They are listed as follows.

1. The full width at half height of the elastic peak is of the order of 1 ev, yet two energy levels in argon located as close as 0.6 ev are clearly resolved.

2. In the H<sub>2</sub> spectrum the peak positions occur at onset energies, whereas for the case of C<sub>2</sub>H<sub>4</sub> they occur at

energies corresponding to absorption maxima.

3. Two helium spectra with beam energies of 25 and 50 ev show no major change in the relative intensities for the spin forbidden and optically allowed transitions.

4. In spite of statement 3, the triplet state in  $C_2H_4$  peaking at about 4.4 ev shows drastic changes in intensity relative to the optically allowed transition when the beam energy is increased from 40 to 75 ev.

The difference in behaviour of the two versions of the apparatus can be assigned mainly to two causes.

a). The use of a small collimating magnet and the presence of some magnetic materials in the scattering chamber of the previous version could produce a disturbance in the scattered electron trajectories.

b). The non-directional nature of the first analyzer grid produces an elastic peak with a large high-energy tail, in which slight fluctuations could produce spurious signals. We conclude that some of the features of the spectra obtained with the previous version of the apparatus are suspect. Therefore, the results obtained with it should not be relied on unless confirmed by the present modified version. As shown in detail in the rest of this thesis, this present version produces results consistent with other measurements and devoid of the inconsistencies mentioned above.

## V. Results and Discussions

Electron impact spectra have been obtained for the helium atom and twelve molecules at  $90^\circ$  scattering angle with incident beam energies of 50, 40, 35 and 30 ev. These twelve molecules are hydrogen, nitrogen, carbon monoxide, ethylene, acetylene, methyl acetylene, allene, propane, 1,3-butadiene, benzene, norbornadiene and quadricyclene.

In taking the spectrum of each molecule the energy loss region is scanned at least six to eight times at each beam energy to make sure that the observed structure is reproducible. The electron beam current is generally between 1.0 and  $1.5 \times 10^{-7}$  amp. The gas sample pressures in the scattering chamber are of the order of  $10^{-4}$  torr as measured by an uncalibrated ion gauge. The potential settings on the electrodes and grids for all experiments are as indicated in Figure 4. The resolution of the instrument is about 1 ev as discussed in section IV.3.9.

Theoretically, the optically allowed transitions are the most intense transitions in an electron impact spectrum when the Born approximation is valid. The conditions for the Born approximation to hold are as follows.

- A. The incident beam energy is high compared to the excitation energy, and
- B. The scattering angle is small.

Our experiments are done at  $90^\circ$  with low incident beam energies since under these conditions the Born approximation breaks down and optically forbidden transitions may be observed.

It is well known that the absolute magnitude of the differential cross section  $\sigma_n(E, \theta, \phi)$  for a given inelastic process,  $n$ , of a given molecule falls off with increasing

scattering angle. Thus the measurable signal drops when a detector with a fixed incoming solid angle is placed at larger and larger scattering angles. This is probably the reason that most of the reported electron impact work is done at small scattering angles.

In order to take advantage of the favorable ratio of optically forbidden to allowed transitions at large angles and still to obtain a measurable signal, one may either use very intense incident electron beams or try to increase the effective incoming solid angle of the detector. Doering<sup>(57,58)</sup> uses the first approach, i.e., his experiments are done with 100 microampere electron beams. In the present work, however, the second approach has been adopted.

It should be pointed out that so far there has been very little work done in 90° electron scattering spectroscopy except the very recent work by Doering on helium<sup>(57)</sup> and on ethylene<sup>(58)</sup>, with which our present work agrees very well.

The helium 2<sup>3</sup>S state at 19.81 ev, which Doering was unable to observe with electron beam energies higher than 40 ev, is clearly resolved at 35 and 30 ev in the present work (see Figure 18).

The energy levels of the diatomic molecules H<sub>2</sub>, N<sub>2</sub> and CO are well known from optical spectroscopy<sup>(8)</sup>. Therefore, the electron impact spectra of these molecules serve as a check on the capability of our instrument to excite molecular electronic energy levels. In addition to optically allowed transitions, the low-lying antibonding b<sup>3</sup>Σ<sub>u</sub><sup>+</sup> state of H<sub>2</sub>, the unresolved A<sup>3</sup>Σ<sub>u</sub><sup>+</sup>, B<sup>3</sup>Π<sub>g</sub> and a<sup>1</sup>Π<sub>g</sub> states of N<sub>2</sub>, the C<sup>3</sup>Π<sub>u</sub> state of N<sub>2</sub>, and the a<sup>3</sup>Π state of CO have all been observed in the present work (see Figures 20, 22, and 24). The intensity ratio of spin forbidden to

optically allowed transitions is of the order of  $\frac{1}{5}$  or better in our experiments. Skerbele, Dillon and Lassetre (39a,b) observed ratios of spin forbidden to optically allowed transitions of the order of  $10^{-3}$  in  $N_2$  and CO with similar incident electron beam energies but at scattering angles between  $0^\circ$  and  $16^\circ$ . Thus it is obvious that low incident beam energies and large scattering angles are indeed favorable conditions for the observation of optically forbidden electronic transitions. (See also sections II.12 and III.4)

The ethylene spectra, shown in Figure 25, agree with Doering's work<sup>(58)</sup> very well. The only two peaks resolved are the  $V \leftarrow N$  and  $T \leftarrow N$  transitions located at about 7.8 and 4.4 electron volts, respectively.

The  $90^\circ$  electron impact spectra of acetylene, methyl acetylene, allene, benzene, norbornadiene and quadricyclene show inelastic peaks that may be correlated with excitations to the lowest triplet states in these molecules. However, perhaps because of the large tail of the elastic peak, no such correlation in 1,3-butadiene is observed. The electron impact spectra of propane (Figure 29) show no apparent structure, in analogy to its ultraviolet absorption spectrum.

In the following sections the available information from existing literature for each molecule is briefly summarized, and the results obtained are described in detail and discussed.

V.1. Helium

The energy levels of the helium atom are very well known. A table of the various excited states of helium is given by Moore<sup>(67)</sup> in units of  $\text{cm}^{-1}$ . For reasons of convenience in comparison, several important excited states are listed below in units of eV. (The conversion factor  $1 \text{ eV} = 8068.32 \text{ cm}^{-1}$  is used).

<u>Designation of state</u>	<u>Energy level in eV</u>
He $1^1\text{S}$ (ground state)	0.0
$2^3\text{S}$	19.812
$2^1\text{S}$	20.608
$2^3\text{P}$	20.956
$2^1\text{P}$	21.210
$3^3\text{S}$	22.710
$3^1\text{S}$	22.912
$3^3\text{P}$	23.000
$3^3\text{D}, 3^1\text{D}$	23.065
$3^1\text{P}$	23.078
$4^1\text{P}$	23.723
$5^1\text{P}$	24.024
$6^1\text{P}$	24.189
$7^1\text{P}$	24.289
$\text{He}^+$ (1s) $2^2\text{S}\frac{1}{2}$ (ionization Potential)	24.580
$\text{He}^+$ (2P) $2^2\text{P}\frac{1}{2}$	40.7

V.1.1. Summary of Previous Electron Impact Work

Schulz<sup>(47)</sup> studied the excitation spectrum of helium with the trapped electron method (see section III.3). The results indicated that the  $2^3\text{S} \leftarrow 1^1\text{S}$  transition was the most pronounced one at energies near threshold.

Kuppermann and Raff<sup>(54,55)</sup> obtained high scattering angle spectra of He, in which they detected among others the  $2^3S \leftarrow 1^1S$  transition, but in view of the difficulties mentioned in section IV.3.13 their results were subject to confirmation.

Early work by Lassetre and Francis<sup>(37a)</sup> using 390 ev beams with about half a volt resolution at zero degree scattering angle showed transitions to helium 2,3, and 4'P states. The 2'P peak was the most intense transition in the spectrum.

Using a counting technique, Lassetre, Berman, Silverman and Kransnow<sup>(37d)</sup> obtained another helium spectrum with 235 ev beam energy (0.3 ev resolution) at  $9^\circ$  scattering angle. In this spectrum the transition to the 2'S state was observed with an intensity of about  $\frac{1}{10}$  of that of the 2'P peak. With the same technique, Lassetre, Kransnow and Silverman<sup>(37e,37i)</sup> demonstrated that by increasing the scattering angle from  $3.8^\circ$  to  $15.3^\circ$  and with beam energies of about 500 ev, the intensity ratio of the  $2^1S \leftarrow 1^1S$  and  $2^1P \leftarrow 1^1S$  transitions increased with angle. At  $15.3^\circ$  this ratio was approximately unity.

Further work by Skerbele and Lassetre<sup>(37j)</sup> showed that by lowering the beam energies from 350 to 250 ev at a fixed observation angle of  $0^\circ$ , the forbidden transition helium  $2^1S \leftarrow 1^1S$  started to show up. The energy width of the incident electron beam was sufficiently reduced by means of an electrostatic velocity analyzer that it was possible to resolve the transitions to 5'P and 6'P states (separated by 0.17 ev) in helium<sup>(37j,68)</sup>.

Lassetre, Meyer and Longmire<sup>(69)</sup> also showed that the differential cross sections at  $0^\circ$  for the series of quadrupole-allowed transitions  $n^1S \leftarrow 1^1S$ , ( $n = 2,3,\dots$ ) in helium did not depend on energy when the incident energy

was large compared to the interaction energy. Therefore one might expect to find the series of  $n'S$  peaks ( $n = 2, 3, \dots$ ) at comparatively high kinetic energies if the resolution was high enough. Using a 202 ev beam with the resolution of about 0.1 ev at  $0^\circ$  scattering angle, they were successful in resolving the  $3'S$  peak which is separated from the 30-fold more intense  $3'S$  peak by only 0.16 ev.

A few years ago, Simpson and Mielczarek<sup>(41)</sup> studied helium using 50 ev electron beams with about 0.15 ev resolution while looking at  $0^\circ$  scattering angles with an angular aperture smaller than 20 milliradians. They were able to resolve the  $2'S$ ,  $2'P$ ,  $3'P$ , and  $4'P$  peak. The ratio of peak heights of the  $2'P$  to  $2'S$  peak was found to be about 7 to 1. No triplet states were observed.

Later, with the same instrument, Chamberlain, et al<sup>(43)</sup> were able to measure the  $0^\circ$  inelastic scattering of electrons by helium with a resolution of 0.1 ev for primary beam energies  $E$  from 80 ev down to near threshold. Energy loss peaks for all the  $n = 2$  states were seen, as well as the  $3^3S$ ,  $3'S$ , and  $3'P$  states. The relative strength of several of the energy loss peaks in helium for different incident energies is reproduced in Table 2.

We see from Table 2 that the triplet peaks are appreciable compared to the  $2'P$  one only at incident energies within about 10 ev off threshold and that they fall off rapidly as the beam energy increases. The  $2'S$  and  $3'S$  peaks have a stronger energy dependence than the  $2'P$  peak, while the  $2'P$ ,  $3'P$  and  $4'P$  peaks have nearly the same energy dependence.

In further work Simpson, Menendez and Mielczarek<sup>(70)</sup> determined the relative cross sections for the helium  $2^3S$ ,  $2'S$ , and  $2'P$  excitations with 56.6 ev beams as a function of scattering angle. This plot is reproduced in

Table 2. The Strength of Electron-Loss Peaks in Helium Relative to the  $2^1P$  Peak

$E_0$ , eV	Loss peak							
	$2^3S$	$3^3S$	$2^1S$	$3^1S$	$2^3P$	$2^1P$	$3^1P$	$4^1P$
	19.82	22.72	20.61	22.92	20.96	20.22	23.08	23.74
22.0	49		410		41	100		
22.5	22		148		31	100		
23.5	13		133		23	100		
24.5	16		113		11	100		
25.5	15	5	93		9	100	22	
26.5	13		79		7	100		
27.7	11	2	65	11	5	100	22	11 <sup>a</sup>
30.7	9	2	51	9	3	100	20	8
35.7	6	0	36	7	2	100	19	8
40.7	4	0	29	6	1	100	20	8
50.7	1	0	16	4	0	100	20	7
80.7	0	0	8	2	0	100	20	8

<sup>a</sup>This value may be high due to contributions from  $4^3S$  and  $4^1S$ .

Table 2. The strength of electron-loss peaks in helium relative to the  $2^1P$  peak,  $0^\circ$  scattering angle. (Taken from the work by Chamberlain, Heideman, Simpson, and Kuyatt<sup>(43)</sup>.)

Figure 17. The scattered current was multiplied by the sine of the scattering angle to correct for a change in the effective path length. These authors suggested that the cross section was expected to be largest for the optically allowed  $2^1P$  excitation, which could include important contributions from partial waves with moderately large  $\ell$  values, next largest for  $2^1S$ , and smallest for  $2^3S$  whose excitation required electron exchange, and therefore,  $\ell$  must be relatively small.

From Figure 17, we see that the relative cross sections for all transitions, at a fixed incident energy, fall off with respect to increasing scattering angle. However, the ratio of forbidden to allowed transition increases with angle.

Recently, Doering<sup>(57)</sup> reported some  $90^\circ$  low energy electron impact work on helium. The beam energies were from 40 ev to 100 ev with about 1 ev resolution. The only two peaks resolved were the prominent  $2^1P$  and the weaker  $3^1P$  transitions. In no case was the spin forbidden transition to the  $2^3S$  state observed. He pointed out, therefore, that the transition to the  $2^3S$  state at these energies and at  $90^\circ$  must be at least a factor of 5 less intense than the transition to the  $2^1P$  state.

Most recently, Rice, Trajmar, and Kuppermann<sup>(71)</sup> studied the electron impact spectra of helium with 35 ev electron beams (resolution better than 0.1 ev) in an angular range from  $0^\circ$  to  $70^\circ$ . The results indicate that the  $2^3P$  and  $2^1P$  peak heights become equal at  $54^\circ$ . Therefore the broad  $2^1P$  peak in Doering's work<sup>(57)</sup> must contain a large contribution from the  $2^3P$  excitation. In addition they found that the  $2^3S$  to  $2^1P$  peak height ratio was about 0.5 at  $70^\circ$  scattering angle, indicating again the importance of spin forbidden transitions at low energies and large scattering angles.

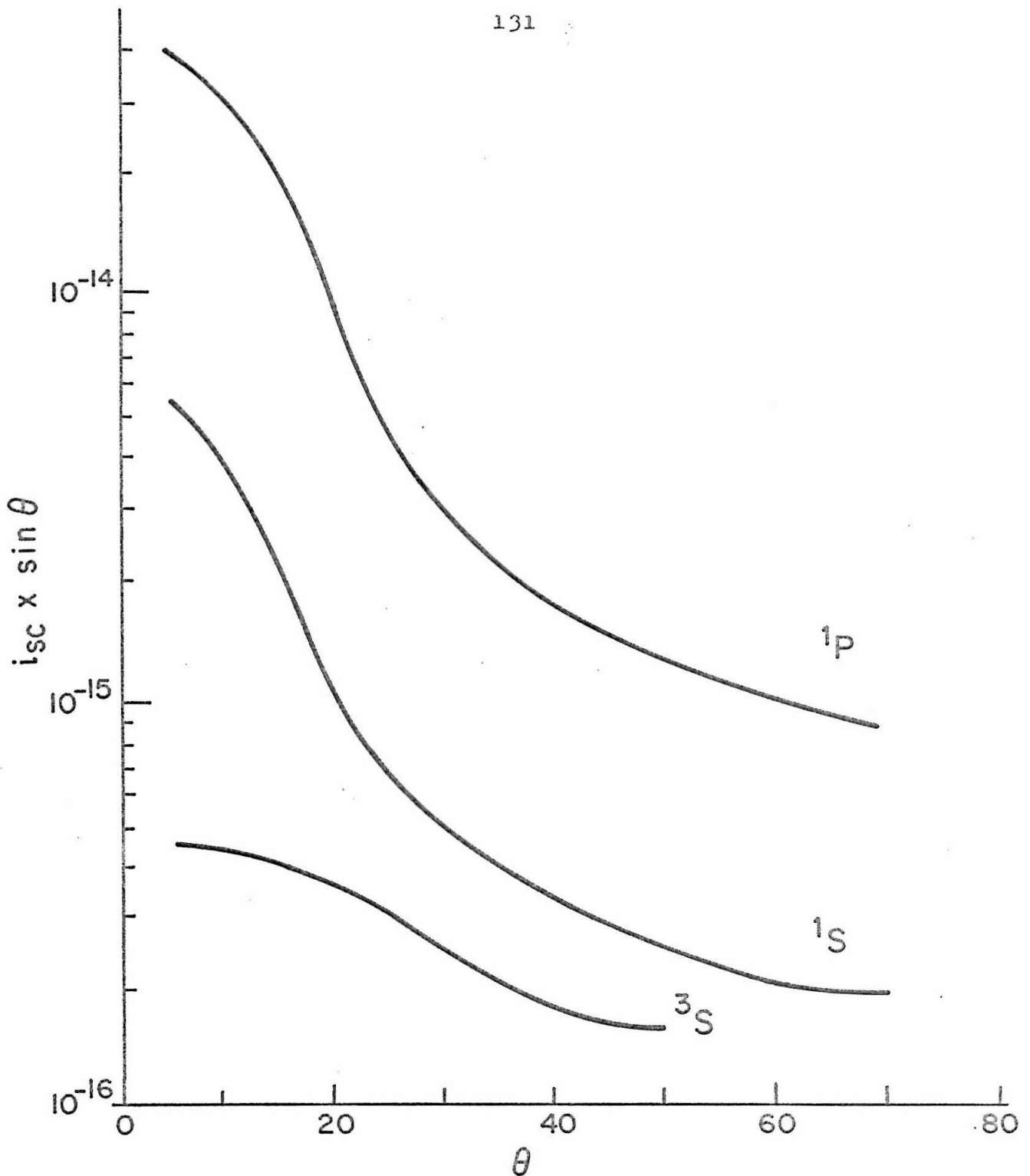


Figure 17. Logarithm of the relative cross section at 56.5 eV versus angle for the  $2^3S$ ,  $2^1S$ , and  $2^1P$  excitations in helium. (Taken from the work by Simpson, Menendez, and Mielczarek<sup>(70)</sup>.)

### V.1.2. Electron Impact Spectra of Helium

The  $90^\circ$  electron impact spectra of helium with beam energies of 50, 40, 35, and 30 eV are shown in Figure 18. The increments of the scattered current per unit energy loss are plotted against the energy loss instead of  $V_{G3}$ . We recall from section IV.2.5. that the energy loss is related to  $V_{G3}$  by an additive constant known as the contact potential. The elastic peaks corresponding to the helium spectra in Figure 18 are shown in Figure 14. The 30 eV helium spectrum which includes the elastic peak and the rising background is shown in Figure 16.

We see from Figure 18 that the most prominent feature of the spectrum is the unresolved  $2^1P$  and  $2^3P$  peak with a shoulder due to the  $2^1S$  excitation. The  $2^3S$  excitation is too small to be observed at energies of 50 and 40 eV. However, at 35 and 30 eV it becomes more intense and clearly visible. The relative peak heights are difficult to estimate because of the rising background. We see that the background problem is worse at lower beam energies.

The 50 eV helium spectra in Figure 18 d and Figure 15c are in very good agreement with Doering's 60 eV,  $90^\circ$  electron impact spectrum<sup>(57)</sup>. The results shown in Figure 18 are generally consistent with the optical data and with the  $0^\circ$  angle work by Chamberlain, et al<sup>(43)</sup>, and that by Simpson, Menendez and Mielczarek<sup>(70)</sup>, as reproduced in Table 2 and Figure 17, respectively.

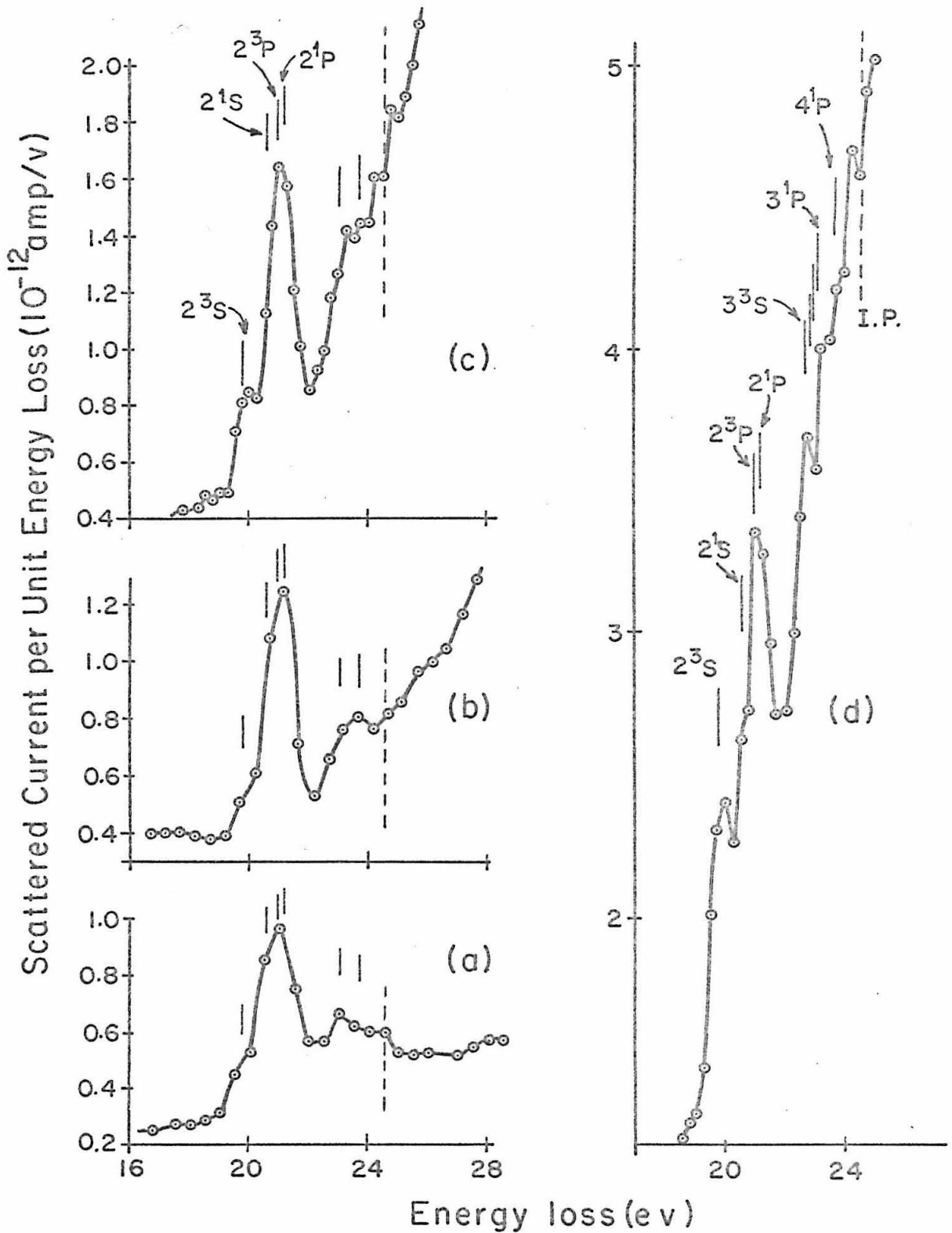


Figure 18.  $90^\circ$  electron impact spectra of helium at beam energies of a) 50, b) 40, c) 35, and d) 30 ev.

$i_{BC} = 0.98 \times 10^{-7}$  amp,  $P_{SC} = 3.2 \times 10^{-4}$  torr.

## V.2. Hydrogen

The ground state of hydrogen is designated as  $X'\Sigma_g^+$  and has an electron configuration of  $(1s\sigma)^2$ <sup>(8)</sup>. Excitation of one or both of the electrons from the lowest orbital to excited orbitals leads to various excited electronic states. There are more than forty observed electronic states with only one electron being excited. Transitions involving the  $(1s\sigma)^2 X'\Sigma_g^+$  ground state have been observed optically to the  $(1s\sigma)(2p\sigma) B'\Sigma_u^+$  state, known as the Lyman bands, to the  $(1s\sigma)(2p\pi) C'\Pi_u$  state, known as the Werner bands, and to the  $(1s\sigma)(3p\pi) D'\Pi_u$  state. The ionization potential of  $H_2$  has been determined to be 15.422 eV from the preionization limit of the  $D \rightarrow X$  emission bands.

Figure 19 shows a plot of the potential energy curves for several of the lowest electronic states of molecular hydrogen. These curves were plotted by Cartwright and Kuppermann<sup>(34)</sup> using results from recent theoretical calculations for  $H_2$ <sup>(72)</sup>. At room temperature, the only important vibrational level of the ground electronic state is the  $v = 0$  level which is represented by the horizontal line segment at the bottom of the  $X'\Sigma_g^+$  curve in Figure 19. According to the Franck-Condon principle, transition from the ground state must occur vertically within the shaded area. The most probable excitation energy involved in the  $b \leftarrow X$  transition at an internuclear distance  $R^{(1)}$  is  $E_1$ . We see from Figure 19 that the spin forbidden  $b \leftarrow X$  transition with excitation energies between 8.8 and 11.8 eV is the only one not overlapped by other transitions.

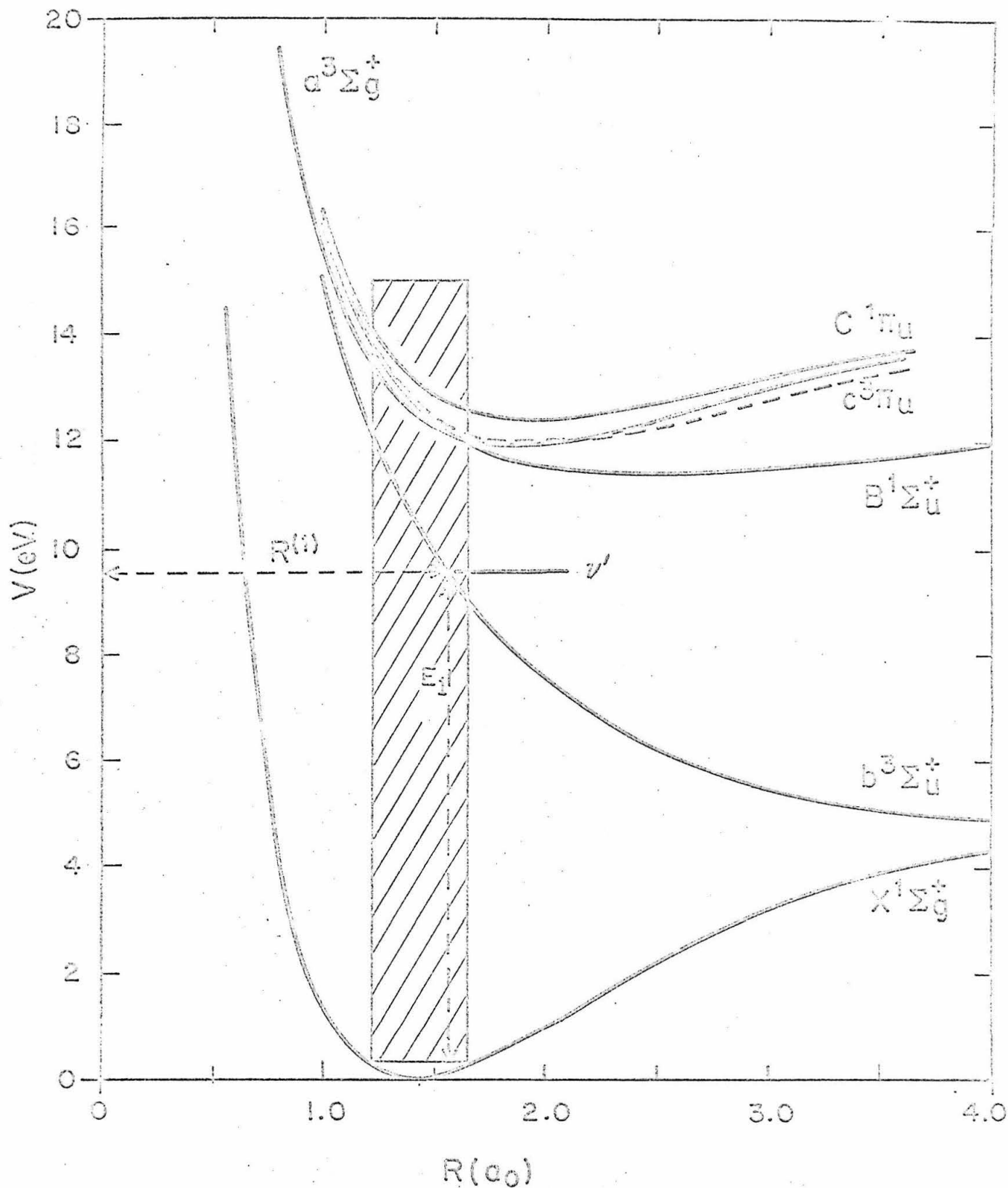


Figure 19. Potential energy curves for the hydrogen molecule.  
 (Taken from Cartwright and Kuppermann's work<sup>(34)</sup>.)

### V.2.1. Summary of Previous Electron Impact Work

Using the trapped-electron method, Schulz<sup>(46)</sup> obtained an excitation spectrum for molecular hydrogen. Schulz observed two bands with peaks located at 9.5 and 11.7 ev (contact potential not corrected) and an intensity ratio of about 1 to 8. The first band was assigned to the  $b^3\Sigma_u^+ \leftarrow X^1\Sigma_g^+$  transition, and the second band was attributed to transitions to the  $B^1\Sigma_u^+$  and higher states.

Kuppermann and Raff<sup>(54,55)</sup> obtained high scattering angle spectra of  $H_2$ , in which they detected among others the  $b^3\Sigma_u^+ \leftarrow X^1\Sigma_g^+$  transition. However, in view of the difficulties mentioned in section IV.3.13., their results were subject to confirmation.

Work by Lassetre and Francis<sup>(37a)</sup> with 390 ev beams (0.6 ev resolution) at  $0^\circ$  scattering angle showed an electron impact spectrum of hydrogen with a broad band peaking at 12.7 ev which corresponded to unresolved transitions from the ground state to the B, C, and D optically allowed singlet states. Further work by Lassetre and Jones<sup>(37c)</sup> with electron beam energies ranging from 324 to 461 ev and between  $0^\circ$  and  $5^\circ$  showed similar results.

Recently, Kuyatt, Mielczarek, and Simpson<sup>(42)</sup> investigated the  $0^\circ$  electron impact spectra of  $H_2$ , HD and  $D_2$  with electron beam energies between 30 and 90 ev (resolution 0.05 ev). Wellresolved vibrational lines due to transitions to the B, C, and D optically allowed singlet states were reported for the first time. In another publication, Kuyatt, Mielczarek and Simpson<sup>(73)</sup> presented a 33 ev,  $0^\circ$  electron impact spectrum of  $H_2$ . The  $C \leftarrow X$  vibrational series (starting at 12.27 ev and with the highest peak at 12.6 ev) was the strongest series in the spectrum. The  $B \leftarrow X$  series (starting at 11.19 ev) was also clearly

shown. The region above 14 eV appeared to be composed of at least two overlapping series, one of them being the  $D \leftarrow X$  transition. However, the  $(1s\sigma)(2p\sigma) b^3\Sigma_u^+$  repulsive state, found by Schulz<sup>(46)</sup> with the trapped-electron method, was not seen by these authors. They concluded, therefore, that the probability of exciting this state in forward scattering must be less than  $10^{-3}$  of that for exciting the  $C^1\Pi_u$  state.

Additional work with this instrument<sup>(45)</sup> furnished  $H_2$  spectra at  $0^\circ$  scattering angle with beam energies from 50.7 down to 13.7 eV. For incident energies below about 16 eV, two energy-loss peaks at 11.77 and 12.06 eV were observed to be different from the nearby  $B^1\Sigma_u^+$  state. These two peaks were attributed to excitations of triplet states. From spectroscopy data<sup>(8)</sup>, the  $c^3\Pi_u$  state, starting at 11.76 eV, has a vibrational spacing of 0.30 eV, while the  $a^3\Sigma_g^+$  state, starting at 11.79 eV, has a vibrational spacing of 0.33 eV. These authors were unable to tell whether the triplet-loss peaks were caused by one or both of the triplet states.

### V.2.2. Electron Impact Spectra of Hydrogen

The  $90^\circ$  electron impact spectra of hydrogen with beam energies of 50, 40, 35, and 30 eV are shown in Figure 20. The main features of the spectra consist of two broad bands peaking at 10.2 and 12.7 eV. (The accuracy in determining the position of the peak is approximately 0.2 eV). The first band at 10.2 eV is assigned to the spin-forbidden  $b^3\Sigma_u^+ \leftarrow X^1\Sigma_g^+$  transition. The second band lying between 11 and 14 eV may be due to unresolved transitions to the  $B^1\Sigma_u^+$  and  $C^1\Pi_u$  allowed states, to the  $a^3\Sigma_g^+$  and  $c^3\Pi_u$  triplet

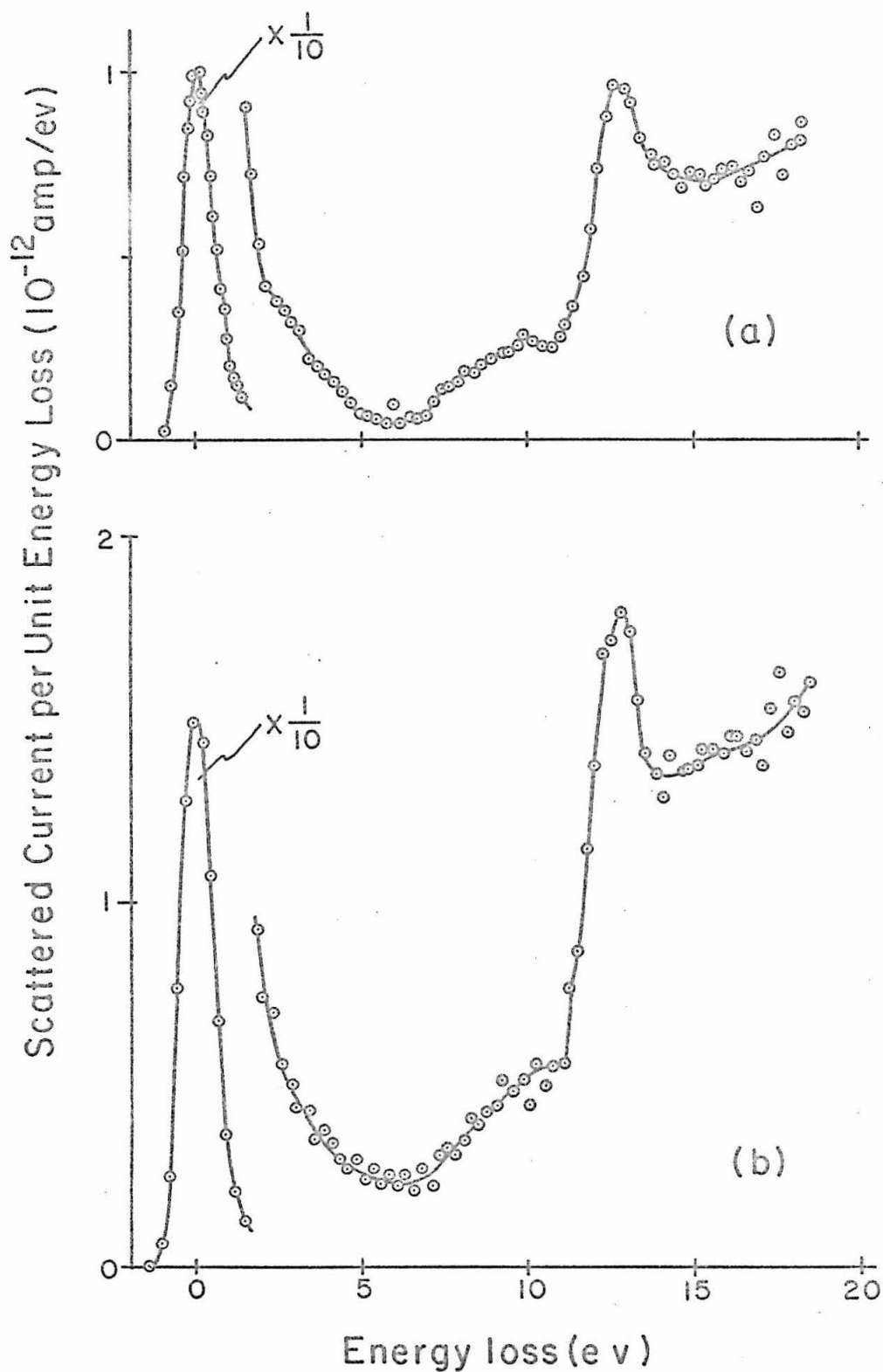


Figure 20.  $90^\circ$  Electron impact spectra of hydrogen at beam energies of a) 50, b) 40, c) 35, and d) 30 ev.  
 $i_{BC} = 1.45 \times 10^{-7}$  amp,  $P_{SC} = 4.3 \times 10^{-4}$  torr.

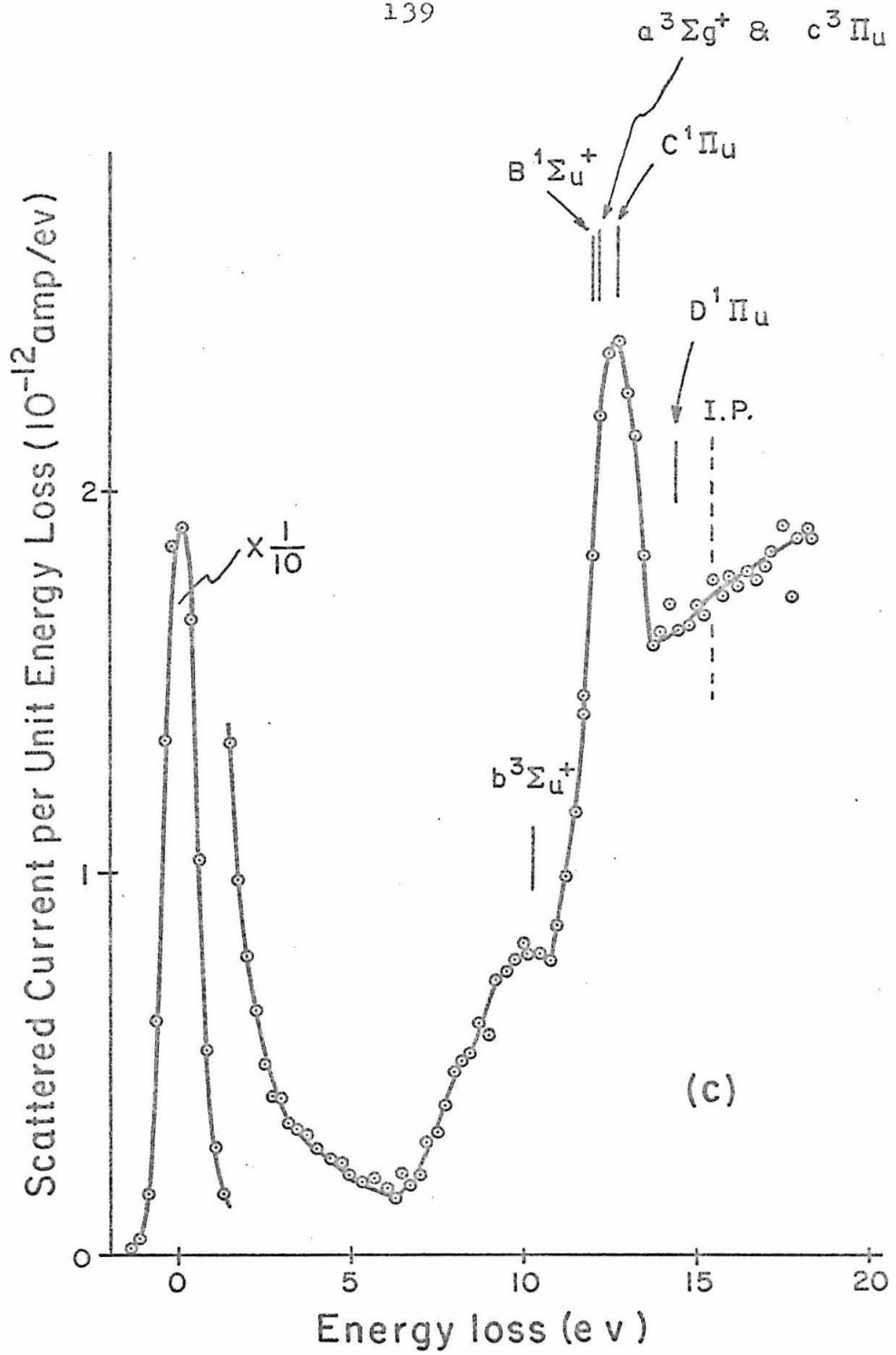


Figure 20. (Continued)

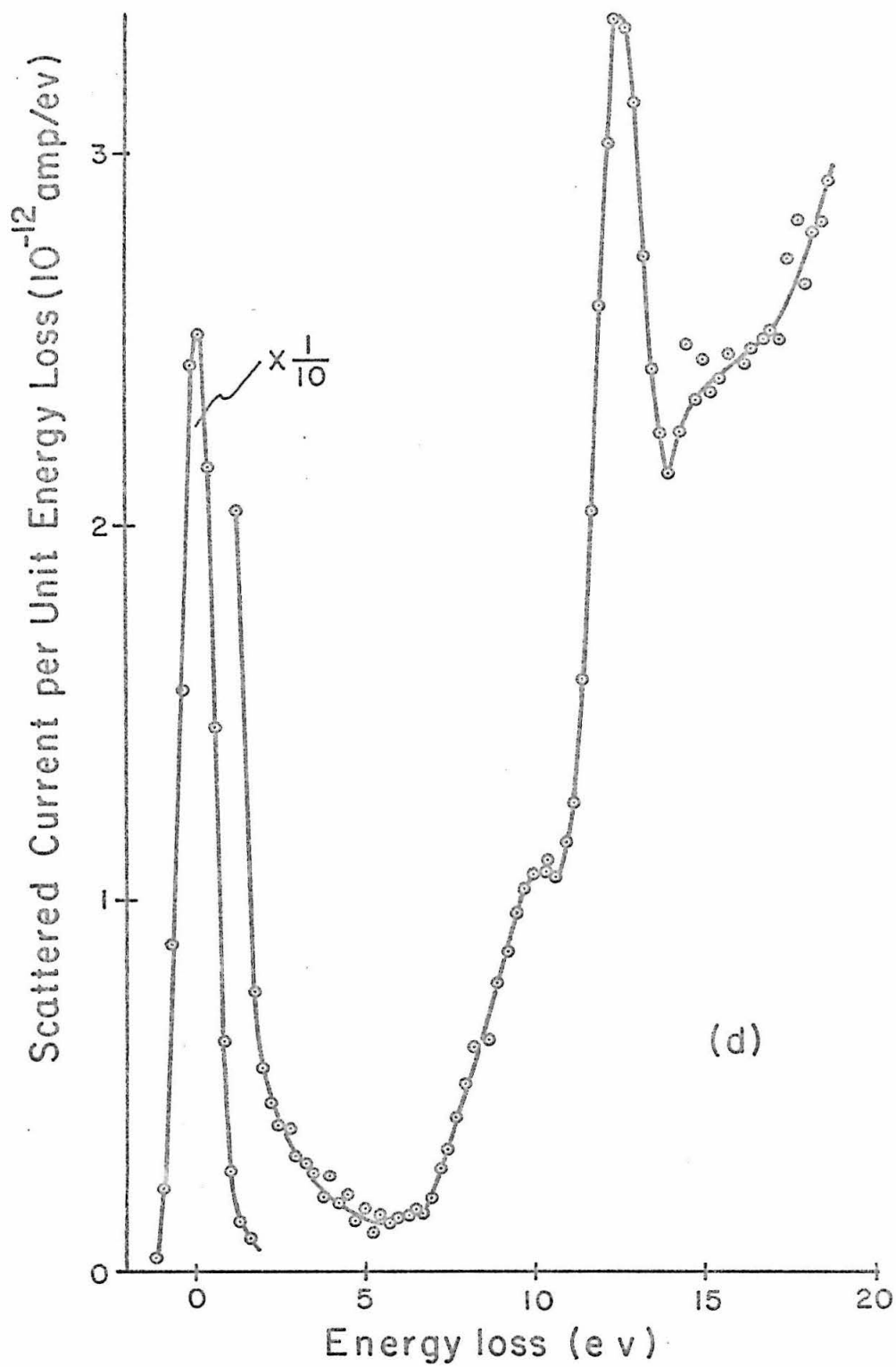


Figure 20. ( Continued )

states, and to other excited states. The  $D'\pi_u$  state and other closely spaced higher exciter states blend into a continuum beyond 14 ev.

The assignment of the  $90^\circ$  electron impact spectra of  $H_2$  is generally consistent with the optical spectroscopy data and with the previous electron impact work. It seems that this is the first time that the  $b^3\Sigma_u^+ \leftarrow X^1\Sigma_g^+$  transition has been reliably observed by electron impact spectroscopy with incident energies away from threshold. It should be pointed out that the general envelope of the bands observed in this work agrees qualitatively with Schulz's work of excitation near threshold. (46)

The ratios of intensity of the 10.2 ev band to that of the 12.7 ev band are 0.27, 0.31, 0.32, and 0.33 for electron beam energies of 50, 40, 35, and 30 ev, respectively. The increasing ratio with lowering of beam energy may have the significance that the differential cross section at  $90^\circ$  for the excitation to a triplet state has a stronger energy dependence.

Recently, Cartwright and Kuppermann (34) performed some calculations for the electron impact excitation cross sections of  $H_2$  for the  $b^3\Sigma_u^+ \leftarrow X^1\Sigma_g^+$  and the  $a^3\Sigma_g^+ \leftarrow X^1\Sigma_g^+$  transitions using the Ochkur and Ochkur-Rudge approximations. However, comparison of our results with theory is difficult to make because of the poorness of our intensity measurements. Further studies on the energy and angular dependences of the electron impact spectrum of  $H_2$  at a better resolution are required for detailed comparison between theory and experiment.

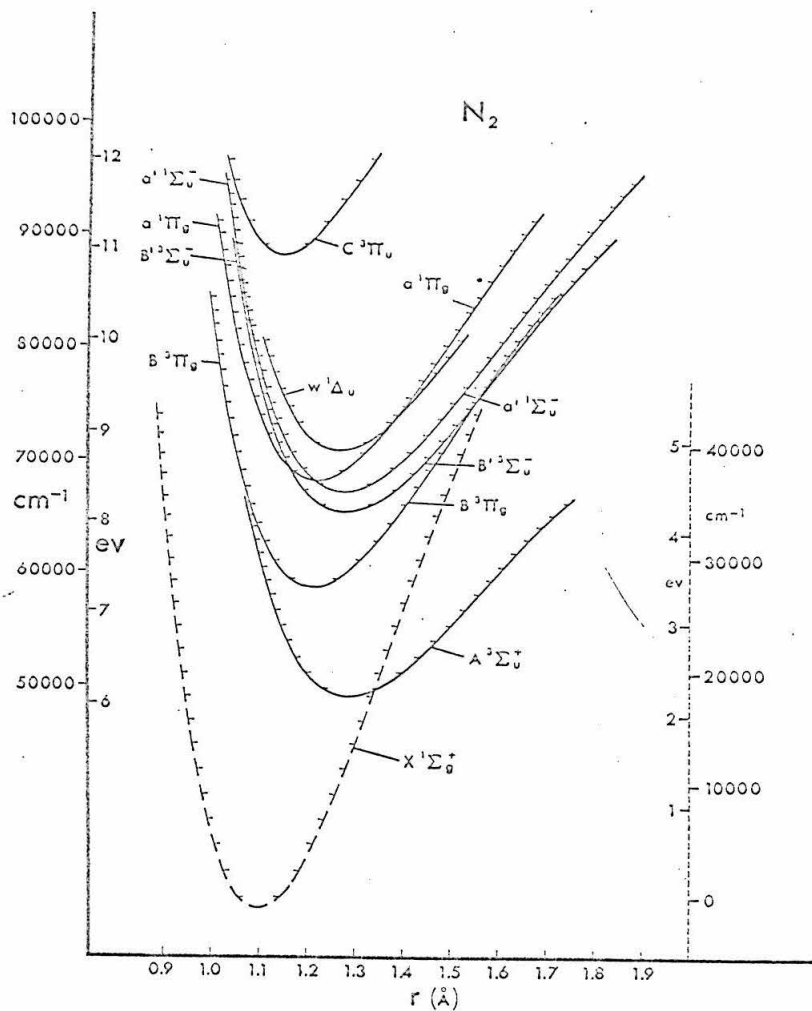
### V. 3. Nitrogen

The properties of the excited electronic states of nitrogen have been studied by many authors. The first optically allowed state of  $N_2$  is the  $b'\pi_u$  state which lies at about 12.7 eV above the  $x'\Sigma_g^+$  ground state and the first ionization potential is at 15.576 eV<sup>(8)</sup>.

For energies below that of the  $b'\pi_u$  state, many electronic states, though optically forbidden, have been observed in the vacuum ultraviolet region as weak absorptions<sup>(74,75)</sup>. For example, the  $a'\pi_g \leftarrow x'\Sigma_g^+$  transitions (lying between 8.55 and about 10 eV with a vibrational spacing of 0.19 eV), known as the Lyman-Birge-Hopfield bands, are electric dipole forbidden but magnetic dipole and electric quadrupole allowed; the  $A^3\Sigma_u^+ \leftarrow X'\Sigma_g^+$  (lying between 6.5 and 8.25 eV) transitions known as the Vegard-Kaplan bands, are spin forbidden; the  $B^3\Pi_g$  state (lying between 7.3 and 8.4 eV) and the  $E^3\Sigma_g^+$  state (starting at 11.87 eV) are both spin and "g to g" symmetry forbidden; the  $C^3\pi_u$  state (starting at 11.04 eV, with a vibrational spacing of 0.25 eV) is spin forbidden; etc.

Potential energy curves for the observed low-lying states of nitrogen have been separately presented by Tanaka, Ogawa, and Jursa<sup>(74)</sup>, and by Benesch, Vanderslice, Tilford, and Wilkinson<sup>(75)</sup>. A summary of the potential energy curves for the diatomic molecules  $N_2$ ,  $N_2^-$ , and  $N_2^+$  is presented by Gilmore<sup>(76)</sup>. Franck-Condon factors for the electronic band systems  $A^3\Sigma_u^+ \leftrightarrow X'\Sigma_g^+$ ,  $a'\pi_g \leftrightarrow x'\Sigma_g^+$ , and  $C^3\pi_u \leftrightarrow x'\Sigma_g^+$  in nitrogen have been calculated by Zare, Larson, and Berg<sup>(77)</sup>.

Figure 21 shows the potential energy diagram reproduced from the work by Benesch et al<sup>(75)</sup> for the observed states of  $N_2$  below 11 eV.



Potential curves for the observed states of  $N_2$  below  $\sim 11$  eV. The  $X^1\Sigma_g^+$  state has been displaced upward and the right-hand ordinate scale refers only to this one state. The energies of all other curves refer to the left-hand ordinate scale.

Figure 21. Potential energy curves for the nitrogen molecule. (Taken from the work by Benesch, Vanderslice, Tilford, and Wilkinson (75).)

### V.3.1. Summary of Previous Electron Impact Work

Using the trapped-electron method, Schulz<sup>(47)</sup> obtained excitation (near threshold) spectra of  $N_2$  at different potential well depths. Transitions to the very short lived  $N_2^-$  ground state and the  $N_2$   $A^3\Sigma_u^+$  (and  $B^3\Pi_g$ ),  $a^1\Pi_g$ , and  $C^3\Pi_u$  states were observed.

Schulz showed that for electron beam energies close to threshold the cross sections for excitation for triplet states were higher than those for the singlet states. He also demonstrated that the excitation function for the  $C^3\Pi_u$  state might peak less than 0.8 eV above threshold.

Recently, Bowman<sup>(52)</sup> used the trapped-electron technique to investigate the excitation spectra for some cyanide molecules. A nitrogen spectrum almost identical to that obtained by Schulz<sup>(47)</sup> was also shown.

Most recently, a high resolution (0.1 eV) trapped-electron spectrometer was put into operation by Brongersma and Oosterhoff<sup>(53)</sup>. The first strong transition in  $N_2$ , which was previously assigned to the  $A \leftarrow X$  transition by Schulz<sup>(47)</sup>, was partially resolved and shown to be the  $B \leftarrow X$  transition

When Lassette and Kransnow<sup>(37f)</sup> reported electron impact studies of  $N_2$  for the first time, electron beams with energies of about 500 eV, (resolution 0.5 eV) were used. The strongest transition in the forward scattered spectrum was located at 12.85 eV correlating with the first optically allowed transition in  $N_2$ . In changing the scattering angle from  $0^\circ$  to  $9.6^\circ$ , another weak band system peaking at 9.10 eV started to gain intensity in the spectrum relative to the 12.85 eV one. This 9.10 eV peak was assigned to the  $a^1\Pi_g \leftarrow X^1\Sigma_g^+$  transition which was optically forbidden but magnetic dipole and electric quadrupole allowed.

Further work by Skerbele and Lassettre<sup>(38a)</sup> with 250 ev electron beams (0.4 ev resolution) at zero scattering angle showed the partially resolved Lyman-Birge-Hopfield transition in nitrogen. However, its intensity was only about 0.5% of the most intense peak. No singlet-triplet transitions were observed.

With improved resolution Lassettre, Meyer, and Longmire<sup>(38b)</sup> were able to resolve the vibrational structure of the L.B.H. bands. This experiment was done with 200 ev electron beams while looking at zero scattering angles.

Later, Heideman, Kuyatt, and Chamberlain<sup>(44)</sup> obtained forward scattering electron energy-loss spectra of  $N_2$  for losses between 8.5 and 14 ev at incident energies of 15.7 and 35 ev. In addition to the optically allowed transition and the well-resolved Lyman-Birge-Hopfield bands, another electric quadrupole allowed transition at 12.26 ev and the spin forbidden  $C^3\Pi_u$  state were also observed.

Further work by Lassettre, Skerbele, and Meyer<sup>(38d)</sup> on nitrogen with electron beam energies between 60 and 400 ev showed that the 12.25 ev transition and another transition at 11.86 ev were compatible with an electric quadrupole transition.

Recently, Skerbele, Dillon, and Lassettre<sup>(39a)</sup> reported further electron impact work on  $N_2$  with electron beam energies between 30 and 80 ev and at scattering angles between  $0^\circ$  and  $16^\circ$ . Vibrational series of transitions to the  $A^3\Sigma_u^+$  and the  $B^3\Pi_g$  as well as to the  $C^3\Pi_u$  triplet states were observed. The intensities of the singlet-triplet transitions and the  $a^1\Pi_g \leftarrow X^1\Sigma_g^+$  transition were about 1% and 10%, respectively, relative to that of the strongest optically allowed transition at 12.93 ev.

The cross sections for the excitation of nitrogen

to the  $B^3\pi_g$  and  $C^3\pi_u$  states by electron impact with electron beam energies from threshold to 100 ev were measured by Zapesochnyi and Skubenich<sup>(78)</sup> by observing the light emitted subsequent to excitation. The cross sections reached maximum shortly after onset and then tailed off quickly with increasing energies. The cross sections for excitation to the  $B^3\pi_g$  state were about twice as large as those to the  $C^3\pi_u$  state around 40 ev beam energies.

### V.3.2. Electron Impact Spectra of Nitrogen

The  $90^\circ$  electron impact spectra of nitrogen with electron beam energies of 50, 40, 35, and 30 ev are shown in Figure 22. Three broad bands are observed below the 15.576 ev ionization potential.

The lowest band between 6.5 and 10.3 ev is due to unresolved transitions to the  $A^3\Sigma_u^+$ ,  $B^3\pi_g$  and  $a^1\pi_g$  states, (with Franck-Condon envelopes peaking at 7.4, 7.8, and 9.1 ev, respectively). The second small band peaking at about 11.1 ev can be assigned to the  $C^3\pi_u$  state which is partially resolved because no other electronic states lie in its vicinity. The most intense band peaking at about 13.2 ev is probably due to transitions to the optically allowed as well as spin forbidden electronic states in this region. This may account for the difference in peak position compared to the optical (and Lassetre's) value of 12.9 ev<sup>(39a)</sup>.

The assignment of the  $N_2$  spectra is generally consistent with optical spectroscopic data and with previous electron impact work. Comparison of the intensities for various electronic transitions is difficult because they are not completely resolved. We see that the spin forbidden

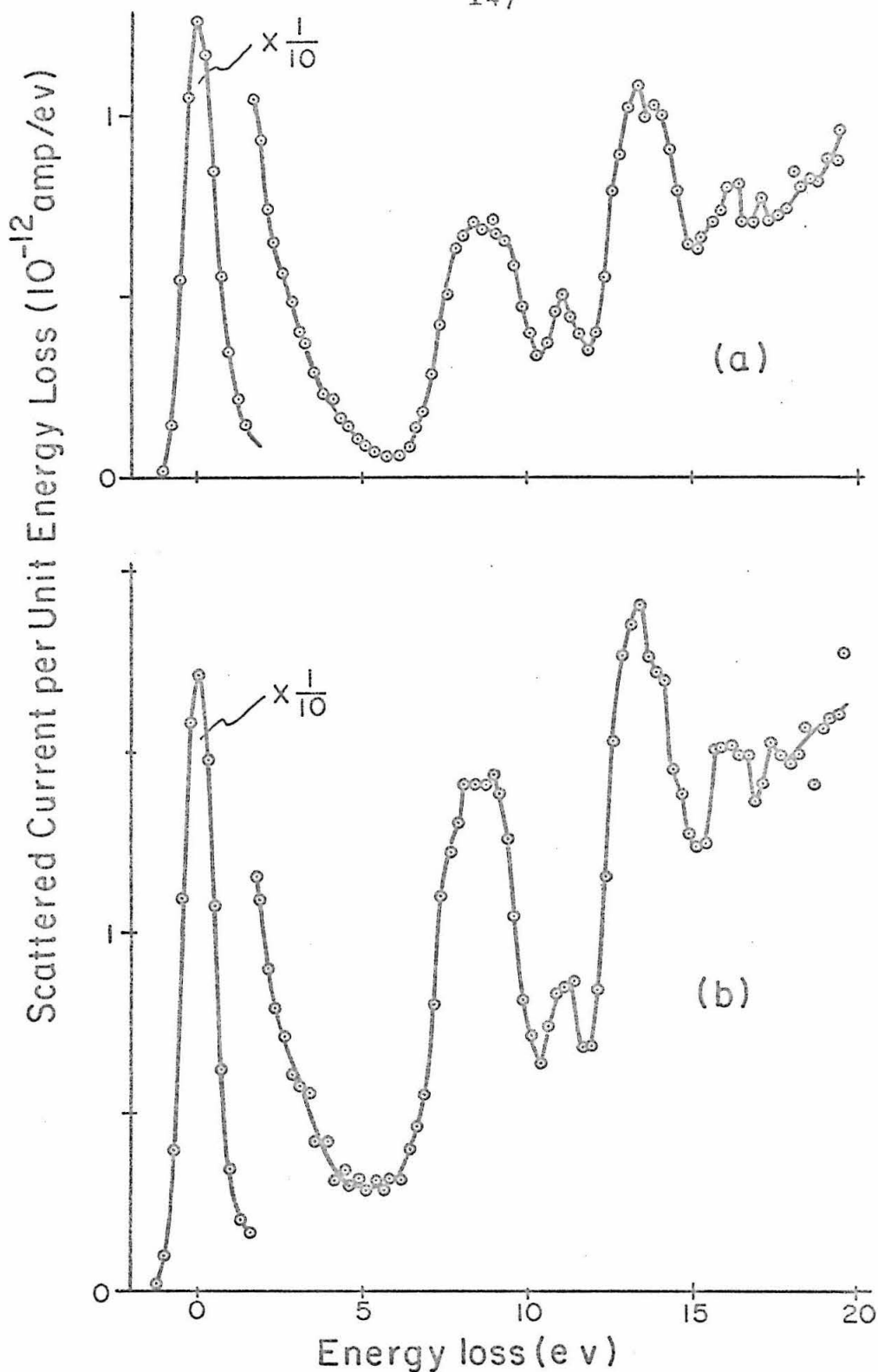


Figure 22.  $90^\circ$  Electron impact spectra of nitrogen with electron beam energies of a) 50, b) 40, c) 35, and d) 30 eV.  $i_{BC}=1.40 \times 10^{-7}$  amp,  $P_{SC}=5.5 \times 10^{-4}$  torr.

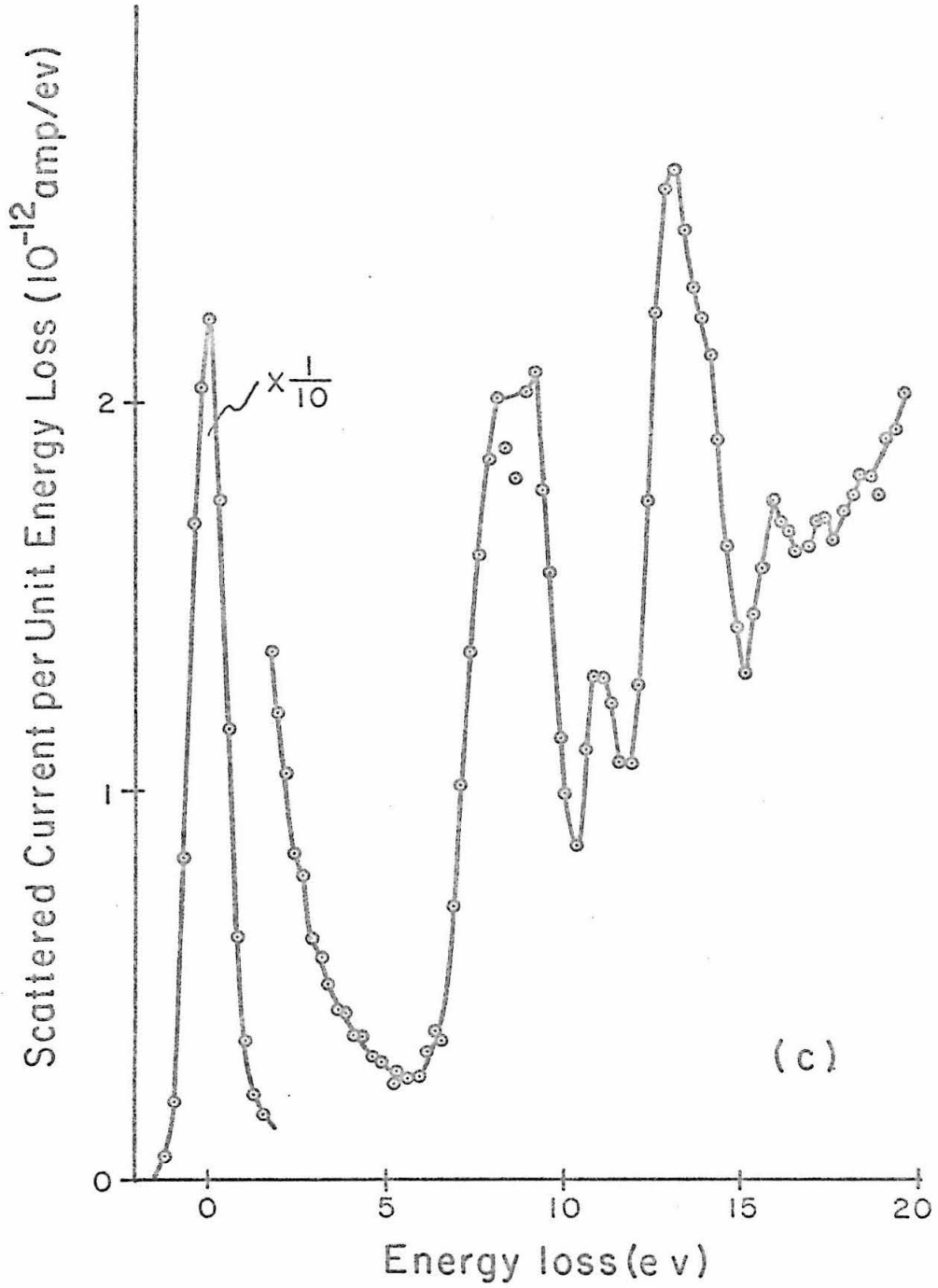


Figure 22. ( Continued )

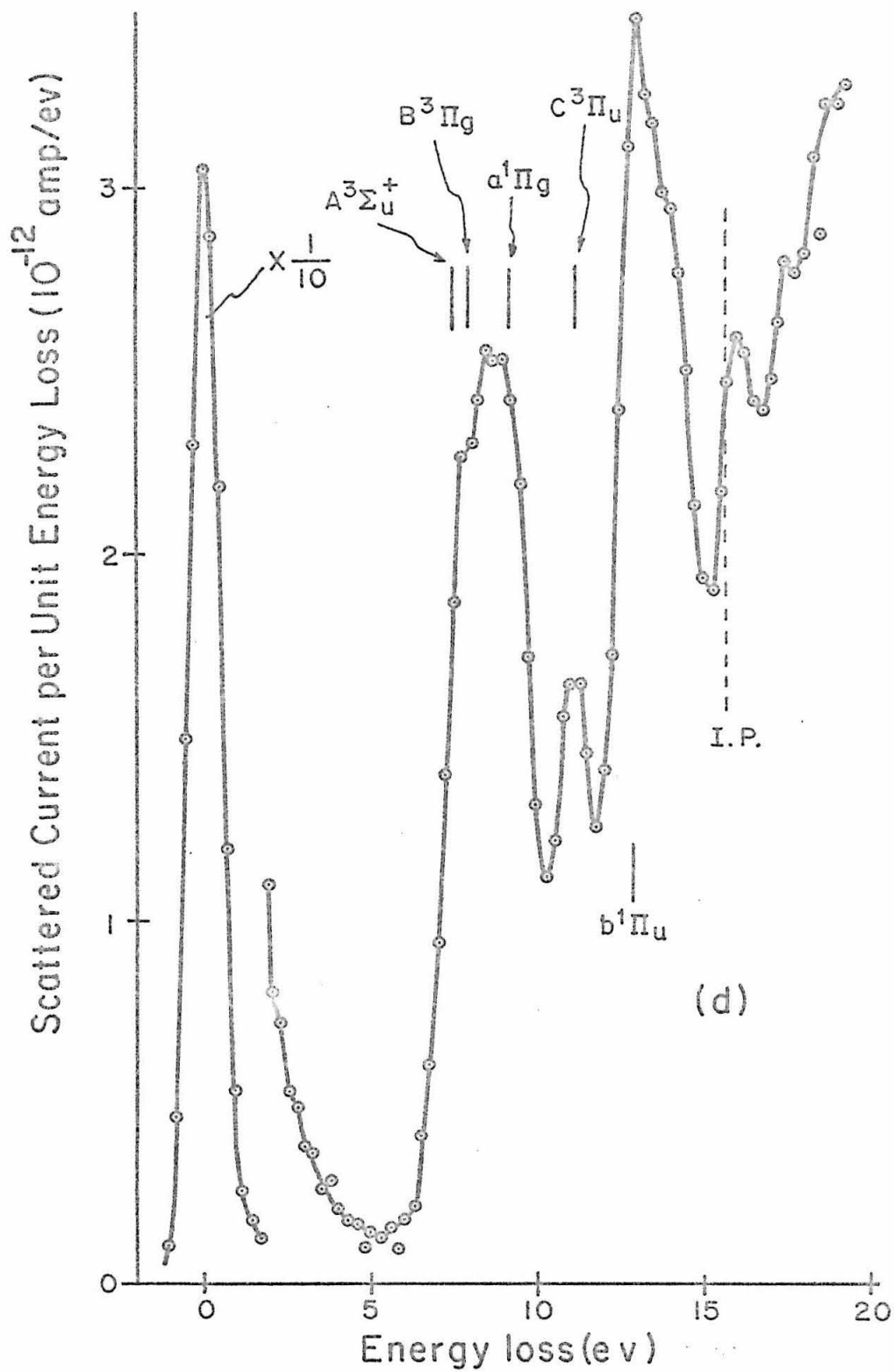


Figure 22. ( Continued )

(A  $^3\Sigma_u^+$  and B  $^3\Pi_g$ ) band is almost as intense as the optically allowed band (peaking at 13.2 eV). This could be due to the large scattering angle, as in the  $2^3P$  transition in He. It is also possibly because the triplet states are mixed with the neighboring singlet states, such as the  $a'^1\Pi_g$  state, to gain in intensity. The weak absorptions of these forbidden states in the vacuum ultraviolet region may be accounted for in the same way.

Comparing the results from forward scattering (39a) with those of this work, we may say that the ratio of the differential cross sections for electron scattering from optically forbidden states to those from optically allowed states definitely increases with increasing scattering angle. Thus large scattering angles are favorable for detecting optically forbidden states. The angular and energy dependence of various types of transitions in  $N_2$  would be of interest to the understanding of the theoretical basis for electron scattering.

#### V.4. Carbon Monoxide

Having 14 electrons, CO is isoelectronic with  $N_2$ . Therefore, the electronic structure and the spectroscopic characteristics of CO are very similar to  $N_2$ . Earlier work on CO was summarized in the book by Herzberg<sup>(8)</sup>. Recently, absorption studies in the vacuum ultraviolet region were done by Tanaka, Jursa, and LeBlanc<sup>(79)</sup> between 1070 and 2500 Å, and by Huffman, Larrabee, and Tanaka<sup>(80)</sup> in the 600 to 1006 Å wavelength region.

The ground state of CO is an  $X^1\Sigma^+$  state. Allowed transitions to the low-lying  $A^1\Pi$ ,  $B^1\Sigma^+$ ,  $C^1\Sigma^+$ ,  $E^1\Pi$ ,  $F^1(\Pi)$ , and  $G^1(\Pi)$  states, form the strongest absorption bands below the ionization potential of 14.009 eV. Intercombination band systems from the  $X^1\Sigma^+$  state to the  $a^3\Pi_r$ ,  $a^3\Sigma^+$ ,  $d^3\Pi_i$ , and  $e^3\Sigma^-$  states have been observed as weak UV absorptions by Tanaka, Jursa and LeBlanc<sup>(79)</sup>. The  $b^3\Sigma^+ \leftarrow X^1\Sigma^+$  band, observed by earlier workers but not by Tanaka, Jursa, and LeBlanc under the same condition for the observation of the other triplet states, seems to be more strongly forbidden. The electric dipole forbidden  $I^1\Sigma^- \leftarrow X^1\Sigma^+$  absorption bands have been investigated by Herzberg, Simmons, Bass and Tilford<sup>(81)</sup>. The weak  $D^1\Delta \leftarrow X^1\Sigma^+$  absorption bands have been reported by Simmons and Tilford<sup>(82)</sup>. Potential energy curves for the low-lying states of CO and  $CO^+$  have been calculated by Krupenie and Weissman<sup>(83)</sup>.

Figure 23a shows a plot of the potential energy curves for CO and  $CO^+$ . Figure 23b shows the energy level diagram for CO and  $CO^+$ . These figures are reproduced from the recent review book on the band spectrum of CO compiled by Krupenie<sup>(84)</sup>.

Figure 23a.  
Potential energy curves for CO and CO<sup>+</sup>.

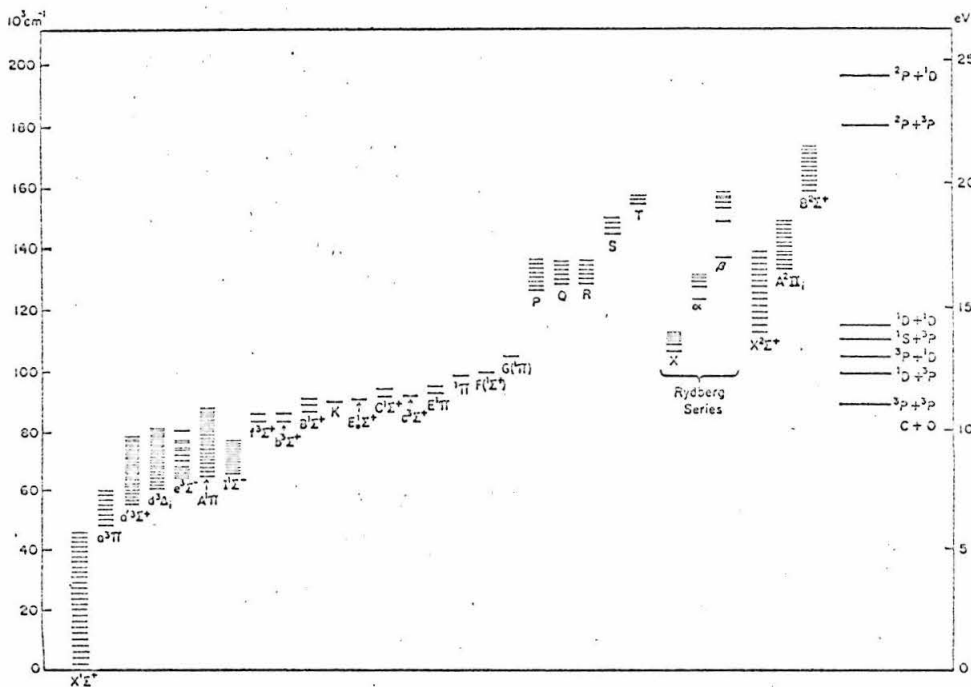
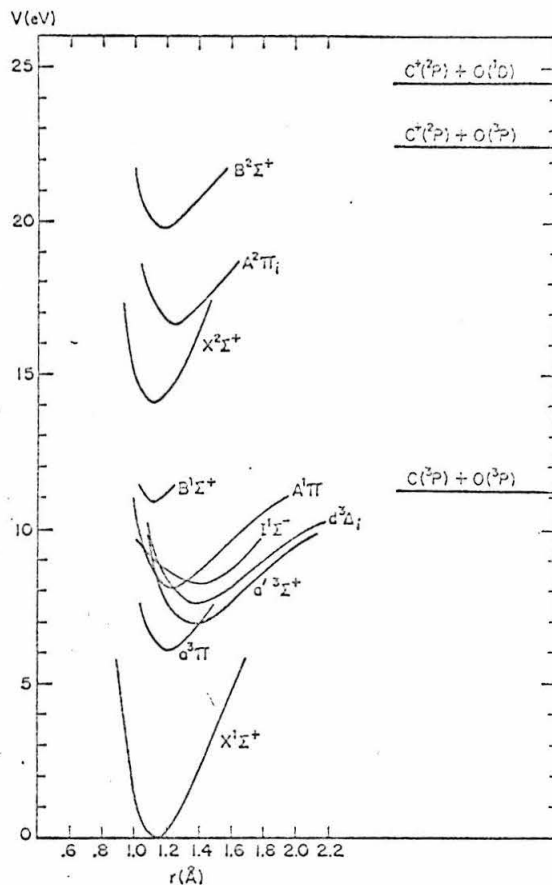


Figure 23b. Energy level diagram for CO and CO<sup>+</sup>.  
(Taken from Krupenie's work (84)).

#### V.4.1. Summary of Previous Electron Impact Work

With the trapped-electron method, Schulz<sup>(47)</sup> obtained an excitation spectrum of CO using a potential well depth of 0.7 volt. The most prominent bands in the spectrum were the  $a^3\pi_r \leftarrow X^1\Sigma^+$  transitions, known as the Cameron bands. Transitions to the  $A^1\pi$  and the  $b^3\Sigma^+$  states showed up with much less intensities. The resemblance of the CO and  $N_2$  spectra was remarkable in Schulz's work.

Recently, Brongersma and Oosterhoff<sup>(53)</sup> obtained a high resolution (0.1 eV) trapped-electron spectrum of CO. Vibrational levels in the  $a \leftarrow X$  band was partially resolved.

In a series of publications, Lassetre and his co-workers have reported their low energy electron impact studies on CO at near zero scattering angles.

Using an electron beam with energy of 508 eV (resolution about 0.5 eV), Lassetre, Berman, Silverman, and Kransnow<sup>(37d)</sup> first investigated the angular dependence between  $4^\circ$  and  $15^\circ$  of the scattered signal from the first allowed  $A^1\pi \leftarrow X^1\Sigma^+$  transition which peaked at 8.35 eV ( $v' = 3$ ).

Further work by Lassetre and Silverman<sup>(37g)</sup> with electron beam energies between 400 and 600 eV and at scattering angles between  $3^\circ$  and  $15^\circ$  showed the angular dependence of the  $B^1\Sigma^+ \leftarrow X^1\Sigma^+$  transition at 10.78 eV ( $v' = 0$ ), and the  $C^1\Sigma^+ \leftarrow X^1\Sigma^+$  transition at 11.41 eV ( $v' = 0$ ). Their results indicated that the intensity of the  $C^1\Sigma^+ \leftarrow X^1\Sigma^+$  transition fell off more rapidly than that of the  $B^1\Sigma^+ \leftarrow X^1\Sigma^+$  transition with increasing scattering angle, although both transitions were optically allowed.

Silverman and Lassetre<sup>(85)</sup> further determined the envelope shape for the unresolved  $A^1\pi \leftarrow X^1\Sigma^+$  transition in CO excited by 508 eV electron beams. The agreement

with the calculated Franck-Condon factors was good.

Another 200 ev,  $0^\circ$  electron impact spectrum was reported by Skerbele and Lassette<sup>(38a)</sup> in an attempt to resolve the vibrational structure of the  $A'\pi$  state (vibrational spacings 0.18 ev). This attempt was unsuccessful while the nitrogen  $a'\pi_g \leftarrow X'\Sigma_g^+$  transition (vibrational spacings 0.20 ev) was partially resolved under similar experimental conditions.

With an improved electron spectrometer, Meyer, Skerbele, and Lassette<sup>(86)</sup> were able to partially resolve the vibrational structure of the  $A'\pi$  state ( $v' = 0 \rightarrow 8$ ) in a 200 ev,  $0^\circ$ , CO spectrum for the first time. Transitions to the  $A'\pi$ ,  $B'\Sigma^+$ ,  $C'\Sigma^+$ ,  $E'\pi$  and  $F'\pi$  states with 0-0 bands lying at 8.03, 10.78, 11.40, 11.52, and 12.37 ev, respectively, were observed.

Another high resolution electron impact spectrum of CO at 200 ev and  $0^\circ$  by Skerbele, Meyer, and Lassette<sup>(87)</sup> showed a completely resolved  $A'\pi$  state. Transitions to the  $G'\pi$  state (starting at 13.05 ev) were also resolved.

Recently, with still improved resolution, Skerbele, Dillon, and Lassette<sup>(39b)</sup> were able to observe the singlet-triplet transitions in CO (50 ev beam energy at  $2^\circ$  angle) for the first time. Four vibrational lines in the ( $a \leftarrow X$ ) Cameron bands (starting at 6.0 ev, with vibrational spacings of 0.22 ev) were resolved. The  $v' = 0$  level of the  $b^3\Sigma^+$  state was also observed at 10.5 ev. The relative intensities of the level  $v' = 0$  of the  $b^3\Sigma^+$  state and the level  $v' = 1$  of the  $a^3\pi$  state were 0.004 and 0.0006 respectively, relative to the level  $v' = 2$  of the ( $A \leftarrow X$ ) fourth positive bands.

#### V.4.2. The Electron Impact Spectra of Carbon Monoxide

The  $90^\circ$  electron impact spectra of CO with electron beam energies of 50, 40, 35, and 30 eV are shown in Figure 24. Three bands peaking at 6.2, 8.5 and 13.5 eV are observed. The 6.2 and the 8.5 eV bands may be assigned to the  $a^3\pi \leftarrow X^1\Sigma^+$  and the  $A^1\pi \leftarrow X^1\Sigma^+$  transitions, respectively. The 13.5 eV band with a long shoulder starting at about 11 eV may be attributed to the unresolved  $B, C, E, F, G$  and higher singlet states and other triplet states.

A careful look at the spectra in the energy loss region about 10.6 eV indicates that an inelastic process, though not resolved from the 13.5 eV band, gains intensity relative to the  $A \leftarrow X$  transition with decreasing beam energy (see Figure 24c, and 24d). This shoulder may be assigned to the  $b^3\Sigma^+$  state.

The assignments of the spectrum are generally consistent with optical spectroscopic data and with previous electron impact work.

The ratio of intensities of the 6.2 and the 8.5 eV bands stays approximately constant with decreasing beam energies. This indicates that the differential cross sections at  $90^\circ$  for the excitation of the  $a^3\pi$  and of the  $A^1\pi$  state have nearly the same energy dependence. Excitation to the  $b^3\Sigma^+$  state, on the other hand, seems to be more strongly dependent on energy than the  $a^3\pi$  state. The observation above may have the significance that the  $b^3\Sigma^+$  state has the "triplet" character while the  $a^3\pi$  state has borrowed some "singlet" character, probably from the neighboring  $A^1\pi$  state<sup>(88)</sup>. This may account for the weak vacuum UV absorption of the Cameron bands.

Our results indicate that the  $b^3\Sigma^+ \leftarrow X^1\Sigma^+$  transition is more strongly forbidden than the  $a^3\pi \leftarrow X^1\Sigma^+$  one. This

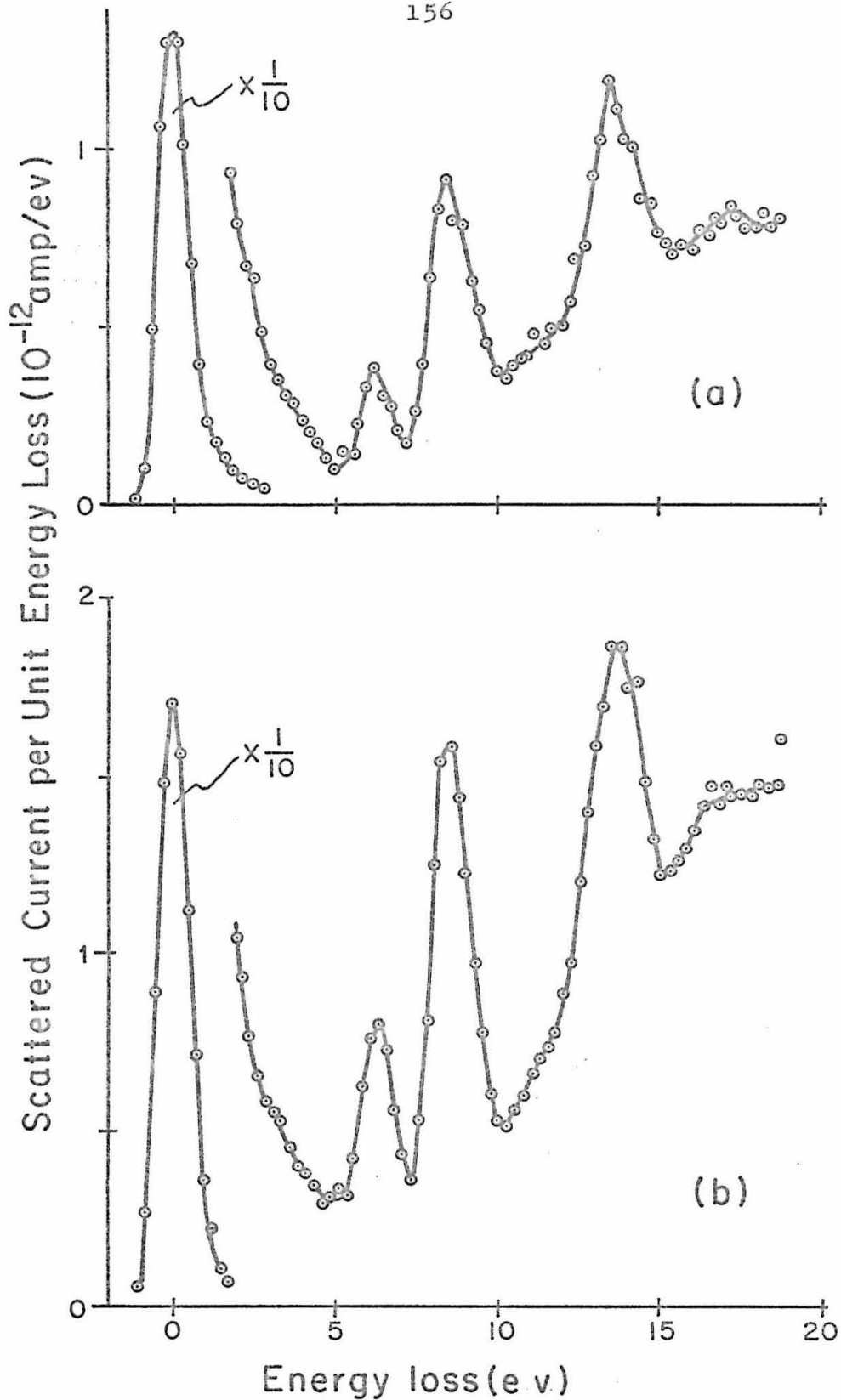


Figure 24. 90° Electron impact spectra of carbon monoxide with electron beam energies of a) 50, b) 40, c) 35, and d) 30 ev.  $i_{BC} = 1.40 \times 10^{-7}$  amp,  $P_{SC} = 4 \times 10^{-4}$  torr.

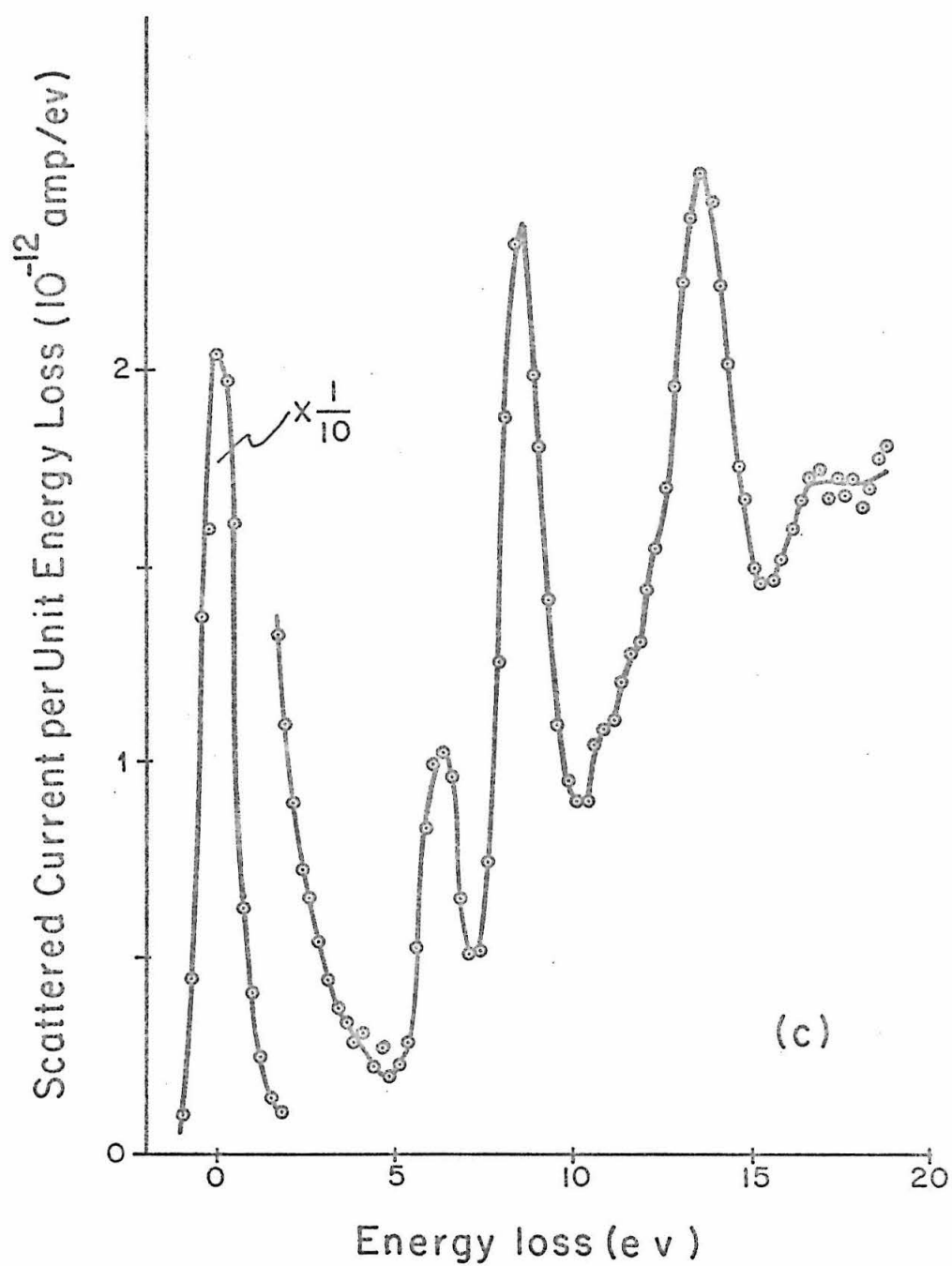


Figure 24. ( Continued )

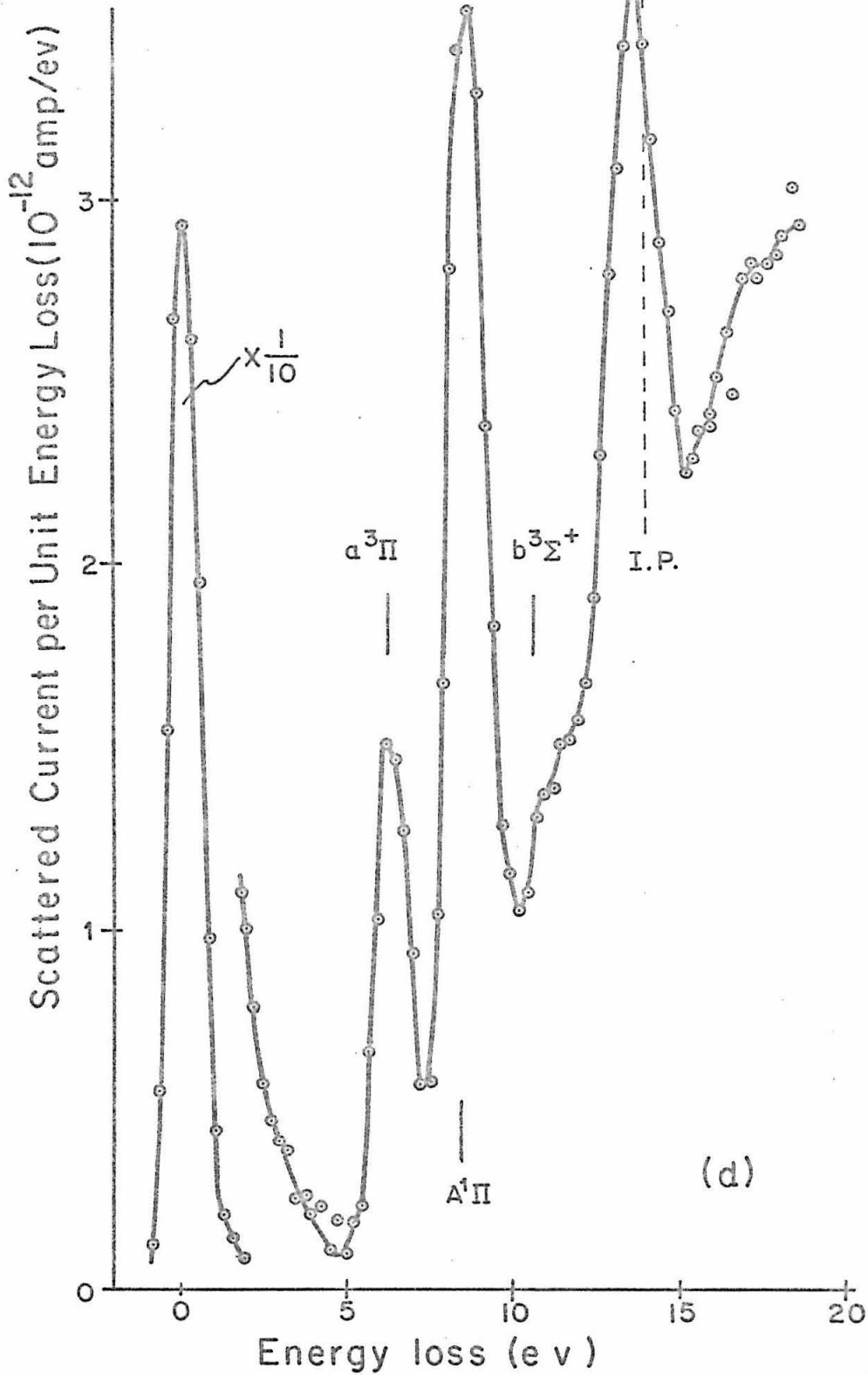


Figure 24. ( Continued )

is in agreement with the optical absorption work by Tanaka, Jursa, and LeBlanc<sup>(79)</sup>. However, Skerbele, Dillon, and Lassette<sup>(39b)</sup> have observed a stronger intensity for the  $b^3\Sigma^+$  state than that for the  $a^3\pi$  state in a 50 eV  $2^\circ$  electron impact spectrum of CO.

Further experimental studies on the energy and angular dependence of the differential cross sections at higher resolution for the  $a^3\pi$  and the  $b^3\Sigma^+$  triplet states, as well as other states, may lead us to better understanding on the nature of the electronic structure of CO.

Comparison of previous work<sup>(39b)</sup> with the present results indicates that the ratio of intensities of spin-forbidden to optically allowed transitions is much larger at  $90^\circ$  than at  $0^\circ$ . Thus, large scattering angles and low energies are favorable conditions for the observation of forbidden transitions.

V.5. Ethylene

Ethylene is the simplest hydrocarbon that has a  $\pi$ -electron system. The electronic states and the observed spectroscopic data are discussed and summarized by Herzberg<sup>(89)</sup>.

Ultraviolet absorptions of ethylene in the gas phase were studied by Price and Tutte in the wavelength region between 1000 and 2000 Å<sup>(90)</sup>, by Zelikoff and Watanabe in the region between 1065 and 2000 Å<sup>(91)</sup>, by Wilkinson and Mulliken in the region 1500-2050 Å<sup>(92)</sup>, and by Wilkinson in the region 1280-1520 Å<sup>(93)</sup>.

Following Herzberg's notation for the electronic states of polyatomic molecules<sup>(89)</sup>, the ground state of ethylene is a  $\tilde{X}'A_{1g}$  state which is planar and has  $D_{2h}$  symmetry. Transitions from the ground state to the first excited singlet state  $\tilde{A}'B_{1u}$ , which is believed to have  $D_{2d}$  symmetry with the two  $CH_2$  groups twisted by  $90^\circ$  with respect to each other, consist of a progression of diffuse bands starting at 5.9 eV with rapidly increasing intensity. The progression merges into a continuum at about 7.1 eV and has a maximum at 7.65 eV<sup>(91,92)</sup>.

The first and strongest Rydberg series (the  $\tilde{B} \leftarrow \tilde{X}$  transition) starts at 7.1 eV<sup>(91,92)</sup>. The  $\tilde{B}$  state has been shown<sup>(92)</sup> to have  $D_{2h}$  symmetry. Four other Rydberg series starting at 8.26, 8.61, 8.90, and 9.05 eV have also been identified<sup>(93)</sup>.

Another continuum is observed<sup>(91)</sup> in the region between 9.5 and 10.3 eV with a maximum at about 9.9 eV. This continuum is superimposed with the remaining members of the five Rydberg series. The ionization potential of 10.507 eV is obtained from an extrapolation of the strongest Rydberg series<sup>(90)</sup>.

In 1950 Reid<sup>(94)</sup> examined the near ultraviolet absorption spectrum of a 1.4 meter path in liquid ethylene at 120°K in the region 2000-4000 Å. He found a series of bands extending from 3.7 to 4.7 ev, merging into much stronger absorption at shorter wavelengths. The absorption coefficient:  $(\frac{1}{l c}) \log (\frac{I_0}{I})$ , was approximately  $10^{-4}$  which corresponded to a highly forbidden transition. Reid tentatively assigned this band as due to the transition to the lowest triplet state (believe to have a  $D_{2d}$  symmetry) of ethylene, namely, the  $\tilde{a}^3B_{1u} \leftarrow \tilde{X}^1A_{1g}$  transition.

In 1960 Evans<sup>(95)</sup> studied the near ultraviolet spectrum of ethylene with high pressure oxygen present in the absorption cell. (Two sets of experiments were done with a 5.2 cm cell: a).  $C_2H_4$  50 atm and  $O_2$  25 atm, b).  $C_2H_4$  2 atm and  $O_2$  2 atm). The presence of oxygen intensified the singlet-triplet transition, supporting Reid's assignment. Evans attributed this to a paramagnetic perturbation on ethylene by the  $O_2$  molecules. He concluded that the vertical energy corresponding to an intensity maximum of the  $\tilde{a} \leftarrow \tilde{X}$  transition was about 4.6 ev.

Another notation used by Mulliken<sup>(96)</sup> in designating the various electronic states of ethylene is often seen in the literature. In this notation the  $\tilde{X}$ ,  $\tilde{A}$ ,  $\tilde{B}$ , and  $\tilde{a}$  states of ethylene are referred to as the N, V, R, and T states, respectively.

In studying the ultraviolet absorption spectra of four alkyl-substituted ethylenes, (e.e., tetramethylethylene, trimethylethylene, cyclohexene, and hexene -1), Potts<sup>(97)</sup> found T $\leftarrow$ N transitions of these olefins in the region between 5 and 6 ev. Extrapolation from the methylated ethylenes to the case of zero methyl groups indicates a location of the triplet upper level of these bands in ethylene itself at a vertical energy of about 6.4 ev. Mulliken<sup>(98)</sup> postulated that this transition might have

a Rydberg triplet state  ${}^3B_{3u}$  as the upper state which has the same electron configuration as the  $\tilde{B}'B_{3u}$  state.

Recently, this postulated 6.4 ev transition in ethylene, referred to as the "mystery band", received extensive discussions by many authors (99). However, this band has not yet been positively observed in ultraviolet absorptions (100).

#### V.5.1. Summary of Previous Electron Impact Work

Kuppermann and Raff (54,55) reported low energy large angle electron impact spectra of ethylene. They detected transitions peaking at 4.6, 6.5, 7.7, 8.8 and 10.5 ev. The first was assigned to the spin forbidden  $\tilde{a}^3B_{1u} \leftarrow \tilde{X}'A_{1g}$  transition on the basis of its energy dependence. The 6.5 ev transition did not behave as a triplet and its existence has not been confirmed by other measurements. In view of the difficulties mentioned in section IV.3.13., the presence of this peak could have been an artifact of the measurement and is subject to suspicion.

Lassetre and Francis (37a) studied the  $0^\circ$  electron impact spectrum of ethylene using 390 ev beams with a resolution of about 0.6 ev. A prominent peak at 7.66 ev and two smaller peaks at 9.03 and 9.95 ev were observed below the ionization potential, in agreement with the ultraviolet absorption work (91).

Simpson and Mielczarek (41) obtained a 50 ev,  $0^\circ$  electron impact spectrum of ethylene. The resolution was about 0.1 ev. The first band lying between 6.8 and 8.6 ev, though not resolved, showed good agreement with UV measurements (91).

Geiger and Wittmaack (101) reported a high resolution

(0.025 ev) electron impact spectrum with 33 K ev electron beams at zero scattering angle. The spectrum obtained under these conditions showed exact agreement with UV absorption work<sup>(91)</sup>. The vibrational structure associated with the  $\tilde{B}$  Rydberg state was resolved.

Ross and Lassette<sup>(102)</sup> further studied the zero angle electron impact spectrum of ethylene with 150 ev beams (resolution 0.026 ev). The results agreed with the work by Geiger and Wittmaack at 33 k ev, and with UV absorptions<sup>(91)</sup>.

It is worthwhile to note that, in both the UV absorption<sup>(91)</sup> and high energy  $0^\circ$  electron impact<sup>(101)</sup> spectra of ethylene, the maximum absorption intensity occurs at 7.28 ev. On the other hand,  $0^\circ$  electron impact work at energies of 390 ev<sup>(37a)</sup>, 150 ev<sup>(102)</sup> and 50 ev<sup>(41)</sup>, yielded a maximum at about 7.5 ev for the  $V \leftarrow N$  and  $R \leftarrow N$  overlapping region. Ross and Lassette<sup>(102)</sup> pointed out that the shift of the maximum position might be attributed to an electric quadrupole transition occurring in this region induced by low energy electron impact.

Using the trapped-electron technique, Bowman and Miller<sup>(51)</sup> obtained an electron impact excitation spectrum of ethylene. Three bands peaking at 4.4, 7.7 and 9.2 ev were resolved with the relative intensities 0.29, 1.00, and 0.71, respectively. The 4.4 ev band was assigned to the  $\tilde{a}^3B_{1u} \leftarrow \tilde{X}^1A_{1g}$  (or  $T \leftarrow N$ ) transition. The other two bands were in agreement with UV absorptions and with  $0^\circ$  electron impact work.

Recently, Doering<sup>(58)</sup> studied the  $90^\circ$  electron impact spectra of ethylene with beam energies of 35, 50, and 70 ev (resolution 1 ev). The most intense inelastic peak was found to be at about 8 ev. A peak was observed at about 4.7 ev which was assigned to a forbidden singlet-triplet transition (the  $\tilde{a} \leftarrow \tilde{X}$  transition). A small peak at

about 10.7 ev was also observed and was assigned as a transition to a bound state near the ionization limit.

It should be noted that Doering's apparatus<sup>(57,58)</sup> also has an instrumental background which increases with decreasing beam energy. The rising background problem in the present work has been discussed in section IV.3.11.

### V.5.2. Electron Impact Spectra of Ethylene

Figure 25 shows the 90° electron impact spectra of ethylene from the present work with electron beam energies of 50, 40, 35, and 30 ev. The ethylene sample is from a Phillips 66 lecture bottle (Phillips Petroleum Company, mole per cent purity 99.86%) without further purification.

The general features of the spectrum agree very well with Doering's work<sup>(58)</sup>. The most prominent band peaking at 7.8 ev may be correlated to the unresolved  $\tilde{B} \leftarrow \tilde{X}$  (or  $R \leftarrow N$ ) and  $\tilde{A} \leftarrow \tilde{X}$  (or  $V \leftarrow N$ ) transitions.

A broad band peaking at about 4.4 ( $\pm 0.2$ ) ev is observed. It appears that the intensity of this band relative to the 7.8 ev band increases with decreasing beam energy, which is the correct energy dependence of a singlet-triplet transition. Hence the 4.4 ev band is assigned to the  $\tilde{a} \leftarrow \tilde{X}$  (or  $T \leftarrow N$ ) transition, which has been observed optically by Reid<sup>(94)</sup> and Evans<sup>(95)</sup>.

A weak band peaking at about 10.0 ev is also observed in this work. This band may be correlated to the weak continuum between 9.5 and 10.3 ev, observed by Zelikoff and Watanabe in ultraviolet absorptions<sup>(91)</sup>.

In regard to the postulated 6.4 ev "mystery band" of ethylene, there is no indication that it appears in the present work, although the spin-forbidden  $T \leftarrow N$  transition

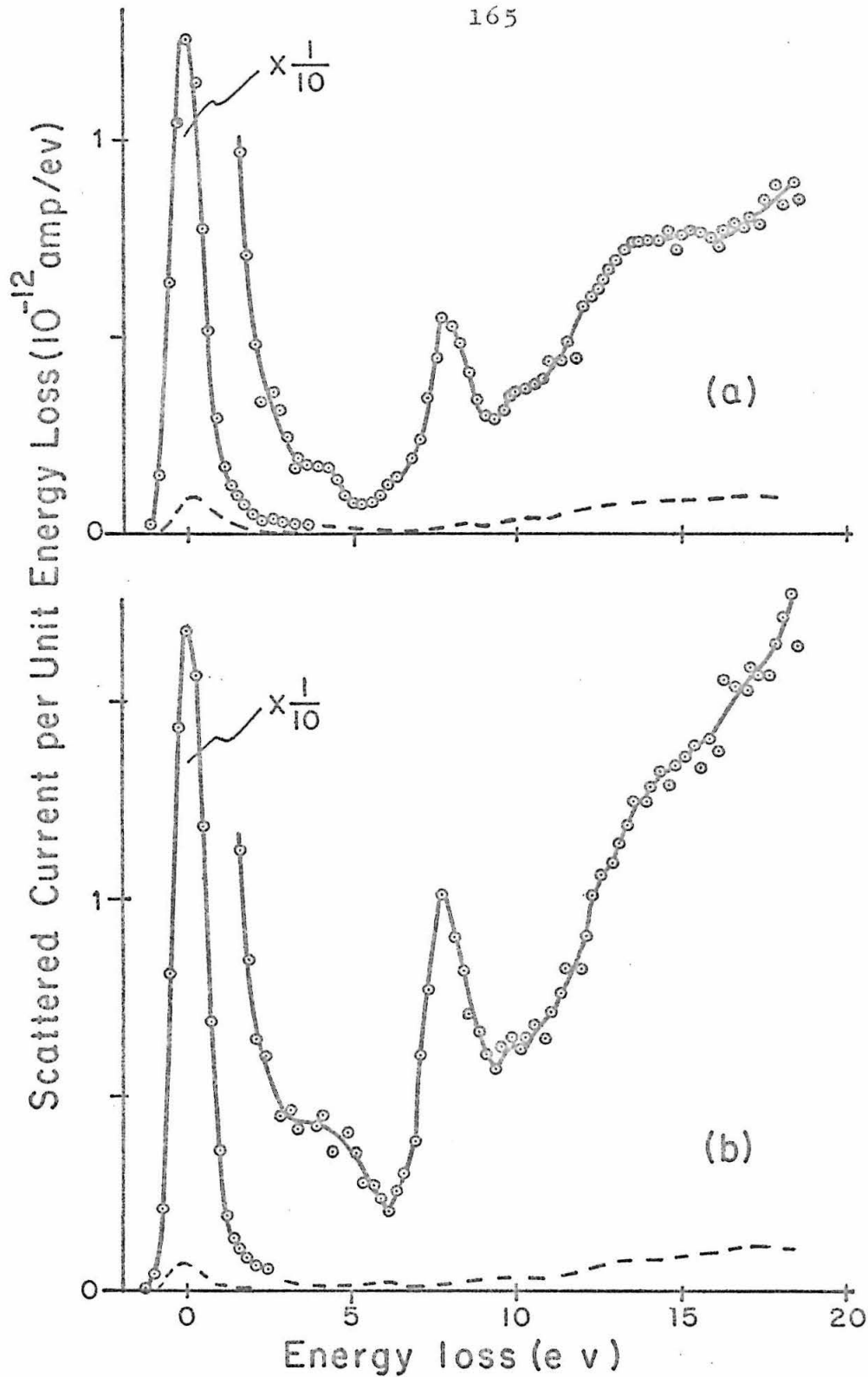


Figure 25. 90° Electron impact spectra of ethylene with electron beam energies of a) 50, b) 40, c) 35, and d) 30 ev.  $i_{BC} = 1.15 \times 10^{-7}$  amp,  $P_{SC} = 8 \times 10^{-4}$  torr. Dashed curves are blank runs with  $P_{SC} = 4 \times 10^{-6}$  torr.

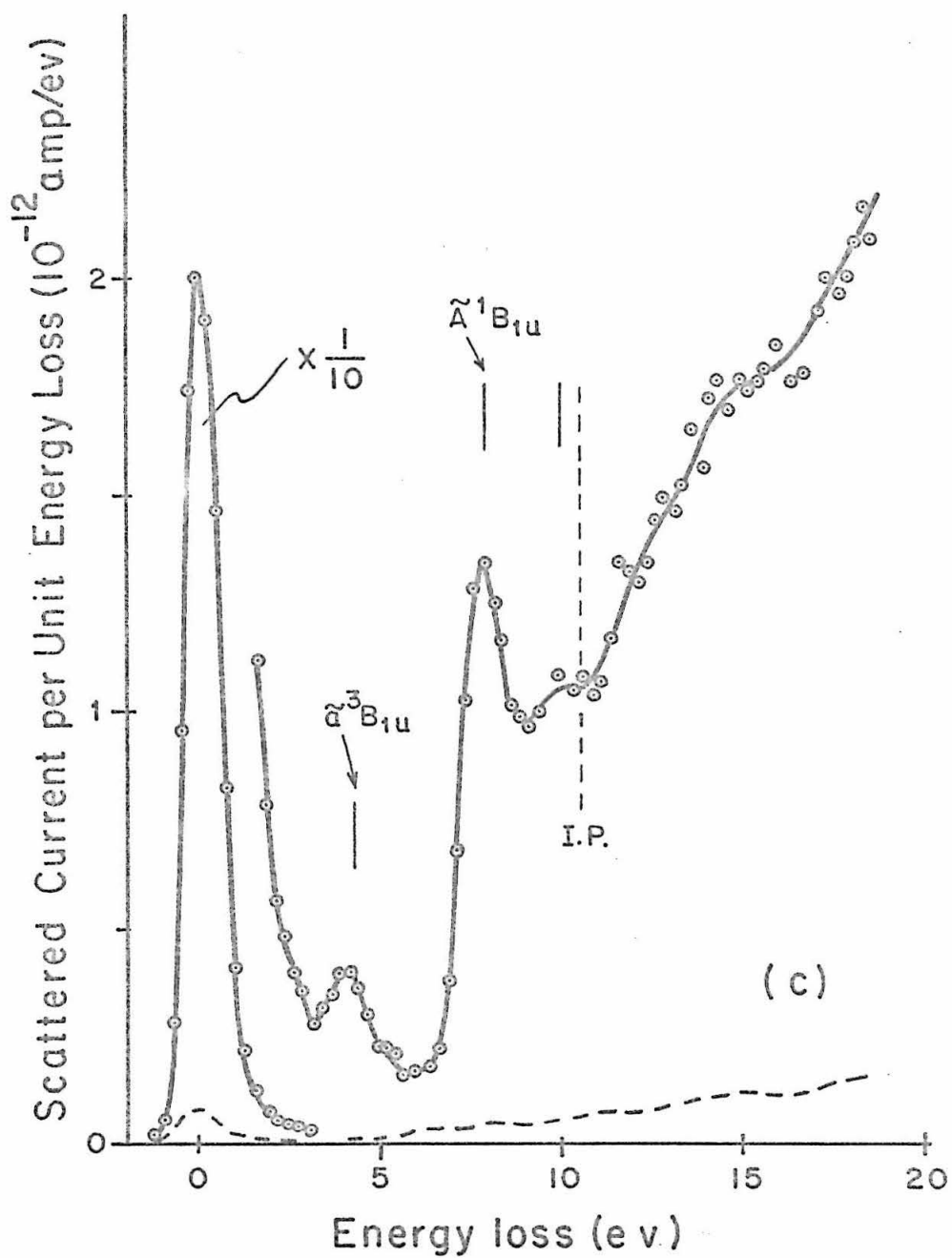


Figure 25. ( Continued )

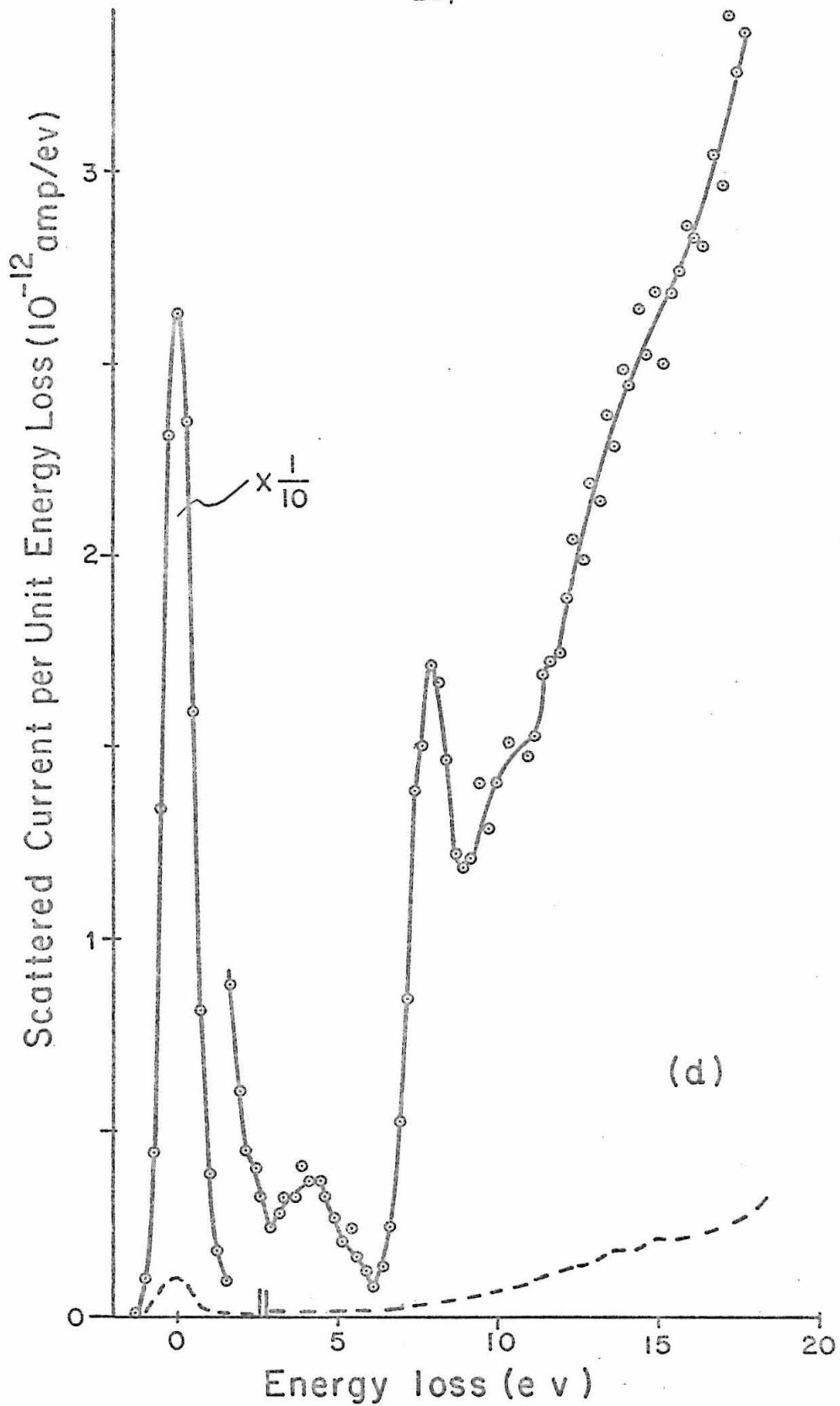


Figure 25. ( Continued )

does show up). This is in agreement with the work by Bowman and Miller<sup>(51)</sup> and with that by Doering<sup>(58)</sup>, and as mentioned above, in disagreement with the work of Kuppermann and Raff<sup>(54,55)</sup>.

From these results, we conclude that the general characteristics of the electron impact spectrum of ethylene (a polyatomic molecule) do not differ drastically from those of an atom or a diatomic molecule. Forbidden transitions much weaker or not observed in the 0° electron impact and ultraviolet absorption work can be observed by low energy electron impact at a 90° scattering angle.

V.6. Acetylene

$C_2H_2$  has 14 electrons and is isoelectronic with  $N_2$  and CO. The ground state of acetylene is a  $\tilde{X}'\Sigma_g^+$  state which is known to be linear and have a  $D_{\infty h}$  symmetry<sup>(89)</sup>.

Ultraviolet absorptions of acetylene in the gas phase have been studied by Ingold and King in the wavelength region between 2100 and 2500 Å<sup>(103)</sup>, by Innes in the region 1790-2470 Å<sup>(104)</sup>, by Nakayama and Watanabe in the region 1050-2000 Å<sup>(105)</sup> by Wilkinson in the region 1280-1520 Å<sup>(106)</sup>, and by Price<sup>(107)</sup> and Moe and Duncan<sup>(108)</sup> in the region 1050-1520 Å.

The near UV absorption of acetylene commences very weakly (observable with a 20 meter-atm path<sup>(103)</sup>) at about 5.23 ev and continues with increasing strength to about 6.0 ev. The average oscillator strength of the transition in this region is less than  $f = 10^{-4}$ <sup>(103)</sup> which is much weaker than an ordinary electric dipole allowed transition ( $f \geq 0.1$ ).

The assignment of the weak UV absorption band of acetylene has been of interest to spectroscopists for many years. When Herzberg<sup>(109)</sup> first studied the UV absorption of  $C_2H_2$  in 1931, he suggested that the weak absorption band below 6 ev might be due to a transition to the lowest triplet state of acetylene in resemblance to the nitrogen  $A^3\Sigma_u^+ \leftarrow X^1\Sigma_g^+$  transition. In 1953 Ingold and King<sup>(103)</sup> performed an extensive vibrational and rotational analysis of the 5.23 ev band. They were able to show that the first excited state of acetylene had a trans-bent geometry ( a  $D_{2h}$  symmetry ) instead of being linear. The weak intensity was explained as due to a "Franck-Condon forbidden" transition because the change of geometry was so drastic that the 0-0 transition was far from being a

"vertical" transition. The presence of weak bands with  $\Delta k=0, \pm 2$ , in addition to the allowed  $\Delta k=\pm 1$  bands in the 5.23 ev transition of acetylene observed by Ingold and King<sup>(103)</sup> and by Innes<sup>(104)</sup> recently led Herzberg<sup>(110)</sup> once more to think that this must be considered as strong evidence that the upper state was a triplet state. However, in 1965 Hougen and Watson<sup>(111)</sup> argued against the triplet-singlet assignment since no Zeeman splitting was observed in a magnetic field, contrary to the way a spin-forbidden transition should behave. They showed that the forbidden subbands with  $k=0, \pm 2$ , occurring in the 5.23 ev system of acetylene could be satisfactorily explained by an axis-switching effect. It appears that the linear-to-bent  $\tilde{A}'\text{Au} \leftarrow \tilde{X}'\Sigma_g^+$  assignment for the 5.23 ev system of acetylene is the most convincing assignment at the present time.

The second weak UV absorption system of acetylene, lying between 6 and 8 ev and peaking at 7.3 ev, consists of unassigned, complicated diffuse bands<sup>(105,106)</sup>. There was speculation that this system was the vertical transition part of the  $\tilde{A} \leftarrow \tilde{X}$  system<sup>(112)</sup>. However, Herzberg<sup>(109)</sup> suggested that this 7.3 ev transition in acetylene might correspond to the Lyman-Birge-Hopfield ( $a'\pi_g \leftarrow X'\Sigma_g^+$ ) bands of nitrogen, and listed this 6 to 8 ev system of acetylene as the  $\tilde{B} \leftarrow \tilde{X}$  transition<sup>(89)</sup>.

In 1935 Price<sup>(107)</sup> first observed two strong Rydberg series starting at 8.15 ev and 9.24 ev (the  $\tilde{C}$  and  $\tilde{D}$  states, respectively, both linear). In 1958 Wilkinson<sup>(106)</sup> studied the vacuum UV absorptions between 6 and 10 ev under high resolution and found onsets of transitions starting at 9.25 and 9.26 ev of a non-Rydberg nature (the  $\tilde{E}$  and  $\tilde{F}$  states, respectively, both of  $C_{2h}$  symmetry). Another absorption band lying between 9.9 and 10.7 ev (overlapping

with the Rydberg series) was observed by Nakayama and Watanabe<sup>(105)</sup>. This 9.9 eV band was resolved under higher resolution by Herzberg<sup>(110)</sup> and was shown to be of a linear  $D_{\infty h}$  symmetry (the  $G'\pi_u$  state). The first ionization potential of acetylene has been determined by both the photionization curves and the Rydberg series yielding a value of 11.41 eV<sup>(105)</sup>.

#### V.6.1. Summary of Previous Electron Impact Work

In 1964 Bowman and Miller<sup>(51)</sup> investigated the electron impact spectrum of acetylene using the trapped-electron technique (excitation near threshold). The spectrum obtained contained five bands peaking at 2.0, 6.2, 8.2, 9.2 and 10.0 eV with relative intensities of 0.34, 0.60, 1.00, 0.90, and 0.81, respectively. The last three bands seemed to correlate well with optical data. The 6.2 eV band was assigned to the  $\tilde{A} \leftarrow \tilde{X}$  transition.

Furthermore, they suggested that the assignment of the 2.0 eV maximum as excitation of a low-lying triplet state was plausible. However, a careful look shows that the low-energy inelastic peak around 2.0 eV appears in each spectrum of five different molecules presented by these authors. For ethylene and propylene the low-energy inelastic peaks were interpreted as the formation of temporary negative-ion states. For propyne and 1-butyne the peak around 2.0 eV was attributed as part of the tail of the elastic peak. For the case of acetylene, oddly enough, the 2.0 eV peak was assigned to the lowest triplet state. It seems therefore to us that this assignment is not reliable. Unfortunately, in studying the role of the triplet excited states in the formation and thermal conversions of acetylene, several authors<sup>(113)</sup> seriously

considered this questionable 2.0 ev assignment as a basis for their arguments.

There seem to be no other inelastic electron impact studies on acetylene appearing in the literature except the recent work by Trajmar, Kuppermann and Rice,<sup>(114)</sup> Using a high-resolution low-energy electron impact spectrometer similar to that developed by Simpson<sup>(40)</sup>, they studied the electron impact spectrum of acetylene at several scattering angles and at different beam energies with a resolution of about 0.1 ev. In a 45 ev, 10° spectrum of acetylene, transitions from the ground state to the  $\tilde{B}$  state (peaking at 7.25 ev), to the  $\tilde{C}$  Rydberg state (starting at 9.3 ev), to the unresolved  $\tilde{D}$  Rydberg state and the  $\tilde{E}$ ,  $\tilde{F}$  non-Rydberg states (starting at 9.3 ev), and to the  $\tilde{G}'\pi_u$  state (starting at 9.95 ev) were observed. The strongest peaks were the 9.3 and the 8.15 ev transitions. The ratio of intensity of the  $\tilde{B}$  state to the  $\tilde{C}$  state was about 0.043. The spectrum agreed very well with the vacuum ultraviolet absorption spectrum reported by Nakayama and Watanabe<sup>(105)</sup> in the wavelength region 1050-2000 Å.

Further 40 ev electron impact spectra at larger angles obtained at higher sensitivity showed a weak transition peaking at about 5.3 ev. The intensity of the Rydberg transition  $\tilde{C} \leftarrow \tilde{X}$  decreased very rapidly as the scattering angle increased while the  $\tilde{B} \leftarrow \tilde{X}$  transition at 7.25 ev decreased less rapidly with increasing angle. The 5.3 ev transition, on the other hand, had much less angular dependence, so that its intensity relative to the  $\tilde{C} \leftarrow \tilde{X}$  transition became larger with increasing scattering angle from 20° to 60°. Therefore, this transition has the characteristics of an spin-forbidden transition while the  $\tilde{B} \leftarrow \tilde{X}$  system is similar to an electric quadrupole allowed transition.

From the broad envelope of the 40 ev, 60° acetylene spectrum in the energy loss region between 5 and 7.25 ev, Trajmar, Kuppermann and Rice,<sup>(114)</sup> suggested that there might exist another unresolved state between the  $\tilde{A}$  and the  $\tilde{B}$  states, peaking at about 6.2 ev, which also has triplet characteristics. However, further theoretical support and experimental evidence are needed to confirm this hypothesis.

#### V.6.2. The Electron Impact Spectra of Acetylene

Figure 26 shows the 90° electron impact spectra of acetylene with electron beam energies of 50, 40, 35, and 30 ev. The sample gas is from a tank of purified acetylene from the Matheson Company.

The spectrum is characterized by two bands peaking at 5.9 and 9.4 ev. The 9.4 ev band, starting from about 8.0 ev, is the most intense inelastic peak in the spectrum. This band may be correlated with the unresolved  $\tilde{C}$ ,  $\tilde{D}$ ,  $\tilde{E}$  and  $\tilde{F}$  states. It is noted that, the differential cross sections at 90° for inelastic scattering from the  $\tilde{C}$  and  $\tilde{D}$  Rydberg states of acetylene seem to be very small. (Similar results have been observed for ethylene).

From Figure 26 we see that the 5.9 ev band gains intensity relative to the 9.4 ev one with decreasing beam energies and it is unusually broad (extending from 4.5 to 7.2 ev). The full-width at half-maximum of the elastic peak is 1.1 ev which represents the resolution of our instrument. Thus the observed broad band is not a result of this resolution only but includes the effect of the shape of the Franck-Condon envelope for the transitions involved in this region.

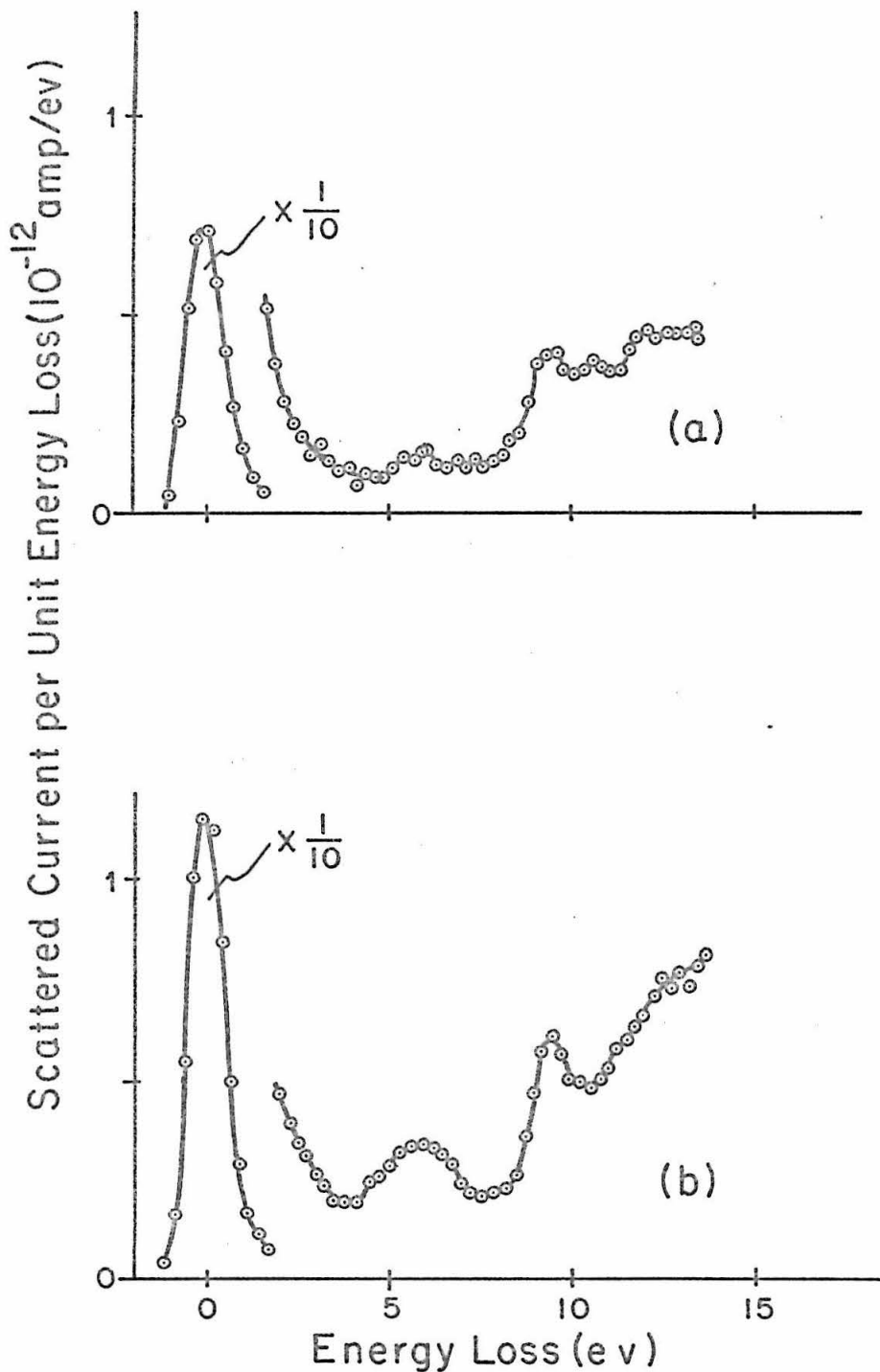


Figure 26. 90° Electron impact spectra of acetylene with electron beam energies of a) 50, b) 40, c) 35, and d) 30 ev.  $i_{BC}=1.30 \times 10^{-7}$  amp,  $P_{SC}=4.3 \times 10^{-4}$  torr.

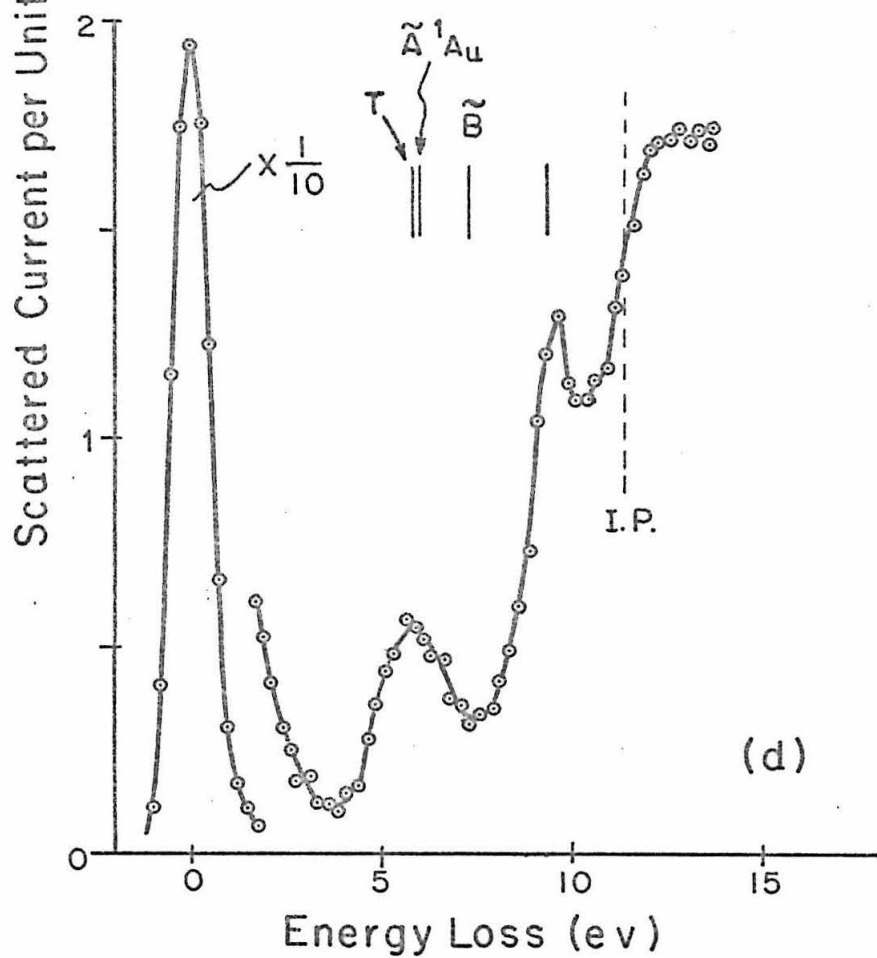
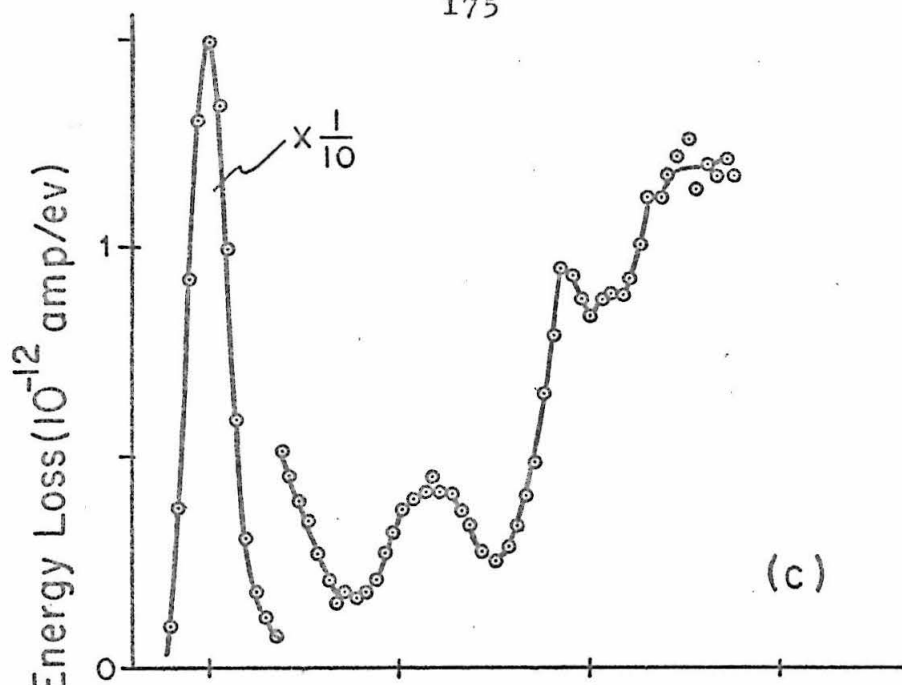


Figure 26. ( Continued )

It is noted that in the work by Bowman and Miller (51), the 6.2 ev band in the trapped-electron spectrum of  $C_2H_2$  also extends between 4.5 and 7.2 ev while their resolution is about 0.25 ev.

From the present work, we may conclude that we have observed a transition (or more than one unresolved transitions) in  $C_2H_2$  at 5.9 ( $\pm 0.2$ ) ev which shows characteristics similar to a spin-forbidden transition.

The results of this experiment do not exclude the possibility that the observed 5.9 ev band is different from the weak  $\tilde{A}'A_u \leftarrow \tilde{X}'\Sigma_g^+$  transition observed optically (103,104,111). In UV absorptions the intensity of the  $\tilde{A} \leftarrow \tilde{X}$  system relative to the  $\tilde{C} \leftarrow \tilde{X}$  Rydberg system is less than  $10^{-4}$ . If the  $\tilde{A} \leftarrow \tilde{X}$  system is a Franck-Condon forbidden transition in optical spectroscopy then it should also be Franck-Condon forbidden in electron scattering at each scattering angle, and would be expected to be weak compared to the  $\tilde{C} \leftarrow \tilde{X}$  transition even at  $90^\circ$ . Therefore, it is consistent with all of the known facts to assume that the transition we observe peaking at 5.9 ev is a triplet, whereas the weak optical one peaking at about 5.3 ev is the  $\tilde{A}'A_u \leftarrow \tilde{X}'\Sigma_g^+$  singlet one.

V.7. Propyne

Propyne is often called methyl acetylene. It has been shown by Franklin and Field<sup>(115)</sup> in electron impact ionization studies that alkyl substitutions on the acetylene molecule lead to lowering of the ionization potential. For example, the first ionization potentials they obtained for acetylene, propyne, 1-butyne, and 2-butyne are 11.46, 10.48, 10.34 and 9.85 ev, respectively. The lowering of the ionization potential is explained as due to a hyperconjugation effect between the  $C\equiv C$  triple bond and the substituted alkyl group. It is therefore of interest to study the electron scattering spectra of propyne in order to compare it with the results obtained for acetylene.

Propyne is transparent to near ultraviolet light. So far there seems to exist no high sensitivity UV absorption work on this molecule for the wavelength region longer than 2000 Å. In 1945 Price and Walsh<sup>(116)</sup> first investigated photographically the vacuum UV absorption of propyne in the region 960-2040 Å. Two Rydberg series starting at 8.05 and 9.11 ev were obtained which converged to an ionization potential of 11.30 ev. Furthermore, two weak bands peaking separately at 6.45 and 7.64 ev were observed (referred to as the  $\tilde{A}$  and the  $\tilde{B}$  states by Herzberg<sup>(89)</sup>). However, Price and Walsh's observation was not confirmed by subsequent electron impact ionization measurements<sup>(115)</sup> and other vacuum UV absorption work<sup>(117,105)</sup>.

In 1956 Watanabe and Namioka<sup>(117)</sup> determined the ionization potential of propyne by the photo-ionization method. They also studied photoelectrically the absorption spectrum in the region 1200-1600 Å. Two Rydberg series different from those of Price and Walsh<sup>(116)</sup> were obtained. Both the photo ionization curve and the Rydberg series

yielded the same ionization potential of 10.36 eV, in agreement with electron impact results.

In 1964 Nakayama and Watanabe<sup>(105)</sup> reported further UV absorption work on acetylene, propyne, and 1-butyne in the region 1050-2000 Å by a photoelectric technique. This work represents the most reliable UV measurements on propyne that we are aware of.

According to it, propyne starts to absorb very weakly at about 6.2 eV. The absorption intensity increases to a maximum at 7.04 eV and is joined by a continuum. Strong and discrete absorption peaks start at 7.85 eV (the  $\tilde{C}$  state). Other strong peaks between 8 and 10 eV can be assigned to three Rydberg series starting at 8.05, 8.45, and 8.83 eV (referred to by Herzberg<sup>(89)</sup> as the  $\tilde{D}$ ,  $\tilde{E}$ , and  $\tilde{F}$  states, respectively). All three Rydberg series converge to the same ionization continuum starting at 10.36 eV.

Although none of the excited states of propyne has been fully analyzed, there seems to be little doubt that the Rydberg series do arise from the excitation of a  $\pi$ -electron of the  $C\equiv C$  bond. After all, the propyne spectrum closely resembles the spectra of acetylene and 1-butyne.

#### V.7.1. Summary of Previous Electron Impact Work

In 1965 Bowman and Miller<sup>(51)</sup> studied the electron impact spectrum of propyne by the trapped-electron technique. Two bands peaking at 7.1 and 8.3 eV with relative intensities of 1.00 and 0.93, respectively, were observed. A shoulder starting at 4.5 eV joined the 7.1 eV band at about 6.1 eV with a relative intensity of 0.71. Another small band peaking at 2.8 eV was attributed to the tail of

the elastic peak.

We see from the trapped-electron spectrum of propyne that the 7.1 ev band may be correlated with the 7.04 ev UV absorption maximum observed by Nakayama and Watanabe<sup>(105)</sup>. The 8.3 ev band may correspond to the unresolved  $\tilde{D}$  and  $\tilde{E}$  states. However, the broad shoulder between 4.5 and 6.1 ev has not been observed optically. Bowman and Miller<sup>(51)</sup> gave no explanation for the occurrence of this low-energy shoulder either.

#### V.7.2. The Electron Impact Spectra of Propyne

Figure 27 shows the 90° electron impact spectra of propyne with electron beam energies of 50, 40, 35, and 30 ev. The gas sample is obtained from a lecture bottle of C.P. grade methyl acetylene from the Matheson Company. An analysis by A.L. Lane<sup>(118)</sup> shows that it contains 1.9% of propylene, 1.8% of acetylene, 0.19% of allene and trace amounts of other impurities.

The main features of the propyne spectrum consist of a continuum starting at about 7.5 ev with increasing intensity towards higher energy loss region. This continuum is very similar to that observed for propane, a saturated hydrocarbon (see Figure 29). As in the cases for ethylene and acetylene, no Rydberg transitions seem to have large differential cross sections at 90°.

Very strikingly, a band between 4.5 and 7.0 ev shows up with increasing intensity relative to the continuum when one goes to lower and lower beam energies. This band, peaking at about 5.9(±.2) ev, is small in intensity compared to the 5.9 ev band in the acetylene spectrum (Figure 26) under similar experimental conditions. Since the scattered

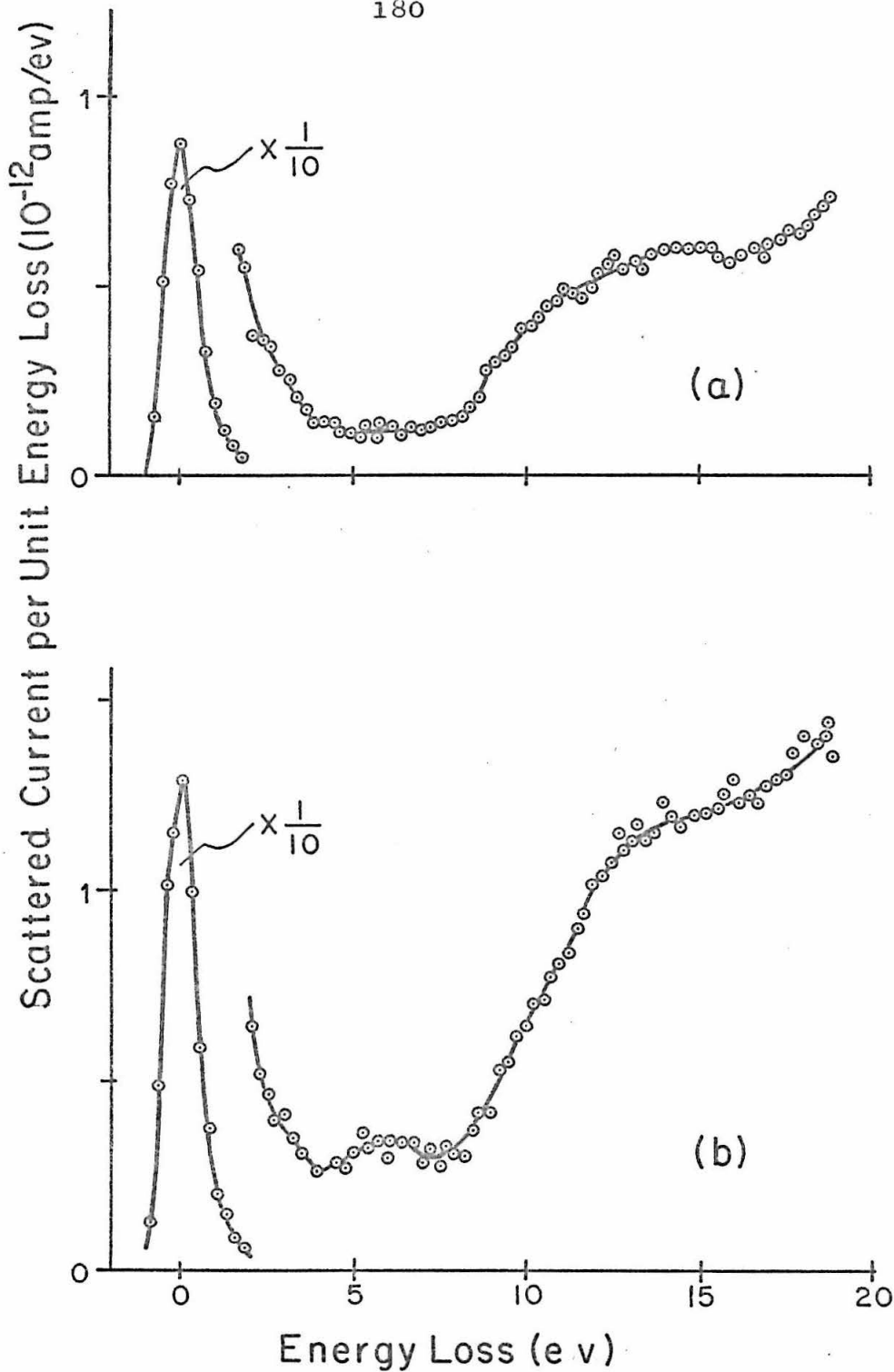


Figure 27. 90° Electron impact spectra of propyne with electron beam energies of a) 50, b) 40, c) 35, and d) 30 eV.  $i_{BC} = 1.50 \times 10^{-7}$  amp,  $P_{SC} = 4 \times 10^{-4}$  torr.

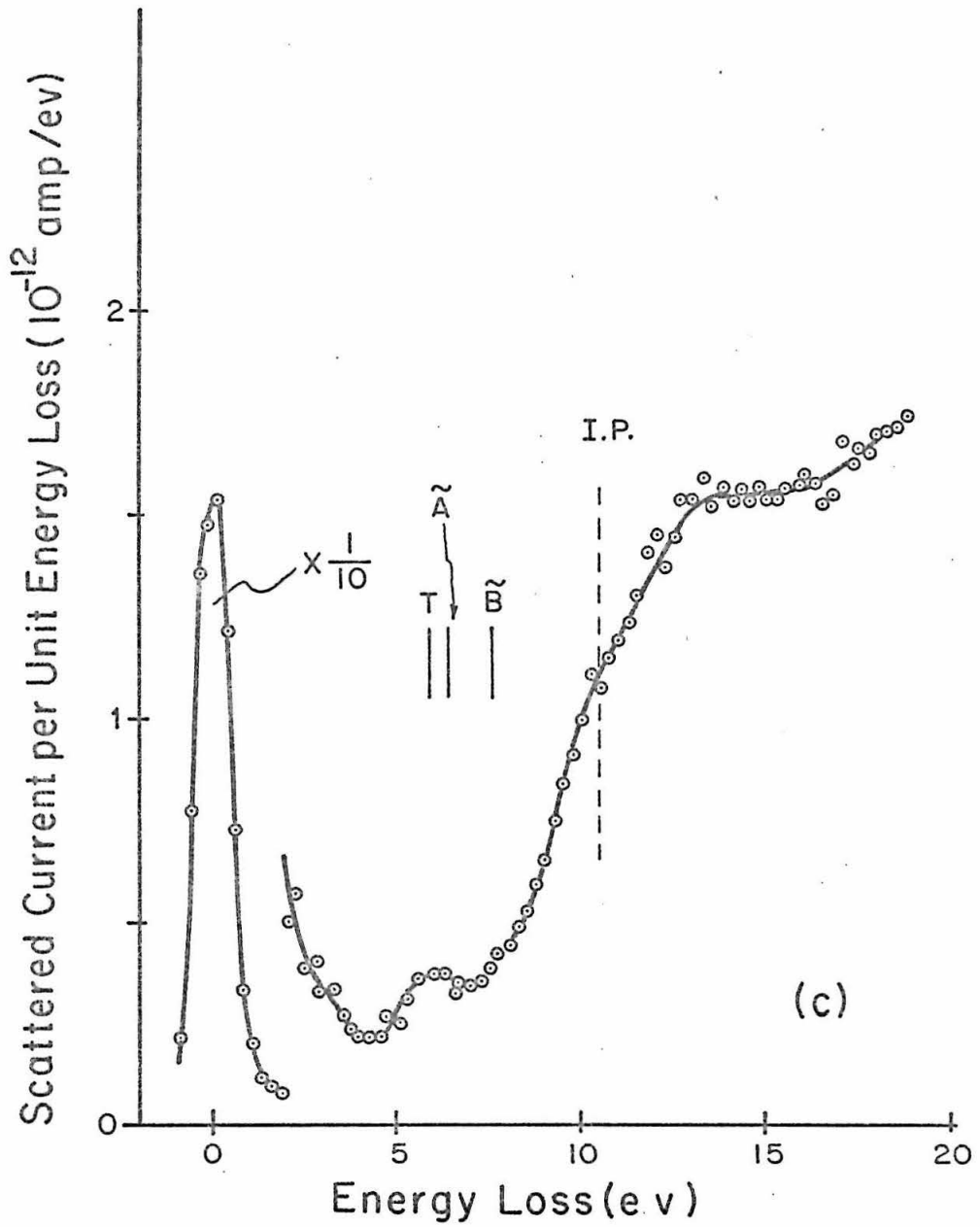


Figure 27. ( Continued )

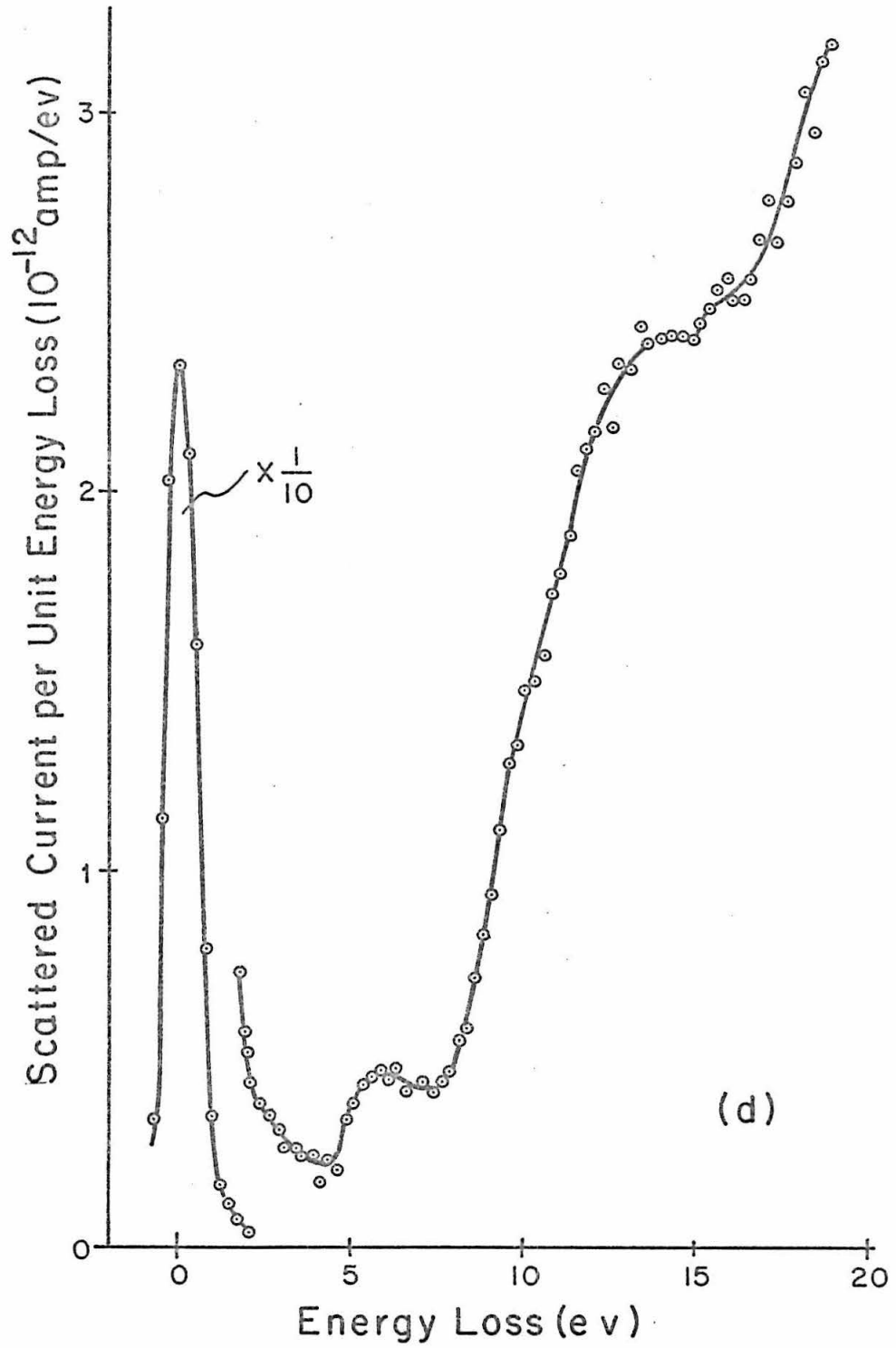


Figure 27. ( Continued )

signal from  $C_2H_2$  has a known magnitude, it seems unlikely that the 5.9 eV band in the propyne spectrum could be due to the 1.8% impurity of  $C_2H_2$ .

The ground state of propyne is an  $\tilde{X}^1A_1$  state with  $C_{3v}$  symmetry<sup>(89)</sup>. The energy dependence of the 5.9 eV band leads us to the conclusion that it is due to a singlet-triplet transition. In the trapped-electron spectrum obtained by Bowman and Miller<sup>(51)</sup>, the 6.1 eV shoulder may be correlated with this band. From this experiment we feel that we have successfully demonstrated the powerfulness of the technique of performing an energy dependence study at large scattering angles of the electron impact spectra in order to distinguish spin-forbidden transitions from allowed ones.

In adding a methyl group to the acetylene molecule, although the first ionization potential is lowered by about 1 eV, the first Rydberg transition is only lowered by 0.1 eV (The  $\tilde{C}$  state of  $C_2H_2$  start at 8.15 eV while the  $\tilde{D}$  state of  $CH_3C\equiv CH$  starts at 8.05 eV), whereas the triplet state is not shifted to within  $\pm 0.2$  eV. These results indicate that the methyl group does not have a large effect on the  $\pi$ -electron system of the  $C\equiv C$  bond, as far as the lowest excited states are concerned.

V.8. Propadiene

Propadiene is also called allene. This is the smallest molecule that has two adjacent carbon-carbon double bonds. The ground state of propadiene ( $\tilde{X}'A_1$ ) is believed to have a  $D_{2d}$  symmetry with the two  $CH_2$  planes at  $90^\circ$  to each other<sup>(89)</sup>. Accurate bond parameters of this molecule have been obtained from an analysis of the vibrational-rotational bands measured with high resolution by Maki and Toth<sup>(119)</sup>. Its physical and chemical properties have been reviewed by Griesbaum<sup>(120)</sup>.

The vacuum ultraviolet absorption spectrum of allene has been studied photographically by Sutcliffe and Walsh<sup>(121)</sup> in the region 1150-2150 Å. It starts to absorb very weakly at about 6.1 ev. This weak absorption extends continuously to about 7.0 ev, and is referred to by Herzberg<sup>(89)</sup> as the  $\tilde{A} \leftarrow \tilde{X}$  transition. The most intense absorption occurs between 7.16 and 7.8 ev (with a maximum at 7.25 ev), and is referred to as the  $\tilde{B} \leftarrow \tilde{X}$  system. In view of the large intensity, the  $\tilde{B} \leftarrow \tilde{X}$  system must be an allowed transition. At higher energies, moderately strong bands occur at 8.02, 8.15, 8.31, and 8.40 ev, and are referred to as excitations to the  $\tilde{C}, \tilde{D}, \tilde{E}$ , and  $\tilde{F}$  electronic states, respectively<sup>(89)</sup>. More bands lying between 8.55 and 9.90 ev with decreasing intensity towards the high energy side have the appearance of Rydberg bands. The first ionization potential of 10.19 ev is obtained from an extrapolation of the Rydberg series<sup>(121)</sup>.

According to Sutcliffe and Walsh<sup>(121)</sup>, precise measurements were difficult partly because of the diffuseness of the bands and partly because of the presence of emission lines in the Lyman continuum. Nevertheless, these authors were able to arrange the observed bands into 9 Rydberg series

(some of them were fragmentary) converging to the same ionization limit. Five of the Rydberg series were made to join the electronic states  $\tilde{B}$  to  $\tilde{F}$ .

So far the complicated UV absorption spectrum of allene has not been satisfactorily assigned because of the possibility of changing geometry in excited states. For example carbon dioxide, which is isoelectronic with allene, has low-lying excited states with a bent  $C_{2v}$  symmetry while the ground state of  $CO_2$  is linear<sup>(89)</sup>.

#### V.8.1. Summary of Theoretical Calculations

There have been several theoretical calculations on the electronic structure and low-lying excited states of allene. We will briefly mention the results of these calculations in order to understand this molecule better.

In 1951 Parr and Taylor<sup>(122)</sup> performed an LCAO self-consistent field calculation of the twisting frequency and  $\pi$ -electron energy levels of allene. The C-C-C skeleton was assumed to be linear. The two  $CH_2$  planes undergo a twisting vibration with respect to each other about an equilibrium angle of  $90^\circ$  (a  $D_{2d}$  symmetry). The molecule was treated as a four  $\pi$ -electron system with the effects of the underlying single-bonded structures represented by an effective potential. From the calculated results, they predicted a mean value of the first allowed singlet absorption band and the companion triplet lying near 5.1 eV. They also predicted the first ionization potential of allene to be about 10.4 eV which was not too far from the spectroscopic value of 10.19 eV.

In 1956 Serre<sup>(123)</sup> did some calculations on the  $\pi$ -electron systems of several poly-unsaturated hydrocarbons

in which he used the molecular orbital method developed by Pariser and Parr<sup>(124)</sup>. The transition from the ground state to the first allowed singlet state was predicted to lie between 5.95 and 7.35 eV, depending on different choices for the value of a resonance integral  $\beta$ . Again, a linear C-C-C configuration and a  $D_{2d}$  symmetry were assumed.

In 1966 Borden<sup>(125)</sup> carried out a Pariser-Parr-Pople<sup>(124,126)</sup> type calculation to determine the energies of the electronic states in two conformations of allene. These were of  $D_{2d}$  and  $D_{2h}$  symmetries with the two  $CH_2$  planes being perpendicular and coplanar, respectively. Correlation diagrams of singlet states and triplet states between these two configurations were shown. He predicted that, the lowest triplet state was planar.

From Borden's results<sup>(125)</sup>, the first allowed singlet excited state would lie at about 7.9 eV above the ground state in the perpendicular conformation. The lowest triplet state, lying at 2.7 eV above the ground state in the planar form, may be correlated to a vertical transition energy of 4.3 eV above the ground state in the perpendicular form.

#### V.8.2. Electron Impact Spectra of Propadiene

Figure 28 shows the  $90^\circ$  electron impact spectra of propadiene with electron beam energies of 50, 40, 35, and 30 eV. The gas sample is taken from a lecture bottle of research grade allene from the Matheson Company. An analysis by A.L. Lane<sup>(118)</sup> shows that it contains 0.62% of propylene and trace amounts of other impurities.

The main features of the spectrum, containing slightly resolved bands peaking at 7.6, 8.7, and 9.5 ( $\pm 0.2$ ) eV may be attributed to transitions to the  $\tilde{B}$ ,  $\tilde{C}$ ,  $\tilde{D}$ ,  $\tilde{E}$  and

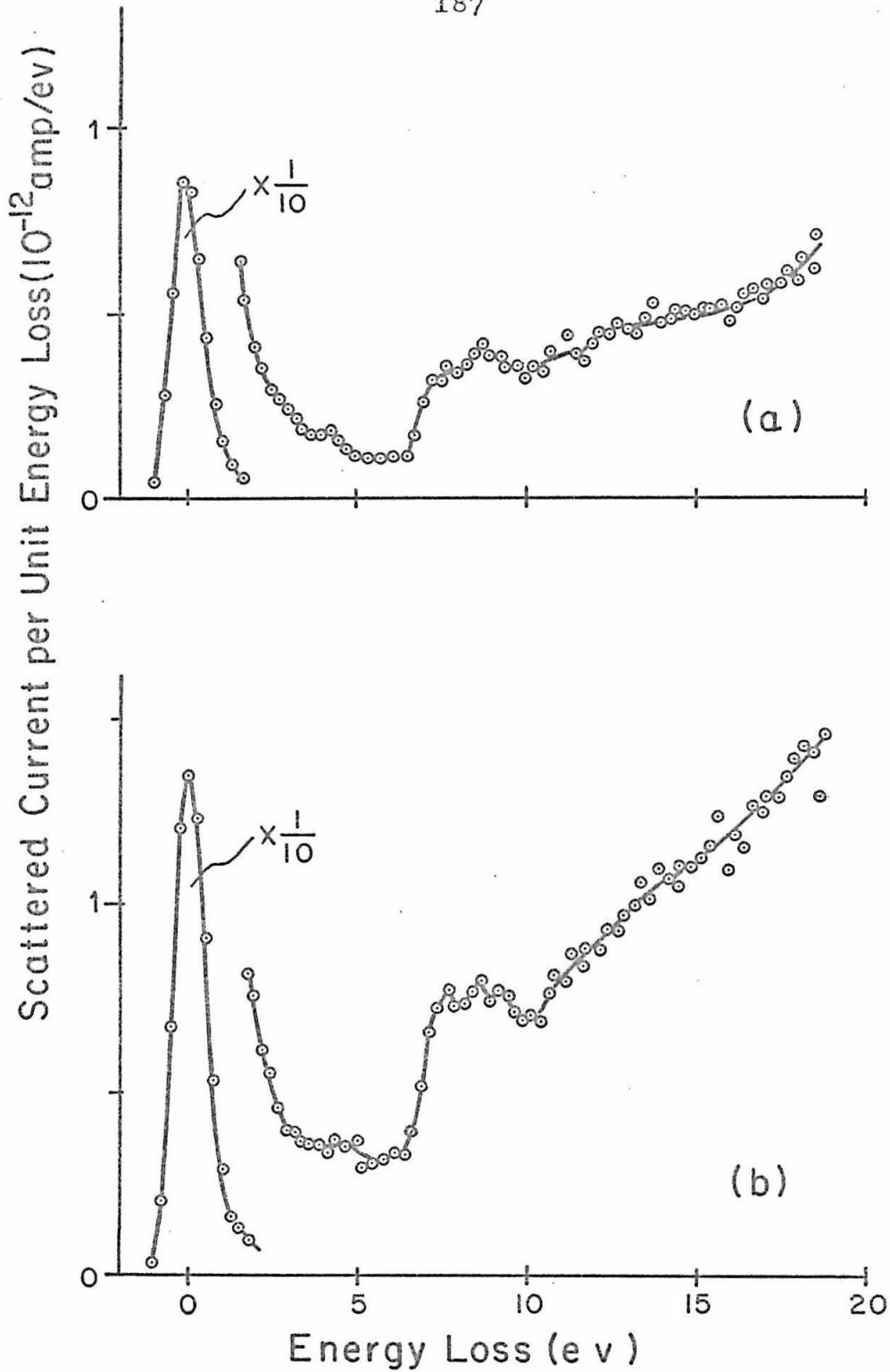


Figure 28. 90° Electron impact spectra of propadiene with electron beam energies of a) 50, b) 40, c) 35, d) 30 ev.  $i_{BC}=1.4 \times 10^{-7}$  amp,  $P_{SC}=4 \times 10^{-4}$  torr.

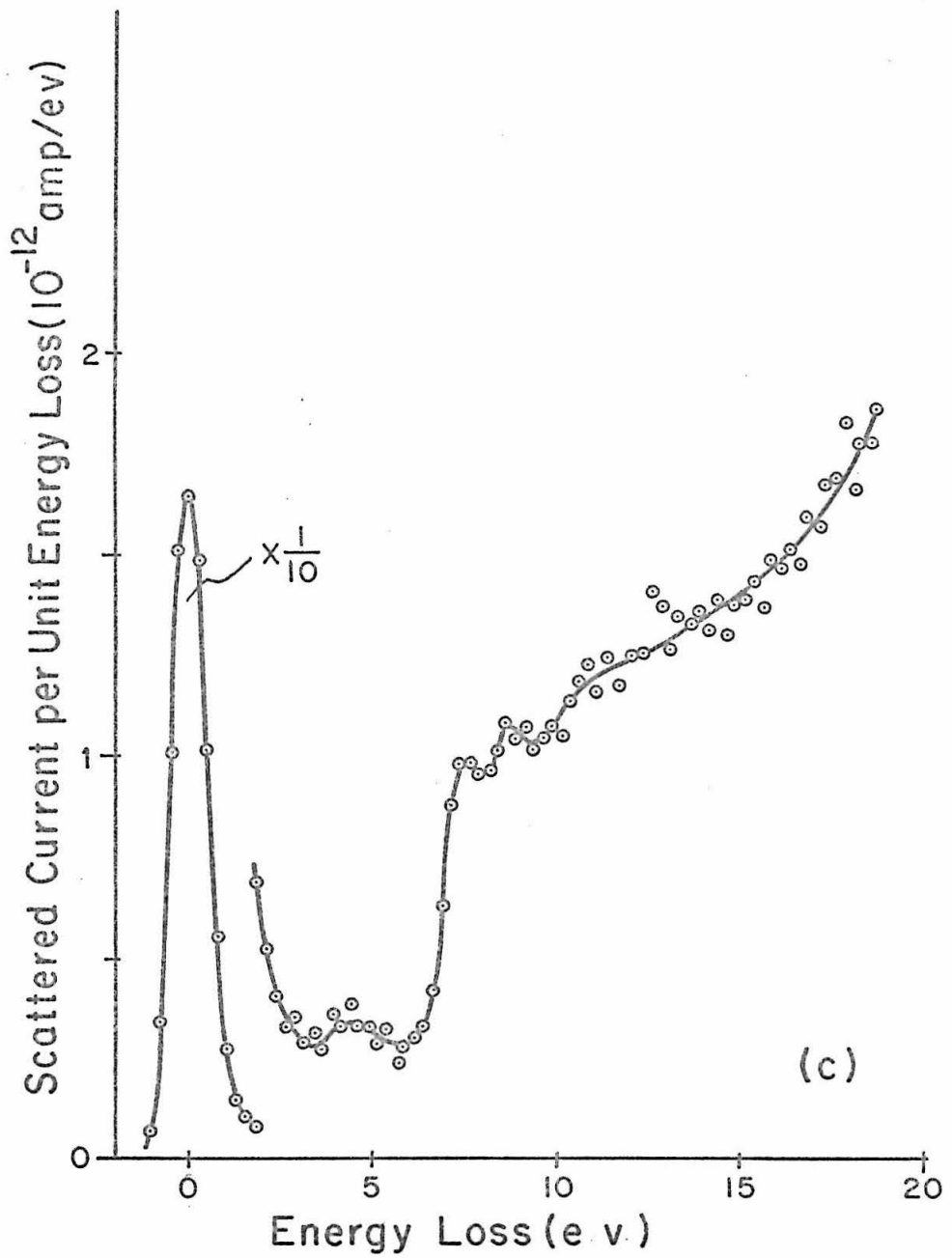


Figure 28. ( Continued )

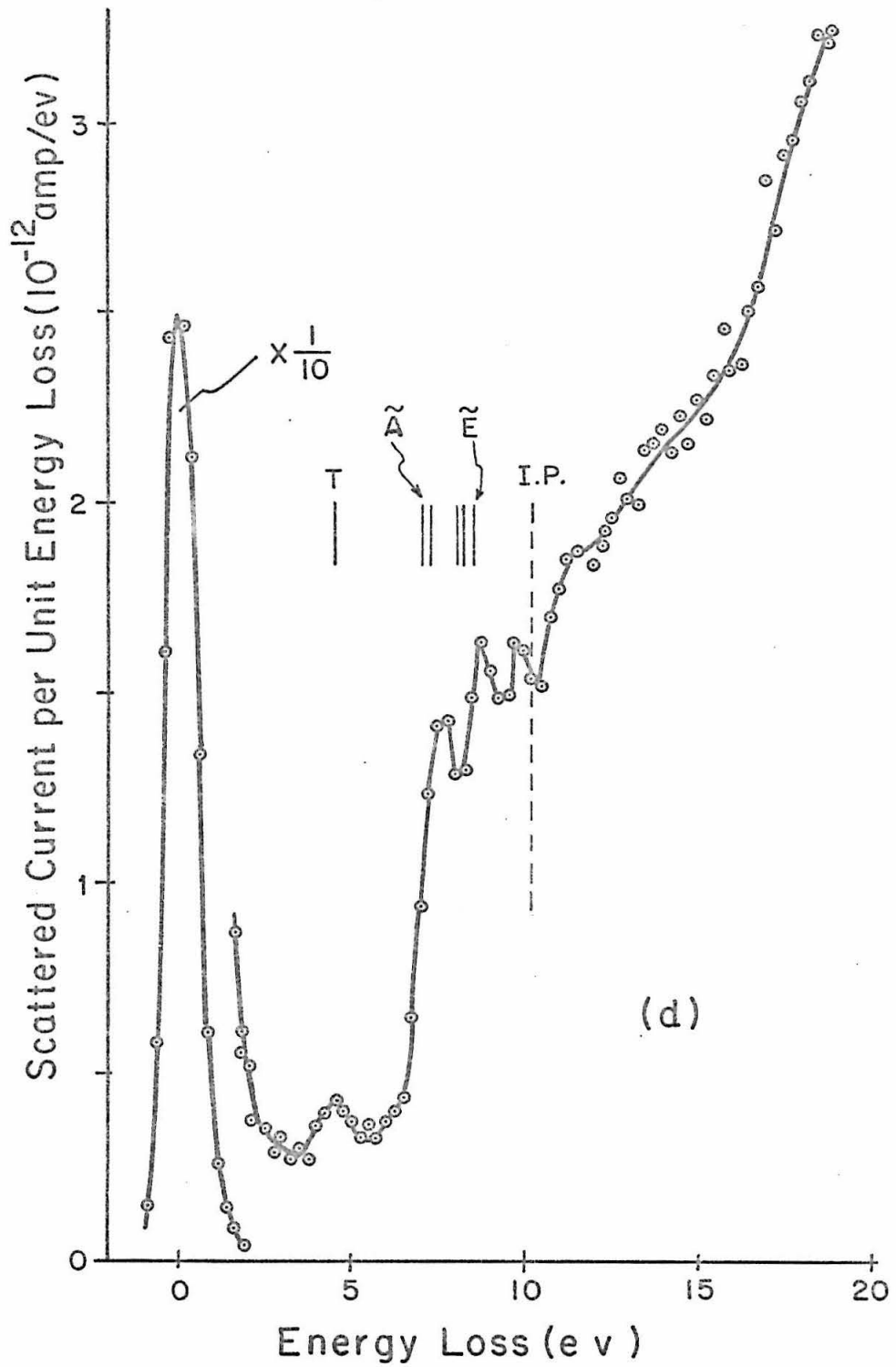


Figure 28. ( Continued )

$\tilde{F}$  states. The 7.6 eV band has an onset at about 6 eV which may include the  $\tilde{A} \leftarrow \tilde{X}$  transition of allene.

A small band peaking at about 4.5 ( $\pm 0.2$ ) eV has not been observed in ultraviolet absorptions. This band gains intensity (relative to the 7.6 eV one) with lowering beam energies, which is the correct energy dependence for spin forbidden transitions. We hereby assign this 4.5 eV band to the singlet-triplet transition in allene. This assignment is consistent with previous assignments in the 90° electron impact spectra of other unsaturated hydrocarbons.

It should be noted that although the ionization potential of allene (10.19 eV) is lower than that of ethylene (10.507 eV), its first Rydberg state ( $\tilde{E}$  state, starting at 7.16 eV) lies higher than that of ethylene ( $\tilde{E}$  state, starting at 7.10 eV). Therefore it seems reasonable that the observed triplet state in allene (at 4.5 eV) should lie slightly higher than that in ethylene (4.4 eV). However, the difference between these two values is smaller than the experimental error in their determination.

Our results of a triplet excitation band peaking at 4.5 eV are in good agreement with Borden's calculations<sup>(125)</sup>. However, the present work yields no information concerning the excited state geometry.

## V.9. Propane

Propane has no known discrete electronic spectra (89). Its ultraviolet absorption has been studied by Okabe and Becker in the wavelength region 1200-1630 Å (127), and by Schoen in the region 500-1200 Å (128).

Propane starts to absorb at about 7.6 eV with increasing intensity towards the high energy side. Onsets superimposed on a rising continuum are observed at 7.60, 8.42, 9.25 and 10.15 eV. The maximum absorption occurs at 16 eV after which the intensity decreases with decreasing wavelength. Another absorption maximum is observed at 9.52 eV.

For a resolution of about 1 Å, the absorption appears to be continuous for propane over the spectral region 1200-1630 Å (127) indicating that the upper electronic states are strongly predissociated. This may be explained by assuming that the equilibrium positions of the upper states lie at larger internuclear distances than does the ground state such that transitions from the ground state are to the repulsive part of the potential energy surfaces of the upper states (89). From the order of magnitude of the absorption coefficients ( $10^3 \text{ cm}^{-1}$ ) we would expect the transitions to be allowed ones, and probably singlet to singlet transitions.

The first ionization potential of propane has been determined to be 11.07 eV by Al-Joboury and Turner (129) using photoelectron spectroscopy.

Although the excited electronic states of alkanes have no obvious structures, there has been increasing interest in the vacuum UV photochemistry of these molecules during recent years (130). Photolyses of propane and isotopic propanes have been studied by Okabe and McNesby

with resonance lines of xenon (1470 and 1295 Å) and of krypton (1236 and 1165 Å) at room temperature<sup>(131)</sup>, by Laufer and McNesby at 1470 Å and 25°C<sup>(132)</sup>, and by Rebbert and Ausloos with resonance lines of xenon, krypton, and argon (1067 and 1048 Å) at 20°K and 77°K on solid propanes<sup>(133)</sup>. Mass spectrometric studies on various ions produced by photo ionization of propane have been performed by Schoen<sup>(128)</sup> and Berkowitz and Chupka<sup>(134)</sup>.

It appears that an investigation of the low energy electron impact spectrum of propane may give us some more information on the electronic structure of this molecule.

#### V.9.1. Summary of Previous Electron Impact Work

In 1964 Lassetre and Francis<sup>(37a)</sup> reported a 0° electron impact spectrum of propane using 390 ev beams with a resolution of about 0.6 ev. However, no interpretation was given for the spectrum.

This spectrum consists of two maxima at 13.8 and 11.3 ev and a shoulder at 9.0 ev, with the relative intensities of 1.00, 0.88 and 0.66, respectively. The onset for the 9.0 ev shoulder is at about 7.6 ev. The general feature of the impact spectrum agrees with the UV absorption except that the maximum intensity is located at 13.8 ev which is 2.2 ev lower than the corresponding UV absorption maximum<sup>(128)</sup>.

In 1965 Ehrhardt, Linder, and Meister<sup>(135)</sup> studied the inelastic scattering of 70 ev electrons (0.3 ev half width) by propane in the angular range of 0° to 145°. The scattered electron intensity from propane as a function of energy loss at scattering angles of 0°, 3°, 6°, 12°, 18°, and 27° were plotted with the intensity normalized to 100 at an arbitrarily chosen point of 16.0 ev. The 0° curve at 16.0

ev was actually 350 times higher than the  $27^\circ$  curve at the same energy loss, indicating sharply forward peaked scattering.

The 70 ev propane spectrum consists of four peaks, located at 9.0, 11.5, 13, and 14.3 ev, superimposed on a continuum. The 9.0 ev peak decreases with increasing angle so rapidly that, although at  $0^\circ$  it is the strongest peak, the 13 ev peak becomes the highest one in the spectrum at  $6^\circ$ . For scattering angles larger than  $12^\circ$ , the maximum intensity of the spectrum gradually shifts towards higher energies. The  $27^\circ$  propane spectrum shows a structureless continuum with a maximum at about 16 ev.

#### V.9.2. The Electron Impact Spectra of Propane

Figure 29 shows the  $90^\circ$  electron impact spectra of propane with electron beam energies of 50, 40, 35, and 30 ev. The gas sample is taken from a lecture bottle of research grade propane from the Phillips Petroleum Company. An analysis by A.L. Lane<sup>(118)</sup> shows that it has 0.23% of propylene, 0.02% of ethane and trace amounts of other impurities.

The propane spectrum shows a continuum with an onset at about 8 ev. The intensity of this continuum increases with the energy loss to about 13 ev then starts to level off. The 50 ev spectrum shown in Figure 29a is similar to the 70 ev,  $27^\circ$  propane spectrum obtained by Ehrhardt, Linder, and Meister<sup>(135)</sup>, i.e., the spectrum is structureless. The qualitative feature of the spectrum at  $90^\circ$  scattering angle does not change very much in going to lower energies. The results are generally consistent with optical spectroscopic data.

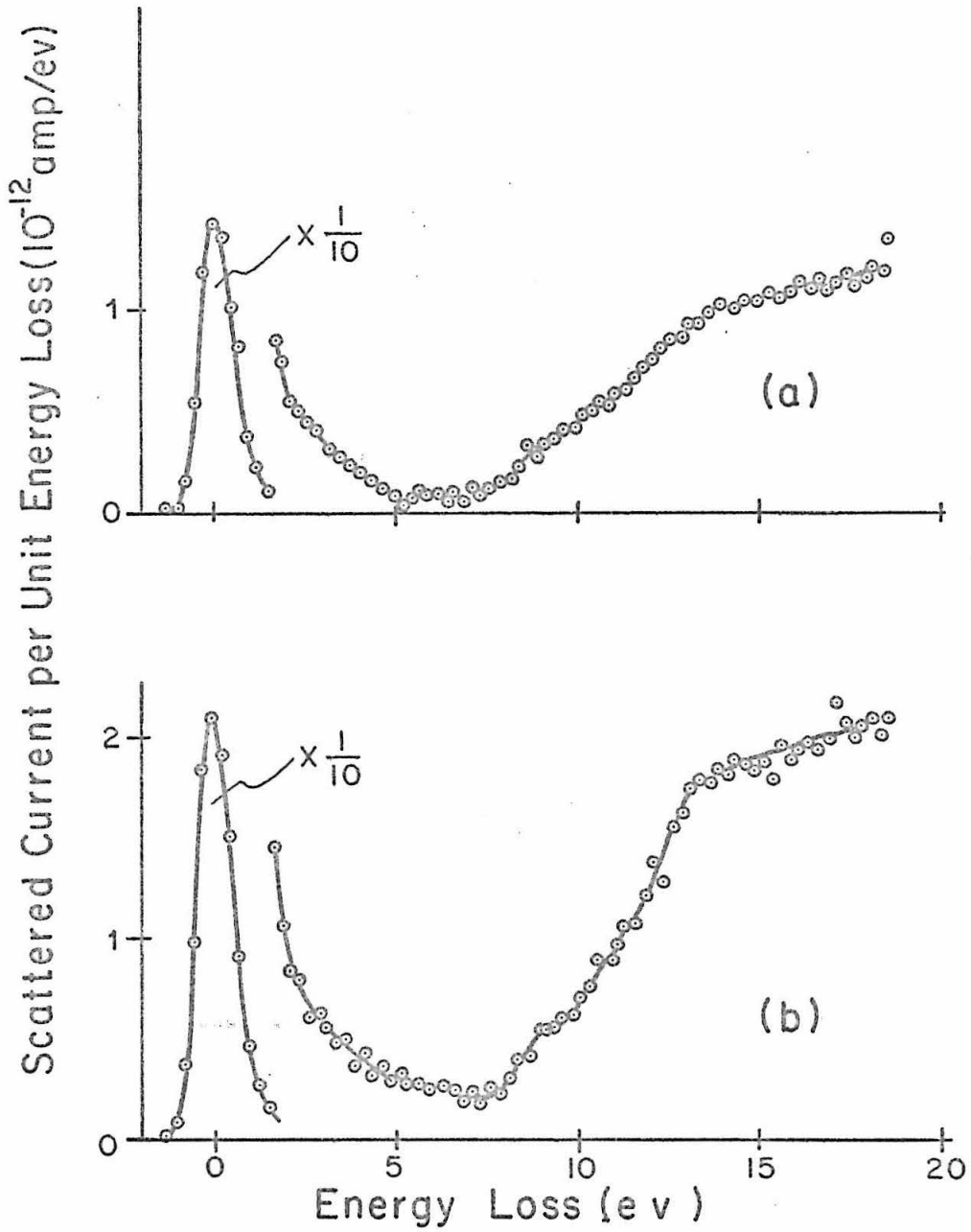


Figure 29. 90 Electron impact spectra of propane with electron beam energies of a) 50, b) 40, c) 35, and d) 30 eV.  $i_{BC} = 1.44 \times 10^{-7}$  amp,  $P_{SC} = 3.2 \times 10^{-4}$  torr.

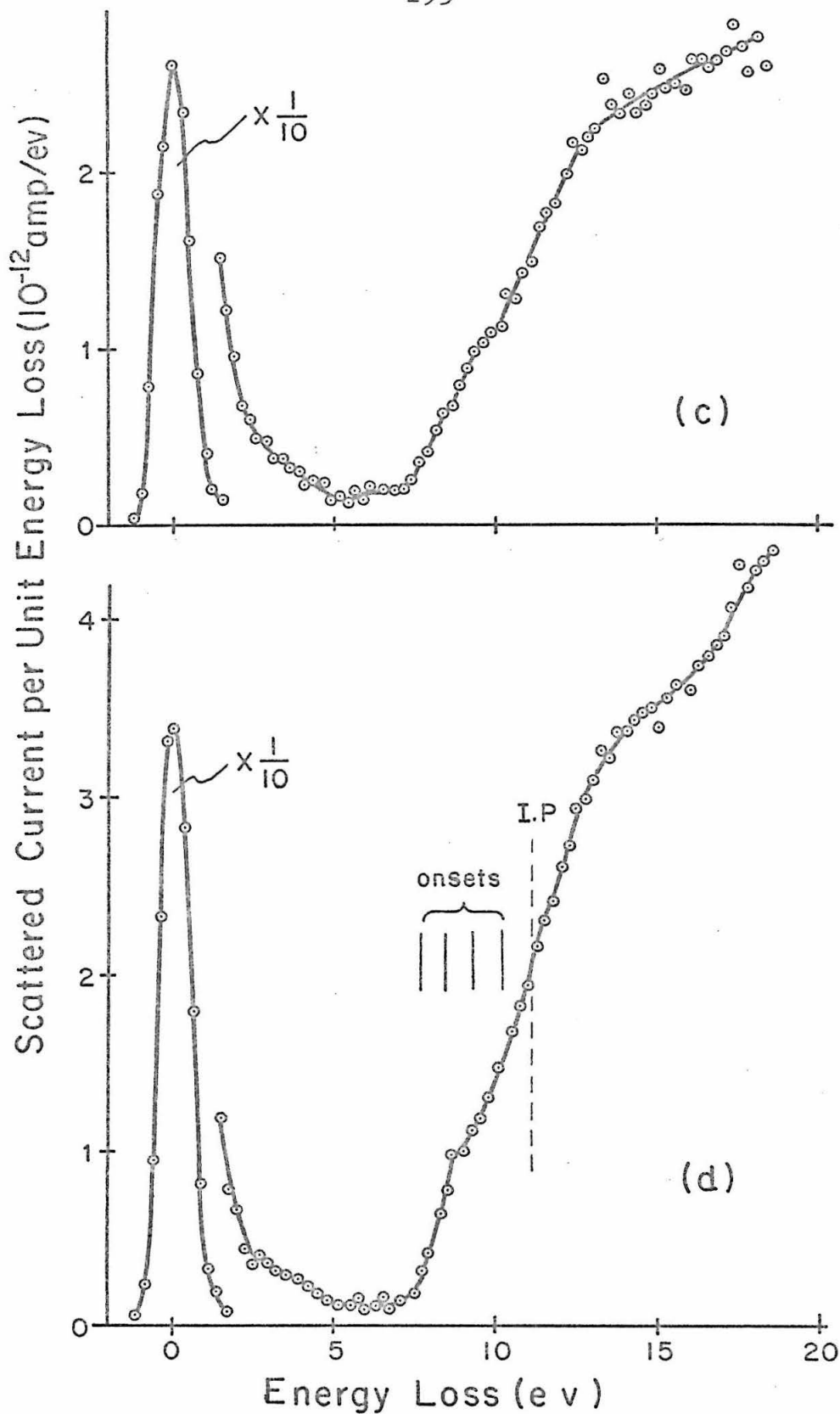


Figure 29. ( Continued )

We conclude that no optically forbidden transitions have <sup>been observed</sup> for propane although the experimental conditions are favorable for such observation.

V.10. 1,3-Butadiene

The vacuum ultraviolet absorption spectrum of 1,3-Butadiene was first taken in 1934 by Scheibe and Grieneisen (136) in the wavelength region 1660-2300 Å. In 1940 Price and Walsh (137) restudied this molecule in the region 1250-2300 Å and performed a detailed analysis.

According to Price and Walsh (137), butadiene starts to absorb weakly at 5.4 ev with increasing strength toward the shorter wavelength side. A strong and diffuse progression joins the weak absorption at 5.7 ev and extends to about 6.3 ev. This progression has a maximum at about 5.9 ev and is referred to by Herzberg (89) as the  $\tilde{A} \leftarrow \tilde{X}$  transition. Some fairly strong bands located at 6.25, 6.65, 6.81, 7.04, 7.06, 8.00, and 8.17 ev, because of their irregular appearance, are referred to as different electronic states:  $\tilde{B}$ ,  $\tilde{C}$ ,  $\tilde{D}$ ,  $\tilde{E}$ ,  $\tilde{F}$ ,  $\tilde{G}$ , and  $\tilde{H}$ , respectively (89). Two Rydberg series between 8 and 9 ev joining on to the  $\tilde{G}$  and  $\tilde{H}$  states have been assigned by those authors. They converge to the same ionization potential of 9.061 ev which is in good agreement with the first ionization potential of 9.07 ev obtained by Watanabe (138) and with that of 9.08 ev by Al-Joboury and Turner (129) from photo electron energy experiments. Certain other strong bands have been observed at energies higher than the first ionization potential with a maximum at about 9.7 ev.

In 1939 Mulliken (139) first considered the intensities of electronic transitions in molecular spectra of conjugated dienes. The 1,3-Butadiene molecule was treated in both the trans-( $C_{2h}$ ) and the cis-( $C_{2v}$ ) form as a 4-electron problem with the  $CH_2-CH=CH-CH_2$  skeleton (containing 26 more tightly bound electrons) lying in a plane. In Mulliken's notation (139) the ground state N (the normal state) has the

$\pi$ -electron configuration of  $(X_1)^2 (X_2)^2$ . Excitation of a  $\pi$ -electron to the lowest unoccupied  $\pi$ -electron orbitals ( $X_3$ ) or ( $X_4$ ) leads to four singlet excited states (ignoring the corresponding triplet states for a while):  $V_1$ ,  $V_2$ ,  $V_3$ , and  $V_4$ , with the electron configurations of  $(X_1)^2 - (X_2)(X_3)$ ,  $(X_1)^2 (X_2)(X_4)$ ,  $(X_1)(X_2)^2 (X_3)$ , and  $(X_1)(X_2)^2 - (X_4)$ , respectively, where  $V_1$  is the lowest excited state,  $V_2$  and  $V_3$  have the same excitation energy and lie higher than  $V_1$ , and  $V_4$  lies still higher. On symmetry considerations<sup>(139)</sup>, transitions from the N state to the  $V_1$ ,  $V_2$ ,  $V_3$ , and  $V_4$  states are all allowed for the cis- isomer. However, only  $V_1 \leftarrow N$  and  $V_4 \leftarrow N$  transitions are allowed for the trans- isomer.

In an attempt to correlate the observed spectrum with theory, Mulliken<sup>(140)</sup> arrived at the following assignments. The strong  $\tilde{A} \leftarrow \tilde{X}$  transition peaking at 5.9 eV was assigned to the  $V_1 \leftarrow N$  transition. The weak and diffuse bands at 7.04 and 7.06 eV ( the  $\tilde{E}$  and  $\tilde{F}$  states, respectively) were attributed to the  $V_{2,3} \leftarrow N$  transitions. From the intensities of the  $V_{2,3} \leftarrow N$  transitions relative to those of the  $V_1 \leftarrow N$ , he suggested that there might be as much as 20% of the cis- isomer of butadiene present in the vapor phase (not confirmed, see below). Price and Walsh<sup>(137)</sup> further assigned the 9.7 eV band to the  $V_4 \leftarrow N$  transition.

In an electron impact ionization study on butadiene, Sugden and Walsh<sup>(141)</sup> reported an anomalous behavior of the "ion current versus accelerating potential" curve. Their curve had a small "hump" between 8.7 and 9.3 volts with a peak at about 9.0 volts (contact potential not corrected). These authors interpreted the anomaly as the observation of two ionization potentials for 1,3-butadiene at 8.7 and 9.3 volts corresponding to the cis- and the trans- isomers, respectively. (Not confirmed, see below.)

As a support for their assignments, Sugden and Walsh<sup>(141)</sup> further selected a third Rydberg series, converging to the ionization potential of 8.71 ev, out of the weaker bands from the spectrum obtained by Price and Walsh<sup>(137)</sup>.

In 1950 Parr and Mulliken<sup>(142)</sup> performed a LCAO self-consistent field calculation of the  $\pi$ -electron energy levels of cis- and trans- 1,3-butadiene. The results indicated that the trans- form was 0.12 ev more stable than the cis- form and that the first ionization potential was computed to be 9.7 ev for both isomers, whereas the observed value was about 9.1 ev (probably for trans-). They also arrived at the value 5.4 ev for the cis- and 5.7 ev for the trans-, for the average excitation energy to the lowest singlet-triplet states. The experimental value for the lowest singlet state (probably for trans-) is about 6.0 ev.

The speculation on the existence of the cis- isomer of butadiene in the gas phase has been of interest to many authors since it was brought up<sup>(139,141,142)</sup>. However, photo ionization work by Watanabe<sup>(138)</sup> and by Al-Joboury and Turner<sup>(129)</sup> has failed to confirm the 8.7 ev ionization potential reported by Sugden and Walsh<sup>(141)</sup>. Furthermore, infrared and Raman spectra yield no support for the presence of the cis- isomer<sup>(143)</sup>. Thus, the questionable assignment of the  $V_{2,3} \leftarrow N$  transitions at about 7.05 ev (forbidden for the trans- isomer) indicates the incorrectness of Mulliken's theory<sup>(139)</sup>.

The lowest triplet states of butadiene were first studied by Evans<sup>(95)</sup> using the oxygen perturbation technique. Although butadiene is transparent to near ultraviolet and visible light, it starts to absorb at about 4800 Å in the presence of a high pressure  $O_2$  (butadiene 2.5 atm,  $O_2$  130 atm) or in ethyl iodide solution. He was able to observe two triplet states with 0 - 0 bands lying at 2.58

and 3.56 eV and absorption maxima located at 3.22 and about 3.9 eV, respectively.

In studying the photo sensitized dimerization of butadiene and its derivatives with a number of sensitizers having different triplet state energies, Hammond and Liu (144) demonstrated that the lowest triplet state of butadiene observed by Evans (95) with the 0 - 0 band lying at 2.58 eV belonged to the trans- isomer, while the corresponding 0 - 0 band for the cis- isomer was probably at 2.32 eV.

According to Price and Walsh (137) the  $\tilde{A} \leftarrow \tilde{X}$  transition of butadiene starts at 5.4 eV. Since the absorption is diffuse and contains very little structure, analysis of the spectrum has not been carried out. Hammond, Turro, and Leermakers (145) once placed the 0 - 0 band at 5.4 eV. However, a lower value of 4.6 eV, suggested recently by Srinivasan (146) based on some photochemical reactions sensitized by the mercury  $^3P_1$  atom at 2537 Å, seems to be more reasonable. The 0 - 0 band in the  $\tilde{A} \leftarrow \tilde{X}$  transition is probably a Franck-Condon forbidden transition, too weak to be observed optically.

#### V.10.1. Summary of Previous Electron Impact Work

1,3-Butadiene has been studied by Bowman (51) using the trapped electron technique (excitation near threshold). The excitation spectrum shows two bands peaking separately at 4.05 and 6.6 eV with relative intensities of 0.21 and 1.00, respectively. No interpretation of the spectrum was given.

We see from the optical spectroscopic data that the maximum absorptions for the first triplet and the first singlet states (trans- isomer) lie at 3.22 and 5.90 eV, respectively. The separation between these two maxima is

2.68 ev. It is obvious that Bowman's spectrum may be correlated with the optical data if the energy scale is lowered by 0.7 ev. However, since the spectra of other molecules such as  $N_2$ ,  $C_2H_2$ ,  $CH_3 - C\equiv CH$ , etc, reported by him in the same article, do appear with the correct energy scale, it is not immediately clear why the shifting of energy scale becomes necessary for the case of butadiene.

#### V.10.2. Electron Impact Spectra of 1,3-Butadiene

Figure 30 shows the  $90^\circ$  electron impact spectra of 1,3-butadiene with electron beam energies of 50, 40, 35, and 30 ev. The gas sample is taken from a research grade lecture bottle of 1,3-butadiene from the Phillips Petroleum Company with a specified purity of 99.69 mol per cent.

The butadiene spectrum is characterized by two strong bands peaking separately at 5.9 and 9.7 ev. The 5.9 ev band may be assigned to the  $\tilde{A} \leftarrow \tilde{X}$  transition, or  $V_1 \leftarrow N$  in Mulliken's notation<sup>(139)</sup>. The 9.7 ev band, corresponding to the strong UV absorption beyond the 9.061 ev first ionization potential of butadiene, may be assigned to the  $V_4 \leftarrow N$  transition suggested by Price and Walsh<sup>(137)</sup>. A broad band peaking at 13 ev is probably another inelastic scattering process occurring further beyond the first ionization potential. The 7.05 ev region, where the  $V_{2,3} \leftarrow N$  transitions should lie, appears in the present spectrum as a valley, indicating that the differential cross sections at  $90^\circ$  for inelastic scattering from the  $\tilde{E}$  and  $\tilde{F}$  states are small.

No specific structure can be distinguished below 4 ev, although Evans<sup>(95)</sup> has shown that the first and the second triplet states have absorption maxima at 3.22 and

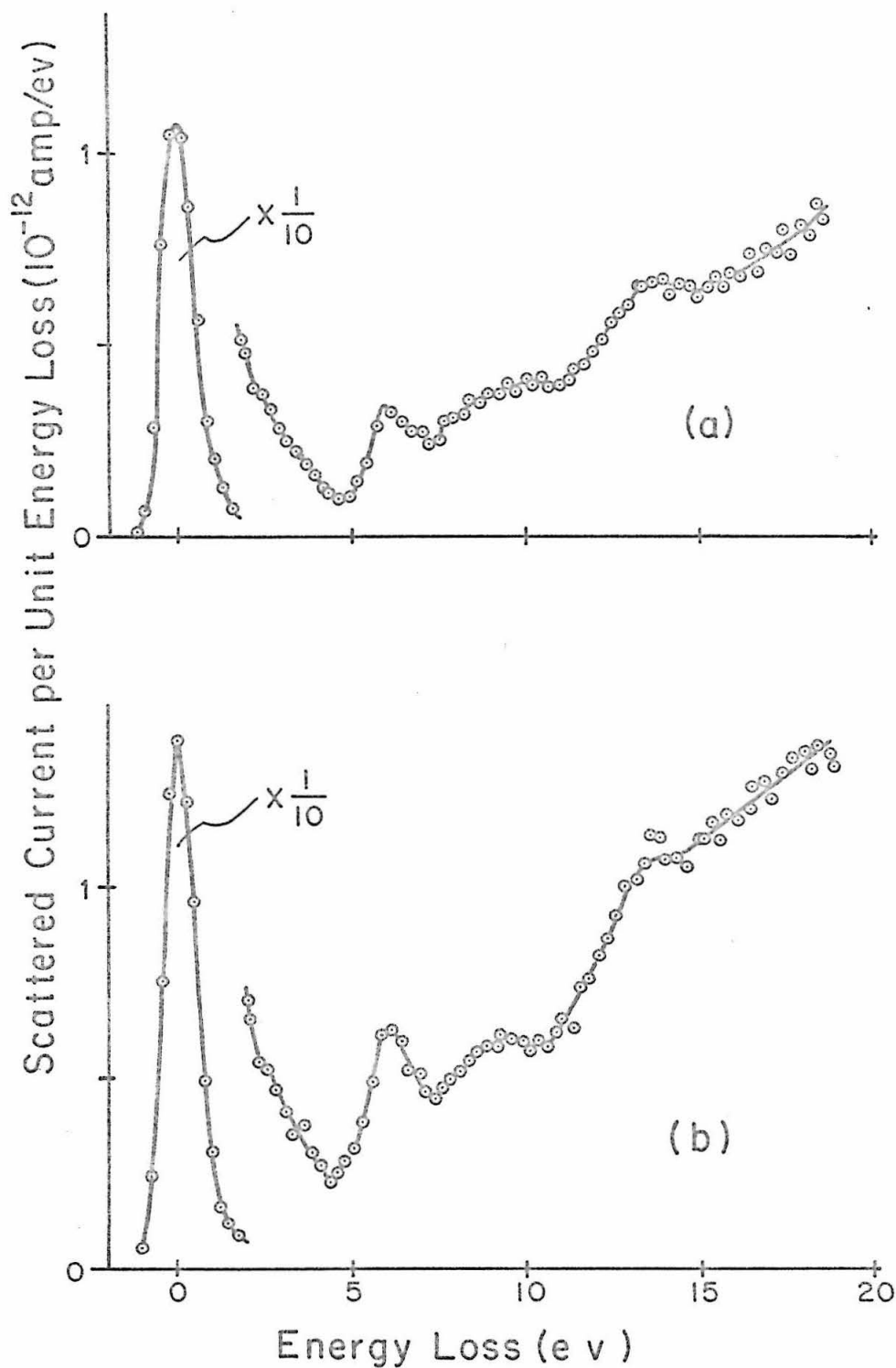


Figure 30. 90° Electron impact spectra of 1,3-butadiene with electron beam energies of a) 50, b) 40, c) 35, and d) 30 eV.  $i_{BC}=1.46 \times 10^{-7}$  amp,  $P_{SC}=4.5 \times 10^{-4}$  torr.

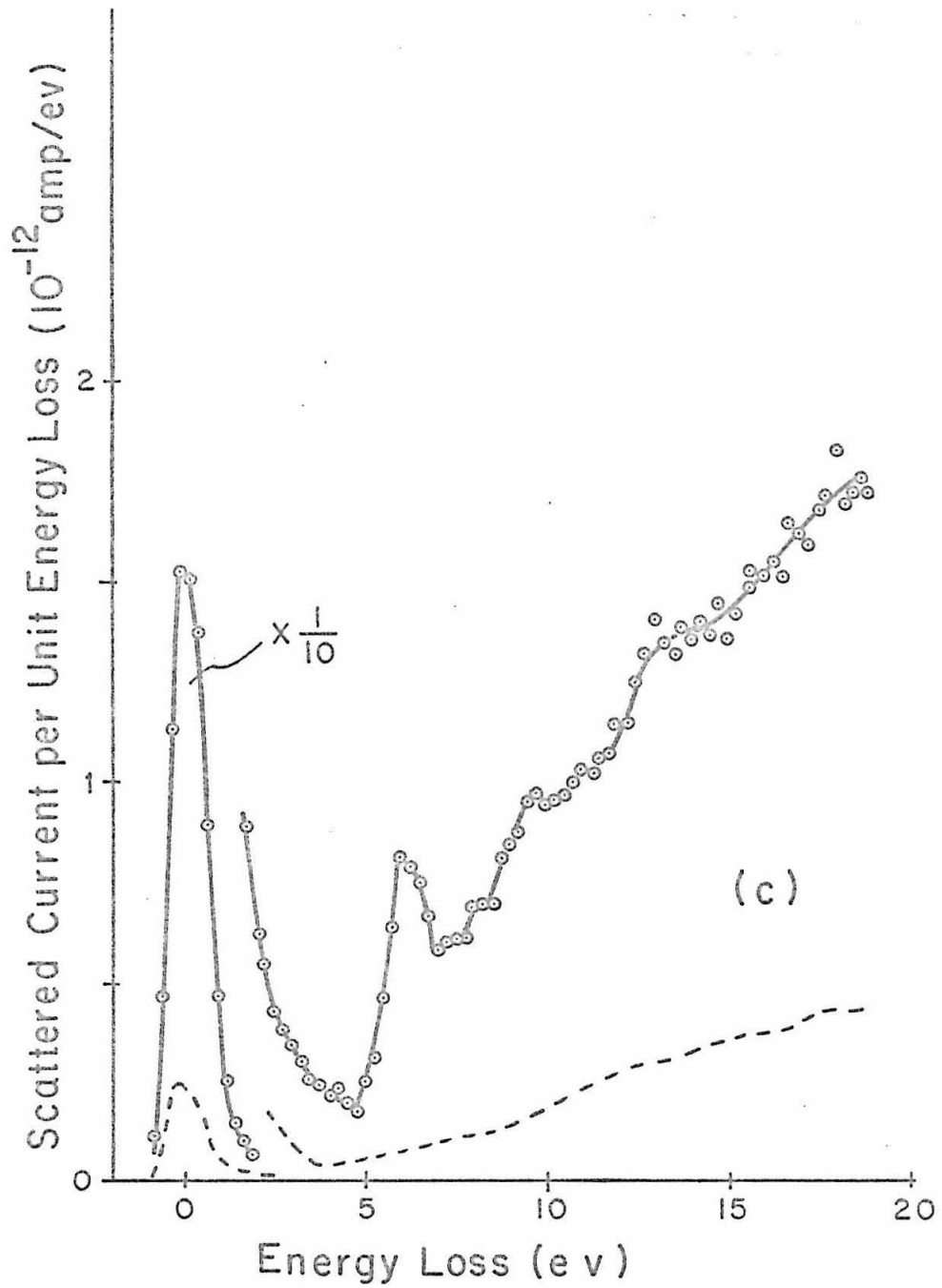


Figure 30. ( Continued ) Dashed curve is a blank run with  $P_{SC} = 8 \times 10^{-6}$  torr.

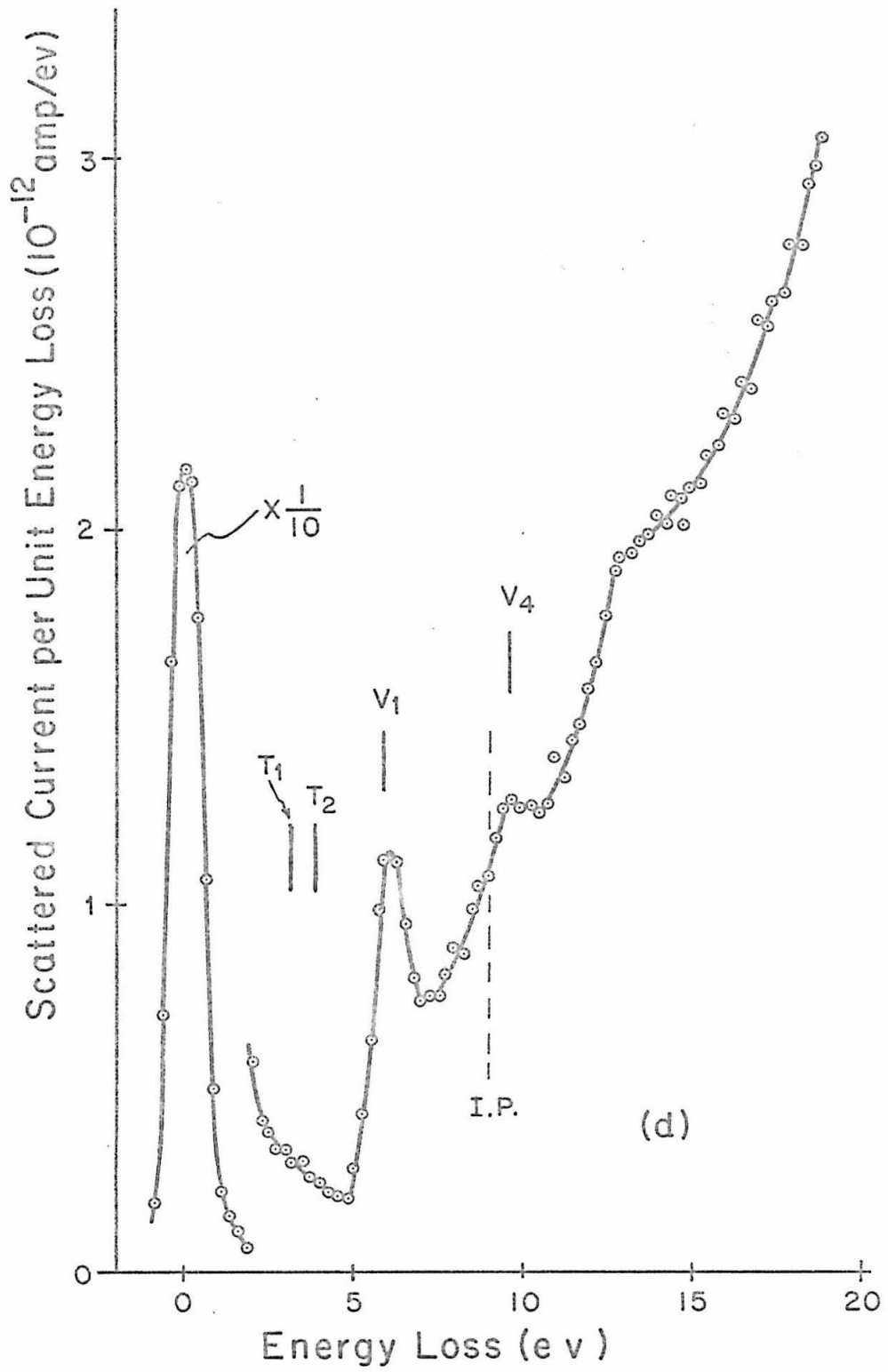


Figure 30. ( Continued )

3.9 eV, respectively. This could be due to masking of the inelastic structures by the tail of the elastic peak, which is still appreciably large in this region.

We conclude that the assignments of the observed electron impact spectra of butadiene are consistent with the optical spectroscopic data and with the characteristics of our instrument.

V.11. Benzene

Benzene is well known to have six  $\pi$ -electrons bound to the skeleton of a  $C_6$  ring. The ground state of benzene has  $D_{6h}$  symmetry. According to Herzberg<sup>(89)</sup> four molecular orbitals:  $(a_{2u})$ ,  $(e_{1g})$ ,  $(e_{2u})$ , and  $(b_{2g})$ , in the sequence of increasing energy, arise from the six  $2p_z$  carbon atomic orbitals. The  $(e_{1g})$  and  $(e_{2u})$  orbitals are doubly degenerate. In addition,  $(a_{2u})$  and  $(e_{1g})$  are bonding orbitals, whereas  $(e_{2u})$  and  $(b_{2g})$  are anti-bonding. The ground state of benzene can be described by the  $\pi$ -electron configuration of  $(a_{2u})^2 (e_{1g})^4$ , which is totally symmetric and is designated by  $\tilde{X}^1A_{1g}$ .

Excitation of a  $\pi$ -electron from the highest filled  $(e_{1g})$  orbital to the next unoccupied  $(e_{2u})$  orbital leads to six lowest excited states:  $\tilde{a}^3B_{1u}$ ,  $\tilde{b}^3E_{1u}$ ,  $\tilde{A}^1B_{2u}$ ,  $\tilde{C}^3B_{2u}$ ,  $\tilde{B}^1B_{1u}$ , and  $\tilde{C}^1E_{1u}$ , in the sequence of increasing energy. Extensive work done by many authors on the observations and assignments of the  $\tilde{a}^3B_{1u}$  and the  $\tilde{A}$ ,  $\tilde{B}$ , and  $\tilde{C}$  singlet states has been summarized by Herzberg<sup>(89)</sup>. We will only briefly mention some important characteristics concerning these states.

The extremely weak  $\tilde{a}^3B_{1u} \leftarrow \tilde{X}^1A_{1g}$  transition in benzene is both spin and symmetry forbidden. It lies between 3.66 and 4.2 eV above the ground state with a Franck-Condon maximum at 3.87 eV. This transition has an oscillator strength of less than  $f = 10^{-10}$ <sup>(147)</sup>, and it can only be observed in the liquid state<sup>(148)</sup> or using the high pressure oxygen enhancement technique<sup>(149)</sup>. There is evidence that the molecular geometry of the  $\tilde{a}^3B_{1u}$  state in the condensed phase is of a  $D_{2h}$  symmetry<sup>(150)</sup>.

The weak  $\tilde{A}^1B_{2u} \leftarrow \tilde{X}^1A_{1g}$  transition is symmetry forbidden. It lies between 4.72 and 5.6 eV with a Franck-Condon maximum at 4.85 eV<sup>(148b)</sup>. This transition is more intense than the

$\tilde{a} \leftarrow \tilde{X}$  transition by a factor of  $10^5$  (148c). Values for the oscillator strength ranging from  $f = 10^{-4}$  (151a) to  $f = 0.002$  (151b) have been reported.

The vacuum UV absorption spectrum of benzene in the region between 1600 Å and 2100 Å (152) shows a moderately strong transition ( $\tilde{B}^1B_{1u} \leftarrow \tilde{X}^1A_{1g}$ ) between 6.08 and 6.55 eV with a maximum around 6.2 eV, and a very intense transition ( $\tilde{C}^1E_{1u} \leftarrow \tilde{X}^1A_{1g}$ ) between 6.45 and 7.69 eV with a maximum at 6.98 eV. The  $\tilde{B} \leftarrow \tilde{X}$  transition is symmetry forbidden with a reported oscillator strength ranging from  $f = 0.094$  (152b) to  $f = 0.12$  (152a). The  $\tilde{C} \leftarrow \tilde{X}$  transition is allowed and has a reported oscillator strength ranging from  $f = 0.88$  (152b) to  $f = 1.23$  (152a). The occurrence of the symmetry forbidden transitions in benzene from the ground state to the  $\tilde{A}^1B_{2u}$  and  $\tilde{B}^1B_{1u}$  states may be explained by a vibronic coupling mechanism (89).

Many Rydberg states lying higher than the  $\tilde{C}^1E_{1u}$  states have been reported (153). In 1956 Wilkinson (153c) performed a detailed analysis of the vacuum UV spectra of  $C_6H_6$  (and  $C_6D_6$ ) in the region 1300-1850 Å. He observed 31 Rydberg transitions between 6.9 and 9.2 eV which could be arranged into four Rydberg series extrapolating to the same ionization potential of 9.247 eV, corresponding probably to the removal of an ( $e_{1g}$ ) electron. These Rydberg states are referred to by Herzberg (89) as the electronic states  $\tilde{D}$  to  $\tilde{P}$ . The  $\tilde{D}$  state is superimposed on the continuum of the  $\tilde{C}^1E_{1u}$  state.

Beyond the first ionization potential, two rather sharp and well-developed Rydberg series converging to the same ionization limit of 11.489 eV have been observed by El-Sayed, Kasha, and Tanaka (153d). This second ionization potential may be attributed to the removal of an ( $a_{2u}$ ) electron.

A further Rydberg series lying beyond 14.6 eV and converging to the ionization limit of 16.84 eV has been assigned by El-Sayed, Kasha, and Tanaka<sup>(153d)</sup> as the excitation and ionization of a  $\sigma_{C-C}$  electron. All three ionization potentials derived from the Rydberg series mentioned above have been confirmed by photo ionization experiments done by Al-Joboury and Turner<sup>(129)</sup>, and by Clark and Frost<sup>(154)</sup>.

The location of the second triplet state ( $\tilde{b}^3E_{1u}$ ) of benzene has been of interest to various authors for many years<sup>(155)</sup>. Recently, Colson and Bernstein<sup>(156)</sup> were able to observe the  $\tilde{b} \leftarrow \tilde{x}$  transition for the first time in single crystals of benzene<sup>(156a)</sup> and in mixed-crystals of benzene- $O_2$ <sup>(156a)</sup> and benzene- $NO$ <sup>(156b)</sup> at 4.2°K. The 0-0 band for the benzene  $\tilde{b} \leftarrow \tilde{x}$  transition, which is usually masked by the hot bands of the more intense  $\tilde{A} \leftarrow \tilde{X}$  transition at room temperature, does occur at 4.2°K in crystals in the region between 4.63 and 4.68 eV. The  $\tilde{a} \leftarrow \tilde{X}$  transition was also observed in the mixed-crystals but not in pure crystals<sup>(156)</sup>.

#### V.11.1. Summary of Previous Electron Impact Work

In 1965 Skerbele and Lassetre<sup>(38a)</sup> reported the electron impact spectrum of benzene at zero scattering angle with 300 eV electron beams (resolution about 0.4 eV).

The most intense peak they reported is located at 6.96 eV corresponding to the allowed  $\tilde{C}^1E_{1u} \leftarrow \tilde{X}^1A_{1g}$  transition. Two weak bands peaking at 4.93 and 6.21 eV with intensities of 0.007 and 0.142, relative to that of the most intense peak, were assigned to the symmetry forbidden transitions  $\tilde{A} \leftarrow \tilde{X}$  and  $\tilde{B} \leftarrow \tilde{X}$ , respectively. Further peaks superimposed on a continuum between 8.4 and 17 eV are also shown in the

spectrum. No singlet-triplet transitions were observed.

The good agreement between Skerbele and Lassetre's work (38a) and the ultraviolet absorption spectra (148b, 152a, 152b) indicates that the Born Approximation is good at high-energy, small-angle scattering.

Read and Whiterod (157) carried out some calculations with the Born approximation to obtain differential and total cross sections for inelastic electron scattering from benzene. The three lowest excited singlet states are treated. The simple  $\pi$ -electron antisymmetric molecular orbitals are used as the electronic wave functions, and the cross sections are averaged over initial, and summed over final, rotational-vibrational states. The effects of vibronic interactions on the cross sections are included. For an incident energy of 300 ev at  $0^\circ$  scattering angle, the calculated differential cross sections have the proportions:  $6 \times 10^{-8}$ ,  $10^{-6}$ , and 1.0 for excitation to the states  $\tilde{A}^1B_{2u}$ ,  $\tilde{B}^1B_{1u}$ , and  $\tilde{C}^1E_{1u}$ , respectively, in qualitative agreement with the experimental results (38a). This, however, indicates probably the poorness of the wave functions chosen.

#### V.11.2. The Electron Impact Spectra of Benzene

Figure 31 shows the  $90^\circ$  electron impact spectra of benzene ( $C_6H_6$ ) with electron beam energies of 50, 40, 35, and 30 ev. The gas sample is distilled from a cold trap containing Baker and Adamson Reagent Grade benzene (Allied Chemical, General Chemical Division, purity 99.97%). The trap is chilled by an ice-water mixture to avoid liquid film formation on the sealing surface of the Granville-Phillips variable leak which is operated at room temperature during a run.

We see from Figure 31 that the most prominent feature

in the benzene spectrum is the band peaking at 7.0 eV which corresponds to the allowed  $\tilde{C}^1E_{1u} \leftarrow \tilde{X}^1A_{1g}$  transition. The symmetry forbidden transitions  $\tilde{A} \leftarrow \tilde{X}$  and  $\tilde{B} \leftarrow \tilde{X}$ , which have absorption maxima at about 4.9 and 6.2 eV, respectively, are not resolved under present experimental conditions.

As we go to lower electron beam energies, a very weak band peaking at about 3.8 ( $\pm 0.2$ ) eV starts to show up in the benzene spectrum (see Figure 31d). Although weak, this peak *has been* observed in 10 independent runs and is definitely present. This band may be correlated to the ( $\tilde{a}^3B_{1u} \leftarrow \tilde{X}^1A_{1g}$ ) singlet-triplet excitation which is not observed by Skerbele and Lassette<sup>(38a)</sup> at 300 eV beam energy and at zero scattering angle.

The second prominent band peaking at 10.0 eV in the 90° electron impact spectrum of benzene may be attributed to excitations of a  $\pi$ -electron from the next highest filled ( $a_{2u}$ ) orbital, to the unoccupied  $\pi$ -electron orbitals. This is in agreement with El-Sayed, Kasha, and Tanaka's assignment<sup>(153d)</sup> that the two Rydberg series, lying beyond the first ionization potential of 9.247 eV and converging to the ionization limit of 11.489 eV, are due to excitations originating from the ( $a_{2u}$ ) orbital.

It is of interest to compare the results for benzene and 1,3-butadiene, two different molecules with conjugated C=C double bonds. From Figure 30 and Figure 31 we see that the 90° electron impact spectra of these molecules are quite similar. The  $V_1 \leftarrow N$  transition in 1,3-butadiene has a maximum at 5.9 eV whereas the corresponding one in benzene is the  $\tilde{C}^1E_{1u} \leftarrow \tilde{X}^1A_{1g}$  transition peaking at 7.0 eV. The  $V_4 \leftarrow N$  transition in butadiene peaking at 9.7 eV may be corresponded to the 10.0 eV band in benzene. Furthermore, transition from the ground states to the lowest triplet

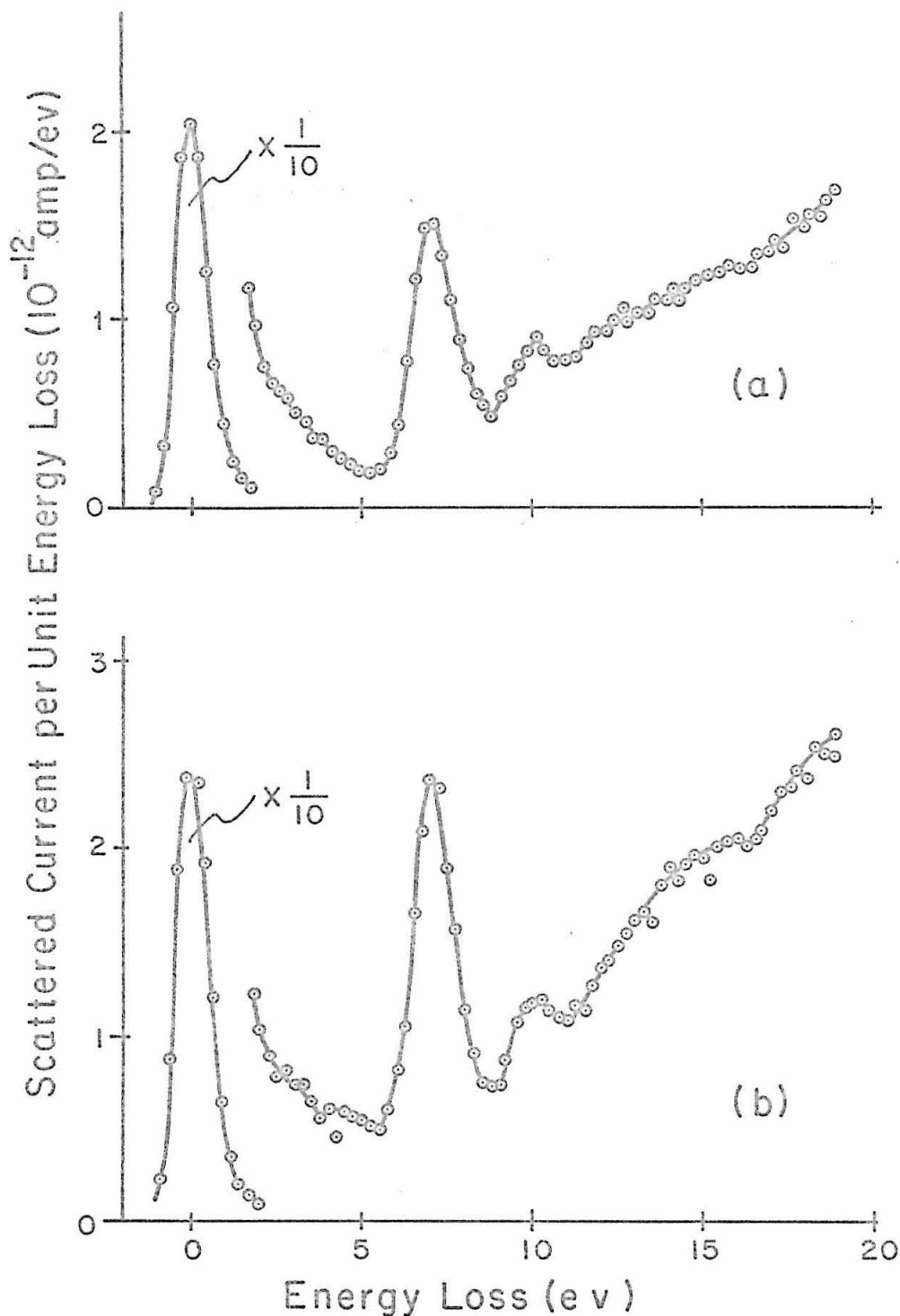


Figure 31.  $90^\circ$  Electron impact spectra of benzene with electron beam energies of a) 50, b) 40, c) 35, and d) 30 ev.  $i_{BC}=1.52 \times 10^{-7}$  amp,  $P_{SC}=4.3 \times 10^{-4}$  torr.

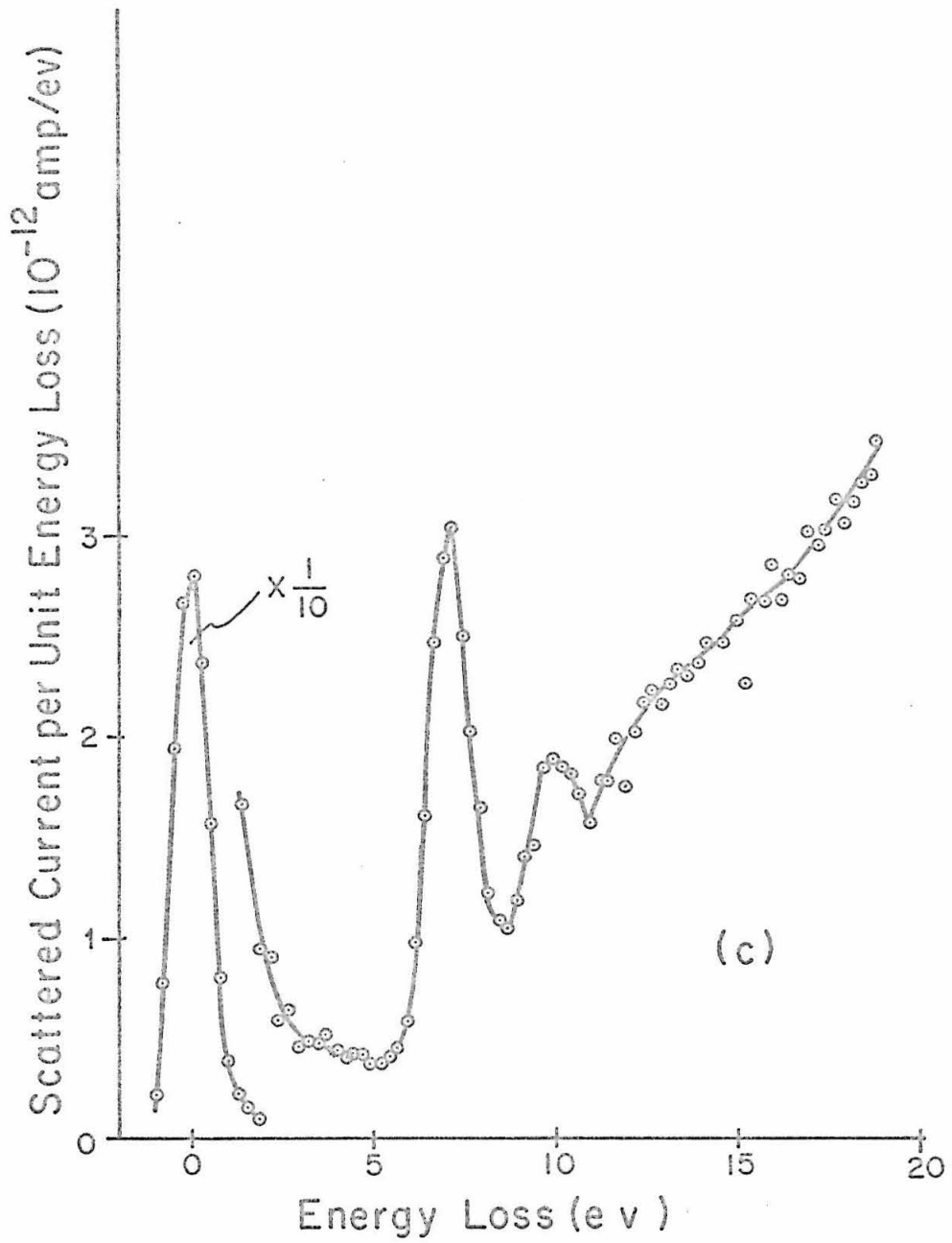


Figure 31. ( Continued )

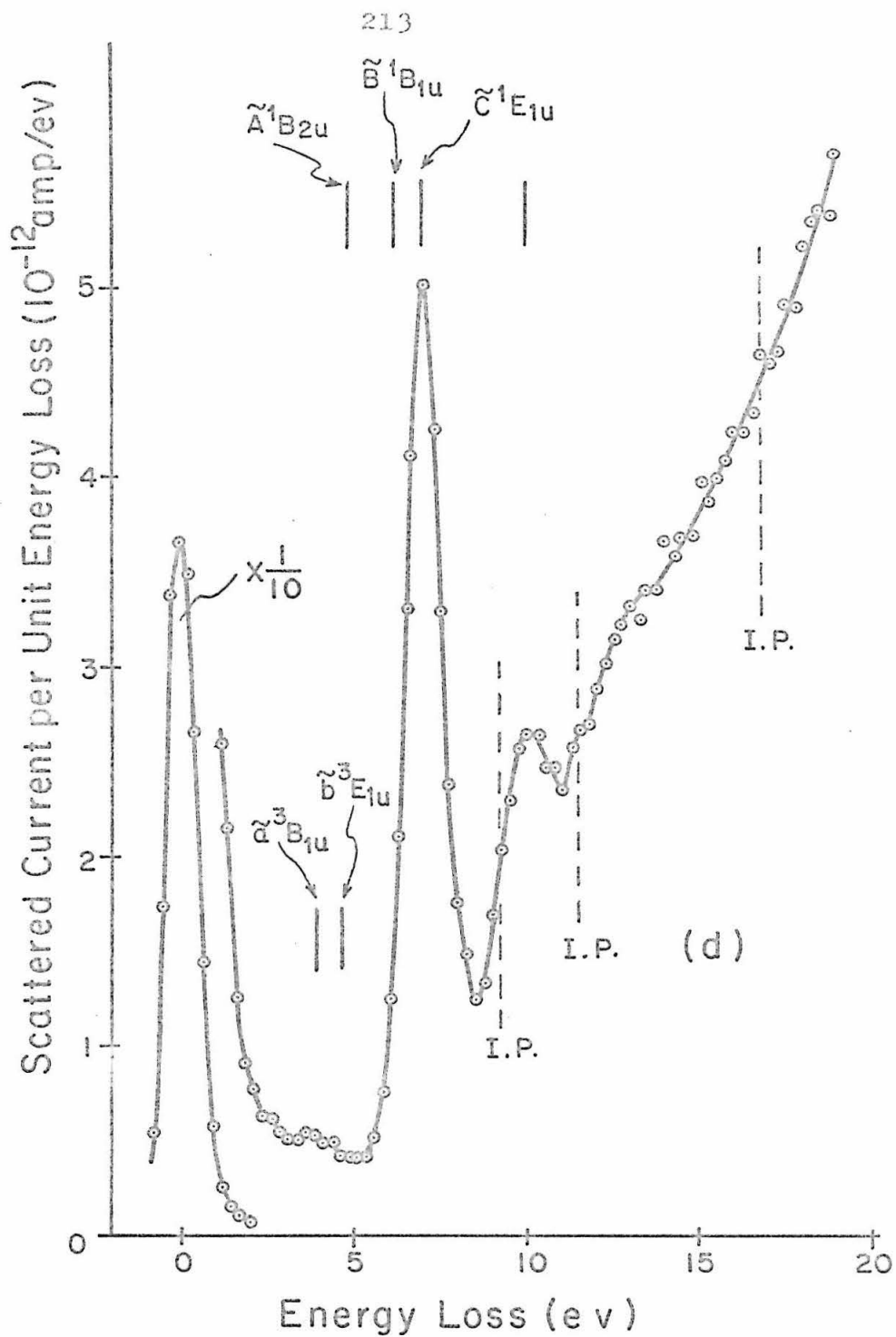


Figure 31. ( Continued )

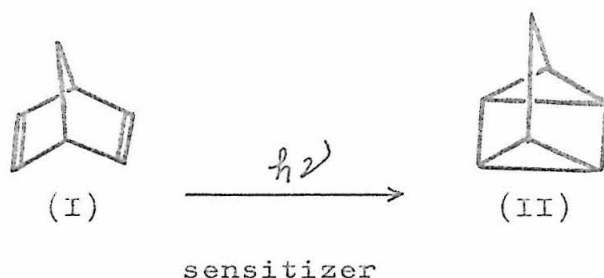
states have maxima at 3.22 and 3.87 ev for butadiene and benzene, respectively. (The triplet state in butadiene is not resolved from the tail of the elastic peak).

In addition to the similarities in the energy levels of benzene and butadiene, a simple relationship concerning the relative peak heights in the  $90^\circ$  electron impact spectra of these molecules may be attributed to the population of the  $\pi$ -electron orbitals. The ground state of 1,3-butadiene has the  $\pi$ -electron configuration of  $(X_1)^2(X_2)^2$ . If we assume that excitations originating from the two orbitals have the same probability, then the  $V_1 \leftarrow N$  and  $V_4 \leftarrow N$  transitions should have equal intensity. This is approximately true in Figure 30. On the other hand, the ground state of benzene has the  $\pi$ -electron configuration of  $(a_{2u})^2(e_{1g})^4$ . Thus we would expect the 7.0 ev band to be twice as intense as the 10.0 ev band. We see in Figure 31 that this is also qualitatively the case. Detailed calculation must be carried out in order to compare the ratio of differential cross sections for various transitions.

In conclusion, we may say that the assignments of the benzene spectrum are consistent with the optical data and with previous electron impact work. It is worthwhile to point out that this seems to be the first time that the lowest triplet state in benzene has been observed by electron impact spectroscopy.

V.12 Norbornadiene and Quadricyclene

The chemistry of norbornadiene (I) and its valence bond isomer quadricyclene (II) has received considerable attention in recent years. Hammond, Turro, and Fischer (158) were the first to observe the following photo-sensitized isomerization reaction in isopentane solutions with various sensitizers (acetone, acetophenone, and benzophenone).



Norbornadiene  
(also called  
bicyclo [2.2.  
1] heptadiene)

Quadricyclene  
also called  
quadricyclo [2.2.  
1.0<sup>2.6</sup>.0<sup>3.5</sup>]-  
heptane)

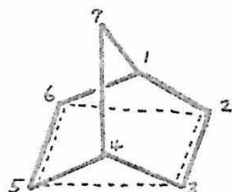
The thermal reversion from (II) to (I) was also observed (158).

Further work by Hammond, Wyatt, DeBoer and Turro (159) showed that an equilibrium between (I) and (II) could be reached when either pure (I) or (II) was exposed to light in the presence of a suitable sensitizer.

The reversible photosensitized isomerization between (I) and (II) can be explained by a transfer of the

triplet excitation energy from the sensitizer to the acceptor molecule. The latter then isomerizes through its excited triplet state. The energy transfer process is known to be nonvertical, i.e., it does not conform to the Franck-Condon principle<sup>(160)</sup>. Therefore, the triplet energy of the sensitizer, sufficient to cause isomerization, gives an upper limit for the energy of the 0 - 0 band for the lowest singlet-triplet transition in the acceptor molecule. In the particular reversible isomerization reaction between norbornadiene (I) and quadricyclene(II), four sensitizers, acetophenone, benzophenone, 2-naphthaldehyde, and benzil with triplet state energies, 3.19, 2.97, 2.58, and 2.34 ev, respectively, are found<sup>(159)</sup> to be decreasingly effective for the process.

It is conceivable that the intermediate triplet excited state for the reversible photosensitized isomerization may have the following geometry,



(III). Excited state of norbornadiene and quadricyclene

The bonding between carbon atoms 2 and 3 is weaker than a double bond, and there is a weak bonding between atoms 2 and 6<sup>(161,162)</sup>.

Concurrent with the first work by Hammond et al<sup>(158)</sup>, Dauben and Cargil<sup>(163)</sup> found that an ether solution of norbornadiene (I) was isomerized by ultraviolet irradiation to the valence tautomeric quadricyclene (II) in 67% yield. Heating (II) reformed (I).

However, subsequent photolysis work by Roquitte<sup>(161)</sup> with norbornadiene in ether or cyclohexane solutions failed to confirm Dauben and Cargil's observation. Instead, Roquitte<sup>(161,164)</sup> found that norbornadiene decomposed in the photolysis to yield equal amounts of acetylene and cyclopentadiene as major products and toluene as a minor product. Roquitte also carried out the experiment with gaseous norbornadiene in a mercury-free vacuum system. The photolysis yields of acetylene and cyclopentadiene were independent of temperature and pressure in the gas phase. Several gases added to the photolysis chamber were found to have no effect either. He suggested, therefore, that the photolysis of norbornadiene in the gas phase and in solutions without sensitizers must have followed a primary process other than the photosensitized isomerization.

Mass spectroscopic studies on norbornadiene were first reported by Meyerson, McCollum, and Rylander<sup>(165)</sup>. It is found that the mass spectrum of (I) is quite similar to those of its  $C_7H_8$  isomers, toluene and cycloheptatriene. The only difference is that the mass spectrum of (I) has higher intensities for mass peaks 66 ( $C_5H_6^+$ ) and 39 ( $C_3H_3^+$ ). Presumably, the molecular ion  $C_7H_8^+$  dissociates partly into a molecule of acetylene and a cyclopentadiene ion,  $C_5H_6^+$ . The latter then breaks up again to yield another  $C_2H_2$  molecule and the  $C_3H_3^+$  ion. On the other hand, Spectra of all three  $C_7H_8$  isomers have their highest peak at mass 91 which corresponds to the  $C_7H_7^+$  ion. Thus, it seems that the dissociation follows at least two competing paths depending upon the initial  $C_7H_8$  isomer.

The mass spectrum of quadricyclene (II) was first studied by Dolejšek, Hanuš, and Prinzbach<sup>(166)</sup> and found to be remarkably similar to that of norbornadiene (I). These authors suggest that the molecular ions resulting

from (I) and (II) may be nearly identical .

Further work by Hanuš and Dolejšek<sup>(167)</sup> on a series of eight  $C_7H_8$  isomers shows that upon electron impact, six isomers form ions with a seven membered ring without side reactions, whereas the other two, norbornadiene and quadricyclene, dissociate to form  $C_5H_6^+$  and  $C_2H_2$ .

#### V.12.1. Electronic Structure and Spectrum of Norbornadiene

The norbornadiene molecule (I) has two weakly coupled carbon-carbon double bonds and  $C_{2v}$  symmetry. According to Wilcox, Winstein and McMillan<sup>(162)</sup>, the ground state of (I) has the  $\pi$ -electron configuration  $\tilde{X}'A_1 (a_1)^2 (b_1)^2$  in the simple LCAO model. Single excitations of a  $\pi$ -electron from the highest filled orbital ( $b_1$ ) to the lowest unoccupied ( $b_2$ ) and ( $a_2$ ) orbitals give rise to the lowest singlet excited states  $\tilde{A}'A_2$  and  $\tilde{B}'B_2$ , respectively. From symmetry considerations the  $\tilde{A}'A_2 \leftarrow \tilde{X}'A_1$  transition is forbidden while the  $\tilde{B}'B_2 \leftarrow \tilde{X}'A_1$  one is allowed. (They are referred to as the  $V_1 \leftarrow N$  and  $V_2 \leftarrow N$  transitions, respectively).

The ultraviolet absorption spectrum of norbornadiene (I) was first studied by Wilcox, Winstein, and McMillan<sup>(162)</sup> in the wavelength region 1925-2260 Å in the gas phase and in ethanol solution. A progression of weak bands between 5.48 and 6.23 eV (with a Franck-Condon maximum at 5.85 eV) was observed in the gas phase spectrum and was assigned to the symmetry forbidden  $\tilde{A} \leftarrow \tilde{X}$  transition.

Hermann<sup>(168)</sup> obtained another vapor phase absorption spectrum of (I) from 1800 to 2400 Å. In addition to the  $\tilde{A} \leftarrow \tilde{X}$  transition, a strong band peaking at 6.57 eV was observed and assigned to the allowed  $\tilde{B} \leftarrow \tilde{X}$  transition.

Recently, Robin and Kuebler<sup>(169)</sup> performed an extensive study on the UV absorption spectrum of (I) in the

vapor phase at 25°C and 135°C, and in polycrystalline form at 24°K over the wavelength region 1637-2300 Å. They demonstrated that the weak progression between 5.48 and 6.23 ev which had been assigned by previous workers as the  $\tilde{A} \leftarrow \tilde{X}$  (or  $V_1 \leftarrow N$ ) transition could be correlated with a  $\sigma-\pi$  transition near 6 ev common to olefins. Robin and Kuebler further suggested that the structureless continuum superimposed with the weak progression might be attributed to the  $V_1 \leftarrow N$  transition.

Electron impact experiments yield values of 8.76 and 8.58 ev<sup>(165)</sup> and 8.60 ev<sup>(166)</sup> for the first ionization potential of norbornadiene.

#### V.12.2. Electron Impact Spectra of Norbornadiene

Figure 32 shows the 90° electron impact spectra of norbornadiene (I) with electron beam energies of 50, 40, 35, and 30 ev. The gas sample is distilled from a cold trap containing a liquid sample chilled with an ice-water mixture. The samples were prepared by C.C. Wamser<sup>(170)</sup>. Vapor phase chromatography<sup>(170)</sup> showed that the purity was better than 99%.

We see from Figure 32 that the norbornadiene spectrum has a weak band peaking at  $7.4 \pm 0.4$  ev. This band can be correlated with the strong UV absorption between 6.5 ev and 7.5 ev observed by Robin and Kuebler<sup>(169)</sup>.

The energy loss region below 5 ev does not exhibit structure in the 50 and 40 ev spectra. However, as we go to lower beam energies, a very weak band peaking at about  $3.8 \pm 0.2$  ev appears reproducibly (in 6 independent runs). The 3.8 ev band has not been observed in the optical absorption spectrum of (I). Furthermore, this band seems to be sensitive to electron beam energy, which is similar to the

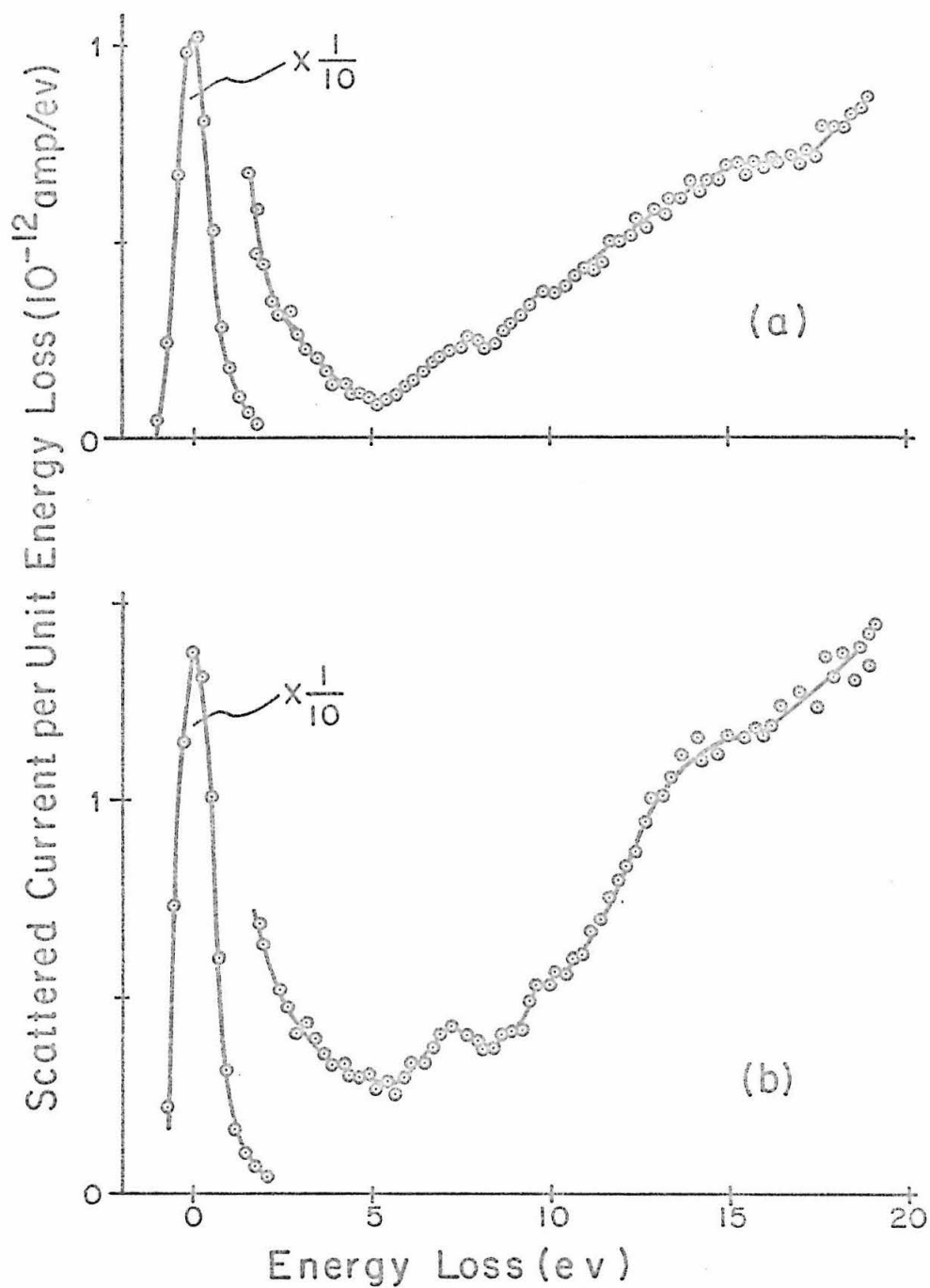


Figure 32.  $90^\circ$  Electron impact spectra of norbornadiene with electron beam energies of a) 50, b) 40, c) 35, and d) 30 eV.  $i_{BC} = 1.50 \times 10^{-7}$  amp,  $P_{SC} = 4 \times 10^{-4}$  torr.

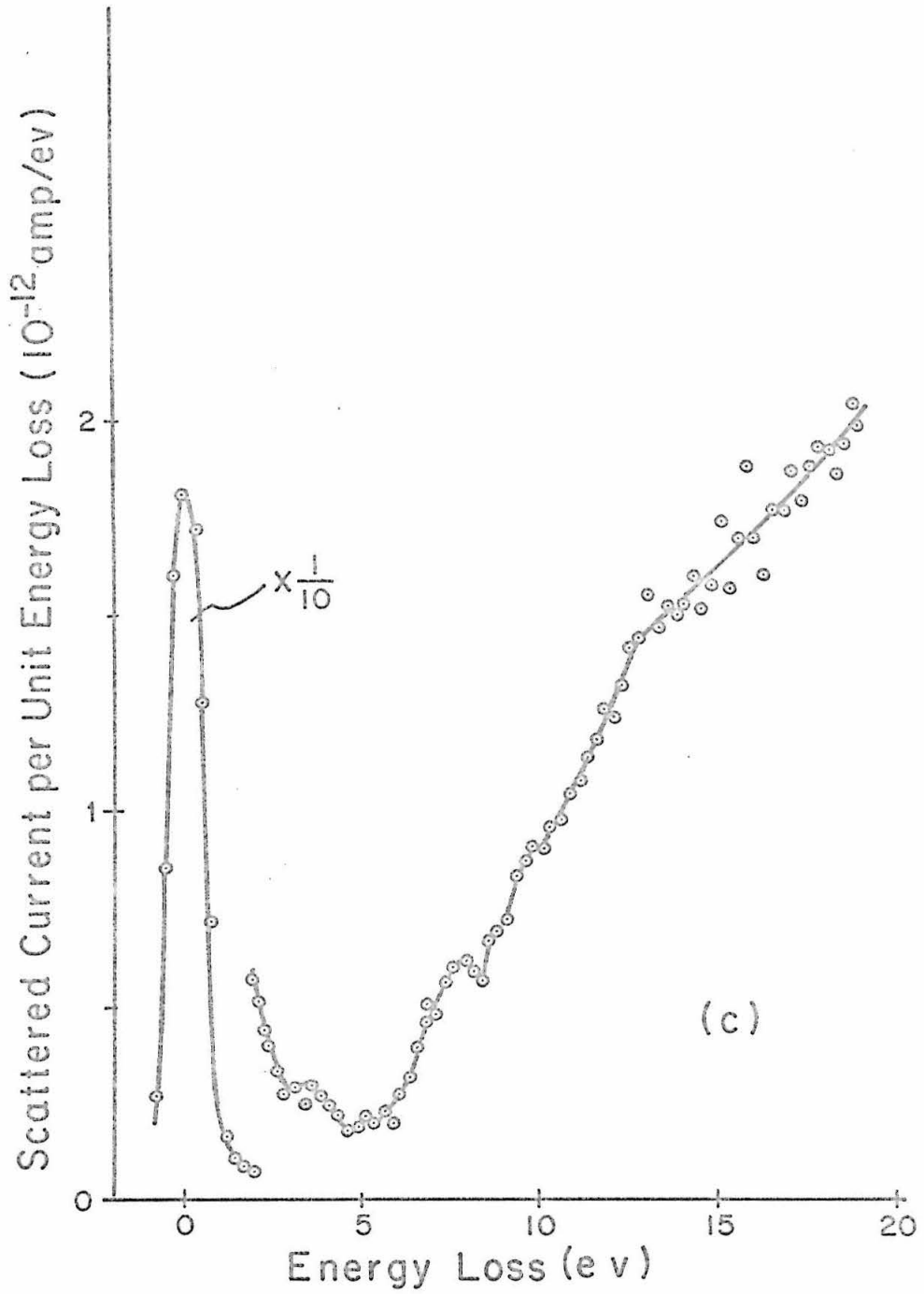


Figure 32. ( Continued )

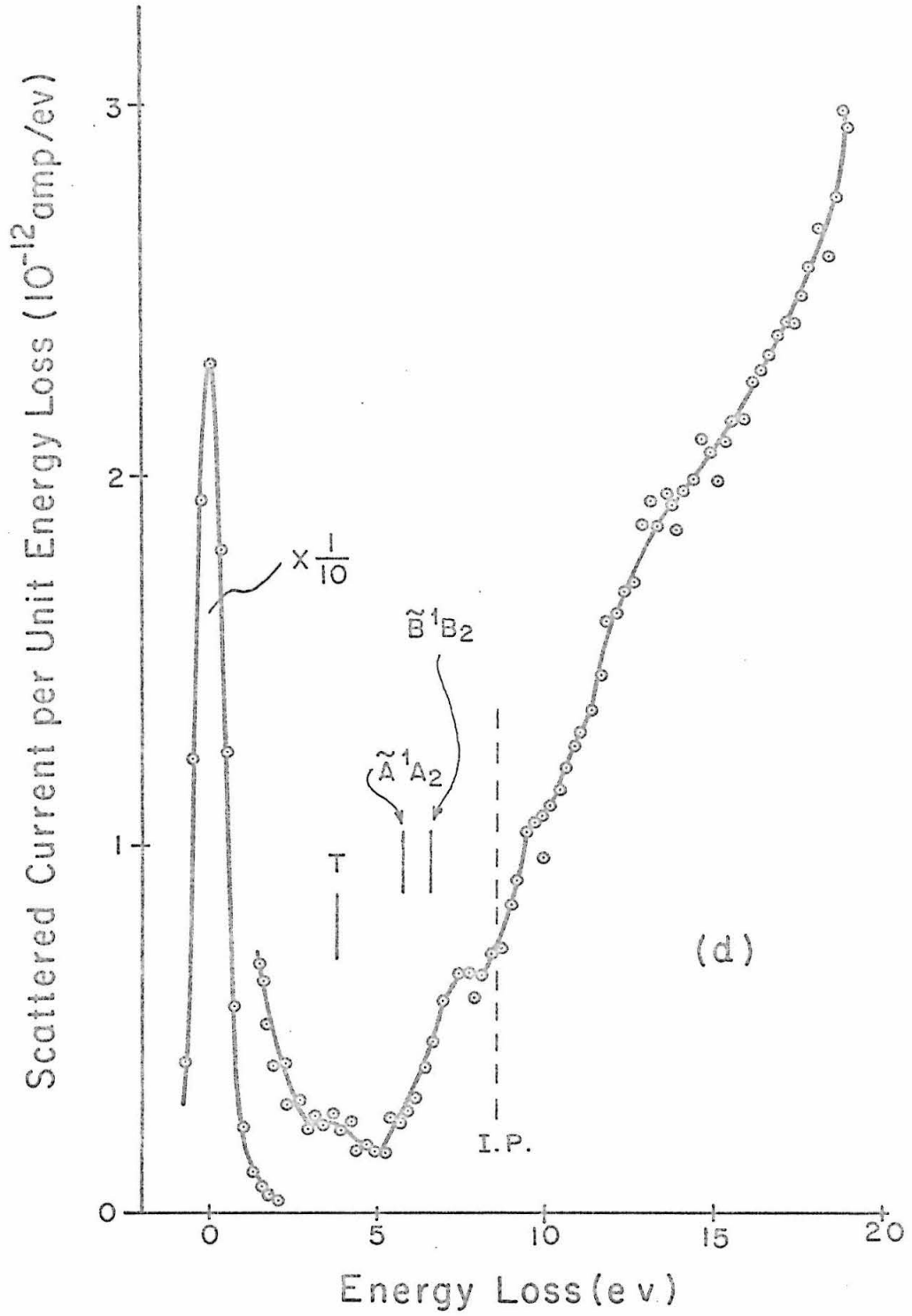


Figure 32. ( Continued )

behavior of singlet-triplet transitions in other unsaturated molecules. We hereby assign the 3.8 ev band to a singlet-triplet transition in norbornadiene. Since the Franck-Condon principle must be obeyed in electron impact excitations, the 3.8 ev value corresponds to the occurrence of the maximum intensity of a "vertical" transition from the ground state. Therefore the upper limit for the 0 - 0 band at 2.3<sup>4</sup> ev derived from photosensitized isomerization of (I)<sup>(159)</sup> is not inconsistent with the assignment.

It is of interest to compare the lowest singlet-triplet excitation energies for a mono-olefin, a conjugated diene, and a conjugated aromatic system with an unconjugated diene. The absorption maxima for the  $T_1 \leftarrow S_0$  transitions in ethylene, 1,3-butadiene, and benzene occur at 4.60, 3.22<sup>(95)</sup>, and 3.87 ev<sup>(89)</sup>, respectively. Thus, for the weakly coupled diene molecule (I) the occurrence of the  $T_1 \leftarrow S_0$  maximum at 3.8 ev is reasonable.

### V.12.3. Ultraviolet Absorption Spectrum of Quadricyclene

The quadricyclene molecule (II) is a saturated but highly cyclically constrained hydrocarbon. Fischer and Hammond<sup>(171)</sup> have studied the ultraviolet absorption of (II) in a cyclohexane solution and obtained the following results.

$\lambda$ (m $\mu$ )	250	240	230	220	210	200	190
$\epsilon$ (cm <sup>-1</sup> )	1.6	9	43	95	360	800	1400

Dauben and Cargil's result<sup>(163)</sup> that the molecule (II) has an extinction coefficient  $\epsilon=400$  at 205 m $\mu$

(probably in an ether solution) agrees with Fischer and Hammond's measurements<sup>(171)</sup>.

Electron impact experiments yield values of 8.70 and 8.85 ev<sup>(166)</sup> for the first ionization potential of quadricyclene.

#### V.12.4. Electron Impact Spectra of Quadricyclene

Figure 33 shows the 90° electron impact spectra of quadricyclene (II) with electron beam energies of 50, 40, 35, and 30 ev. The gas sample is distilled from a cold trap containing a liquid sample chilled with an ice-water mixture. The samples were prepared by N.J. Turro in 1963 and sealed under nitrogen atmosphere in a glass ampule. The ampule had been kept in a dark place at room temperature for four years. Vapor phase chromatography by C.C. Wamser<sup>(170)</sup> showed that the purity was about 99%, with 1% of norbornadiene as the major impurity.

From Figure 33 we see that the quadricyclene spectrum has a nearly structureless continuum starting at about 5.5 ev. This continuum is similar to that observed for the other saturated hydrocarbon propane.

A very weak band peaking at about  $4.0 \pm 0.2$  ev appears reproducibly (in 8 independent runs) in the 30 ev spectrum of (II). This 4.0 ev band may be correlated with the 3.8 ev band observed in the spectra of (I). We hereby tentatively assign this 4.0 ev band to the lowest singlet-triplet excitation in quadricyclene (II).

A comparison between the ultraviolet absorption spectrum of (II) in cyclohexane<sup>(171)</sup> and that of (I) in ethanol<sup>(162)</sup> indicates that the first singlet-singlet transition has a higher excitation energy in (II) than in

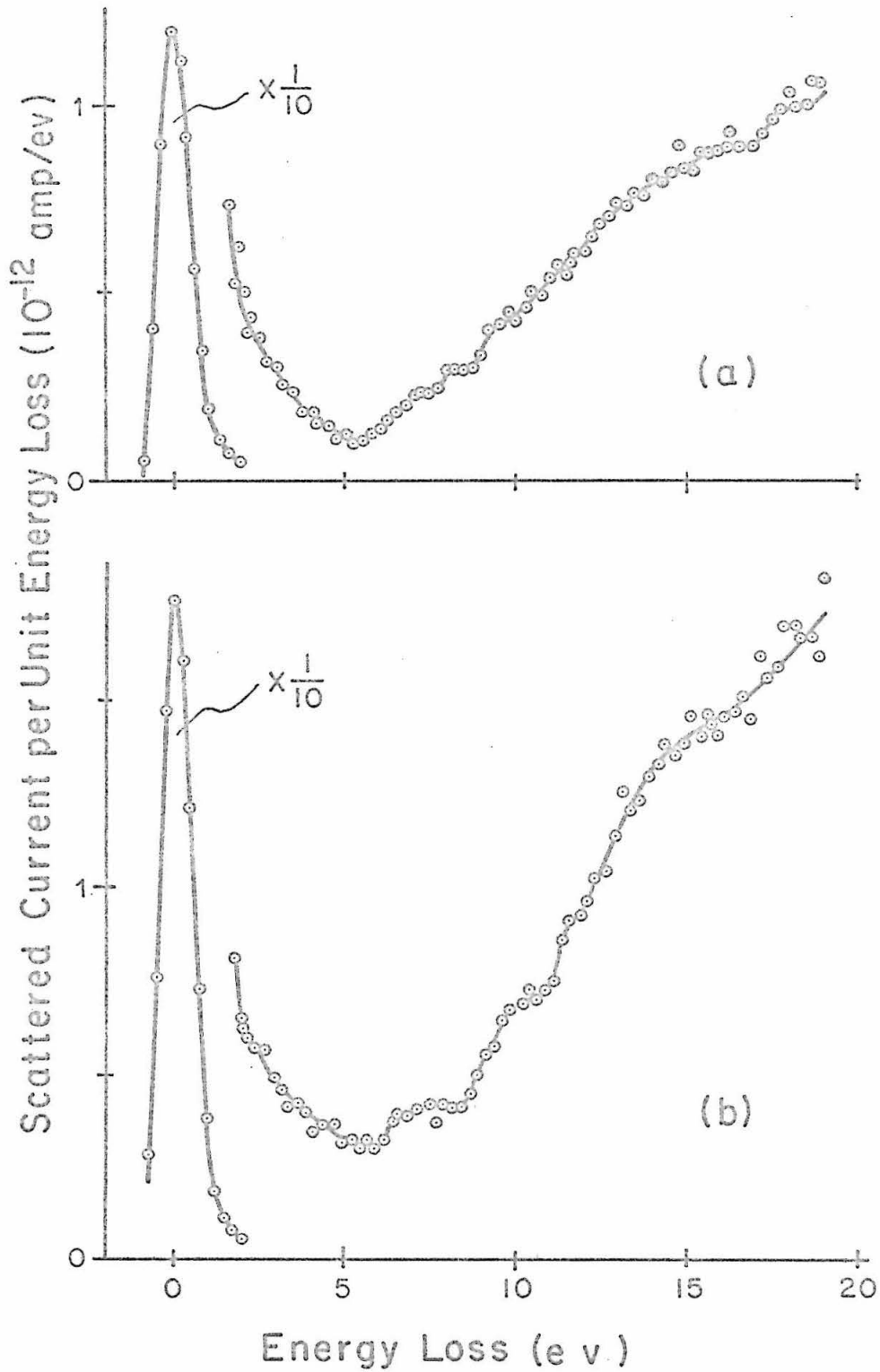


Figure 33.  $90^\circ$  Electron impact spectra of quadricyclene with electron beam energies of a) 50, b) 40, c) 35, and d) 30 ev.  $i_{BC} = 1.47 \times 10^{-7}$  amp,  $P_{SC} = 4 \times 10^{-4}$  torr.

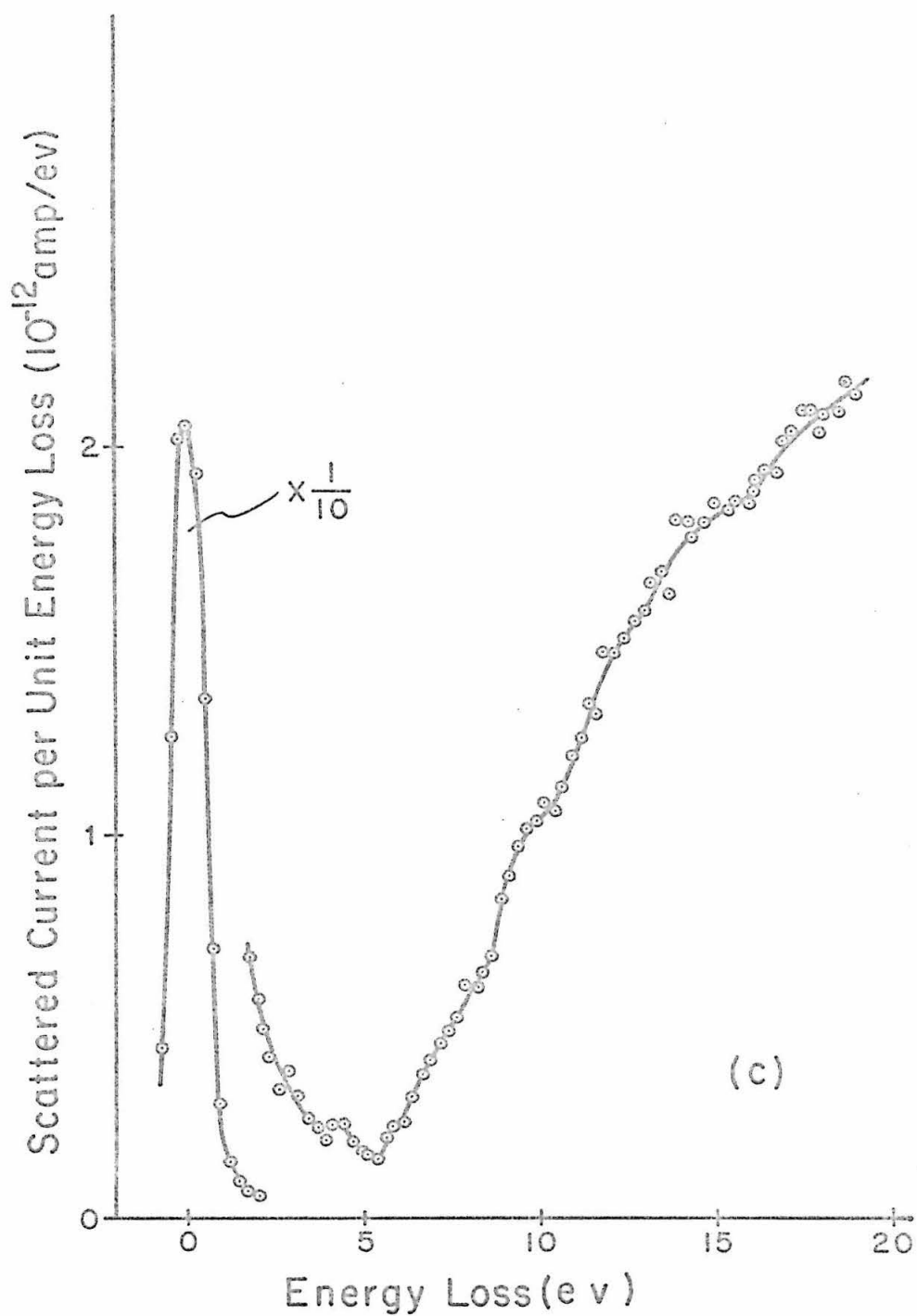


Figure 33. ( Continued )

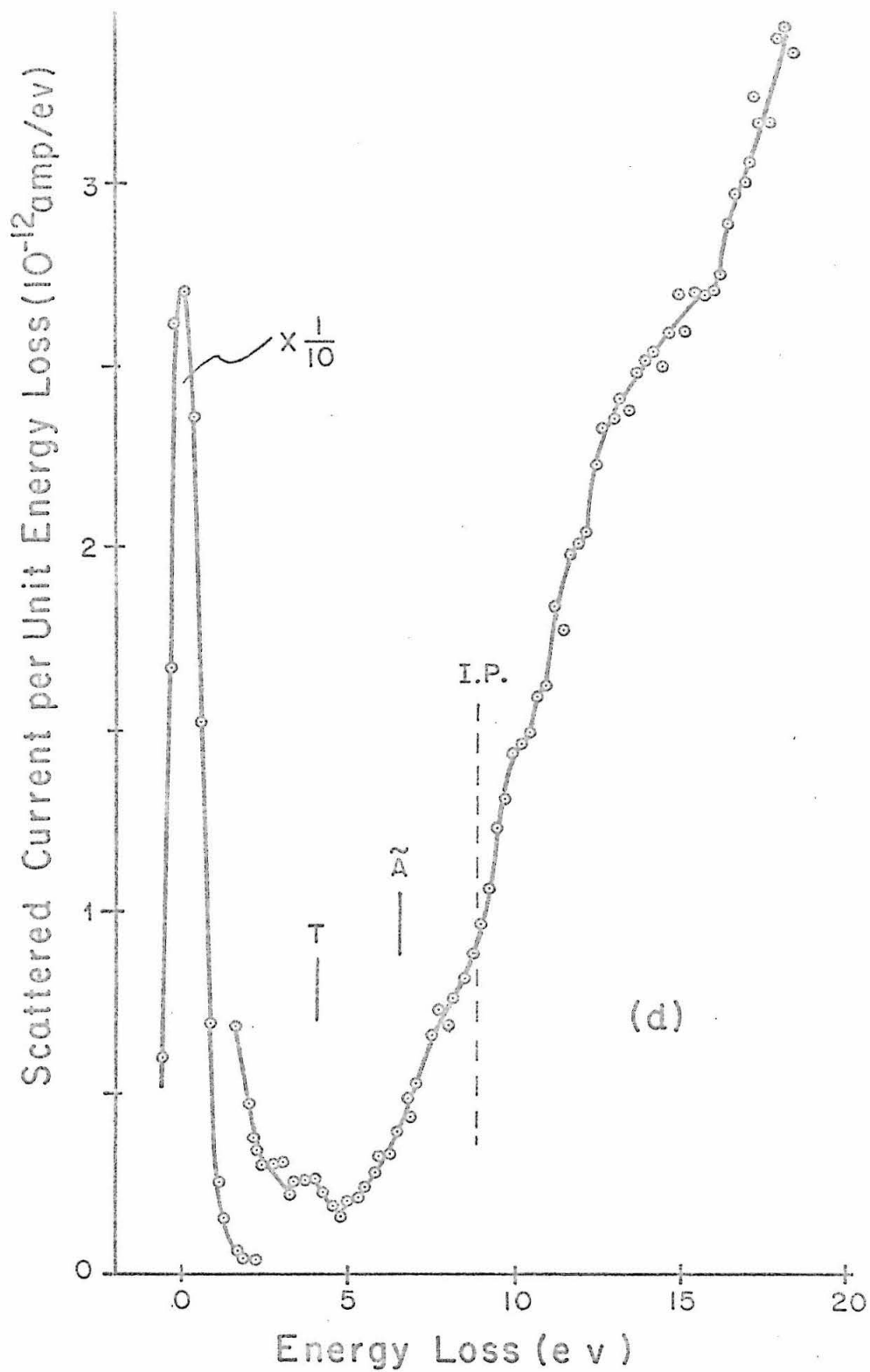


Figure 33. ( Continued )

(I). Therefore, it is expected that the lowest singlet-triplet transition in (II) lies slightly higher than the corresponding one in (I), in agreement with the present results.

Since (II) isomerizes upon heating to yield (I)<sup>(158)</sup><sup>(163)</sup>, there seems to be no doubt that the ground state of (I) lies lower than that of (II), i.e., (II) is a high-energy isomer of (I). Results of photosensitized isomerization reaction with fluorenone as the sensitizer (triplet energy 2.34 eV) at low conversion also indicate<sup>(159)</sup> that the energy gap between (I) and the intermediate triplet state isomer, say (III), is larger than the corresponding gap between (II) and (III). This, however, does not contradict the present results because those energy gaps are not vertical ones<sup>(160)</sup>.

## REFERENCE

1. J. R. Oppenheimer, Phys. Rev. 32, 361 (1928).
2. D. Bohm, "Quantum Theory", (New York, Prentice-Hill, 1951), chapter 3.
3. N. F. Mott and H. S. W. Massey, "Theory of Atomic Collisions", (Oxford at the Clarendon Press, 3rd edition, 1965), chapters 17 and 18.
4. Ref. 3, p.77.
5. Ref. 2, p.83.
6. H. Bethe, Ann. der Physik, 5, 325 (1930).
7. H. B. Dwight, "Tables of Integrals and Other Mathematical Data", (The MacMillan Co., New York, 3rd edition, 1957), p.125.
8. G. Herzberg, "Spectra of Diatomic Molecules", (D. Van Nostrand Company, Inc., 2nd edition, 1950).
9. H. S. W. Massey and E. H. S. Burhop, "Electronic and Ionic Impact Phenomena", (Oxford at the Clarendon Press, 1st edition, 1952), p.139.
10. Ref. 3, chapter 15.
11. L. Pauling, E. B. Wilson, Jr., "Introduction to Quantum Mechanics", (McGraw-Hill, 1935), p.218.
12. Ref. 9, p.143.
13. a) Ref. 9, p. 159.  
b) Bates, Fundaminsky, Massey, and Leech, Phil. Trans. Roy. Soc. (London) A243, 93 (1950).
14. E. Merzbacher, "Quantum Mechanics", (J. Wiley, New York, 1961), p. 207.
15. Ref. 14, chapter 12.
16. J. Irving and N. Mullineux, "Mathematics in Physics and Engineering, (Academic Press, 1959), chapter 3.
17. Ref. 16, p. 350.
18. Ref. 2, p. 560.

19. Ref. 16, p. 131.
20. Ref. 16, p. 182.
21. Ref. 9, pp. 113-118.
22. Ref. 16, p. 84.
23. Ref. 3, p. 324.
24. H. S. W. Massey and B. L. Moiseiwitsch, Proc. Roy. Soc, (London) A227, 38 (1954).
25. H. S. W. Massey and B. L. Moiseiwitsch, Proc. Roy. Soc. (London) A258, 147 (1960).
26. I. C. Percival and M. J. Seaton, Proc. Cambridge Phil. Soc. 53, 654 (1957).
27. a) P. G. Burke and K. Smith, Rev. Mod. Phys, 34, 458 (1962).  
b) P. G. Burke and H. M. Schey, Phys. Rev. 126, 147 (1962).
28. P. G. Burke, H. M. Schey, and K. Smith, Phys. Rev. 129, 1258 (1963).
29. V. I. Ochkur, Soviet Physics JETP 18, 503 (1964).
30. Ref. 3, p.422.
31. M. R. H. Rudge, Proc. Phys. Soc. 85, 607 (1965).
32. M. R. H. Rudge, Proc. Phys. Soc. 86, 763 (1965).
33. D. C. Cartwright, Ph.D. thesis, Division of Chemistry, California Institute of Technology, June 23, 1967.
34. D. C. Cartwright and A. Kuppermann, Phys. Rev. forthcoming.
35. J. D. Craggs and H. S. W. Massey, "The Collisions of Electrons with Molecules", Handbuch der Physik, herausgegeben von S. Flugge, 37, 333 (1959).
36. J. Franck and G. Hertz,
  - a) Verh. dtsh. Physik. Ges. 16, 457 (1914).
  - b) Physik. Z. 17, 407 (1916).
  - c) Physik. Z. 20, 132 (1919).
37. a) E. N. Lassetre and S. A. Francis, J. Chem. Phys. 40, 1208 (1964).

- b) E. N. Lassettre and E. A. Jones, *ibid* 40, 1218 (1964).
  - c) E. N. Lassettre and E. A. Jones, *ibid* 40, 1222 (1964).
  - d) E. N. Lassettre, A. S. Berman, S. M. Silverman, and M. E. Kransnow, *ibid* 40, 1232 (1964).
  - e) E. N. Lassettre, M. E. Kransnow, and S. Silverman, *ibid* 40, 1242 (1964).
  - f) E. N. Lassettre and M. E. Kransnow, *ibid* 40, 1248 (1964).
  - g) E. N. Lassettre and S. M. Silverman, *ibid* 40, 1256 (1964).
  - h) E. N. Lassettre, S. M. Silverman and M. E. Kransnow *ibid* 40, 1261 (1964).
  - i) S. M. Silverman and E. N. Lassettre, *ibid* 40, 1265 (1964).
  - j) A. M. Skerbele and E. N. Lassettre, *ibid* 40, 1271 (1964).
38. a) A. Skerbele and E. N. Lassettre, *J. Chem. Phys.* 42, 395 (1965).
- b) E. N. Lassettre, V. D. Meyer and M. S. Longmire, *ibid*, 42, 807 (1965).
- c) S. M. Silverman and E. N. Lassettre, *ibid*, 42, 3420 (1965).
- d) E. N. Lassettre, A. Skerbele and V. D. Meyer, *ibid* 45, 3214 (1966).
39. A. Skerbele, M. A. Dillon and E. N. Lassettre,  
a) *J. Chem. Phys* 46, 4161 (1967).  
b) *ibid*, 46, 4162 (1967).
40. J. A. Simpson, *Rev. Sci. Instr.* 35, 1698 (1964).
41. J. A. Simpson and S. R. Mielczarek, *J. Chem. Phys.* 39, 1606 (1963).
42. C. E. Kuyatt, J. A. Simpson and S. R. Mielczarek, *Bull. Am. Phys. Soc.* 9, 266 (1964).
43. G. E. Chamberlain, H. G. M. Heideman, J. A. Simpson and C. E. Kuyatt, *Fourth International Conf. on Phys. of Electronic and Atomic Collisions, Abstracts.* (Science Bookcrafters Inc., Hastings-on-Hudson, New York, 1965) pp. 378-381.
44. H. G. M. Heideman, C. E. Kuyatt, and G. E. Chamberlain *J. Chem. Phys.* 44, 355 (1966).

45. H. G. M. Heideman, C. E. Kuyatt, and G. E. Chamberlain  
J. Chem. Phys. 44, 440 (1966).
46. G. J. Schulz, Phys. Rev. 112, 150 (1958).
47. G. J. Schulz, *ibid*, 116, 1141 (1959).
48. G. J. Schulz, J. Chem. Phys. 33, 1661 (1960).
49. G. J. Schulz, J. Chem. Phys. 34, 1778 (1961).
50. G. J. Schulz and J. T. Dowell, Phys. Rev. 128, 174  
(1962).
51. C. R. Bowman and W. D. Miller, J. Chem. Phys. 42,  
681 (1965).
52. C. R. Bowman, Technical Report No. AFWL-TR-66-37,  
General Dynamics, Fort Worth, Texas, (April 25, 1966).
53. H. H. Brongersma and L. J. Oosterhoff, Chem. Phys.  
Letters, 1, 169 (1967).
54. A. Kuppermann and L. M. Raff, J. Chem. Phys. 37, 2497  
(1962).
55. A. Kuppermann and L. M. Raff, Disc. Farad. Soc. 35,  
30 (1963).
56. A. Kuppermann and L. M. Raff, J. Chem. Phys. 39, 1607  
(1963).
57. J. P. Doering, J. Chem. Phys. 45, 1065 (1966).
58. J. P. Doering, J. Chem. Phys. 46, 1194 (1967).
59. F. L. Arnot and G. O. Baines, Proc. Roy. Soc. A151,  
256 (1935).
60. L. M. Raff, Ph.D. thesis, University of Illinois,  
Urbana, Illinois, (1962).
61. W.W. Lozier, Phys. Rev. 44, 575 (1935).
62. Ref. 60, pp. 83-88.
63. From ref. 9, p.215, the total collision cross section  
Q of 35 ev electrons in  $N_2$  is  $14\pi a_0^2$ . The number  
density n of  $N_2$  at  $10^{-4}$  torr and  $25^\circ C$  is  $3.25 \times 10^{12}$   
molecule/cc. Hence the mean free path  $L = (1.414 Q n)^{-1}$   
= 175 cm.

64. J. A. Simpson and C. E. Kuyatt, J. Appl. Phys. 37, 3805 (1966).
65. M. Pirani and J. Yarwood, "Principles of Vacuum Engineering", (Chapman and Hall, London, 1961) p.11.
66. The tube on the collision chamber side is  $16\frac{1}{2}$ " in length and  $1\frac{5}{8}$ " in inner diameter. The tube on the gun chamber side is  $17\frac{1}{2}$ " in length and  $1\frac{7}{8}$ " in inner diameter. The conductances are calculated for air at 20°C.
67. C. E. Moore, "Atomic Energy Levels", vol. 1, National Bureau of Standards, Circular No. 467, (U.S. Government Printing Office, 1949) p.4.
68. E. N. Lassette, F. M. Glaser, V. D. Meyer, and A. Skerbele, J. Chem. Phys. 42, 3429 (1965).
69. E. N. Lassette, V. D. Meyer, and M. S. Longmire, J. Chem. Phys. 41, 2952 (1964).
70. J. A. Simpson, M. G. Menendez and S. R. Mielczarek, Phys. Rev. 150, 76 (1966).
71. J. K. Rice, S. Trajmar, and A. Kuppermann, forthcoming.
72. a) For the states  $X^1\Sigma_g^+$ ,  $b^3\Sigma_u$ , and  $C^1\Pi_u$ : W. Kolos and L. Wolniewicz, J. Chem. Phys. 43, 2429 (1965);  
 b) For the  $B^1\Sigma_u^+$  state: W. Kolos and L. Wolniewicz, LMSS Technical Report, University of Chicago, p. 85, (1965).  
 c) For the  $a^3\Sigma_g^+$  state: C. B. Wakefield and E. R. Davidson, J. Chem. Phys. 43, 834 (1965).  
 d) For the  $c^3\Pi_u$  state: J. C. Browne, J. Chem. Phys. 40, 43 (1964).
73. C. E. Kuyatt, S. R. Mielczarek, and J. A. Simpson, Phys. Rev. Lett. 12, 293 (1964).
74. Y. Tanaka, M. Ogawa, and A. S. Jursa, J. Chem. Phys. 40, 3690 (1964).
75. W. Benesch, J. T. Vanderslice, S. G. Tilford, and P. G. Wilkinson, Astrophys. J. 142, 1227 (1965).
76. F. R. Gilmore, J. Quant. Spectr. Radiat. Transfer, 5, 369 (1965).

77. R. N. Zare, E. O. Larson, R. A. Berg, J. Mol. Spectr. 15, 117 (1965).
78. I. P. Zapesochnyi, and V. V. Skubenich, Optics and Spectroscopy 21, 83 (1966).
79. Y. Tanaka, A. S. Jursa, and F. LeBlanc, J. Chem. Phys. 26, 862 (1957).
80. R. E. Huffman, J. C. Larrabee, and Y. Tanaka, J. Chem Phys. 40, 2261 (1964).
81. G. Herzberg, J. D. Simmons, A. M. Bass, and S. G. Tilford, Can. J. Phys. 44, 3039 (1966).
82. J. D. Simmons, and S. G. Tilford, J. Chem. Phys. 45, 2965 (1966).
83. P. H. Krupenie and S. Weissman, J. Chem. Phys. 43, 1529 (1965).
84. P. H. Krupenie, "The Band Spectrum of Carbon Monoxide", National Standard Reference Data Series, U.S. National Bureau of Standards, 5, 1 (1966).
85. S. M. Silverman, and E. N. Lassette, J. Chem. Phys. 41, 3727 (1964).
86. V. D. Meyer, A. Skerbele, and E. N. Lassette, J. Chem. Phys. 43, 805 (1965).
87. A. Skerbele, V. D. Meyer, and E. N. Lassette, J. Chem. Phys. 44, 4069 (1966).
88. R. M. Hexter, J. Chem. Phys. 46, 2300 (1967).
89. G. Herzberg, "Molecular Spectra and Molecular Structure vol. 3, Electronic Spectra and Electronic Structure of Polyatomic Molecules", (D. Van Nostrand Co., 1966).
90. W. C. Price and W. T. Tutte, Proc, Roy. Soc. 174A, 207 (1940).
91. M. Zelikoff and K. Watanabe, J. Opt. Soc, Am. 43, 756 (1953).
92. P. G. Wilkinson and R. S. Mulliken, J. Chem. Phys. 23, 1895 (1955).
93. P. G. Wilkinson, Can. J. Phys. 34, 643 (1956).

94. C. Reid, J. Chem. Phys. 18, 1299 (1950).
95. D. F. Evans, J. Chem. Soc. 1735 (1960).
96. R. S. Mulliken, Rev. Mod. Phys. 14, 265 (1942).
97. W. J. Potts, Jr., J. Chem. Phys. 23, 65 (1955).
98. R. S. Mulliken, J. Chem. Phys. 33, 1596 (1960).
99. a) R. S. Berry, J. Chem. Phys. 38, 1934 (1963).  
b) M. B. Robin, R. R. Hart, and N. A. Kuebler, J. Chem. Phys. 44, 1803 (1966).  
c) H. Berthod, J. Chem. Phys. 45, 1859 (1966).  
d) B. G. Ramsey, J. Phys. Chem. 70, 4097 (1966).
100. A. Lubezky and R. Kopelman, J. Chem. Phys. 45, 2526 (1966).
101. J. Geiger and K. Wittmaack, Z. Naturforschung, 20A 628 (1965).
102. K. J. Ross and E. N. Lassetre, J. Chem. Phys. 44, 4633 (1966).
103. C. K. Ingold and G. W. King, J. Chem. Soc. pp. 2702-2755 (1953).
104. K.K.Innes, J. Chem. Phys. 22, 863 (1954).
105. T. Nakayama and K. Watanabe, J. Chem. Phys. 40, 558 (1964).
106. P. G. Wilkinson, J. Mol. Spec. 2, 387 (1958).
107. W. C. Price, Phys. Rev. 47, 444 (1934).
108. G. Moe and A. B. F. Duncan, J. Am. Chem. Soc. 74, 3136 (1952).
109. G. Herzberg, Trans. Farad. Soc. 27, 378 (1931).
110. G. Herzberg, Disc. Farad. Soc. 35, 7 (1963).
111. J. T. Hougen and J. K. G. Watson, Can. J. Phys. 43, 298 (1965).
112. I. G. Ross, Trans. Farad. Soc. 48, 973 (1952).

113. Yu. P. Yampol'skii and A. M. Brodskii, Doklady Physical Chemistry, 168, 411 (1966).
114. S. Trajmar, A. Kuppermann, and J. K. Rice, private communication.
115. J. L. Franklin and F. H. Field, J. Am. Chem. Soc. 76, 1994 (1954).
116. W. C. Price and A. D. Walsh, Trans. Farad. Soc. 41, 381(1945).
117. K. Watanabe and T. Namioka, J. Chem. Phys. 24, 915 (1956).
118. A. L. Lane, analyses done by gas chromatography, private communication.
119. A. G. Maki and R. A. Toth, J. Mol. Spec. 17, 136 (1965).
120. K. Griesbaum, Angewandte Chem. International Ed. in Eng. 5, 933 (1966).
121. L. H. Sutcliffe and A. D. Walsh, J. Chem. Soc. 899 (1952).
122. R. G. Parr and G. R. Taylor, J. Chem. Phys. 19, 497 (1951).
123. J. Serre, J. Chim. Phys. 53, 284 (1956).
124. R. Pariser and R. G. Parr, J. Chem. Phys. 21, 466 (1953); and *ibid* 21, 767 (1953).
125. W. T. Borden, J. Chem. Phys. 45, 2512 (1966).
126. J. A. Pople, Trans. Farad. Soc. 49, 1375 (1953).
127. H. Okabe and D. A. Becker, J. Chem. Phys. 39, 2549 (1963).
128. R. I. Schoen, J. Chem. Phys. 37, 2032 (1962).
129. M. I. Al-Joboury and D. W. Turner, J. Chem. soc. 4434 (1964).
130. J. R. McNesby and H. Okabe, Adv. Photochem. 3, 157 (1964).

131. H. Okabe and J. R. McNesby, J. Chem. Phys. 37, 1340 (1962).
132. A. H. Laufer and J. R. McNesby, J. Phys. Chem. 70, 4094 (1966).
133. R. E. Rebert and P. Ausloos, J. Chem. Phys. 46, 4333 (1967).
134. J. Berkowitz and W. A. Chupka, Physics Division Summary Report, Argonne National Laboratory, (Argonne, Illinois) ANL-7108, p.57 (1965).
135. H. Ehrhardt, F. Linder and G. Meister, Z. Naturforschung, 20a, 989 (1965).
136. G. Scheibe and H. Grieneisen, Z. physik. Chem. B25, 52 (1934).
137. W. C. Price and A. D. Walsh, Proc. Roy. Soc. 174A, 220 (1940).
138. K. Watanabe, J. Chem. Phys. 26, 542 (1957).
139. R. S. Mulliken, J. Chem. Phys. 7, 121 (1939).
140. R. S. Mulliken, J. Chem. Phys. 7, 373 (1939).
141. T. M. Sugden and A. D. Walsh, Trans. Farad. Soc. 41, 76 (1945).
142. R. G. Parr and R. S. Mulliken, J. Chem. Phys. 18, 1338 (1950).
143. a) D. J. Marais, N. Sheppard, and B. P. Stoicheff, Tetrahedron 17, 163 (1961).  
b) Yu. N. Panchenko, Yu. A. Pentin, V. I. Tyulin, and V. M. Tatevskii, Optics and Spect. 13, 488 (1962).
144. G. S. Hammond and R. S. H. Liu, J. Am. Chem. Soc. 85, 477 (1963).
145. G. S. Hammond, N. J. Turro, and P. A. Leermakers, J. Phys. Chem. 66, 1144 (1962).
146. R. Srinivasan, Adv. Photochem. 4, 113 (1966).
147. a) G. W. Robinson, J. Mol. Spec. 6, 58 (1961).  
b) A. C. Albrecht, J. Chem. Phys. 38, 354 (1963).

148. a) A. L. Sklar, J. Chem. Phys. 5, 669 (1937).  
b) G. N. Lewis and M. Kasha, J. Am. Chem. Soc. 67, 994 (1945).  
c) A. C. Pitts, J. Chem. Phys. 18, 1416 (1950).
149. a) D. F. Evans, J. Chem. Soc. 1351, 3885 (1957).  
b) G. W. King and E. H. Pinnington, J. Mol. Spec. 15, 394 (1965).  
c) A. Grabowska, J. Mol. Spec. 20, 96 (1966).
150. a) S. Leach, R. Lopez-Delgado, and L. Grajcar, J. Chim. Phys. 63, 205 (1966).  
b) G. C. Nieman and D. S. Tinti, J. Chem. Phys. 46 1432 (1967).
151. a) M. Goepfert-Mayer and A. Sklar, J. <sup>6</sup>Chem. Phys. 6, 645 (1938).  
b) H. B. Klevens and J. R. Platt, J. Chem. Phys. 17 470 (1949).
152. a) L. W. Pickett, M. Muntz, and E. M. McPherson, J. Am. Chem. Soc. 73, 4862 (1951).  
b) V. J. Hammond and W. C. Price, Trans. Farad. Soc. 51, 605 (1955).
153. a) W. C. Price and R. W. Wood, J. Chem. Phys. 3, 439 (1935).  
b) W. C. Price and A. D. Walsh, Proc. Roy. Soc. 191A, 22 (1947).  
c) P. G. Wilkinson, Can. J. Phys. 34, 596 (1956).  
d) M. A. El-Sayed, M. Kasha, and Y. Tanaka, J. Chem. Phys. 34, 334 (1961).
154. I. D. Clark and D.C. Frost, J. Am. Chem. Soc. 89, 244 (1967).
155. J. R. Platt, J. Mol. Spec. 9, 288 (1962).
156. a) S. D. Colson and E. R. Bernstein, J. Chem. Phys. 43, 2661 (1965).  
b) E. R. Bernstein and S. D. Colson, J. Chem. Phys. 45, 3873 (1966).
157. F. H. Read and G. L. Whiterod, Proc. Phys. Soc. (London) 85, 71 (1965).
158. G. S. Hammond, N. J. Turro, and A. Fischer, J. Am. Chem. Soc. 83, 4674 (1961).
159. G. S. Hammond, P. Wyatt, C. D. DeBoer, and N.J. Turro, J. Am. Chem. Soc. 86, 2532 (1964).

160. G. S. Hammond and J. Saltiel, J. Am. Chem. Soc. 85, 2515 (1963).
161. B. C. Roquette, J. Phys. Chem. 69, 2475 (1965).
162. C. F. Wilcox, Jr., S. Winstein, and W. G. McMillan, J. Am. Chem. Soc. 82, 5450 (1960).
163. W. G. Dauben and R. L. Cargil, Tetrahedron 5, 197 (1961).
164. B. C. Roquette, J. Am. Chem. Soc. 85, 3700 (1963).
165. S. Meyerson, J. D. McCollum, and P. N. Rylander, J. Am. Chem. Soc. 83, 1401 (1961).
166. Z. Dolejšek, V. Hanuš, and J. Prinzbach, Angewandte Chemie, International Ed. in Eng. 1, 598 (1962).
167. V. Hanuš and Z. Dolejšek, Coll, Czech. Chem. Commun. 28, 652 (1963).
168. R. B. Hermann, J. Org. Chem. 27, 441 (1962).
169. M. B. Robin and N. A. Kuebler, J. Chem. Phys. 44, 2664 (1966).
170. Carl C. Wamser, Private communication.
171. A. Fischer and G. S. Hammond, Unpublished work, 1961.

## Proposition 1

## A NITROGEN ATOM BEAM FROM ACTIVE NITROGEN

It is proposed that the technique of differential pumping can be applied to the sampling of active nitrogen in mass spectrometric study. It is hoped that atomic nitrogen beams may thus be obtained.

-----

I. Introduction

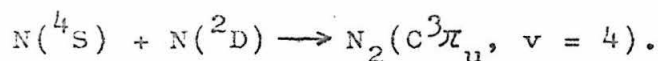
Unlike other homonuclear diatomic molecules, the nitrogen molecule has a very high bond energy of 225 kcal/mole (9.75 ev). Consequently, the equilibrium constant for the thermal dissociation reaction of  $N_2$  is very small even at high temperatures<sup>(1)</sup>. Thus, one of the effective ways to obtain atomic nitrogen is by electric discharge.

The Lewis-Rayleigh afterglow resulting from electric discharge in low pressure nitrogen gas has been known for half a century<sup>(2)</sup>. The first positive bands ( $B^3\Pi_g \rightarrow A^3\Sigma_u^+$ ) and the ( $Y^3\Sigma_u^- \rightarrow B^3\Pi_g$ ) system are the main features in the emission spectrum of the afterglow<sup>(3)</sup>. The chemical reactivity of the nitrogen afterglow with hydrocarbons<sup>(4)</sup>, iodine<sup>(5)</sup>, oxygen<sup>(6)</sup>, etc, gives rise to its name of active nitrogen.

In 1940 Rayleigh<sup>(7)</sup> was able to obtain about 10 ev per molecule from active nitrogen in its interaction with gold. This energy corresponds to the dissociation of an  $N_2$  molecule into an  $N(^4S)$  atom and an  $N(^2D)$  atom. (The nitrogen atom has three low-lying states,  $^4S$ ,  $^2D$ , and  $^2P$ . The  $^4S$  state is the ground state whereas the  $^2D$  and  $^2P$

metastable states lie at 2.383 and 3.574 eV, respectively, above the ground state).

Recently, by cooling the nitrogen afterglow to liquid nitrogen temperature, Tanaka, LeBlanc, and Jursa<sup>(8)</sup> were able to observe the second positive bands of nitrogen ( $C^3\Pi_u \rightarrow B^3\Pi_g$ ). They attributed the excitation of the bands at low temperature by an inverse predissociation process as follows.



Therefore the active nitrogen may contain excited as well as ground state nitrogen atoms and molecules.

## II. Comments on Early Mass Spectrometric Experiments

By measuring the appearance potential of the mass 14 peak with a mass spectrometer, Jackson and Schiff<sup>(9)</sup> were the first to detect the presence of the  $N(^4S)$  atom (about 0.1% to 1%) in active nitrogen. Later, Berkowitz, Chupka, and Kistiakowsky<sup>(10)</sup> also reported the presence of the  $N(^4S)$  atom (about 1%) with the same technique. However the metastable  $N(^2D)$  and  $N(^2P)$  atoms were not observed in these experiments although the presence of metastables was highly probable.

A typical case of sampling in the above mentioned mass spectrometric work is the situation in Berkowitz, Chupka, and Kistiakowsky's set-up<sup>(10)</sup>. Nitrogen gas (at the pressure of 1 torr) passes the discharge region, flows through about 1.2 meters of glass tubes (diameter 1.5 cm), and comes to the mass spectrometer leak. The

latter because of the pressure difference ( 1 torr to  $10^{-6}$  torr) has to be as small as 0.04 mm in diameter. According to these author's estimation, the flow time from the discharge region to the leak is about 0.25 second.

Simple calculations assuming the translational temperature of the N atoms at 25°C and a collision diameter of 3 Å show that the mean free path of the N atom is 0.077 mm at a pressure of 1 torr. An N atom on the average has to suffer  $2.2 \times 10^6$  collisions before it can leak into the mass spectrometer. We feel that even if the metastable atoms are produced in the discharge they may have lost their energy before they can be detected.

The purpose of this proposition is to suggest an improved sampling system on treating the problem by mass spectrometric method so that a nitrogen atom beam with known composition of ground and metastable states can be produced.

### III. The Sampling System With Differential Pumping

In principle, several regions of gradually decreasing pressure can be maintained between the discharge region and the ion source of the mass spectrometer. Large pinholes can be used to separate small pressure difference. Since the mean free path of the N atom increases to about half a meter when the pressure is reduced to  $10^{-4}$  torr, the active particles will not suffer as many collisions as before and may probably be detected.

In fact this differential-pumping-sampling technique has been adopted by Nutt and Biddlestone<sup>(11)</sup> who find the metastable  $O(^1D)$  atom in a discharge through oxygen gas by appearance potential measurements with a mass

spectrometer. Similar experiments by Foner and Hudson<sup>(12)</sup> also lead to the identification of the metastable  $N(^2D)$  and  $N(^2P)$  atoms in active nitrogen.

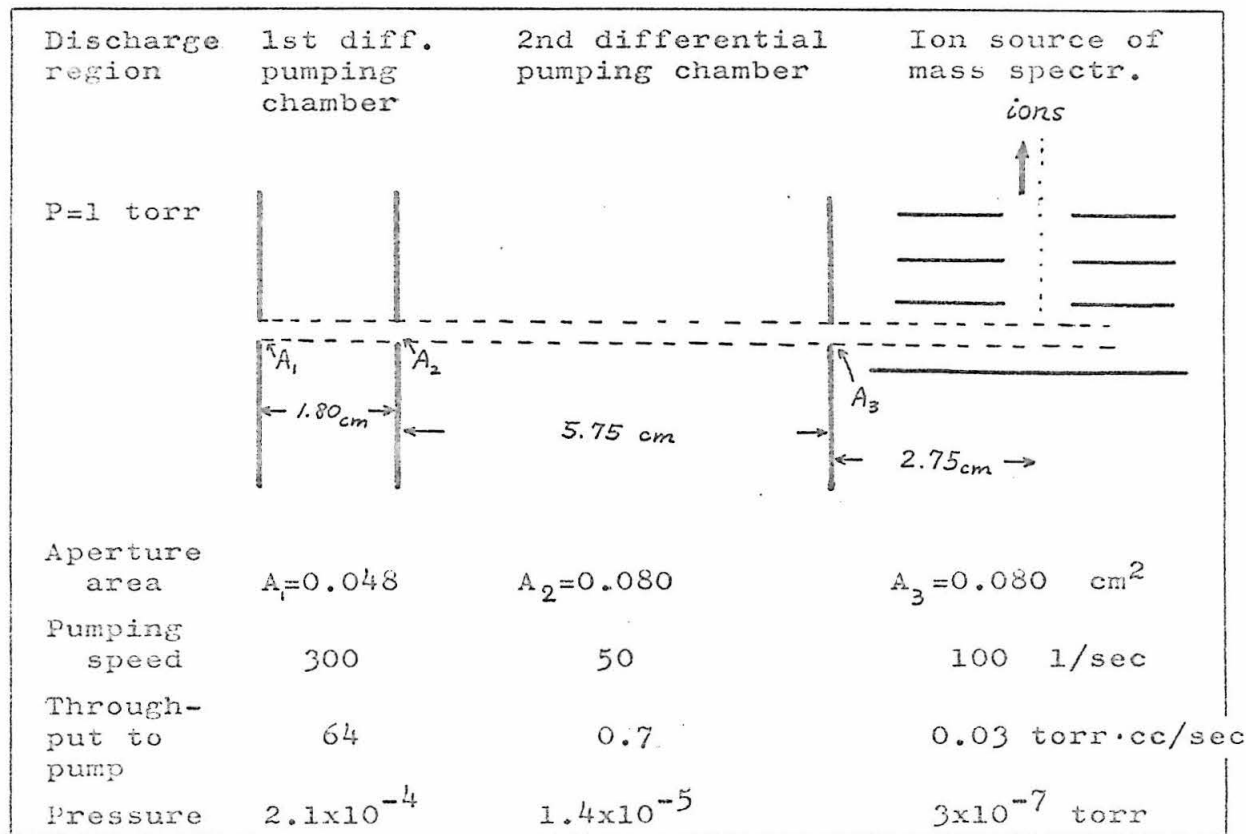


Figure 1. The sampling system with differential pumping.

Figure 1 shows a schematic diagram of the differential-pumping-sampling system. The geometry of Nutt and Biddleston's apparatus<sup>(11)</sup> is taken to demonstrate the feasibility of the experiment. The arbitrarily chosen pumping speed, the calculated throughput and the resulting pressure in each region are as indicated in Figure 1. A 30% dissociation in  $N_2$  at 25°C has been assumed.

According to the cosine law of distribution, there will be a throughput of 0.029 torr cc/sec of nitrogen atoms and molecules entering the ion source directly from the discharge region (with a flow time of less than  $2 \times 10^{-4}$  second). This is equivalent to a total number of  $9.35 \times 10^{14}$  molecule/second, or a flux of  $1.16 \times 10^{16}$  molecule/cm<sup>2</sup>/sec. If a 30% dissociation of  $N_2 \rightarrow N(^4S) + N(^2D)$  occurs and an average translational speed of  $6.71 \times 10^4$  cm/sec for the N atom is assumed, then there will be a density of  $4 \times 10^{10}$  atoms/cc of  $N(^2D)$  atoms present in the ion source. If the efficiency of the ion source and the mass analyzer is  $10^{-4}$ , then an ion current of  $6.4 \times 10^{-13}$  amp will be recorded on account of the presence of the  $N(^2D)$  atoms.

The number density of background molecules arising from the ambient pressure of  $3 \times 10^{-7}$  torr at 25°C in the ion source chamber is calculated to be  $9.7 \times 10^9$  molecule/cc. However, Nutt and Biddlestone<sup>(11)</sup> have shown that the actual number density of background molecules arising from the ambient pressure is two orders lower than the calculated value for this type of molecular beam input.

If we use an electron multiplier which measures currents as small as 10 ions per second, then about one part per million of  $N(^2D)$  atoms present in the active nitrogen will still be detectable.

The experiment proposed above has an important prospect, namely, an N atom beam of known composition can be generated. The  $N_2$  bond energy is too high for thermal dissociation method to give appreciable yields. Thus, the electric discharge seems to be a practical way in obtaining nitrogen atom beams. A prospective crossed-molecular-beam study involving the nitrogen atom beam is

discussed in the next proposition.

### References

1. The equilibrium constants  $K_p$  of dissociation reactions for  $N_2, O_2, H_2, Cl_2$ , and  $Br_2$  in the temperature range  $600^\circ$  to  $2000^\circ K$  have been tabulated by W. J. Moore, "Physical Chemistry", 3rd edition, (Prentice-Hall Inc. Englewood Cliffs, N. J., 1962) p. 179. For  $N_2$  at  $2000^\circ K$ ,  $K_p = 9.8 \times 10^{-13}$  (atm).
2. a) E. P. Lewis, *Astrophys. J.* 12, 8 (1900).  
b) Lord Rayleigh, *Proc. Roy. Soc.* A180, 123 (1942).
3. K. D. Bayes and G. B. Kistiakowsky, *J. Chem. Phys.* 32, 992 (1960).
4. R. A. Back and C. A. Winkler, *Can. J. Chem.* 32, 718 (1954).
5. C. G. Freeman and L. F. Phillips, *J. Phys. Chem.* 68, 362 (1964).
6. W. E. Wilson, *J. Chem. Phys.* 46, 2017 (1967)
7. Lord Rayleigh, *Proc. Roy. Soc.* A176, 16 (1940).
8. Y. Tanaka, F. LeBlanc, and A. Jursa, *J. Chem. Phys.* 30, 1624 (1959).
9. D. S. Jackson and H. I. Schiff, *J. Chem. Phys.* 23, 2333 (1955).
10. J. Berkowitz, W. A. Chupka, and G. B. Kistiakowsky, *J. Chem. Phys.* 25, 457 (1956).
11. C. W. Nutt and A. J. Biddlestone, *Trans. Farad. Soc.* 58, 1368 (1962).
12. S. N. Foner and R. L. Hudson, *J. Chem. Phys.* 37, 1662 (1962).

## Proposition 2

Reactive Collisions In Crossed Molecular Beams,  
The reaction of Nitrogen Atoms With Oxygen Molecules

It is proposed that the reaction  $N + O_2 \rightarrow NO + O$  can be studied by crossed molecular beams.

Preliminary calculations show that the activation energy is 5.9 kcal/mole and the reaction cross section is  $0.28 \text{ \AA}^2$  at  $2000^\circ\text{K}$ . A kinematic analysis of  $N$  (at  $3500^\circ\text{K}$ ) and  $O_2$  (at  $2000^\circ\text{K}$ ) crossing at  $90^\circ$  is presented, showing that such a study is feasible.

-----

I. Introduction

It is well known that the molecular mechanics and individual steps in chemical reactions can be studied most directly and efficiently by measuring the reaction cross sections. However, almost all of the bimolecular exchange reactions studied so far involves only alkali atoms and halogen compounds (1-5). The reasons for this are simply as follows.

a). The reaction products (alkali halides) can be easily detected by the two-filament surface-ionization detectors (6).

b). Large cross sections and small activation energies of these reactions lead to high collision yields which is a favorable experimental condition.

Recently in Professor Aron Kuppermann's laboratories,

a crossed molecular beam apparatus has been designed and constructed by Crawford<sup>(7)</sup> and Cross<sup>(8)</sup>. This instrument allows both in-the-plane and out-of-plane scanning of the reaction products from two beams crossing at 90°. The detector is a high efficiency ion source followed by a quadrupole mass filter and then an electron multiplier. Velocity selections on the faster beam give rise to well-defined relative initial kinetic energies (RIKE). Modulation on one of the beams at audio frequency permits the method of phase sensitive detection to enhance the signal-to-noise ratio. It is hoped that information concerning the reaction cross sections can be obtained by measuring the distribution of products as a function of the RIKE.

Two reactions have been picked and preliminarily analyzed by Crawford<sup>(7)</sup> and Cross<sup>(9)</sup>. The results are tabulated as follows.

<u>Reaction</u>	<u>E*, the activation energy</u>	<u><math>PX\sigma^2</math>, the estimated cross section</u>	<u>Remarks</u>
$\text{Cl} + \text{D}_2$ $\rightarrow \text{DCl} + \text{D}$	5 kcal/mole	$3.6 \text{ \AA}^2$	DCl will form a cone with a maximum half angle of 25° from the center-of-mass velocity vector <sup>(7)</sup>
$\text{O} + \text{H}_2$ $\rightarrow \text{OH} + \text{H}$	6 kcal/mole	$1 \text{ \AA}^2$	(9)

The purpose of this proposition is to present some preliminary analyses on the prospective reaction:



## II. Discussions

### II.1. Summary of rate constant measurements

The rate constants for reaction (1) at various temperatures have been measured by several groups of workers. The results are tabulated as follows.

Temperature, (°K)	rate constant, (cm <sup>3</sup> /mole/sec)	Reference
394° - 517°	$2 \times 10^{12} \exp(-6200/RT)$	Kistiakowsky and Volpi (10)
1500°-1700°	$1.7 \times 10^{13} \exp(-7500/RT)$	Kaufman and Decker (11)
412° — 755°	$8.3 \times 10^{12} \exp(-7100/RT)$	Clyne and Thrush (12)
350°	$5 \times 10^7$	Kretschmer and Peterson (13)
300° - 910°	$1.41 \times 10^{13} \exp(-7900/RT)$	Wilson (14)

A plot of  $\log_{10}k$  versus  $1/T$  including all experimental points except that of reference (13) has been presented by Wilson (14). It seems that the rate constant

$$k = 1.41 \times 10^{13} \cdot \exp(-7900/RT) \quad (2)$$

is the best fit on the experimental points in the temperature

range from 300° to 1700°K (14).

## II.2. Estimate of Reaction Cross Section and Activation energy

The rate constant in equation (2) is in the famous Arrhenius form. In order to estimate the reaction cross section and the activation energy let us consider the collision model for bimolecular reactions<sup>(15)</sup>. The rate constant predicted from the collision model can be written as

$$k = p \pi \sigma^2 \left( \frac{8RT}{\pi \mu} \right)^{\frac{1}{2}} \exp(-E^*/RT), \quad (3)$$

where  $Z = \pi \sigma^2 \left( \frac{8RT}{\pi \mu} \right)^{\frac{1}{2}}$  is the specific collision frequency,  $\pi \sigma^2$  is the hard sphere collision cross section,  $R$  is the gas constant,  $\mu$  is the reduced mass per mole,  $p$  is a steric factor, and  $E^*$  is the activation energy with the assumption that a collision may lead to reaction if and only if the relative kinetic energy along the line of centers at impact is larger than or equal to  $E^*$ .

We see that equation (2) has the Arrhenius form of

$$k = A \exp(-E/RT), \quad (4)$$

whereas equation (3) has a different form of

$$k = BT^{\frac{1}{2}} \exp(-E^*/RT). \quad (5)$$

(The exponential dependence of  $k$  on  $1/T$  makes it difficult

to distinguish between different preexponential factors arising from different models by ordinary experimental data.)

If we assume that equations (4) and (5) represent the same rate constant  $k$  for an arbitrary temperature  $T$ , then it can be shown that

$$E^* = E - \frac{1}{2}RT,$$

$$B = A T^{-\frac{1}{2}} \exp(-\frac{1}{2}).$$

If the experimental rate constant in equation (2) can be extended to say,  $2000^\circ\text{K}$ , then

$$E^* = 5.91 \text{ kcal/mole},$$

and  $p\pi\sigma^2 = 0.275 \text{ \AA}^2.$

If one picks  $\sigma = 3 \text{ \AA}$  arbitrarily, then the steric factor is

$$p = 0.01,$$

which means that about every one collision per hundred with RIKE greater than  $E^*$  will lead to reaction.

### II.3. The Relative Initial Kinetic Energy RIKE

If the calculated activation energy of 5.9 kcal/mole is meaningful, then we would like to perform our experiment with RIKE both above and below this value. Assuming that  $\text{N}(^4\text{S})$  atoms can be generated from a high temperature electric discharge and that the N beam crosses the  $\text{O}_2$  beam at  $90^\circ$ , then the RIKE can be calculated by using the most probable velocities  $v = (2RT/m)^{\frac{1}{2}}$ .

The results are tabulated as follows.

RIKE ( kcal/mole )		N beam temperature		
		2000°k	3000°k	3500°k
O <sub>2</sub> beam temper- ature	1500°k	3.68	5.05	5.76
	2000°k	3.94	5.36	6.09
	2500°k	4.28	5.66	6.37

#### II.4. Prediction on the Distribution of Products

Let us now consider the case of an O<sub>2</sub> beam at 2000°k and an N beam at 2500°k crossing at 90° as an example. The most probable velocities of the reactants are

$$v_N (3500^\circ\text{k}) = 2.04 \times 10^5 \text{ cm/sec, and}$$

$$v_{O_2} (2000^\circ\text{k}) = 1.02 \times 10^5 \text{ cm/sec.}$$

The most probable center-of-mass velocity is (see Figure 1)

$$c = 0.94 \times 10^5 \text{ cm/sec}$$

with  $\theta_c = 48.87^\circ$

= angle between  $\vec{v}_N$  and  $\vec{c}$ .

The most probable relative velocity is

$$v_r = 2.29 \times 10^5 \text{ cm/sec}$$

The rotational energy of O<sub>2</sub> at 2000°k is

$$E_{(\text{rot.})} = 2 \times ( RT/2 ) = 3.97 \text{ kcal/mole.}$$

The vibrational energy of O<sub>2</sub> at 2000°k can be calculated

with the simple harmonic oscillator model (16). With  $\nu = 1556 \text{ cm}^{-1}$  (17), we have

$$E(\text{vib.}) = \frac{h\nu}{e^{h\nu/kT} - 1} = 2.15 \text{ kcal/mole.}$$

The difference in dissociation energies of  $\text{O}_2$  and  $\text{NO}$  is (18)

$$\begin{aligned} \Delta D_0^\circ &= D_0^\circ(\text{NO}) - D_0^\circ(\text{O}_2) \\ &= 32.4 \text{ kcal/mole} \end{aligned}$$

The total reaction energy is then

$$\begin{aligned} E_{\text{total}} &= \Delta D_0^\circ + E(\text{vib.}) + \text{RIKE} + E_{(\text{rot.})} \\ &= 44.61 \text{ kcal/mole.} \end{aligned}$$

From the law of conservation of energy and momentum we can calculate the most probable velocity for the product molecule ( nitric oxide,  $\text{NO}$  ) in the center-of-mass coordinate system for a given relative final kinetic energy (RFKE) of the products. Since it is equally probable for  $\text{NO}$  to fly apart in any direction in the center-of-mass system provided the molecular complex  $\text{NO}_2$  stays long enough, the product  $\text{NO}$  will be evenly distributed around a circle centered at the tip of the center-of-mass velocity vector  $\vec{c}$  with a radius proportional to the most probable relative speed  $v_{\text{NO}}$ . In the laboratory coordinate system,  $\text{NO}$  will confine to a cone if  $v_{\text{NO}}$  is smaller than  $|\vec{c}|$ . The calculated results are tabulated as follows.

RFKE (kcal/mole)	1	4	9
RFKE/ $E_{total}$	2.25%	9%	20.2%
$v_{No}$ cm/sec	$0.312 \times 10^5$	$0.624 \times 10^5$	$0.936 \times 10^5$
distribution of NO in the laboratory system	a cone around $\vec{c}$ , half angle $19.3^\circ$	a cone around $\vec{c}$ , half angle $41.3^\circ$	starts to spread over $4\pi$ steradians

The Newton diagram for N (3500°k) and O<sub>2</sub> (2000°k) crossing at 90° is shown in Figure 1.

## II.5. Experimental considerations

Let us assume that we have a quadrupole mass spectrometer capable of distinguishing a partial pressure of  $10^{-13}$  torr (19) from the background. This corresponds to a minimum detectable density of NO products of  $2.2 \times 10^3$  molecule/cc at 25°c. For the case of RFKE = 4 kcal/mole, the minimum flux of NO must be:

$$\begin{aligned} f_{No} &= v_{No} \times 2.2 \times 10^3 \\ &= 1.37 \times 10^8 \text{ molecule/cm}^2/\text{sec.} \end{aligned}$$

If the entrance slit of the mass spectrometer is 10 cm from the collision center and the products are uniformly distributed within the solid angle subtended by the cone with a half angle of  $41.3^\circ$ , then the minimum rate of production for the NO molecules must be :

$$\begin{aligned} F_{No} &= f_{No} \cdot \int_{0^\circ}^{41.3^\circ} (10 \text{ cm})^2 2\pi \sin\theta d\theta \\ &= 2.14 \times 10^{10} \text{ molecule/sec.} \end{aligned}$$

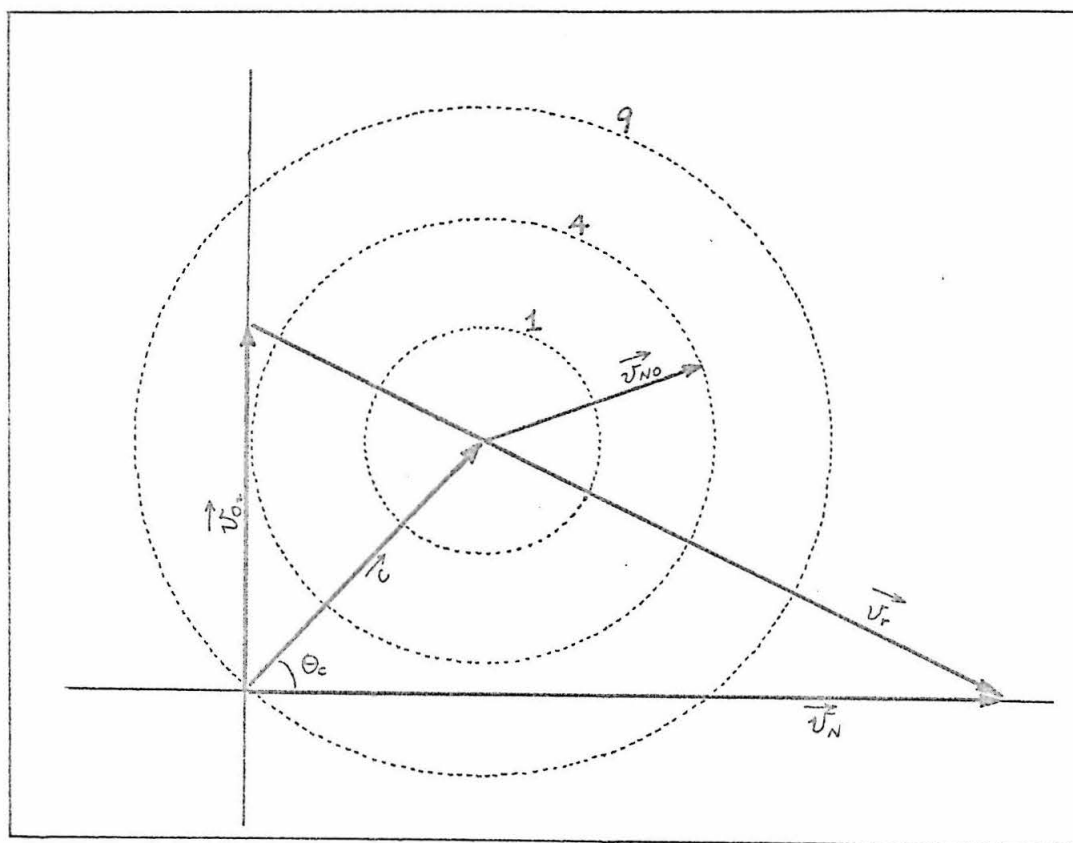


Figure 1. The Newton diagram for N(3500°K) and O<sub>2</sub>(2000°K) crossing at 90°, plotted with most probable velocities. The circles marked with 1, 4, and 9 represent the RFKE of the products in kcal/mole. When the RFKE is 4, the NO products would distribute on the circle "4" in the center-of-mass system.

Assuming the collision center has a volume of  $V=0.125 \text{ cm}^3$ , say, then the number densities of the reactants can be calculated as follows.

$$\begin{aligned} (n_{\text{O}_2}) (n_{\text{N}}) &= \frac{F_{\text{NO}}}{(v_r) V (\rho \pi \sigma^2)} \\ &= (1.65 \times 10^{11} \text{ molecule/cc})^2 . \end{aligned}$$

If  $n_{O_2} = n_N$ , then we must have a minimum reactant density of  $n_{O_2} = n_N = 1.65 \times 10^{11}$  molecules/c c.

The detailed design of the differential pumping chambers and the ovens can be based on these preliminary calculations.

### III. Conclusions

The discussions presented above have been based on the rate constant measured from reactions involving only ground state nitrogen atoms. However, if a reasonable amount of metastable  $N(^2D)$  atoms could be generated from an electric discharge then we would expect to have a different potential energy surface for the reaction. Since the nitrogen ( $^2D$ ) state lies at 55 kcal/mole higher than the ( $^4S$ ) state, the  $N(^2D) + O_2$  reaction would probably proceed with a much lower activation energy and a higher cross section than the  $N(^4S) + O_2$  one. A method to obtain metastable nitrogen atoms in an atomic beam has been discussed in the preceding proposition.

By measuring the distribution of the product NO in the laboratory, we can obtain information concerning the lifetime of the intermediate molecular complex  $NO_2$  as well as the partition of the reaction energy among the relative translational degree of freedom. For example if  $|\vec{v}_{NO}|$  is smaller than  $|\vec{c}|$ , then NO will be confined in a cone around  $\vec{c}$  in the center-of-mass coordinate system. Furthermore, if the distribution is uniform in the c.m. system then we know that the lifetime of the complex must be longer than a typical rotational period, say  $10^{-11}$  second. We see that the ordinary "rate constant as a function of temperature" measurements can not yield this kind of information.

Reference

1. For the reaction  $K + HBr$ :
  - a). E. H. Taylor and S. Datz, J. Chem. Phys. 23, 1711 (1955).
  - b). E. F. Greene, R. W. Roberts, and J. Ross, J. Chem. Phys. 32, 940 (1960).
  - c). D. Beck, E. F. Greene, and J. Ross, J. Chem. Phys. 37, 2895 (1962).
  - d). A. E. Grosser, A. R. Blythe, and R. B. Bernstein, J. Chem. Phys. 42, 1268 (1965).
2. For the reactions  $M (M = K, Rb, Cs) + RI (R = CH_3, C_2H_5, C_3H_7)$ : D. R. Herschbach, Disc. Farad. Soc. 33, 149 (1962).
3. For the reactions  $M (M = K, Rb, Cs) + XY (XY = Br_2, I_2, ICl, IBr)$ :
  - a). S. Datz and R. E. Minturn, J. Chem. Phys. 41, 1153 (1964).
  - b). K. R. Wilson, G. H. Kwei, J. A. Norris, R. R. Herm, J. H. Bireley, and D. R. Herschbach, J. Chem. Phys. 41, 1154 (1964).
  - c). A. E. Grosser and R. B. Bernstein, J. Chem. Phys. 43, 1140 (1965).
4. There are several examples on work not using surface-ionization detectors.
  - a). For the reaction of  $H + D_2$ :  
S. Datz and E. H. Taylor, J. Chem. Phys. 39, 1896 (1963).
  - b). For the reaction of  $D + H_2$ :  
W. L. Fite and R. T. Brackmann, J. Chem. Phys. 42, 4057 (1965).
  - c). For the reaction of  $M (M = K, Cs) + TBr$  :  
L. R. Martin and J. L. Kinsey, J. Chem. Phys. 46, 4834 (1967).
5. An excellent review is given by D. R. Herschbach in "Advances In Chemical Physics", vol. 10, edited by J. Ross, (J. Wiley and Sons, New York, 1966) pp. 319 - 393.

6. E. H. Taylor and S. Datz, J. Chem. Phys. 25, 389, 395 (1956).
7. O. H. Crawford, Ph.D. thesis submitted to the University of Illinois, Urbana, Ill., 1966.
8. J. B. Cross, Ph.D. thesis submitted to the University of Illinois, Urbana, Ill., 1966.
9. J. B. Cross, private communication, 1966.
10. G. B. Kistiakowsky and G. G. Volpi, J. Chem. Phys. 27, 1141 (1957).
11. F. Kaufman and L. J. Decker, International Symposium on Combustion, 7 th, London, Oxford 1958, p. 57 (1959)
12. M. A. A. Clyne and B. A. Thrush, Proc. Roy. Soc. (London) A 261, 259 (1961).
13. C. B. Kretschmer and H. L. Petersen, J. Chem. Phys. 39, 1772 (1963).
14. W. E. Wilson, J. Chem. Phys. 46, 2017 (1967).
15. S. W. Benson, "The Foundations of Chemical Kinetics", (McGraw-Hill Book Co., Inc., New York, 1960) p. 271.
16. G. M. Barrow. " Physical Chemistry ", ( McGraw-Hill Book co., 1961) p. 105.
17. G. Herzberg, "Spectra of Diatomic molecules ", (D. van Nostrand Co., Inc., New York, 2nd edition, 1950) p. 560.
18. A. G. Gaydon, " Dissociation Energies and Spectra of Diatomic Molecules," (Chapman and Hall, London, 2nd edition, 1953).
19. C. Bruneau, L. Delgmann, and K. Kronenberger, Vacuum Tech. 13, 35 (1964).

## Proposition 3

ELECTRONIC ABSORPTION SPECTRA OF OH AND OD  
RADICALS TRAPPED IN RARE GAS MATRICES

It is proposed that the observed fine structure of the  $A^2\Sigma^+ \leftarrow X^2\Pi_i$  transition in OH and OD trapped in rare gas matrices at 4.2°K may have its origin in hindered translation rather than hindered rotation.

Preliminary results of the (0,0) and (1,0) bands are reported. However, the observed fine structure does not show a large isotope effect, nor can it be correlated with the rotational structure of the gas phase spectrum. These facts cast doubt on an interpretation based on hindered rotation.

I. Introduction

The gas phase emission spectra of the  $A^2\Sigma^+ \leftarrow X^2\Pi_i$  system of the hydroxyl radical have been known since early this century <sup>(1)</sup>. A great deal of work has been done to study the various ( $v'$ ,  $v''$ ) bands of OH and OD either by an electrical discharge through water vapor or by an oxyhydrogen flame <sup>(2,3)</sup>. The lifetime of OH in this type of experiment is about 1/8 seconds as shown by the absorption of OH after the discharge is stopped <sup>(4)</sup>.

Recently many papers have been published on the subject of spectroscopic studies on active molecules or radicals trapped in the solids of gases at low temperatures <sup>(5)</sup>. The ultraviolet absorption of OH was first observed by Robinson and McCarty in 1958 <sup>(6,7)</sup> in the solid condensed from a discharge through moist hydrazine and

argon. They assigned the absorption feature at  $32090\text{cm}^{-1}$  to the (0,0) transition of the  $A^2\Sigma^+ \leftarrow X^2\Pi_1$  system of OH. Many free radicals and molecules trapped in inert gas matrices have been studied since then<sup>(8,9)</sup>, but it seems that the important diatomic molecule OH has not received much attention.

The results of this paper show that OH (or OD) radicals can be formed and trapped for hours after the rare gas matrices containing about 1%  $\text{H}_2\text{O}$  (or  $\text{D}_2\text{O}$ ) at  $4.2^\circ\text{K}$  are exposed to X-ray. The (0,0) as well as (1,0) bands of the  $A^2\Sigma^+ \leftarrow X^2\Pi_1$  transition in OH trapped in xenon, krypton and argon and those of OD in xenon are reported. Further possible experiments are suggested.

## II. Experimental

The apparatus used in this experiment has been described by Frosch and Robinson<sup>(9,10)</sup>. A cold trap containing ice is added to the inlet manifold and is cooled to  $-53^\circ\text{C}$  by a dry ice and acetone mixture. The vapor pressure of ice at  $-53^\circ\text{C}$  is 0.020 torr. The rare gas sample from a high pressure tank leaks in through a Pyrex capillary leak to the inlet manifold at the rate of  $3 \pm 2$  ml STP/min. It flows through the cold trap containing water then through a small copper tube leading to the cold finger chamber and deposits on the liquid-helium-cooled sapphire window. The pressures in the cold finger chamber and the inlet manifold are  $1.6 \times 10^{-3}$  and 2.1 torr, respectively, during the deposition. The deposition is generally carried out for four hours.

After the deposition process is stopped, pressure in the cold finger chamber drops to the  $10^{-8}$  torr region.

The solids condensed on the sapphire window are irradiated with 50 kv X-ray for 15 minutes or longer. Then absorption spectra are taken with a prism spectrograph which gives a  $14.7 \text{ \AA/mm}$  (or  $150\text{cm}^{-1}/\text{mm}$ ) resolution around the  $3125 \text{ \AA}$  region where the (0,0) band of OH lies. A high pressure xenon lamp is used as light source. The emission lines from a mercury lamp are used as standards. Exposure times are from 1/2 to 5 minutes with Eastman Kodak 103a-0 plates.

The emission spectra of the solids during X-ray irradiation are also taken. Exposure times are from 5 to 30 minutes with Eastman Kodak 103a-0 and 103a-F plates. *No emission band can be assigned to OH or OD.* However, the nitrogen Vegard-Kaplan bands ( $A^3\Sigma_u^+ \rightarrow X^1\Sigma_g^+$ ) in the region  $2500\text{--}3500 \text{ \AA}$  <sup>(11)</sup> and the oxygen Herzberg bands ( $C^3\Sigma_u^+ \rightarrow X^3\Sigma_g^-$ ) in the region  $3800\text{--}5600 \text{ \AA}$  <sup>(11)</sup> have been observed in some of the runs. This is probably due to residue air in the vacuum system which still remains even after flushing the system with rare gas for several times.

The  $D_2O$  sample is from the General Dynamics Corporation with a specified purity of 99.7%. The vacuum system is saturated with  $D_2O$  vapor for over night before fresh  $D_2O$  is introduced to the cold trap and vice versa for switching from  $D_2O$  to  $H_2O$ .

### III. Results

The ultraviolet absorption spectra of OH in xenon, krypton and argon and those of OD in xenon are observed. The bands are assigned to the (0,0) and (1,0) of the  $A^2\Sigma^+ \leftarrow X^2\Pi$  electronic transition of OH and OD in correlation to gas phase spectra <sup>(12)</sup>.

In general, each vibrational band consists of four

lines with increasing separation and decreasing intensity towards the longer wavelength side. In some bands only three lines can be distinguished whereas in the (1,0) band of OD in xenon, only two lines are measurable. The observed bands and the corresponding estimated intensities are listed in Table 1.

The appearance of the absorption lines is generally broad and diffuse. Their widths as seen from the photographic plates are approximately 3 to 6  $\text{cm}^{-1}$  for the cases of OH in argon and krypton, and are about 10  $\text{cm}^{-1}$  for OH and OD in xenon. However, the mercury standard lines are sharp.

Equivalent lines in the (0,0) and the (1,0) bands can be correlated from their intensity distribution. The difference between two corresponding equivalent lines is taken as the vibrational quantum  $\Delta G_{\frac{1}{2}}$  of the  $A^2\Sigma^+$  excited state. Table 2 lists the  $\Delta G_{\frac{1}{2}}$  values for various cases. Gas phase values are also given. The increasing matrix shifts from argon to krypton to xenon are similar to the situation of NH and ND trapped in these matrices (13).

Table 2 The vibrational quanta and their matrix shifts of the  $A^2\Sigma^+$  excited state in OH and OD

Gas (14)	$\Delta G_{\frac{1}{2}}(\text{OH})$	Matrix shift	$\Delta G_{\frac{1}{2}}(\text{OD})$	Matrix shift
	2989 $\text{cm}^{-1}$	---	2214 $\text{cm}^{-1}$	---
A	2904 $\pm$ 9	-85 $\pm$ 9	---	---
Kr	2860 $\pm$ 20	-129 $\pm$ 20	---	---
Xe	2840 $\pm$ 30	-149 $\pm$ 30	2135 $\pm$ 40	-80 $\pm$ 40

By using the equations relating the vibrational frequencies of isotopic molecules given by Herzberg<sup>(15)</sup>, i.e.,

$$\Delta G_{\frac{1}{2}} = \omega_e - 2 \omega_e x_e \quad , \quad (1)$$

$$\omega_e = \rho \omega_e^c \quad , \quad (2)$$

Table 1. Observed absorption bands of OH and OD in rare gas matrices. ( $A^2\Sigma^+ \leftarrow X^2\Pi_i$ )

Bands	Intensity	$\lambda_{\text{air}}$ ( $\text{\AA}$ )	$\nu_{\text{vac.}}$ ( $\text{cm}^{-1}$ )	Differences	
OH in argon	(0,0)	2	3126.1	31979 $\pm$ 3	
		10	3116.9	32074 3	
		9	3109.6	32149 3	
	(1,0)	1	2865.9	34883 $\pm$ 6	
		4	2858.2	34977 3	
3	2851.8	35055 3			
OH in krypton	(0,0)	1	3143.4	31803 $\pm$ 10	
		6	3132.6	31913 3	
		10	3123.5	32006 3	
		8	3116.3	32080 3	
	(1,0)	< 1	2884.0	34663 $\pm$ 10	
		2	2874.6	34778 3	
4	2866.2	34879 3			
3	2860.2	34953 3			
OH in xenon	(0,0)	< 1	3182.9	31608 $\pm$ 15	
		1	3150.6	31730 15	
		2	3141.2	31825 10	
		2	3133.1	31908 10	
	(1,0)	< 1	2902.1	34448 $\pm$ 15	
		< 1	2891.9	34569 15	
		1	2882.9	34677 15	
1	2876.8	34751 15			
OD in xenon	(0,0)	1	3143.4	31803 $\pm$ 10	
		2	3132.3	31916 10	
		2	3124.2	31999 10	
	(1,0)	0	-----	-----	
		1	2935.9	34051 $\pm$ 30	
1	2929.0	34142 30			

$$\text{and } \omega_e \chi_e = \rho^2 \omega_e^i \chi_e^i, \quad (3)$$

$$\text{where } \rho = \sqrt{\frac{\mu}{\mu_i}} = \sqrt{\frac{\mu_{OH}}{\mu_{OD}}} = 0.727, \text{ and}$$

$$\rho^2 = \left[ \sqrt{\frac{\mu_{OH}}{\mu_{OD}}} \right]^2 = 0.530,$$

and the observed  $\Delta G_{\frac{1}{2}}(\text{OH})$  and  $\Delta G_{\frac{1}{2}}(\text{OD})$  values in xenon, the constants  $\omega_e$  and  $\omega_e \chi_e$  of OH and OD in xenon can be calculated. This is tabulated in Table 3.

Table 3 Vibrational constants of the  $A^2\Sigma^+$  state in OH and OD

		$\omega_e$	$\omega_e \chi_e$
OH	Gas <sup>(12)</sup>	3180.5 cm <sup>-1</sup>	94.93 cm <sup>-1</sup>
	Xe	3200±280	180±140
OD	Gas <sup>(12)</sup>	2319.9	52.0
	Xe	2327±204	95.3±74

We see from Table 3 that the  $\omega_e$  values of OH and OD in xenon are in good agreement with the corresponding gas phase values. This serves as a check to the correctness of the assignments and is also an evidence of the presence of the OH and OD in these solids.

The fact that the  $\omega_e \chi_e$  values are larger in xenon matrices than in the gas phase may be explained as due to increasing anharmonicity of the vibrational motion of OH and OD in the solid matrices.

#### IV. Discussion

It would be of great interest if some correlation could be established between the observed fine structure of the vibrational bands in solids and the rotational structure in the gas phase. For this purpose the energy diagram of the  $A^2\Sigma^+ \leftarrow X^2\Pi_2$  transition of OH in the gas phase is given in Figure 1.

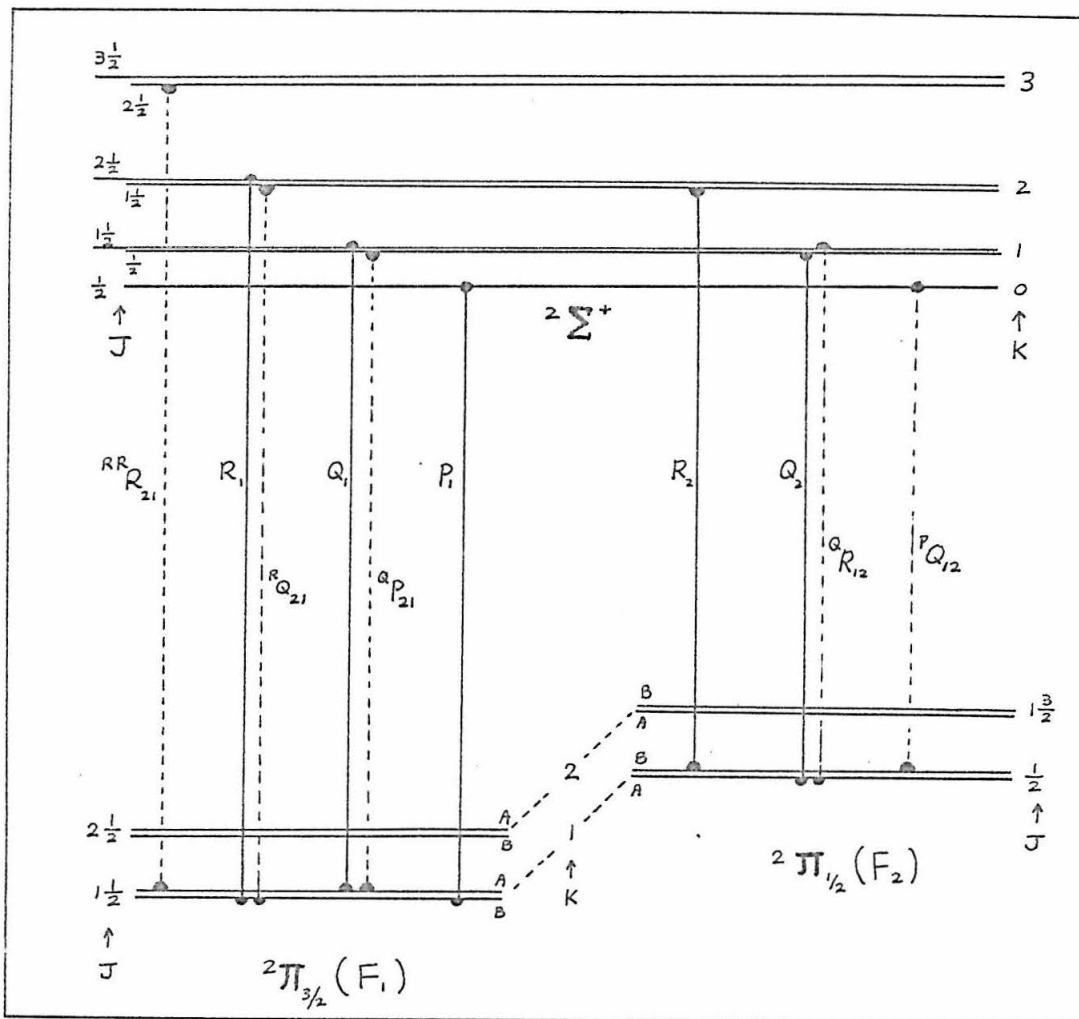


Figure 1. Energy level diagram of the  $A^2\Sigma^+ \leftarrow X^2\Pi_i$  transition in the hydroxyl radical. All allowed transitions from the lowest rotational levels of the  $2\Pi_i$  state are shown as vertical lines. Dashed lines are satellite bands.

The magnitude of  $kT$  at  $4.2^\circ\text{K}$  is  $2.92\text{ cm}^{-1}$ . Therefore, only the lowest rotational states are populated. The  $\Lambda$ -type doubling of the rotational levels in the  $2\Pi$  state is of the order of  $0.1\text{ cm}^{-1}$  (16), which is small compared to  $kT$ . Hence both sublevels are populated.

As a consequence of the relaxation from the first excited  $A^2\Sigma^+$  state, both the  $2\Pi_{1/2}$  and  $2\Pi_{3/2}$  states can be populated. The interconversion from  $2\Pi_{1/2}$  to  $2\Pi_{3/2}$  is forbidden by the

selection rule<sup>(17)</sup>

$$\Delta \Sigma = 0$$

for Hund's case (a), which is the case for the ground state of OH at the lowest rotational levels. Thus one would expect absorptions from the lowest rotational levels of both  ${}^2\Pi_{1/2}$  and  ${}^2\Pi_{3/2}$  to occur at liquid helium temperature.

All possible transitions are shown in Figure 1 by vertical lines. Dashed lines are satellite bands, that is

$$\Delta K \neq \Delta J .$$

Earls<sup>(18)</sup> put the intensity expressions, which were derived by Hill and Van Vleck<sup>(19)</sup> for the transitions in diatomic molecules, in simple algebraic forms. Using Earls' formulae and choosing a value of  $\lambda = A/B = -7.41$ <sup>(20)</sup> the relative intensity of each transition is calculated. Table 4 lists the observed gas phase (0,0) transitions from the lowest rotational levels of the  ${}^2\Pi_i$  state to the  $A^2\Sigma^+$  state. The calculated intensities are included with the assumption that the lowest rotational levels of  ${}^2\Pi_{1/2}$  and  ${}^2\Pi_{3/2}$  are equally populated. The difference between  $P_1(1)$  of the (0,0) and the (1,0) bands of OH (or OD) has been taken as  $\Delta G_{1/2}$  for OH (or OD) in the gas phase.

If we neglect the spin doubling of the  $A^2\Sigma^+$  state and the  $\Lambda$ -type doubling of the  ${}^2\Pi_i$  states, which are on the order of 1 and 0.1  $\text{cm}^{-1}$ , respectively<sup>(16)</sup>, then a gas phase spectrum of the OH(0,0) band (involving only the lowest rotational levels of the  $X^2\Pi_i$  state can be constructed from Table 4. This is shown in Figure 2(a).

Table 4. The gas phase spectrum of the  $A^2\Sigma^+ \leftarrow X^2\Pi_i$  transition in OH originating from the lowest rotational levels of the  $X^2\Pi_i$  state (s=satellite bands).

OH (0,0 ) lines		calculated relative intensity	$\hat{\nu}$ (cm <sup>-1</sup> )	inter-vals
$^2\Sigma^+ \leftarrow ^2\Pi_{3/2}$	<sup>RR</sup> R <sub>2,1</sub> (1), s	0.0462, (sum) ↓	(b)32643.39	101.11
	R <sub>1</sub> (1) <sup>R</sup> Q <sub>2,1</sub> (1), s	0.166 } 0.244 } 0.410	(a)32542.28	
	<sup>Q</sup> Q <sub>1</sub> (1) <sup>a</sup> P <sub>2,1</sub> (1), s	0.564 } 0.390 } 0.954	(a)32474.70	67.58
	P <sub>1</sub> (1)	0.590	(a)32440.89	33.81
	$^2\Sigma^+ \leftarrow ^2\Pi_{1/2}$	R <sub>2</sub> (1)	0.167	(a)32415.67
<sup>a</sup> Q <sub>2</sub> (1) <sup>a</sup> R <sub>1,2</sub> (1), s		0.333 } 0.167 } 0.500	(a)32348.26	67.41
<sup>P</sup> Q <sub>1,2</sub> (1), s		0.333	(a)32314.23	34.04
OH (0,0) (1,0)	P <sub>1</sub> (1) P <sub>1</sub> (1)		(a)32440.89 (c)35429.44	2988.55
	OD (0,0) (1,0)	P <sub>1</sub> (1) P <sub>1</sub> (1)	(d)32529.79 (e)34743.4	2213.6

#### References

- a). M. R. Fortrat, J. de Physique 5, 20 (1924).  
 b). R. S. Mulliken, Phys. Rev. 32, 388 (1928).  
 c). W. W. Watson, Astrophys. J. 60, 145 (1924).  
 d). H. Oura and M. Ninomiya, Proc. Phys. Math. Soc. Japan, 25, 335 (1943).  
 e). M. G. Sastry and K. R. Rao, Ind. J. Phys. 15, 27 (1941).

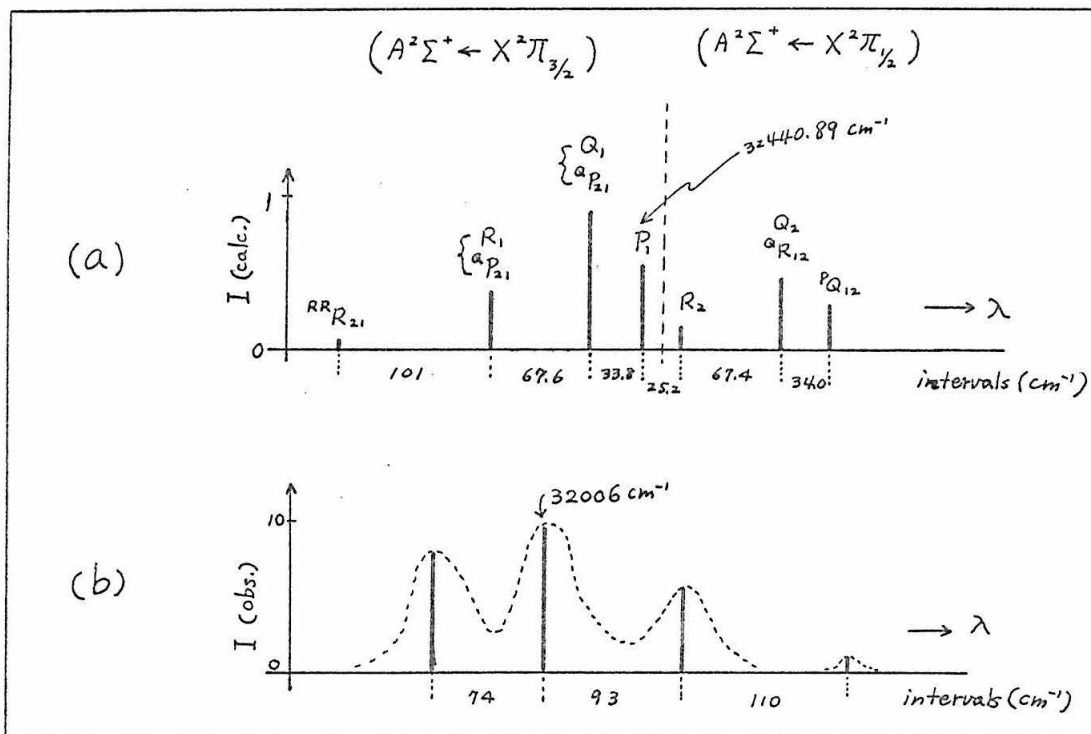


Figure 2. Spectrum of the OH (0,0) band. a) Constructed from gas phase values with calculated relative intensities. Only the lowest rotational levels of the  $X^2\Pi_i$  state are included. b) Observed, OH in krypton.

Figure 2(b) shows the observed spectrum of the OH (0,0) band in krypton. We see that Figure 2(b) is quite different from Figure 2(a). No simple correlation can be made with the presently available data.

Another interesting point is that the observed fine structures of OH and OD in xenon do not seem to show the large isotope effect as one would expect to see in the rotational structure. However, if the fine structure is due partly or mainly to the translational motion of OH and OD in the occupied lattice site rather than due to

hindered rotations in the solids, then one would expect to see only a small isotope effect between OH and OD.

It is felt that higher resolution spectrographs must be used to clarify this, and that the experiments of OD in krypton and argon may be carried out for a complete comparison.

Evidently the molecules OH and OD in their excited states could have more interactions with the host lattice than in the ground states. Thus, it would be of interest if a study on the infrared spectra of these molecules trapped in rare gas solids could be carried out.

Recently, the  $A^2\Sigma^+ \leftrightarrow X^2\Pi$  system of OH and OD in solid neon at 4.2°K has been studied by Tinti<sup>(21)</sup>. Emission spectra are recorded for the first time. According to Tinti, the emission spectra and part of the absorption spectra show an isotope effect and can be interpreted in terms of perturbed rotational motion in the solid.

Since the results of OH and OD in neon are different from those in the other rare gas matrices, we feel that the difference in characteristics of the hydroxyl-rare gas mixed crystals must be responsible. The physical sizes of the OH (or OD) radical and the neon atom are about the same. Furthermore, the melting point of neon (24.5°K) is closer to liquid helium temperature (4.2°K) than the melting points of argon (84.0°K), krypton (116.6°K), and xenon (161.2°K). Thus, the hydroxyl-neon system would form a nearly perfect crystal whereas OH (or OD) radicals may occupy the interstitial sites in the other rare gas matrices. If this explanation is true then the next promising experiment would be to try to grow some hydroxyl-

argon mixed crystals with suitable annealing.

## V. Summary

OH radicals have been trapped in argon, krypton and xenon matrices at 4.2°K. OD radicals have also been trapped in xenon matrices. The (0,0) and (1,0) bands of the  $A^2\Sigma^+ \leftarrow X^2\Pi_1$  transition are observed. A calculation of the vibrational constants in the solids lends support to the identification of OH and OD. A comparison of the observed fine structure with the gas phase rotational structure is made. However, no simple correlation can be established at the present time. Possible experiments are suggested.

## VI. Acknowledgement

The author wishes to express his appreciation to Professor G. W. Robinson for suggesting the problem. He wishes to acknowledge also the immense help given by Dr. R. P. Frosch in the experimental work. He is indebted to Dr. L. Keyser for many interesting discussions.

## Reference

1. Grebe and Holtz, *Annalen der Physik* 39, 1243 (1912).
2. M. G. Sastry, *Ind. J. Phys.* 16, 343 (1942).
3. T. Tanaka and Z. Koana, *Proc. Phys. Math. Soc. Japan* 16, 365 (1934).
4. O. Oldenberg, *J. Chem. Phys.* 3, 266 (1935).
5. A. M. Bass and H. P. Broida, "Formation and Trapping of Free Radicals" Chap. 4, (Academic Press, New York, 1960).

6. G. W. Robinson and M. McCarty, Jr., J. Chem. Phys. 28, 350 (1958).
7. G. W. Robinson and M. McCarty, Jr., Can. J. Phys. 36, 1590 (1958).
8. See for example the most recent papers by the following groups of authors, D. E. Milligan and M. E. Jacox, J. Chem. Phys. 40, 2461 (1964); G. E. Leroi, G. E. Ewing and G. C. Pimentel, J. Chem. Phys. 40, 2298 (1964).
9. R. P. Frosch and G. W. Robinson, J. Chem. Phys. 41, 367 (1964).
10. R. P. Frosch, Ph.D. thesis, California Institute of Technology, (1965).
11. L. J. Schoen and H. P. Broida, J. Chem. Phys. 32, 1184 (1960).
12. G. Herzberg, "Spectra of Diatomic Molecules", (D. Van Nostrand Co., Inc. 2nd edition, 1950) p. 560.
13. M. McCarty, Jr., and G. W. Robinson, J. Am. Chem. Soc. 81, 4472 (1959).
14. See Table 4.
15. Ref. 12, P.92 and P.142.
16. H. Oura and M. Ninomiya, Proc. Phys. Math. Soc. Japan 25, 335 (1943).
17. Ref. 12, P.242.
18. L. T. Earls, Phys. Rev. 48, 423 (1935).
19. E. Hill and J. H. Van Vleck, Phys. Rev. 32, 250 (1928).
20. Ref. 12, P.233.
21. D. S. Tinti, Ph.D. thesis, California Institute of Technology, to be published in 1967.

Proposition 4  
A STUDY OF THE ANGULAR DISTRIBUTION  
OF PHOTOELECTRONS

It is proposed that the angular distribution of electrons resulting from photoionization of atoms and molecules can be studied with the Lozier type direction-selecting grids.

I. Introduction

In the molecular photoionization process, the ejected electron carries practically all of the excess energy because of the small electron-to-molecule mass ratio. Thus, the ionization potential of the molecule can be obtained by measuring the kinetic energy of the ejected electron. If the molecule has more than one occupied molecular orbitals and the incident photon is energetic enough, ionization of more tightly bound electrons can occur. This gives a direct measurement on the energies of the molecular orbitals.

Turner and Al-Joboury (1) were the first to use the helium resonance line ( $584 \text{ \AA}$  or  $21.21 \text{ e v}$ ) to develop a molecular photoelectron spectrometer. Further work by Al-Joboury, May, and Turner (2,3) has successfully demonstrated that valuable information concerning higher ionization potentials, vibrational structures of the lowest and excited ionic states, bonding characteristics of the molecular orbitals, and Franck-Condon factors in ionization can be obtained from the photoelectron spectra of many diatomic and polyatomic molecules.

In the early version of Turner and Al-Joboury's

apparatus<sup>(1,2a)</sup>, cylindrically symmetric grids coaxial with the incident photon beam were employed to analyze the photoelectrons by the retardation potential method. The assumption was made that the emission of photoelectrons was in a direction parallel to the electric vector of the incident light, i.e., in a plane normal to its axis. (However, the magnetic field vector perpendicular to both the electric vector and the propagation direction of light was not considered.)

In 1964, Schoen<sup>(4)</sup> studied the photoionization of several diatomic molecules with a light source yielding monochromatic light in the region 500-1000 Å and a set of cylindrically symmetric grids similar to Turner and Al-Joboury's grid system<sup>(1,2a)</sup> to analyze the photoelectrons. Although the grids did not give rise to any directional selection, Schoen<sup>(4)</sup> did a calculation on the effect of angular distribution of photoelectrons and compared with the observed results. He concluded that the latter was far from the expected radial distribution but probably something between cosine square and isotropic distribution.

Recently, Frost, McDowell, and Vroom<sup>(5)</sup> studied the photoelectron spectra of diatomic molecules with the helium resonance line as light source and a spherical grid system to analyze the photoelectrons by the retardation potential method. They showed that the spherical grids centered on the ionization region gave much better resolution than the cylindrical grids coaxial with the light beam.

The first study on the angular distribution of photoelectrons has been reported recently by Berkowitz and Ehrhardt<sup>(6)</sup>. A photon beam of the helium resonance line at 584 Å is crossed at right angle with a molecular

beam, with the photoelectron detector scanning in a plane perpendicular to the latter. The results indicate that for argon and xenon the angular distribution function has a maximum at  $90^\circ$  and a small asymmetry in the forward-backward direction, favoring angles greater than  $90^\circ$ . Whereas for the lowest ionic states in  $N_2O$ ,  $NO$ , and  $O_2$  the angular distribution function is slightly in favor of the forward and backward directions instead of peaking at  $90^\circ$ .

A review on the previous investigations mentioned above seems to indicate that the angular distribution function of photoelectrons may be different for different molecules or even for different ionic states in the same molecule. Since there is no theory yet available<sup>(6)</sup> to adequately describe the angular dependence of photoelectrons resulting from non-central field systems, it occurs to us that experimental studies on this subject may lead to *better understanding of the problem.*

The purpose of this proposition is to suggest that the Lozier type direction-selecting grid systems<sup>(7)</sup> are specifically suitable for the photoelectron experiments.

## II. The Lozier type grids

The  $90^\circ$  Lozier type grids<sup>(7)</sup> have been adopted in the present thesis work of low-energy electron scattering. Similar application is found in the Penning ionization of molecules by metastable helium atoms<sup>(8)</sup>. It is obvious that directional sections at angles other than  $90^\circ$  can be achieved by constructing the grids from cone-shape metal plates instead of planar ones.

As described in Section IV.3.6. of the thesis, the percentage resolution of the Lozier grids is determined by the ratio of the separation of the plates to the annular path length. If the helium resonance line (21.21 e v ) is used as the light source then the energies of the photoelectrons will be about 10 e v or less. Thus, 1% resolution of the grids would correspond to an energy resolution of 0.1 e v or better

A major advantage of the Lozier grids is the long path-length. Since photon beams are much easier to collimate than electron beams, path-lengths up to 5 or 10 inches, say, should present no experimental difficulty.

In fact, the introduction of a light source (microwave discharge in low pressure helium gas) to replace the electron gun in the present 90° electron scattering apparatus will give rise to a photoelectron spectrometer immediately.

#### Reference

1. D. W. Turner and M. I. Al-Joboury, J. Chem. Phys. 37, 3007 (1962).
2. a). M. I. Al-Joboury and D. W. Turner, J. Chem. Soc. 5141 (1963).  
 b). same authors, *ibid*, 4434 (1964).  
 c). M. I. Al-Joboury, D. P. May, and D. W. Turner, *ibid*, 616 (1965).  
 d). Same authors, *ibid*, 6350 (1965).
3. a). D. W. Turner and D. P. May, J. Chem. Phys. 45, 471 (1966).  
 b). Same authors, *ibid*, 46, 1156 (1967).
4. R. I. Schoen, J. Chem. Phys. 40, 1830 (1964).

5. a). D. C. Frost, C. A. McDowell, and D. A. Vroom,  
Phys, Rev. Letters 15, 612 (1965).  
b). Same authors, J. Chem. Phys. 46, 4255 (1967).
6. J. Berkowitz and H. Ehrhardt, Phys, Letters 21, 531  
(1966).
7. W. W. Lozier, Phys. Rev. 44, 575 (1935).
8. V. Čermák, J. Chem. Phys. 44, 3774 (1966), and  
ibid, 44, 3781 (1966).

Proposition 5  
THE NEON RESONANCE LINE LAMP

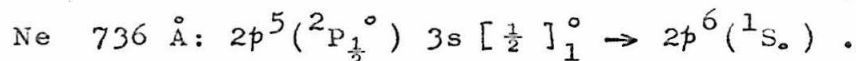
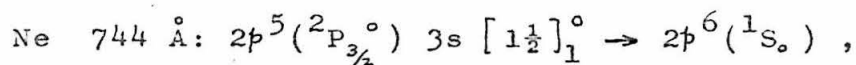
It is proposed that the neon resonance lines located at  $744 \text{ \AA}$  and  $736 \text{ \AA}$  can be used to develop a light source in the far vacuum UV region. Its significance in the studies of photoionization and photolysis of molecules is discussed.

-----

### I. Introduction

The most important characteristics of a light source for the interests of photochemistry are high intensity ( $10^{12}$  to  $10^{14}$  photons/sec) and chromatic purity. Rare gas resonance line lamps in the vacuum UV region have been shown (1-10) to possess these qualities and have been used by many investigators in recent years. For wavelength longer than the lithium fluoride<sup>(11)</sup> cutoff at  $1040 \text{ \AA}$ , resonance line lamps of xenon ( $1470$  and  $1296 \text{ \AA}$ ) and krypton ( $1236$  and  $1165 \text{ \AA}$ ) (1,2), and those of argon ( $1067$  and  $1048 \text{ \AA}$ ) (3-5) have been developed. In region beyond the LiF cutoff, resonance line lamps of helium ( $584 \text{ \AA}$ )<sup>(6-10)</sup> have been used. However, there seems to exist no similar application of neon in the literature.

The most intense neon resonance emission lines<sup>(8)</sup> are the ones located at  $744$  and  $736 \text{ \AA}$  (corresponding to  $16.68$  and  $16.83$  eV, respectively). The transitions are from the lowest excited states to the ground state and are represented as follows<sup>(12)</sup>.



The energies of these resonance lines lie in between those of argon (11.6 and 11.8 ev) and that of helium (21.21 ev).

The purpose of this proposition is to suggest the development of the neon resonance line lamps because of photochemical interests.

## II. Photoionization Studies

In principle, the photoionization cross sections of atoms and molecules can be calculated with quantum mechanical methods. An expression for the ionization cross section of atoms has been discussed by Bates<sup>(13)</sup>. It reads

$$Q_{\nu} = \frac{32\pi^4 m^2 e^2}{3\hbar^3 c} \cdot \frac{1}{\omega_i} \sum_i \sum_f (\nu \nu') \left| \int \Psi_i^* \left( \sum_j \vec{r}_j \right) \Psi_f d\tau \right|^2,$$

where  $\nu$  is the frequency of the incident radiation,  $\nu'$  is the velocity of the ejected electron,  $\Psi_i$  is the wave function for the atom in its initial state with the statistical weight  $\omega_i$ ,  $\Psi_f$  is the wave function for the ionized atom together with the outgoing electron, and  $\vec{r}_j$  is the position vector of the  $j$ -th electron with the  $\sum_j \vec{r}_j$  characterizing the dipole moment.

In order to calculate the cross sections, good wave functions are needed. This presents practical difficulties. Therefore, we usually obtain information concerning cross sections from experimental measurements. Early work in this field has been summarized by Weissler<sup>(14)</sup>, and Ditchburn and Öpik<sup>(15)</sup>. Recently, photoelectron spectroscopy has been developed by many authors<sup>(16)</sup> with the helium resonance line at 584 Å as the light source.

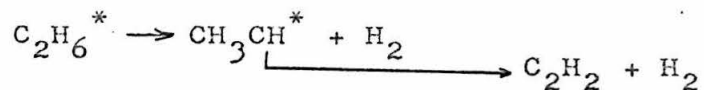
From the available experimental results<sup>(14)</sup>, it is

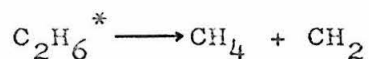
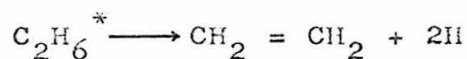
clear that the photoionization cross sections are energy dependent. Generally, they increase with increasing photon energy after threshold towards a maximum, then decrease with further increase of energy. Therefore, photoelectron experiments with photon energies different from that of the  $584 \text{ \AA}$  helium resonance line would certainly yield information on the energy dependence of various ionization processes.

### III. Vacuum UV Photochemistry

Photolysis studies on organic as well as inorganic compounds have been of interest to many workers<sup>(2)</sup>. The purpose of these experiments is to investigate the elementary processes and chemical kinetics involved in the photolysis of molecules as a function of photon energy and other initial conditions by measuring the distribution of the various products present after the UV irradiation. (From spectroscopic experiments one can tell at what energies electronic states are located. From photolysis experiments one studies the chemical properties of these electronic states).

Let us consider the photolysis of ethane<sup>(2,3,17)</sup> for an example. Ethane has been photolyzed at the resonance lines of xenon and krypton<sup>(2,17)</sup> and those of argon<sup>(3)</sup>. The photolysis products consist of hydrogen, ethylene, acetylene, propane and n-butane. By photolyzing mixtures of  $\text{C}_2\text{H}_6$  and  $\text{C}_2\text{D}_6$  as well as  $\text{CH}_3\text{CD}_3$ , the following primary processes have been identified. (The star \* means excited species).





However, it seems that most of the work done so far is at wavelength longer than that of the LiF cutoff<sup>(11)</sup> at about 1040 Å.

Photoelectron experiments by Al-Joboury and Turner<sup>(18)</sup> have shown that ethane has ionization potentials at 11.48 and 14.74 ev. Recently, Berkowitz, Ehrhardt, and Tekaas<sup>(19)</sup> confirmed these values with a crossed-beam photoelectron spectrometer. By taking the derivative of the photoelectron energy curve, they<sup>(19)</sup> obtained the energy-absorption spectrum of ethane. This spectrum shows that the two ionization potentials of ethane are from different molecular orbitals. Therefore, photolysis with photon energies higher than the second I.P. of ethane (such as from the neon resonance line lamps) would demonstrate the participation and importance of the second ionic state in the chemistry on ethane.

#### IV. Experimental Considerations

The construction of the neon resonance line lamp may be very similar to that of helium<sup>(7-10)</sup>, i.e., a differential pumping system is needed to separate the discharge region from the reaction or ionization region. The low pressure discharge technique<sup>(1-10)</sup> used in other rare gas resonance line lamps can hopefully be applied to neon.

In photoelectron experiments, care must be taken on the 0.15 ev energy difference between the two neon

resonance lines. If the two lines have comparable intensities, then the observed photoelectron energy spectrum would be the resultant of two spectra, each originating from one resonance line.

In photolysis studies, the construction of the irradiation cell would be simpler if a thin metal film could be used to withstand a small pressure difference between the differential pumping region and the reaction cell. Such a film could be an aluminum foil which is transparent to far UV light<sup>(9)</sup>. Several ways to analyze the reaction products in the absence of such metal films are as follows.

a) The products can be frozen out on a cold finger downstream from the photolysis region. They can then be studied spectroscopically.

b) A mass spectrometer can be used with the ion source mounted close to the irradiation region.

c) The gas sample after irradiation can be stored in a pre-evacuated bulb for gas chromatographic analysis.

In case a windowed cell is available, the reaction products can be transferred from the cell to a storage bulb with a Toepler pump.

### References

1. H. Okabe, J. Opt. Soc. Am. 54, 478 (1964).
2. H. Okabe and J. R. McNesby, Adv. Photochem. 3, 161 (1964).
3. A. H. Laufer and J. R. McNesby, J. Chem. Phys. 42, 3329 (1965).
4. P. Ausloos and S. G. Lias, J. Chem. Phys. 45, 524 (1966).
5. A. L. Lane and A. Kuppermann, Rev. Sci. Instr., forthcoming.

6. R. A. Back and D. C. Walker, J. Chem. Phys 37, 2348 (1962).
7. M. I. Al-Joboury and D. W. Turner, J. Chem. Soc. p. 5141 (1963).
8. R. E. Huffman, Y. Tanaka, and J. C. Larrabee, Applied Opt. 2, 617 (1963).
9. C. A. Jensen and W. F. Libby, Phys. Rev. A136, 1247 (1964).
10. D. C. Frost, C. A. McDowell, and D. A. Vroom, Proc. Roy Soc. (London) A296, 566 (1967).
11. H. Friedman; in "Physics of the Upper Atmosphere", edited by J. A. Ratcliffe, (Academic Press, New York, 1960) p.160.
12. C. E. Moore, "Atomic Energy Levels", (National Bureau of Standards Circular 467, 1949) p. 76.
13. D. R. Bates, Monthly Notice, Roy. Astron. Soc. 106, 432 (1946).
14. G. L. Weissler, in "Handbuch der Physik", ed. Flugge, (Springer Verlag, Berlin, 1956), vol.21, pp. 304-382.
15. R. W. Ditchburn and U. Öpik, in "Atomic and Molecular Processes", ed. by D. R. Bates, (Academic, New York, 1962), pp. 72-99.
16. For a review, see proposition 4 and the references cited therein.
17. R. F. Hampson, Jr., and J. R. McNesby, J. Chem. Phys. 42, 2200 (1965).
18. M. I. Al-Joboury and D. W. Turner, J. Chem. Soc. 4434 (1964).
19. J. Berkowitz, H. Ehrhardt, and T. Tekaas, Z. Physik 200, 69 (1967).

## VITA

Pax Samuel Pin Wei was born November 11, 1938 in Chungking, China. He attended primary and secondary school in Taipei, Taiwan, China. In June, 1960 he received the degree of Bachelor of Science from the National Taiwan University in Taipei. In June, 1963 he received the degree of Master of Science from the University of Illinois, Urbana, Illinois. In September, 1963 he entered graduate school at the California Institute of Technology.